UNIVERSITY OF BIRMINGHAM

New Considerations and Approaches to the Detection of Overhead Cables by Radar

by

Ben Willetts

A thesis submitted to the University of Birmingham

for the degree of

Doctor of Philosophy

School of Engineering
College of Engineering and Physical Sciences
University of Birmingham
January 2018

Abstract

This thesis reports on research into the electromagnetic backscatter from overhead power cables as this method of distributing electrical power is hazardous to aircraft flying at low-altitudes especially during periods of low visibility. The work presented intends to improve current overhead cable detection techniques by using high-resolution millimetre-wave devices which will also allow compact devices that can be practical on a variety of airborne platforms such as manned aircraft, unmanned aerial vehicles and drones.

The research also presents cable measurements obtained by airborne radar devices that operate at lower frequency bands, Ka-band and Ku-band, which were able to identify power line vulnerabilities due to a change in cable tautness along a power line. The effect of cable tautness on cable signatures measured by currently operating Ka-band and Ku-band devices on board a manned aircraft are supported by a cable sag model described.

A modern, more efficient, overhead power cable type ACCC (Aluminium Conductor Composite Core) is also discussed and the effect of the less prominent surface structure of this cable type, relative to the most commonly used type of overhead power cable ACSR (Aluminium Conductor Steel Reinforced), on the backscattered radar signature is compared using both modelled and measured results for both cable types. The scattering model and measurements presented in this research are the first ever quantitative results reported for the ACCC type of cable.

Publications

Journal papers

B. Willetts, M. B. Stevens, M. Gashinova and A. G. Stove, "Spectrum analysis of high resolution SAR data to obtain Bragg signatures of Power Cables,", IEEE Geoscience and Remote Sensing Letters, Submitted June 2017. Accepted August 2017. Final Submission not completed due to IP restrictions set by the industrial sponsor.

B. Willetts, M. B. Stevens, M. Gashinova and A. G. Stove, "Spectrum analysis of high resolution SAR data to obtain Bragg signatures of Power Cables,", IET Radar, Sonar & Navigation, accepted April 2018.

Conference papers

B. Willetts, M. Gashinova, A. Stove, C.C. Constantinou, E.G. Hoare, E. Marchetti, Low-THz "Overhead Power Cable Signatures: The effect of surface features on Low-THz reflectivities", 2016, 17th International Radar Symposium (IRS).

B. Willetts, M. Gashinova, A. Stove, C.C. Constantinou, E.G. Hoare, "Low-THz Rough Surface Imaging", 2016, 2016 European Radar Conference (EuRAD).

B. Willetts, M. Gashinova, A. Stove and C.C Constantinou, "Distinguishing surfaces with different roughness characteristics by using a wideband 300 GHz device", 2017, 18th International Radar Symposium (IRS).

B. Willetts, M. Stevens, A. Stove, M. Gashinova, "Overhead Power cable Bragg signatures in Ka and Ku band high-resolution SAR imagery", 2017, IET RADAR 2017**.**

Fatemeh Norouzian, Feng Qi, **Ben Willetts**, Marina Gashinova, Costas Constantinou, Peter Gardner; Edward Hoare, Mikhail Cherniakov, “Characterisation of Attenuation at Low THz Frequencies in Radar Sensors”, 2015, 2015 European Radar Conference (EuRAD).

Rui Du, Fatemeh Norouzian, Emidio Marchetti, **Ben Willetts**, Marina Gashinova, Mikhail Cherniakov, “Characterisation of Attenuation by Sand in Low-THz Band”, 2017, 2017 IEEE Radar Conference.

Abbreviations

2D	Two Dimensional
3D	Three Dimensional
ACCC	Aluminium Conductor Composite Core
ACSR	Aluminium Conductor Steel Reinforced
ADC	Analogue to Digital Converter
CR	Cross Range
DFT	Discrete Fourier Transform
DR	Down Range
DSP	Digital Signal Processor
EM	Electromagnetic
FFT	Fast Fourier Transform
FIR	Far Infrared
FMCW	Frequency Modulated Continuous Wave
FMICW	Frequency Modulated Interrupted Continuous Wave
GMTI	Ground Moving Target Indicator
IF	Intermediate Frequency
IFFT	Inverse Fast Fourier Transform
IR	Infrared
ISAR	Inverse Synthetic Aperture Radar
ITU	International Telecommunication Union
LIDAR	Light Detection and Ranging
Low-THz	Low Terahertz
LFMCW	Linear Frequency Modulation Continuous Wave

MISL	Microwave Integrated Systems Laboratory
MTI	Moving Target Indication
mmW	Millimetre wave band
NF	Noise Floor
OH	OverHead
PEC	Perfect Electric Conductor
PRF	Pulse Repetition Frequency
RADAR	Radio Detection and Ranging
RCS	Radar Cross Section
RF	Radio Frequency
Rx	Receiver
SAR	Synthetic Aperture Radar
SCR	Signal to Clutter Ratio
SFR	Stepped Frequency Radar
SLAR	Side-Looking Airborne Radar
SLC	Single-Look Complex
SMA	Sub Miniature version A (coaxial connector type)
SNR	Signal to Noise Ratio
THz	Terahertz
TR	Transceiver
Tx	Transmitter
UV	Ultraviolet
VNA	Vector Network Analyser

Contents

1. Introduction

The Introduction section of the thesis explains why overhead power cable detection using radar devices is necessary to improve the safety of aircraft flying at low altitudes. The section will also briefly discuss the emergence of radar devices in the early 20th century as well as the main parameters that are considered when designing a radar system to perform a specific purpose. The analytical RCS theory for a perfectly smooth cylinder will be displayed that explains the main electromagnetic scattering regions that exist for different wavelength-to-target size ratios. The specular, Bragg and diffuse scattering phenomena will be discussed which encompasses the effects of random surface roughness and deterministic surface periodicity of radar targets. The chapter will finish off with a review of OH power cable detection literature which will put across the measured backscattering from OH power cables for a wide-range of electromagnetic frequency bands.

1.1 Motivation

Due to the fact that Overhead (OH) power cables were the cause of numerous fatal accidents, in the 21st century alone [1]-[3], the operational requirements of a system that can detect the presence of such obstacles are the motivation for this research. The research intends to produce both simulations and measurements that will help in the design of a compact system that can be mounted onto both manned and unmanned aircraft. This system should allow future airborne vessels to react in time to avoid causing a collision when a power cable is in the vicinity of its flight trajectory even whilst operating in adverse weather conditions (Figure 1-1).

Due to the fact certain airborne radar applications require compact devices, low atmospheric losses and an adequate level of range resolution to detect features of potential targets, the frequency range of interest here is 10-300 GHz. Reliable detection of the cables

requires fast scanning over a wide field of view with high resolution, i.e. with a relatively large antenna and at microwave frequencies the scanning system is too large and heavy to justify its place in a small aircraft in comparison with other safety aids. An obvious alternative to the previously stated range of frequencies is the systems that make use of infrared (IR) waves [4][5], and measurements of cables have also been made at such wavebands, but since the atmospheric attenuation, particularly in fog, is much higher at these wavelengths , it has again proved impossible to design systems which are able to detect the cables at the desired range whilst remaining small and light enough to justify their place on the aircraft. A further important requirement for an airborne cable detection system is fast scanning which can be easily achieved with a single beam configuration with a fine range resolution which will also allow a wide field of view at the ranges required.

Figure 1-1: Low flying aircraft in a dangerous environment containing OH power cable [6]

It is a realistic expectation that as technology becomes more mature at the upper end of the millimetre-wave band of frequencies (>100 GHz) [7] [8] and within the Terahertz region

(>300 GHz), wire avoidance systems will still have sufficient atmospheric penetration to detect hazardous cables whilst also being compact enough to operate on small aircraft.

Since the work on millimetre-wave obstacle avoidance systems during the late 1980's there has also been a great increase in the number of unmanned air vehicles, many of which might also benefit from wire-avoidance systems, although the greatest desire to design such systems is the requirement to protect the safety of the occupants of manned aircraft.

The application of modern research that relates to the design and processing of transmitted/received waveforms is expected to allow further enhancement of any airborne measurements although this aspect of the system will not be the focus of this work. The well documented coupling between Doppler and range in linearly modulated chirps, which is discussed in the classical Bell Labs journal paper [9], will not need to be considered in the work presented due to a stationary setup being used or because a compensation has been applied to negate this effect.

1.2 Radar: Definition and Basic Operation

1.2.1 Definition

A radar (RAdio Detection And Ranging) device is a system that makes use of Electromagnetic (EM) waves to detect and estimate the location of an object. According to [10], the first known device to use electromagnetic waves for this application was realised by a young German engineer named *Christian Hülsmeyer*, who in 1904 constructed and demonstrated a radio device that could detect ships and went on to patent the invention. Such a device was required by *Hülsmeyer* when human sight was inadequate to perceive approaching ships at sea when foggy conditions were present. *Hülsmeyer* had witnessed an accident between two ships and this went on to motivate him to build a radar device that can warn crew

on-board a ship of any impending collisions. This concept of using radar to detect objects then went on to be critical during and after WWII in a variety of military and civilian applications such as those based on ground (Chain-Home [10]), mounted on aircraft (H2S [11]) as well as for *Hülsmeyer's* initial maritime application.

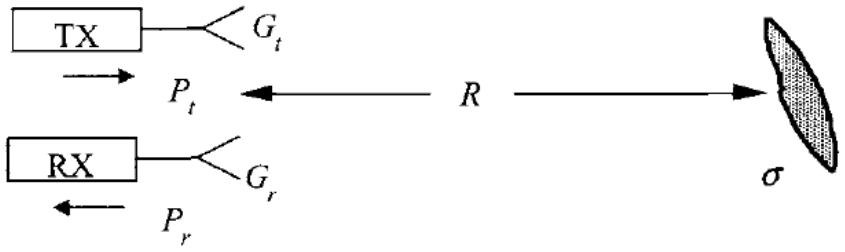

Figure 1-2: Monostatic radar configuration illuminating a target with radar-cross-section σ at distance *R* [12]

The only type of radar of interest in this thesis is the monostatic type of radar configuration that has the receiver and transmitter producing and intercepting electromagnetic echoes at the same location (illustrated in Figure 1-2) that are usually coupled in operation. The term transceiver will be used here-on to combine the transmitter and receiver that jointly perform the detection of objects.

The advent of radar systems in the early 20th century is largely due to the lower atmospheric loss and better propagation attainable at microwave frequencies together with the fact that human vision has a relatively limited view for distances of more than a few hundred metres even in clear conditions. A vast range of frequency bands including the microwave and visible parts of the EM spectrum are visible in Figure 1-3. The rapid growth of the number and capability of potential targets, especially aircraft and missiles, required detection at a range of many kilometres to have an adequate reaction time to deal with the threat and thus furthered the need for devices with better detection capabilities than that achievable with human sight alone.

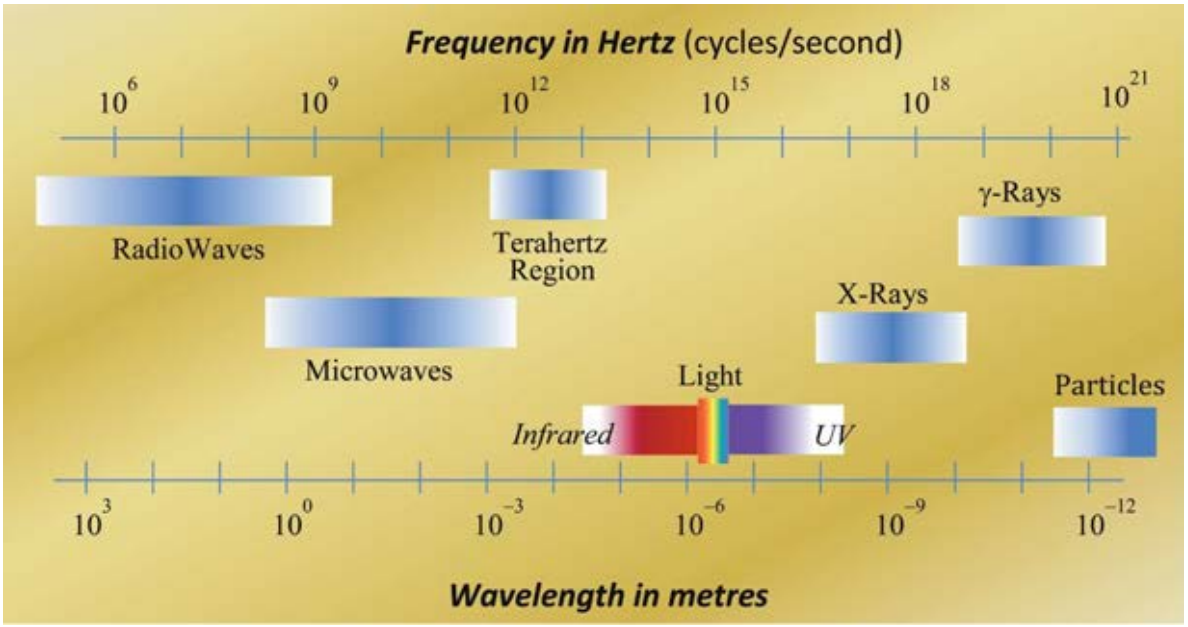

Figure 1-3: Definition and placement of electromagnetic frequency bands within the known EM spectrum [13]

1.2.2 Radar equation

A very useful mathematical expression that encompasses the main parameters when estimating the required system specifications to detect a target of interest is the radar equation used to estimate Signal to Noise Ratio (SNR) (Equation 1-1)[14]. The power losses within a transceiver device is incurred by multiple subsystems such as Mixers, Amplifier and Filters and the effect of these are all usually incorporated into a parameter called the Noise Figure F_n.

$$SNR = \frac{P_{av} G^2 \lambda^2 \sigma}{(4\pi)^3 R^4 k_B T B_n F_n L}$$

Equation 1-1: Radar Equation in Signal Noise Ratio format [14]

where

P_{av} – Average transmit Power [W]

G – Antenna Gain [dBi]

λ – Wavelength [m]

σ – Radar Cross Section [m^2]

R – Range [m]

K_B – Boltzmann Constant ≈ 1.381e-23[m^2 kg s^{-2} K^{-1}]

T – Receiver Temperature [K]

B_n – Receiver Bandwidth [Hz]

F_n – Noise Figure (Equation 2) [Dimensionless]

L – Atmospheric attenuation [Dimensionless]

The radar equation (Equation 1-1) and the equation for the average power of a pulsed waveform (Equation 1-2) jointly create a compromise between resolution (Equation 1-3) and the signal-to-noise ratio.

An additional method of increasing the SNR would be the combining of multiple (n) received pulses (Equation 1-4), if these pulses are fully correlated with coherent integration an ideal gain (neglecting post detection losses) (G^n) of N can be achieved whilst the ideal maximum gain from a completely uncorrelated or partially correlated set of returns that are coherently summed will be a smaller value determined by the probability density function for the specific target type. The fluctuations in target magnitude and phase decides the correlation between consecutive returns and this will decide the amount of gain that con be accumulated. If instead non-coherent (or amplitude) integration is performed over n returns then an estimated maximum integration gain $G^n=\sqrt{N}$ can be used [14].

Match filtering by using prior knowledge of the waveform can further increase the signal-to-noise ratio for each individual detection although a technique known as pulse compression which makes use of frequency/phase modulation can allow a relatively large average power to be transmitted whilst having fine resolution in range compared to traditional pulsed systems.

$$P_{av}^{pulse} = \frac{P_t \tau}{T_P}$$

Equation 1-2: Average Power ($P_{av}{}^{pulse}$) of a pulse waveform in terms of peak power P_t, Pulse duration τ and pulse repetition period T_p

$$\Delta r^{pulse} = \frac{c\tau}{2}$$

Equation 1-3: Theoretical range resolution (Δr^{pulse}) for a pulse waveform in terms of the speed-of –light $c\approx 2.998e8$ ms^{-1} and pulse duration time τ

$$SNR^n = G^n SNR$$

Equation 1-4: Signal to Noise Ratio accumulated (SNR^n) after combining n returns in terms of that for single pulse SNR

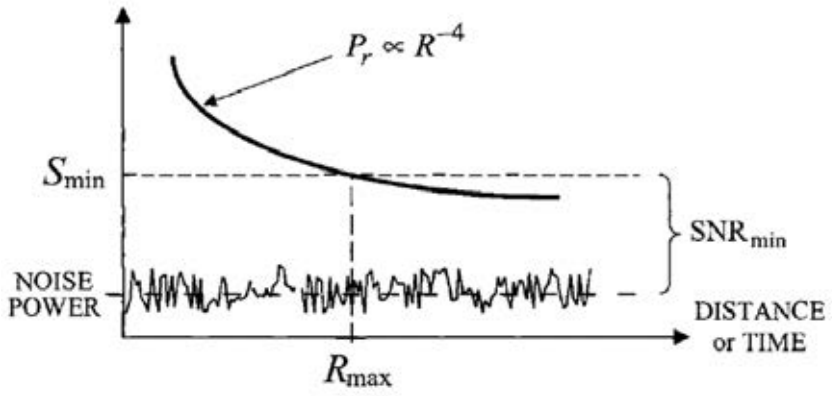

Figure 1-4: Signal with respect to distance which shows the noise power and noise figure concept [12]

Figure 1-4 shows the theoretical R^{-4} relationship for received power whilst also displaying the minimum power measurable due to other loss parameters that exist alongside thermal noise. This theoretical range relationship is obtained from the inverse-square law assumption for the propagation of a spherical EM wave propagating along free-space with a point source at both the transceiver and point target. In reality, both the aperture of the antenna and illuminated target are both finite in size and the physical extent of both, as well as the range between them, will have an effect on the relationship between the return signal and the range of the target.

Another important parameter which develops out of the physical extent of both the antenna and illuminated target is the *Fraunhofer* or far-field criterion.

$$R_F = \frac{2D_{extent}^{\ 2}}{\lambda}$$

Equation 1-5: Far-field distance in terms of the largest extent of a illuminated target or antenna and the wavelength [15]

The far-field distance (Equation 1-5) assures that the EM wave produced by an object (antenna or target) with the largest extent (D_{extent}) is planar because of negligible phase change ($\pi/8$) at this distance and thus can be thought of as a superposition of rays that are parallel to each other. Satisfying the far-field distance simplifies the modelling of both the antenna radiation pattern and also target scattering. Illuminating objects at distances smaller than this value will typically produce nulls in the antenna pattern and increase the magnitude of side lobes and hence can reduce the angular resolution of the system which is usually not desirable.

In radar applications, the term antenna is used for a device that is used to convert electronic signals to electromagnetic waves (or vice-versa) which makes the parameters of such a device imperative to the transmission and reception of EM waves. The antenna Gain (Equation 1-6) is one important parameter, particularly to designers of airborne devices, as it decides the weight and dimensions of the antenna being used to produce controllable propagating electromagnetic waves that can travel at close to the speed of light (≈2.998e8 m/s). A larger antenna that has a larger physical area ($A_{physical}$) will typically produce a larger gain (Equation 1-6, Equation 1-7 and Equation 1-8) for a given efficiency η and thus will have the capability of detecting objects at larger distances. The physical size of an antenna is not a huge issue for ground based radars as such, but becomes an important parameter for airborne systems especially for systems that require to physically rotate the antenna rapidly in order to perform a scan of the surrounding environment. The larger the wavelength the smaller the expected gain which as previously discussed gives a typically lower atmospheric loss and this relationship creates a compromise for a radar designer.

$$G = \frac{4\pi A_e}{\lambda^2} \qquad \text{where} \qquad A_e = A_{physical}\eta$$

Equation 1-6: Gain and effective aperture (A_e) relationship with the proportionality of A_e with the physical antenna area ($A_{physical}$) and antenna efficiency (η) [15]

$$D_H \approx \frac{\lambda}{3.413\sin(\Delta\theta^{3dB})} \text{ and } D_E \approx \frac{\lambda}{3.413\sin(\Delta\phi^{3dB})}$$

Equation 1-7: Diameters of a circular horn antenna in both E-plane and H-plane with respect to 3dB beamwidths (radians) in azimuth and elevation [15]

$$G \quad \frac{\pi^2}{\Delta\theta^{3dB}\Delta\varphi^{3dB}}$$

Equation 1-8: Approximation of antenna gain for a Gaussian beam shape in terms of the 3dB beamwidths (radians) in elevation and azimuth [15]

The transmit power and receiver noise parameters relate to the maturity of devices for a specific frequency band. Different industries have made technological advancements which has enabled mass manufacture at specific frequency ranges. Technology advancements in the design and development of frequency multiplies/dividers broadens the possibility of getting adequate transmit oscillators and receiver parameters. To discuss the advancements made in the design and manufacture of subsections (such as oscillators, antennas and receivers) both during the 20th and 21st centuries would be a momentous task and would be of little value in the thesis. Fortunately, Table 1-1 was presented in [16] and shows applications that are deemed suitable for radar devices that make use of specific frequency bands.

Table 1-1: Typical applications for devices using microwaves up to Ultraviolet [16]

Band Designation	Frequency Range	General Use
VHF	30-300 MHz	Over the horizon radar, communications
UHF	300-1000 MHz	Ground penetrating , communications
L	1-2 GHz	Ground surveillance, astronomy
S	2-4 GHz	Ground surveillance
C	4-8 GHz	Space-based SAR
X	8-12 GHz	Fire control, proximity, airborne/space SAR
K_u	12-18 GHz	Collision avoidance, speed traps
K	18-27 GHz	Fire control radar, collision avoidance
K_a	27-40 GHz	Fire control radar, surveillance
Millimetre	40 – 300 GHz	Astronomy, collision avoidance, missile seekers
Submillimetre	>300 GHz	Astronomy, detection of explosives
Band Designation	Wavelength Range	General Use
Far IR	14-50 um	Properties of molecules
Mid IR	3-5 um	Missile seekers
Long-wave IR	8-14 um	Laser radar, forward-looking IR
Near IR	1-3 um	Personnel detection
Very near IR	0.76-1 um	Imaging, laser ranging (industrial)
Visible	380-760 nm	Imaging, astronomy
Ultraviolet	100-380 nm	Missile plume detection, gas fire detection

1.2.3 Radar Cross Section

σ in Equation 1-9 represents the Radar-Cross-Section (RCS) which is highly dependent on both the target characteristics and the frequency of the transmitted wave [17]. To simplify the EM backscatter calculation from the target when illuminated by a monostatic radar device the concept of RCS was developed. RCS is a theoretical concept that applies to completely illuminated, deterministic targets that exist in the far-field (Equation 1-5) of the radar and thus ideally have a wave-front that is planar in order to simplify target return estimates. Equation 1-9 is a qualitative description of RCS whereas Equation 1-10 is approximately the same concept but in a mathematical format. Due to the typical variations in target returns, especially for a realistic target being illuminated by a millimetre-wave device, the parameter is usually described using the decibel format (dBsm/dBm^2) rather than with linear units (Equation 1-11).

σ = *(total scattered power [W]) / (Incident power density [Wm^{-2}])*

Equation 1-9: Concept of Radar Cross Section in a qualitative form [17]

$$\sigma = \lim_{R\to\infty}\left(4\pi R^2\right)\frac{\left|\mathbf{E_s}\right|^2}{\left|\mathbf{E_i}\right|^2}$$

Equation 1-10: Mathematical definition of Radar Cross Section [17]

$$\sigma[dBsm] = 10\log(\sigma[m^2])$$

Equation 1-11: conversion of RCS from linear units (m^2) to the more widley used logarithmic units (dBsm)

The RCS parameter incorporates different phenomena depending on the ratio between the target dimensions and wavelength, the following three scattering regions can be observed:

- *Rayleigh region* ($L/\lambda<<1$): when the dimensions of the target in the propagation plane are small compared to the wavelength, the phase variation on the surface can be considered zero causing the amplitude and phase of the induced currents to be

approximately constant. Body shape has little effect for this scattering region. The RCS with respect to changes in wavelength in this region fits very well to λ^{-4}.

- *Resonance region* ($L/\lambda \approx 1$): within this region the phase variations become significant due to the effect of constructive and destructive interference along the target surface which allows phase variations to significantly contribute to the scattering pattern. This effect leads to oscillatory behaviour in the wavelength dependence of RCS.
- *Optical region* ($L/\lambda >> 1$): due to a large number of wavelengths across the target's surface in this region, a very large dependence on the angle of the incident wave will be present for complex targets. Large amplitudes in the backscatter will be from isolated points for smooth targets [17].

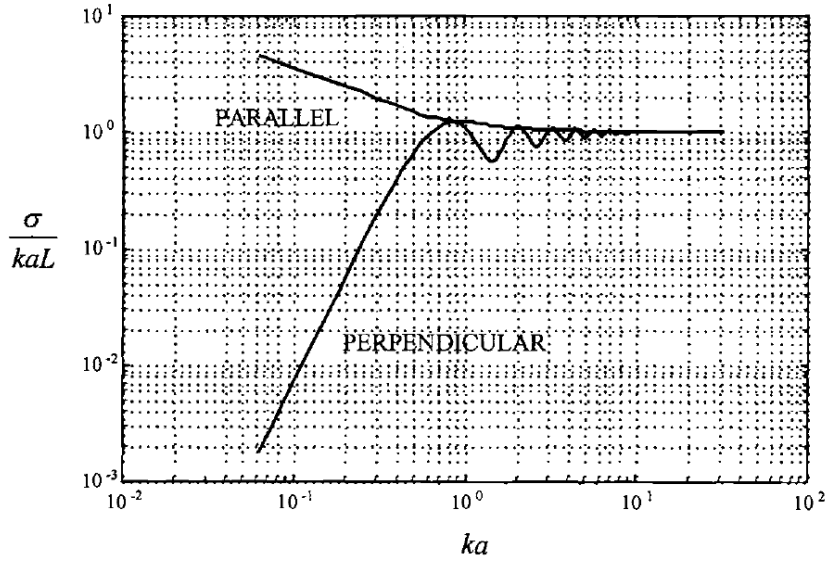

Figure 1-5: RCS of a Perfect Electrical Conductor (PEC) cylinder of radius *a* and length *L* [12]

A fundamental shape that has an analytical solution in terms of the wavelength dependence of RCS is a smooth cylinder of length *L* and radius *a*. Figure 1-5 shows the RCS normalised to the dimensions of a PEC smooth cylinder for two different polarizations of the electric field. The perpendicular behaviour nicely shows the three scattering regions discussed previously when the incident wave is at normal incidence with the cylinder. When the phase constant is much less than the cylinder radius, the λ^{-4} dependence can be seen up to *ka* is just

below unity in which a series of maxima and minima occur which dampen as *ka* goes to infinity and oscillates around the optical RCS value, *kaL*.

The angular dependence of the RCS of a smooth PEC cylinder can also be derived with a simple analytical solution (Equation 1-12) and the parameters of this equation are visible in Figure 1-6. A more accurate derivation is available in [17] although this is a lot more complex than Equation 1-12 but this added complexity doesn't improve the accuracy significantly. A plot that uses Equation 1-12 to show the effect of a change in cable length on the RCS is shown in Figure 1-7 which concludes that the larger the cylinder, the narrower the main and side lobes present on the pattern and thus the more rapid fluctuation there will be when a deviation in angle is present off-normal. Figure 1-8 instead shows the effect of different radius sizes and concludes that this has a significant effect on the amplitudes of the angular profile of the cylinder and not on the lobe widths.

$$\sigma_{cyl} = \frac{2\pi r l^2}{\lambda}\left|\cos\theta \frac{\sin\left(\frac{2\pi l}{\lambda}\sin\theta\right)}{\frac{2\pi l}{\lambda}\sin\theta}\right|^2$$

Equation 1-12: Analytical Physical Optics solution for the RCS of a smooth PEC cylinder [17]

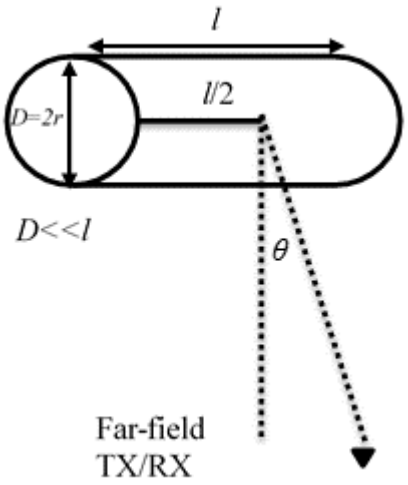

Figure 1-6: Diagram that shows the geometrical proporties of a rotating thin cylinder

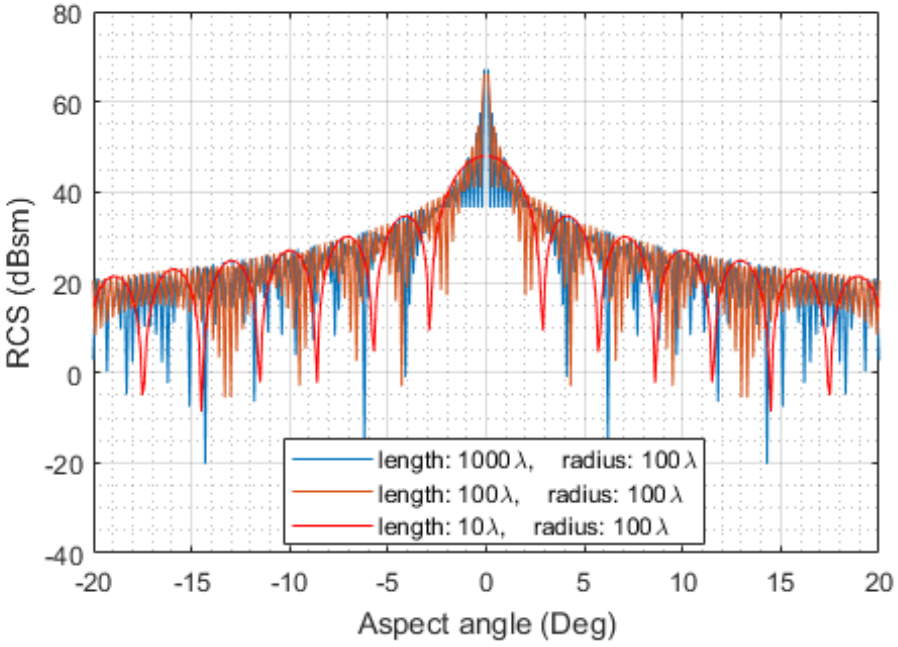

Figure 1-7: Theoretical RCS of a smooth PEC cylinder of different lengths with respect to aspect angle

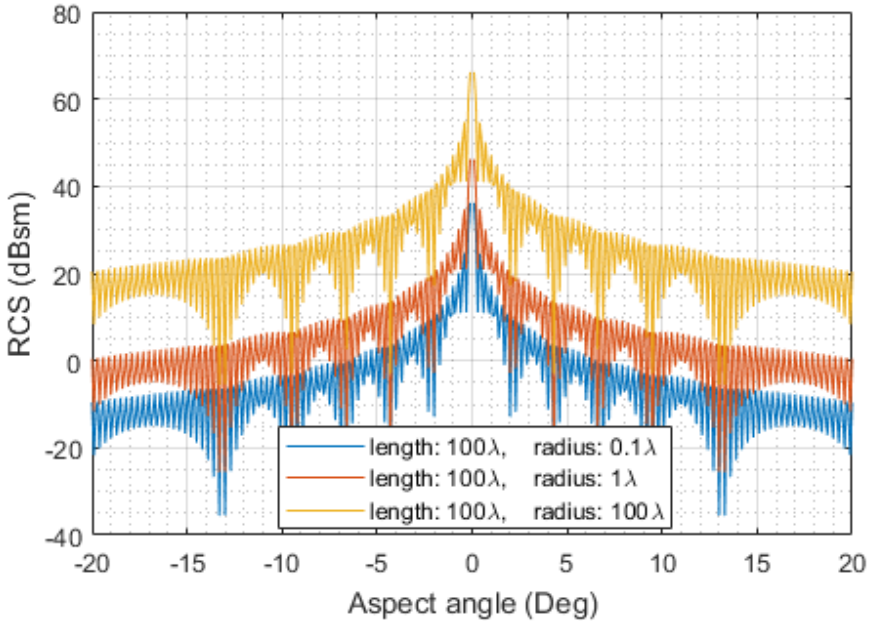

Figure 1-8: Theoretical RCS of a smooth PEC cylinder of different radii with respect to aspect angle

An important factor to note that is discussed in [18], is the effect of illumination length as Figure 1-7 has shown that this will decide the lobe widths of the angular response and this will have a huge effect on detectability. [18] states that for a thin straight cable with a plane-wave incident upon its surface, the majority of backscatter due to phase variations along the wave front will reside in the first Fresnel zone that corresponds to Equation 1-13. This assumed that cable sagging has a negligible effect on the phase variation at detectable distances and that the surface roughness is also negligible at the incident wavelength.

$$L_{fresnel} = 2\sqrt{\lambda R}$$

Equation 1-13: Theoretical Fresnel length for a narrow wire with an incident planar-wave [15]

This thesis concerns the scattering and detection from cylinders with a helical surface pattern although this type of target is expected to behave as a smooth cylinder at frequencies below 10 GHz due to the expected Bragg lobe angles lying outside the range of the surface normal.

1.3 Electromagnetic Scattering

The effect of surface structure, roughness and periodicity when comparable to the incident wavelength, on the scattering of electromagnetic waves will be discussed in this section due to its importance in overhead power cable detection when the wavelength is comparable to the surface structure dimensions.

1.3.1 Specular

The specular component of scattering is when the angle of reflection is equal to the angle of incidence with respect to the surface normal of the illuminated surface. This type of scattering will dominate when the surface micro geometry are minute compared to the phase variation present and so the difference in the macro geometry alignment with respect to the incident vector will dominate.

As aluminium is typically used to construct the outer strands of OH power cables, the subsurface scattering and effect of the refractive index will be neglected due to the very high conductivity.

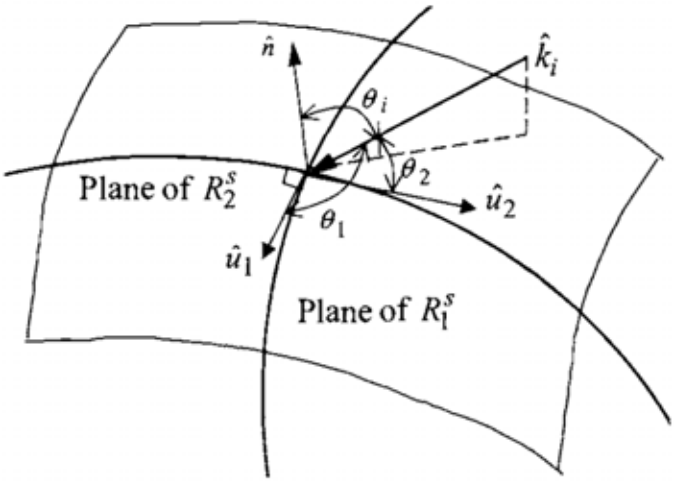

Figure 1-9: Incident and reflected vector for a curved surface using Snell's law [12]

Figure 1-9 shows a point of reflectance on a surface with a facing vector (or unit surface normal vector) $\dot{n}$, with a wave in the direction, k_i, rebounding from the surface. Equation 1-14 and Equation 1-15 shows the vector manipulation required to calculate the vector direction of the reflected wave. Equation 1-14 is known as the vector form of Snell's law. The specular component of the reflection from a smooth surface will have the majority of energy and thus will have a relatively large amplitude. For an illuminated patch, the specular region will reside in the area where the phase changes do not deconstructively interfere and hence will reduce in size at small wavelengths.

$$\hat{k}_r = \hat{k}_i - 2(\hat{n} \cdot \hat{k}_i)\hat{n}$$

Equation 1-14 : Vector form of Snell's law

$$[\theta_i, \theta_1, \theta_2] = [\cos^{-1}\left(\hat{n} \cdot \hat{k}_i\right), \cos^{-1}\left(\hat{u}_1 \cdot \hat{k}_i\right), \cos^{-1}\left(\hat{u}_2 \cdot \hat{k}_i\right)]$$

Equation 1-15: Angles of the reflected vector notated in Figure 9 [12]

1.3.2 Diffuse

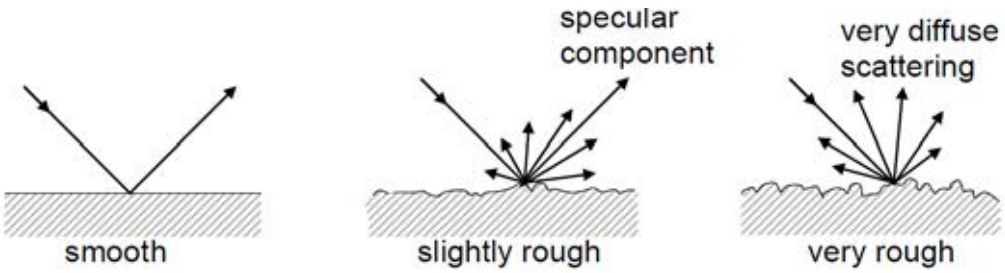

Figure 1-10: Effect of surface deviation on surface scattering [19]

As discussed previously, for a smooth surface the specular reflection dominates but when the surface roughness becomes comparable to the incident wavelength there will be a combination of a diffuse component and a reduced (compared to a smooth surface) specular reflection (shown in Figure 1-10). This effect is present because a rough surface will alter the

phase of the reflected wave for a given point on the surface [19]. For an EM wave with the wavelength λ and an angle of incidence θ, the Rayleigh criterion (Equation 1-16) states that a surface is considered smooth when the height of the surface roughness (h) meets the following condition:

$$h < \frac{\lambda}{8\cos\theta}$$

Equation 1-16: Rayliegh Criterion [19] [20]

As many "real-world" surfaces are considered rough at millimetre-wave frequencies [21] and also due to the fact forces (such as friction) can roughen potential targets (such as with the OH power cables) these effects will be important if THz devices are used for remote sensing. Backscatter from rough surfaces can potentially allow a monostatic transceiver to measure the extent of a target which encompasses many range cells.

Research in [22] investigated the surface roughness of OH power cables exposed to realistic wind erosion. The measurements gained from optical instruments produced surface roughness standard deviations of the order of 10 microns. The Rayleigh criterion would then deem these cables rough and hence diffuse scattering to become significant at around 3.7 THz although the research in [22] didn't consider erosion due to the transportation and installation of overhead power cables.

1.3.3 Bragg

The presence of periodicity on an illuminated surface which is of the order of the incident wavelength gives rise to Bragg scattering. The phenomena emanates from the effect of path lengths summated constructively and destructively for a given wavelength λ and surface period L at certain angles of incidence θ_n (Equation 1-17) [18]. Figure 1-11 shows the basic idea of constructively interfering paths for a plane wave incident on a helical structure. This

type of scattering is of interest to this research due to the dimensions of the periodic structure present on OH power cables and the wavelengths existing in the millimetre wave band.

$$\theta_n = \sin^{-1}\left(\frac{n\lambda}{2L}\right)$$

Equation 1-17: Discrete angles of incidence where constructive interference occurs for a planar wave incident on a perdioic surface

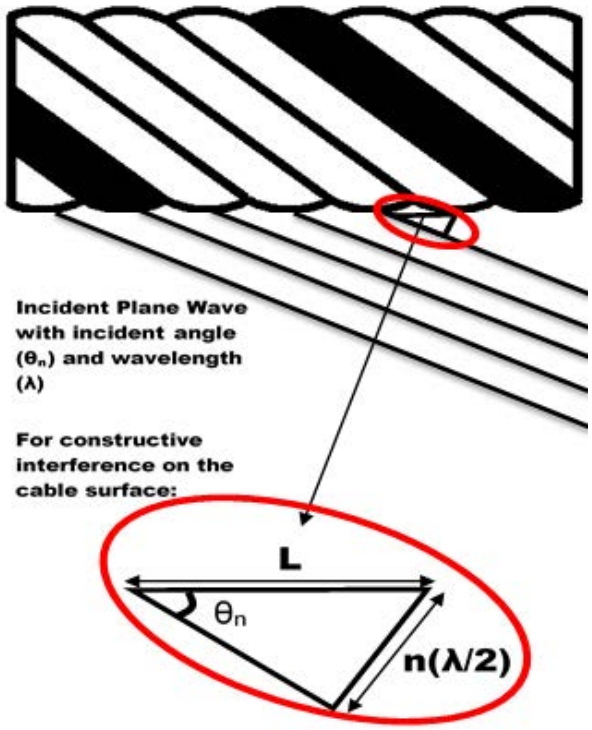

Figure 1-11: Visual representation of Bragg scattering for a planar wave on a helically wound surface

1.3.4 High Resolution Radar

The high-resolution radar discussed in this section is relevant to systems that make use of large bandwidths (Equation 1-18) in order to produce target signatures of many range cells.

$$\Delta r = \frac{c}{2\Delta f}$$

Equation 1-18: Approximation of range resolution with respect to to bandwidth for a frequency modulated radar system

First of all, the improvement of the target-to-clutter ratio due to a finer range resolution allows the enhancement of target detection. The existence of many resolution cells along a target itself allows further target recognition due to the position and migration of multiple scatter centres relative to each other. The orientation of an illuminated object can also be observed by looking at the detectable range bins for a given measurement and this is of particular interest to the research due to its basic processing requirement and uniqueness for certain hazardous targets such as power cables. The range extent over an extended target over time is expected to vary with both statistical and deterministic dynamics that relate to:

- The target size and geometry
- Target surface scattering
- Motion of the transceiver platform
- Motion of the target

A simple method that only requires basic processing is observing the minimum and maximum detectable range cells over a given set of ranges. This is expected to allow the range extent to be measured over time and thus with appropriate thresholding, will allow targets to be separable from clutter as well as noise. In terms of power cable detection consider a thin cylinder extended in range (Figure 1-12):

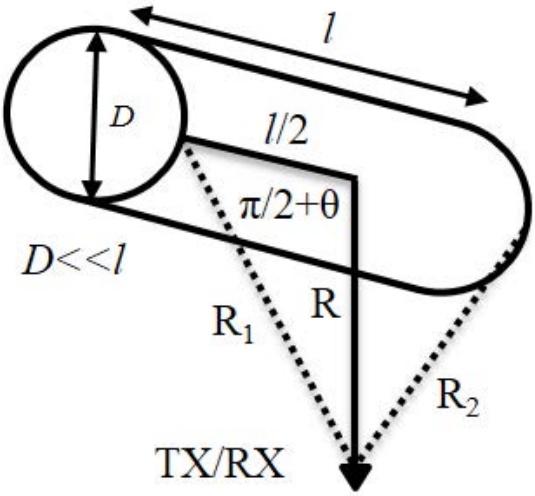

Figure 1-12: Ranges for a finite cylinder rotating about the centre of the circular cross section at half the length of the principal axis

R_1 and R_2 (Equation 1-19 and Equation 1-20) are the maximum and minimum ranges to the cylindrical surface respectively at rotation angle θ:

$$R_1 = \left[\frac{l^2}{4} + R^2 - lR\cos\left(\frac{\pi}{2} + \theta\right)\right]$$

Equation 1-19: Maximum range between the transeiver and the illuminated cylidrical surface in Figure 1-12

$$R_2 = \left[\frac{l^2}{4} + R^2 - lR\cos\left(\frac{\pi}{2} - \theta\right)\right]$$

Equation 1-20: Minimum range between the transeiver and the illuminated cylidrical surface in Figure 1-12

It is assumed that the whole illuminated length, *l,* is detectable.

The range spread, R_{spread}, is, of course, the difference between the maximum and minimum ranges as in Equation 1-21.

$$R_{spread} = R_1 - R_2$$

Equation 1-21: Range Spread

The return may be spread across a number of range cells (Equation 1-22).

$$\Delta N^{cells} = \left\lceil \frac{R_{spread}}{\Delta r} \right\rceil$$

Equation 1-22: Decompostion of Range Spread into different range cells

where Δr is the range resolution and the symbol, $\lceil \cdot \rceil$, denotes the ceiling function (least integer that is greater than or equal to the input).

The previous target's extent, due to being split into multiple range bins, can be measured over time assuming that target is indeed detectable in all range resolution cells. If the target surface is Lambertian, meaning that it can be assumed to have isotropic scatterers that radiate uniformly over a hemisphere regardless of the angle of incidence, then the presence in the target for a certain number of range cells can indeed be expected and the objects extent and even movement can be measured.

If the transceiver is located above ground and hence is susceptible to mechanical disturbances, then measurements of the platform's relative position and/or orientation would enhance this processing. Now in terms of the combination of the variation of range spread over time and surface scattering, the following cases can be considered:

- *Smooth surfaces*: At low frequencies, targets that contain smooth and complex surfaces will have large variations in backscatter due to specular, diffuse, cavity and corner reflectors. This will cause different parts of the object's surfaces to dominate for certain angles of incidence and also to become not detectable at other angles. This would require more complex processing and more prior knowledge to use the range signature to enhance detection compared to the ideal isotropic scatter case.
- *Rough surfaces*: The rougher the surface, the wider the angles at which backscatter becomes detectable. The magnitude of return in the specular direction will reduce although this increases at wider angles. For surfaces that appear very rough for a given

wavelength, the surface will go towards the behaviour of the isotopic case discussed previously. As long as the diffuse return is detectable, the target extent should be able to be estimated with less complex processing techniques. As the Rayleigh criterion in Equation 1-16 suggests this roughness is indeed angle dependent and this may affect the surface point detectability for certain target orientations.

- *Periodic surfaces*: Now for objects with a periodic surface pattern that are illuminated by a signal with a wavelength that is comparable in size, then the backscatter phenomena will be present at discrete angles of incidence where constructive interference occurs (Equation 1-17); this will produce a signature distinct to this surface. The previously discussed range spread behaviour will also only be detectable at these discrete angles and hence will produce backscatter behaviour that is unique for a given surface pattern period with a certain extent.

After considering the previous discussion of the coupling of surface scattering types and measurable range spread for extended targets, power cables are expected to produce distinct signatures compared to those obtained from vegetation or smooth man-made objects even if these objects have the same range extent. This research will look to investigate this coupling in the measurement of overhead power cables with a fine range resolution at a wavelength comparable to the surface structure.

1.3.5 Synthetic Aperture Radar

The previous discussion regarding high bandwidths only enhanced the resolution in range (or Down Range). Considering that a target/area of interest would be illuminated with a narrow 3db beam width of θ^{3dB}, as shown in Figure 1-13, then the resolution in the instantaneous perpendicular plane (or Cross Range (CR)) can be approximated simply by Equation 1-23.

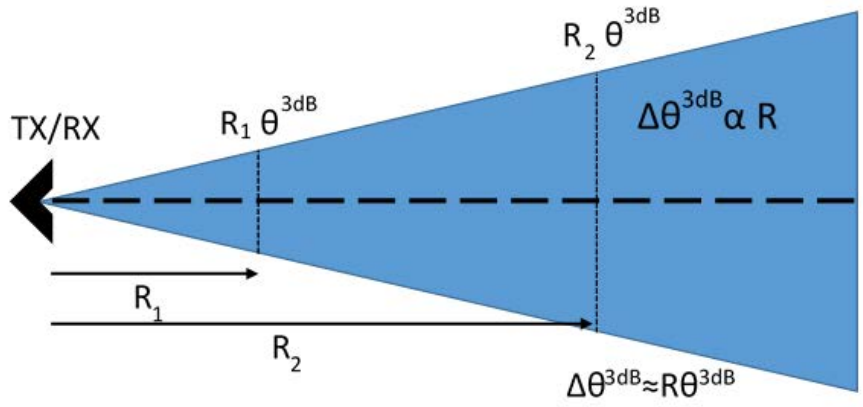

Figure 1-13: Angular resolution for a real-beam monostatic radar with respect to Range

$$L_{\Delta\theta} = R\theta^{3dB}$$

Equation 1-23: 3dB angular resolution with respect to range and 3dB beamwidth

At short ranges, this may produce an adequate signal-to-clutter ratio but at ranges further than a few tens of metres, both the clutter and antenna side-lobe returns could become troublesome as well as having a very poor imaging capability.

A variety of techniques can be used to improve this resolution, most by making use of velocity-dependant Doppler shifts, but the spotlight SAR technique is of interest here due to the permitted access to reliable and information-rich images obtained by the research funders, Thales UK, when using this method.

First of all, SAR stands for Synthetic Aperture Radar and this method processes multiple measurements from a real aperture to form a finer resolution image than would be attainable from the real aperture itself. The longer the synthetic aperture, the finer the CR resolution can be made.

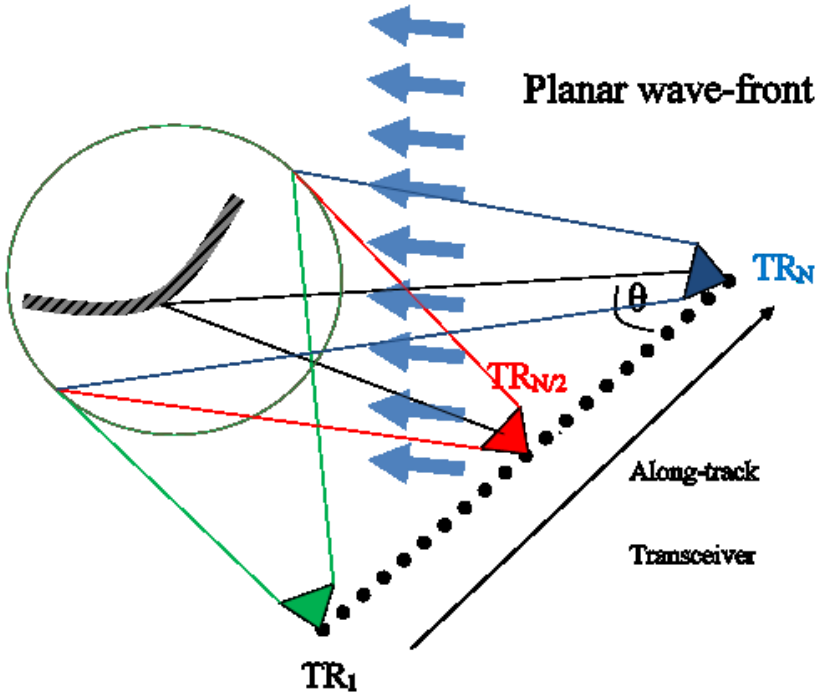

Figure 1-14: Visual representation of a radar conducting measurements in the spotlight SAR mode

Figure 1-14 shows the basis of spotlight SAR imagery, this type of SAR takes multiple measurements of a single ground-based area by rotating the aperture so that the same region is illuminated regardless of the transceiver position or velocity. The cost of achieving highly focused images is the computation power required to obtain several measurements and the accurate orientation/position measurements of the transceiver platform. This method is commonly used by airborne radar devices and thus typically requires a costly INS (Inertial Navigation System) device to form high quality images that typically require a processing time currently not suitable for airborne collision avoidance applications. This type of SAR processing includes assumptions in regards to the relative movement (and hence Doppler shift) of targets and can be supplemented by measurements gained from using other techniques such as GMTI (Ground Moving Target Indicator) as shown in [23] [24] .

A higher resolution allows power cables to be separated from surrounding clutter in both the DR and CR planes whilst also reducing speckle. Equation 1-24 and Equation 1-25 show the

main parameters of the Spotlight SAR processing technique described in [25] which requires the acquisition of a sufficient number of samples, CR_{samp}, over an angle extent of $\Delta\theta$ in order to be able to gain the CR resolution ρ [25]. The CR resolution is in this case designed to be equal to the range resolution in order to gain optical like images which also allowed the processing shown later on in this report simpler.

$$\Delta\theta = \frac{\lambda K_w}{2\rho}$$

Equation 1-24: Angular extent in spotlight SAR [25]

$$\frac{\rho}{K_w} = CR_{samp}$$

Equation 1-25: Cross-Rang sampling in spotlight SAR [25]

Where:

$\Delta\theta$ – apparent angular extend

λ – Transmit centre wavelength

K_w – weighting factor

ρ – cross-range resolution

CR_{samp} – cross range sampling

1.4 Millimetre-wave and Terahertz Radar

This section puts across a brief history of millimetre wave devices and also explains the advantages and disadvantages of such devices compared to devices that operate at higher and lower frequencies when considering an overhead power cable detection system mounted on an aircraft operating outdoors.

1.4.1 History

Experiments using millimetre-wave (or mmW) radiation (30-300 GHz) have been documented since the late 19th century when the late physicist *Jagadis Chandra Bose* performed measurements of EM waves up to the frequency of 60 GHz whilst working at the Royal Institution in London [26]. Although the history of millimetre-wave research spans more than a century, it was not until recent times that the range and detection of objects by using EM in the frequency ranges above 100 GHz was used in widespread applications. Previously the upper end of the mmW band was restricted to specific applications such as astronomy and military applications due to the high costs and lack of maturity in components [27]. Recent technological advancements in a variety of fields have caused a rise of interest in devices that can operate at the upper end of the millimetre wave region and the Terahertz region.

1.4.2 Advantages and Disadvantages

The growing interest in devices that operate above 100 GHz and below the Infrared region is because of the possibility of gaining the resolutions attainable at IR/Optical frequencies alongside the low atmospheric/scattering losses at Microwave frequencies as shown in Figure 1-15; where a non-transparent medium refers to air contaminated with enough dust or smoke to be observed visually.

As mentioned previously, using EM waves in the THz and mmW bands instead of the microwave band has the disadvantage of incurring a higher attenuation whilst propagating in the earth's atmosphere due to the chemical decomposition of the atmosphere [28] but certain relatively low attenuation "windows" (Figure 1-16) are available that reduce the effect of this problem [28]. This attenuation will be more of a problem for non-clear conditions such as rain. The atmospheric attenuation is even higher for IR (Infrared) and visible waves which should give THz devices a larger range compared to these types of devices [29].

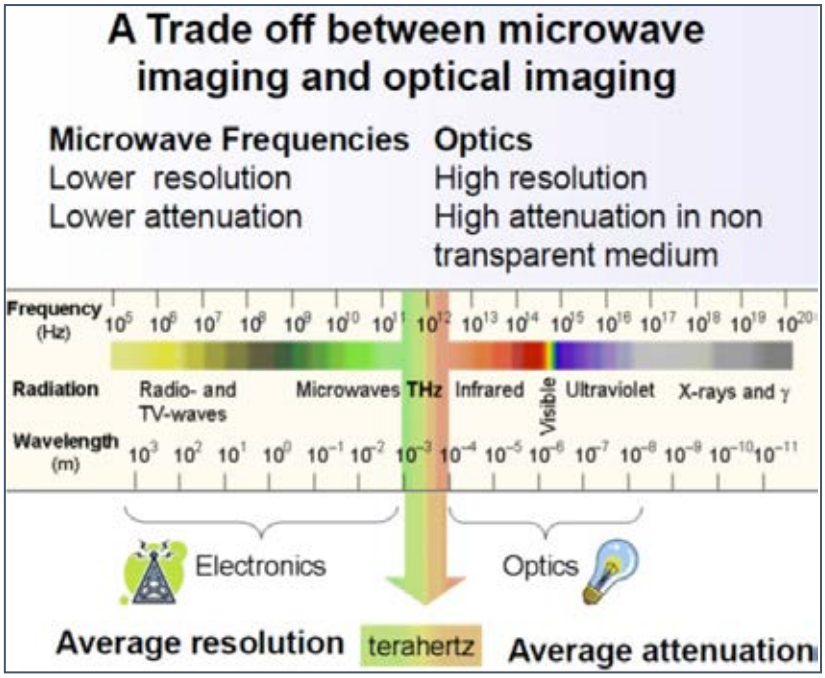

Figure 1-15: Expected advantages of using Terahertz waves relative to both the microwave and optical bands either side [30].

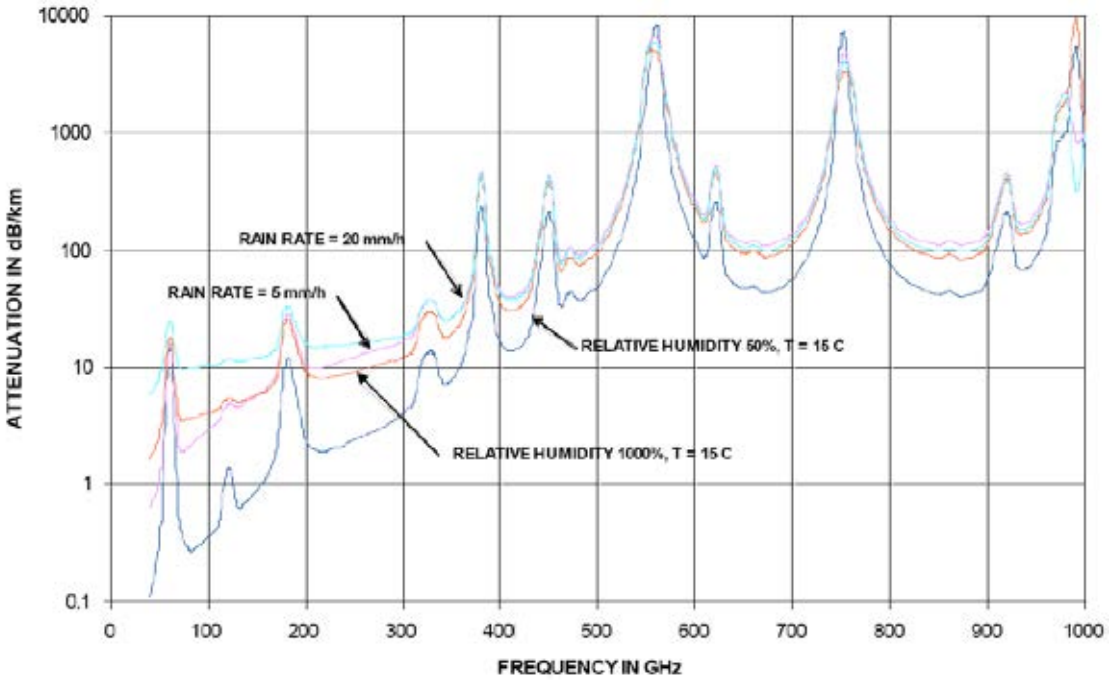

Figure 1-16: Atmospheric attenuation in the range 5–1000 GHz [28]

Another important factor for uncontrollable outdoor applications is scattering loss which can be present due to the presence of smoke or dust particles. The scattering loss caused by the presence of measured airborne particles (such as smoke or dust particulates) is much lower for THz devices compared to the loss present for IR/laser devices [31] [32]. Results in [31] show

the result of measuring a metal reflector with devices at THz, IR and optical frequencies in a burning room, it is shown that the reflector could only be detected with the THz device for both conditions (Figure 1-17).

The advantage of having lower scattering losses compared to higher frequency devices ought to make both THz and mmW devices more robust in environments engulfed in smoke/dust such as rescue or wartime situations.

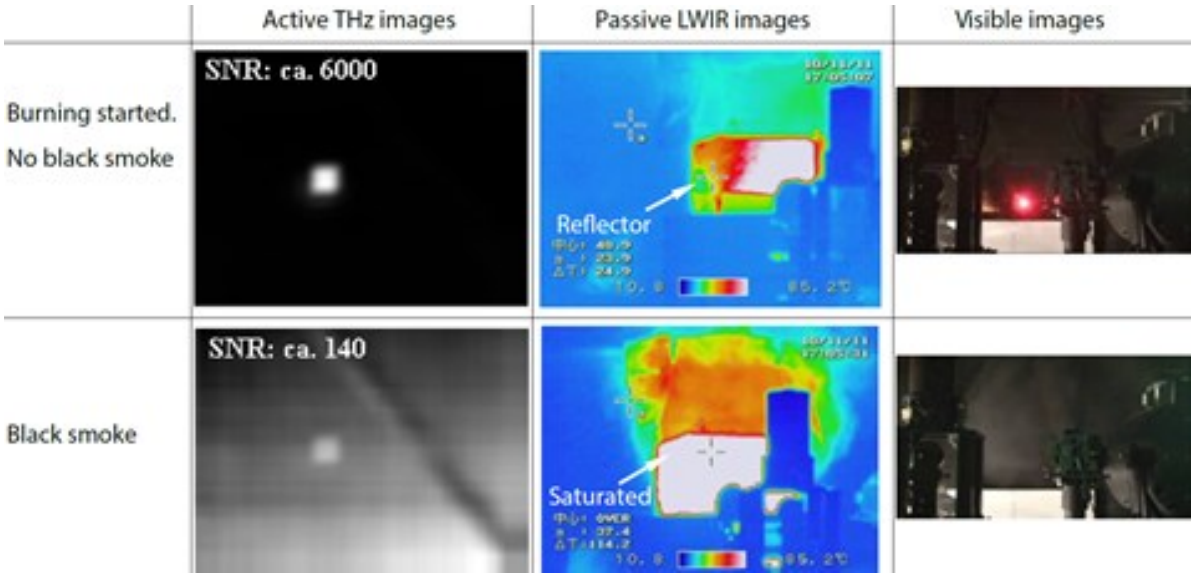

Figure 1-17: Images obtained in [31] that show detectability of a metal object in a smoke-filled burning room at THz, IR and by using an optical camera.

1.4.3 Applications

Although interest in devices above 100 GHz is growing in a variety of fields, a mass production of such devices has yet to materialise due to the lack of maturity of outdoor Terahertz systems. One such area that requires long-range transmission that has already developed high power devices above 100 GHz is the satellite communications industry [33] which is indeed promising for radar applications that can make use of these devices. Applications that can negate the effect of atmospheric gases and particulates will benefit from compact devices, such as satellite-to-satellite communications. The automotive industry also appears to be moving away from the standard automotive devices that operate at 24 GHz and

77 GHz and into higher frequency bands because of the increase in resolution that has the potential to aid in the impending arrival of autonomous automobiles [34][35][36]. Military organisations in the United States have been performing research above 100 GHz for decades [38][39][40] and have just released a statement that devices quoted as being operational in the International Telecommunication Union (ITU) branded EHF band (30-300 GHz) will be used on military fighter jets to aid in the sensing of a variety of weather conditions [37].

1.5 Overhead Power Cable Detection

Previously published research that concerns the detection of overhead power cables using EM waves was used devices in the microwave, millimetre-wave and IR range of frequencies [4] [5] [38] [39] [40] with the exception of [40] which showed a single non-informative range-profile acquired at 330 GHz ; meaning no investigations into low-THz scattering of OH power cables have been made available. The range profile in [40] for a single cable aspect angle at 330 GHz doesn't allow the nature of the scattering to be analysed which is required to assess realistic cable detectability.

Overhead power cables that distribute electrical power are a particular worry as they are difficult to see visually and unlike telephone lines they cannot be severed using cutters due to both safety, cost and possible disruption caused by doing so. The scattering behaviour observed for each of the frequency ranges that have been made available will be described in this section in ascending order (in terms of frequency) prior to a brief description of the typical structure of OH power cables.

The most common type of overhead conductor is the Aluminium Conductor Steel Reinforced type (ACSR) [41] which typically consists of exposed aluminium strands of cylindrical wire, helically wrapped around a steel core [42] (Figure 1-18). The number of strands of wire present depends on the current capacity of the cable. The grating present on

the surface of these cables is considered to be the most important feature with regard to the detection of these targets as these features are expected to be comparable to a wavelength in the microwave frequency band up to the Terahertz band. This is because outer strand sizes that form grooves on the cable surface vary between 1.5-5.5mm [43]. The internal cable structure which is inside the surface of the outer aluminium strands (with respect to any external incoming EM wave) is not expected to affect any EM scattering due to the high conductivity of Aluminium and the compactness of the outer strand for an operational cable.

Figure 1-18: ACSR parameters, physical characteristics once suspended and surface pattern

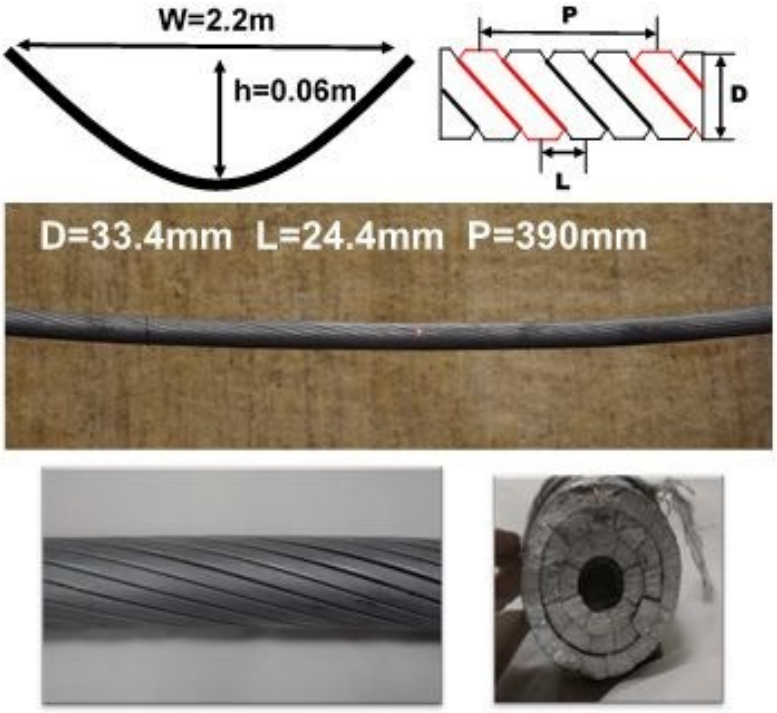

Figure 1-19: ACCC parameters, sagging physical characteristics once suspended and surface pattern

Another development since the earlier work has been in the structure of the cables themselves. More recently, another form of cable construction, the Aluminium Conductor Composite Core (ACCC) type of power cable has been introduced because it can carry higher currents with lighter cables than is possible with the older ACSR type. [44]. The fact that the grooves between the trapezoidal outer strands of the ACCC cable are less prominent than is the case for ACSR cables means that the Bragg scattering off normal incidence is likely to be less prominent. Figure 1-19 shows the construction, parameters and measurement configuration for this cable type. This cable is also much stiffer than the ACSR and hence has significantly less sag between the supports as shown in Figure 1-19. This research will look to investigate the effect of the different surface structure present on the ACCC cable relative to the ACSR type although the remaining research discussed in this chapter will concern the ACSR type as no work ,other than that produced by this research, has been published on the radar returns from ACCC cables.

1.5.1 Microwave research

Four different variations of the ACSR power cable type were measured at 4.75 GHz, 9.5 GHz and 34.5 GHz in [18] and these measurements conclude that below 34.5GHz the scattering of this type of cable is very similar to that of a smooth metallic cylinder with the same dimensions. This observed behaviour was also confirmed in later research [38].

The similarities of the scattering by these helical wounded cables and smooth cylinders is present due to the dimensions of the surface cable structures (such as grooves and outer strand curvature) being much smaller than the wavelength (<30GHz), meaning the variations in phase along the surface currents of the cable are negligible.

The scattering behaviour below 30 GHz suggests that power cables would have a low detection probability when illuminated by an airborne monostatic radar using these frequencies especially considering that realistically, such a device will be susceptible to random variations in motion and alignment.

1.5.2 Millimetre-wave research

OH power cable measurements of straight sections of ACSR (Figure 1-20) have also been performed with devices in the millimetre-wave band which shows additional peaks in the angular response at off-normal incidence.

In the frequency range of 35–94 GHz, the geometrical features of typical OH power cables are comparable to the wavelength, leading to the presence of detectable angular lobes with peaks at certain scattering angles θ_n (Equation 1-26), caused by Bragg mode scattering (see Figure 1-21) [18][38][39]. Equation 1-26 assumes that a planar wave is incident on an infinitely long straight cable with surface period L and this is illustrated in Figure 1-11. The position of these extra peaks that start to appear in the millimetre wave band have been seen to

depend on the ratio of the wavelength, λ, of the incident electromagnetic wave to the surface period, *L*, of the cable. This Bragg scattering broadens the range of angles at which strong backscatter occurs compared to the operation at lower frequencies and helps the detection and identification of OH power cables. This Bragg scattering behaviour was only detectable for incident angles below a cut-off angle of ±α (Equation 1-27) which is the maximum angular extent of the surface normals present on the idealistic structure which limits cable detectability.

Diffuse scattering due to surface roughness appears to be negligible both at 35 GHz and 94 GHz [38] [39] as the scattered energy resides almost entirely in the first *N* Bragg lobes defined by (Equation 1-28) whilst not detectable at other angles.

Figure 1-20: Taut subsection of ACSR cable measured in [18]

$$\theta_n = \sin -1\left(\frac{n\lambda}{2L}\right) \qquad n = \left[-\frac{N}{2}, -\frac{(N-1)}{2}, \ldots, \frac{N}{2}\right]$$

Equation 1-26: Theoretical Bragg mode angles for ACSR cables in the mmW band [18][38]

$$|\alpha| = \tan^{-1}\left(\frac{\pi D}{P}\right)$$

Equation 1-27: Bragg mode cut-off angle for ACSR cables [18][38]

$$N = \left\lfloor \frac{4\pi LD}{\lambda\sqrt{P^2 + \pi^2 D^2}} \right\rfloor$$

Equation 1-28: Number of Bragg peaks expected within an ACSR angular profile at mmW frequencies

where D is the cable diameter and P is the spacing between the turns of a single strand of wire.

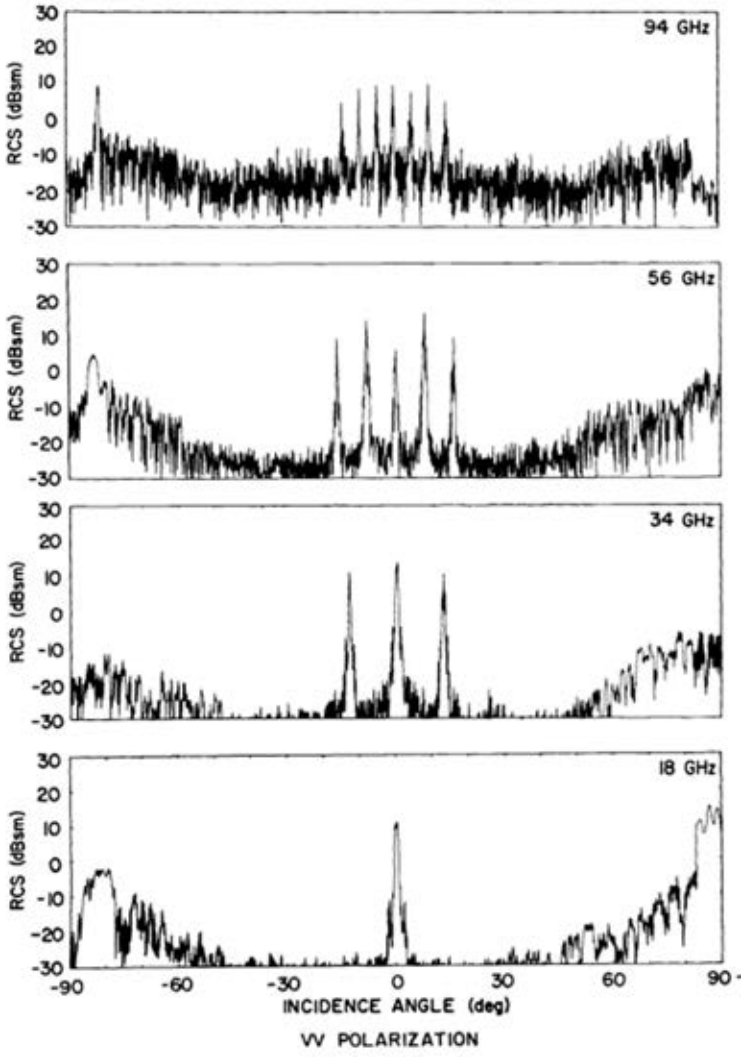

Figure 1-21: Co-polarized backscatter against incident angle for a suspended ACSR power cable at 18, 34, 56 and 94 GHz [18]

1.5.3 Infrared research

The only known non-optical published measurements of OH power cable above the Terahertz range of frequencies were performed using IR (infrared) laser devices at two different wavelengths (1.06um and 10.6um) [4][18]. The Bragg mode peaks seen at lower frequencies were not distinguishable for all IR measurements and the difference in the specular backscatter between normal incidence and beyond the cut-off angle α (Equation 1-27) was reduced in magnitude and remained reasonably constant for the new/pristine cables measured (Figure 1-22 and Figure 1-23). As Equation 1-26 predicts, the Bragg peaks would have a separation of a few hundredths of a degrees at these wavelengths meaning they would appear merged together.

The reduction in backscatter in the specular range of angles has caused an increase in diffused backscatter beyond α which allowed the cable to be detected at all measured incident angles although the ability to classify cables using Bragg mode peak locations is lost. At 10.6um (Figure 1-22), the difference in the magnitude of backscatter between specular and diffuse scattering was higher than for measurements made with a wavelength of 1.06um (Figure 1-23) which corresponds to an increase in the surface roughness to wavelength ratio.

The cable backscatter response is asymmetric at both IR wavelengths which was due to the deterioration of the cable over time [18]; this effect of asymmetry in the results was more apparent for measurements of older/damaged cables (Figure 1-24 and Figure 1-25) which are expected to have experienced a higher severity of surface erosion. An additional decrease in specular backscatter and an increase in diffuse scattering is also seen in old cable measurements due to surface roughness which causes the two specular and diffuse regions to become near indistinguishable.

The two outermost maxima visible in Figure 1-22 to Figure 1-25 were due to the cable supports used in [18].

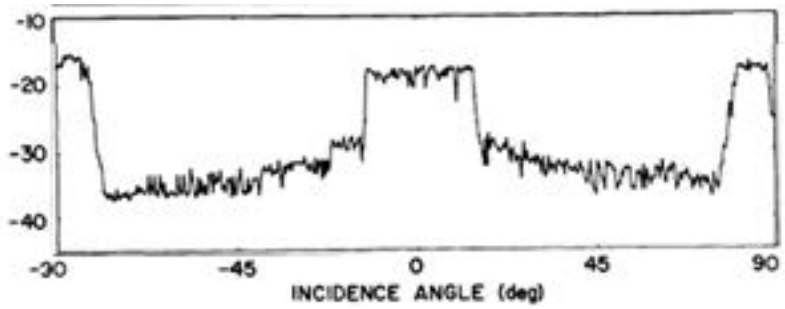

Figure 1-22: IR backscatter (dBsm) from a suspended NEW ACSR power cable with respect to aspect angle for λ=10.6um [18]

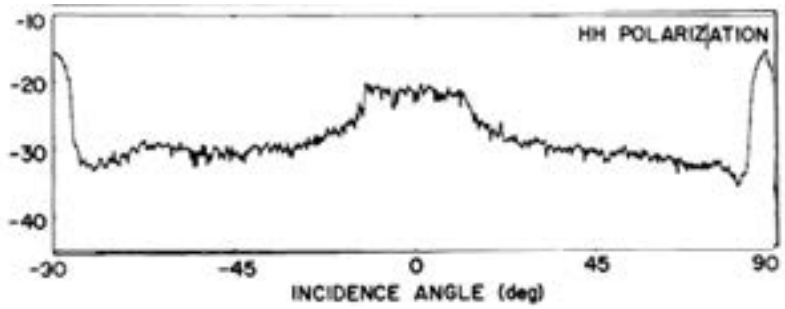

Figure 1-23: IR backscatter (dBsm) from a suspended NEW ACSR power cable with respect to aspect angle for λ=1.06um [18]

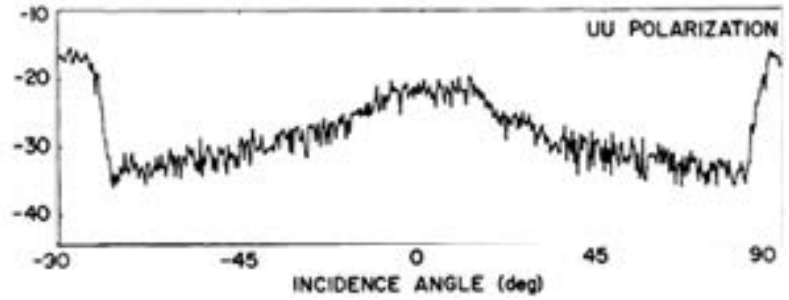

Figure 1-24: IR backscatter (dBsm) from a suspended OLD (Eroded) ACSR power cable with respect to aspect angle for λ=10.6um [18]

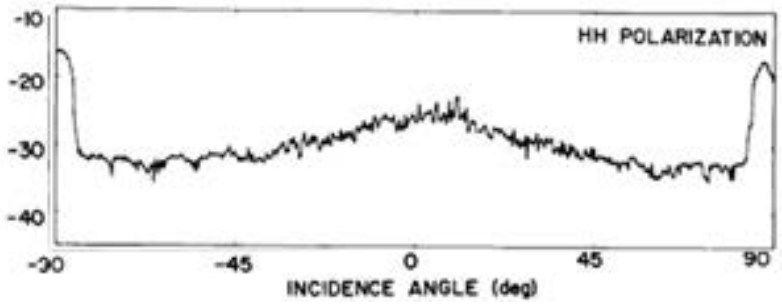

Figure 1-25: IR backscatter (dBsm) from a suspended OLD (Eroded) ACSR power cable with respect to aspect angle for λ=1.06um [18]

1.6 Thesis Outline

Now that all of the important topics of the research have been introduced, this is a brief overview of each of the remaining chapters of the Thesis:

Chapter 2 describes the modelling that was used to estimate the backscattering behaviour for both the ACSR and ACCC types of cable for a realistic scenario. A geometric approximation of the outer surface pattern for both types of cables will be presented alongside its implementation into a physical optics model. A novel method of adding the sagging effect that will be present for hanging cables will be described which has little effect on the simulated Bragg lobe locations (Equation 1-26 and Equation 1-27) although an increase in sagging is shown to widen both the specular and Bragg lobes. A simulation that inserts the angular profile of a straight piece of cable into a sagging structure and the effect of a platform from an aerial position is are described and the results obtained are then discussed in terms of detection probabilities and transmit power requirements.

Chapter 3 describes the experimental equipment used to perform overhead power cable measurements, from low-power laboratory instrumentation radars that operate at 150 GHz and 300 GHz to relatively high-power airborne equipment at K_a and K_u band. Three experimental sites will be explained, one being an indoor THz measurement facility at the University of Birmingham whilst the other two being rural outdoor environments in different parts of the UK.

Chapter 4 has cable backscatter results obtained from 150 GHz and 300 GHz devices discussed in Chapter 3 whilst using the THz measurement facility. A comparison of the straight cable measurements with the physical optics model results using the outer surface structure of two different cable types will be presented and discussed.

Chapter 5 has the Spotlight SAR results of power cables at both K_a band and K_u band for two different scenarios described in Chapter 3. These results will be compared with certain results from past research that measured overhead power cable at similar frequency bands. Extra information gained from high-resolution spotlight SAR images will be used to explain certain anomalies in the results. The results will also be compared to insights gained from earlier modelling and Bragg theory.

In **Chapter 6**, conclusions are drawn and potential future work into overhead power cable detection will be discussed whilst taking into account the results and techniques presented in this thesis.

2. Modelling

2.1 Introduction

This chapter of the Thesis described the theory and simulations used to model the backscatter from realistic overhead power cables when illuminated by an airborne platform. An understanding of cable backscattering behaviour is required in order to recommend transceiver parameters that will permit the aircraft, either unmanned or with a human operator, to be able to detect hazardous cables at a distance which will allow the aircraft to respond effectively when such an obstacle is in the vicinity.

The previous chapter described the standard Bragg theory used in previous literature to estimate the range of incident angles a typical ACSR power cable can be detected over [43] [18]. This Bragg theory assumed that a cable is both straight and infinitely long and doesn't supply much needed information such as Bragg lobe width, precise number of Bragg lobes and also the backscatter magnitudes for different types of cables. This chapter will use the ACSR geometric surface model developed in [43] alongside physical optics theory in order to compute RCS angular profiles for a straight, finite length of cable of the ACSR type.

Also described earlier in this Thesis, was the modern, more electrically and mechanically efficient type of cable called ACCC. This section will show a geometrical model developed to approximate the surface normal structure of the ACCC cable type, in order to gain a RCS angular profile and hence more information regarding detectability.

In reality, suspended overhead cables have substantial sagging geometry due to having finite weight suspended by pylons/poles hundreds of metres apart and this is expected to alter the backscatter behaviour when observed by an airborne radar at high altitude. Due to the fact that previous models do not take sagging into account, a model is presented that includes this

sagging effect by using a catenary function. The main parameters of this catenary function are stated and a method that allows the computation of the surface normal relative to an airborne radar is described.

The chapter goes on to describe the main radar parameters required when performing a power link budget for cable detection in collision avoidance. This will include measured data from past external research such as cable sagging and atmospheric attenuation in order to propose an adequate cable detection system. This analysis will be performed from 16 GHz to 300 GHz, due to the requirement to have compact and light components for lightweight aircraft such as drones/UAVs which is considered practical above 100 GHz.; A sagging cable fluctuation simulation will be shown that can estimate the transmit power required to have a high probability of detection and low probability of false alarms for both types of cables (ACSR and ACCC); which have different surface structures and sagging characteristics.

2.2 Straight ACSR and ACCC Cable RCS

In order to simulate the scattered electric field for the ACSR and ACCC types of cables with no sag, the surface structure is preferred in analytical and differential form. A 3D parametric function for the ACSR type is already described in [43] and thus will be used to compute the angular RCS profile for this type of cable. This modelling is especially required above 94 GHz as there are no published measurements currently available between 94 GHz and Infrared. The only published radar measurements of both the ACSR and ACCC types of cables that will be described here are in [45].

As in [43], Equation 2-1 and Equation 2-2 are used to produce the surface co-ordinates of a number, N, of helically wound (pitch P) cylindrical strands with a diameter of d to form a power cable with diameter D. The parameters for two different types of ACSR cable are shown in Table 2-1 and the corresponding plotted cross section is shown in Figure 2-2. The limits of

the angle φ, Φ, to produce each outer strand surface is used by solving Equation 2-4. The helical rotation of the 2D cross section along the length of the cable is then performed by using Equation 2-3. Equation 2-5 is the resultant parametric equation of the outer surface of an ACSR cable. Figure 2-3 shows three rotated cross-sectional points along the length of the cable (*z*-axis) for both types of cables in Table 2-1.

$$\mathbf{r} = \mathbf{r}_o^n + \mathbf{r}_n = \mathbf{r_x}\hat{\mathbf{x}} + \mathbf{r_y}\hat{\mathbf{y}}$$

Equation 2-1: Vector between ACSR cable centre and outer surface (Cable cross-section) [43]

$$\mathbf{n} = 1,2,...N \qquad size(\mathbf{n}) = N$$

$$\mathbf{r}_o^n = \left[\left(\frac{D-d}{2}\right)\cos\left(\frac{2\pi n}{N}\right)\right]\hat{\mathbf{x}} + \left[\left(\frac{D-d}{2}\right)\sin\left(\frac{2\pi n}{N}\right)\right]\hat{\mathbf{y}}$$

Equation 2-2: Equation 2-1 in terms of the cable geometric parameters [43]

$$\mathbf{r}_n = \left[\frac{d}{2}\cos\left(\frac{2\pi n}{N}\right)\cos\varphi - K\sin\left(\frac{2\pi n}{N}\right)\sin\varphi\right]\hat{\mathbf{x}} + \left[\frac{d}{2}\sin\left(\frac{2\pi n}{N}\right)\cos\varphi + K\cos\left(\frac{2\pi n}{N}\right)\sin\varphi\right]\hat{\mathbf{y}}$$

where: $$K = \frac{d\sqrt{(\pi D)^2 + P^2}}{2P}$$

Equation 2-3: Outer-strand vectors that make up the ACSR cable surface [43]

$$\varphi = -\Phi, -\Phi + \Delta\varphi, ...0, \Delta\varphi, ...\Phi \qquad size(\varphi) = M$$

To derive Φ, solve for:

$$r_n(\varphi) = r_{n-1}(-\varphi)$$

Equation 2-4: Derived equation that represents the angle of vectors (outer strand centre to cable surface) for all outer strands in terms of the cable geometric parameters

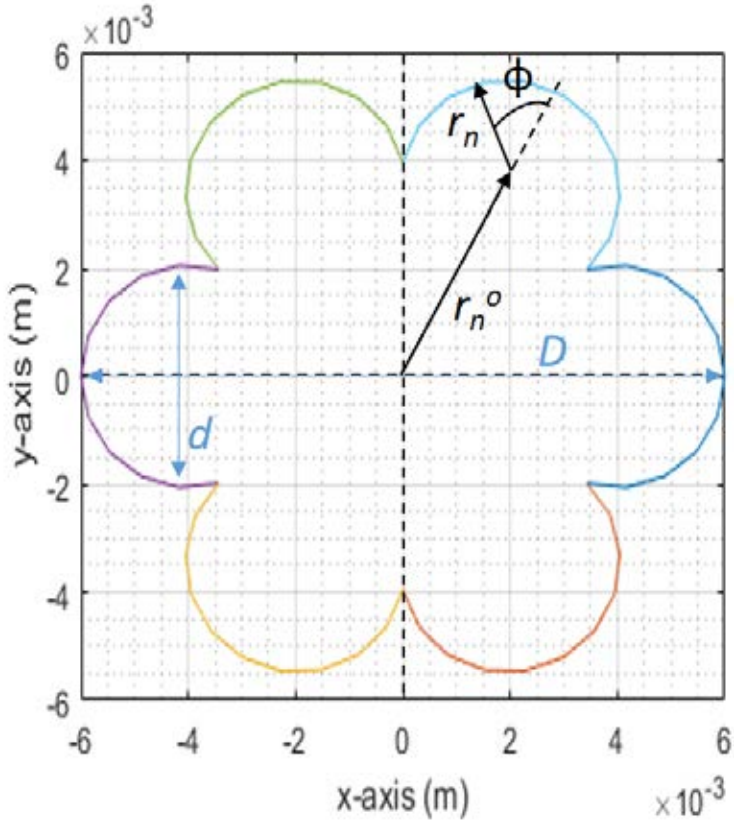

Figure 2-1: Cross-sections of ACSR type with surface structure model parameters [43]

Table 2-1: Parameters of two type of ACSR cables plotted in Figure 2-2

Parameter/Cable	Cable 1	Cable 2
Outer strand diameter (D)	4mm	2.9mm
Cable diameter (d)	12mm	18mm
Helical pitch (P)	146mm;	288mm
Number of outer strands (N)	6	16

$$\mathbf{z} = 0, \Delta z, \ldots L_{cable} \qquad size(\mathbf{z}) = M$$

$$\mathbf{R} = \mathbf{R_x}\hat{\mathbf{x}} + \mathbf{R_y}\hat{\mathbf{y}} + \mathbf{R_z}\hat{\mathbf{z}} = \left[r_x \cos\left(\frac{2\pi \mathbf{z}}{P}\right) - r_y \sin\left(\frac{2\pi \mathbf{z}}{P}\right) \right]\hat{\mathbf{x}} + \left[r_x \sin\left(\frac{2\pi \mathbf{z}}{P}\right) - r_y \cos\left(\frac{2\pi \mathbf{z}}{P}\right) \right]\hat{\mathbf{x}} + \mathbf{z}\hat{\mathbf{z}}$$

Equation 2-5: Cable surface vectors that produce the ACSR cross-section that helically rotates along the cable length (z axis) [43]

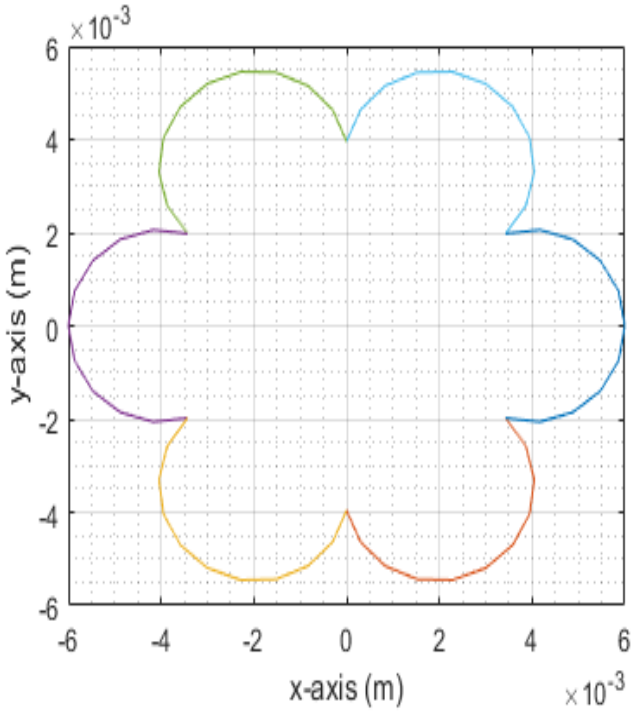

a) Cable 1

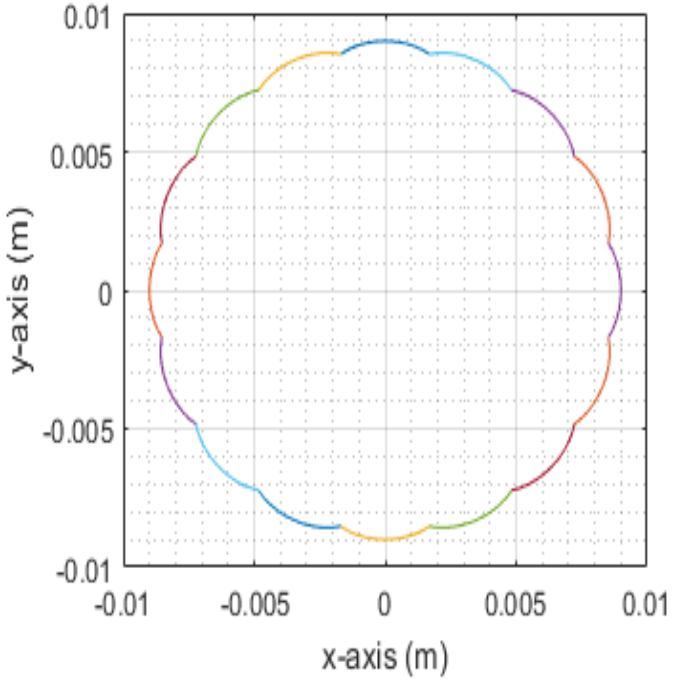

#

b) Cable 2

Figure 2-2: Cross-sections of two types of ACSR cables constructed by using Equation 2-1 and Equation 2-2. The parameters for each are in Table 2-1

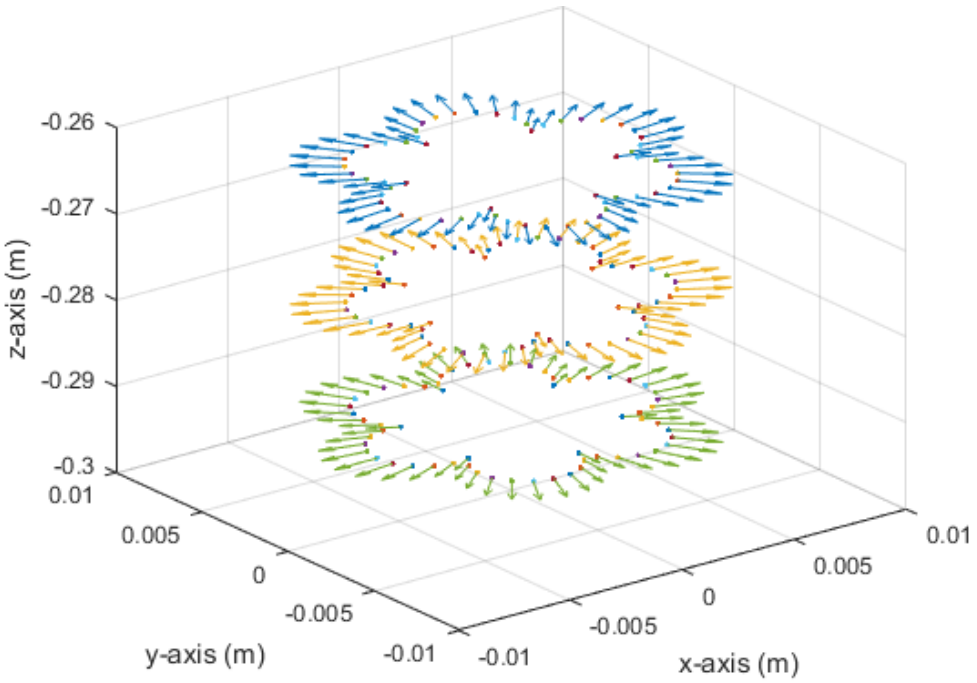

a) Cable 1

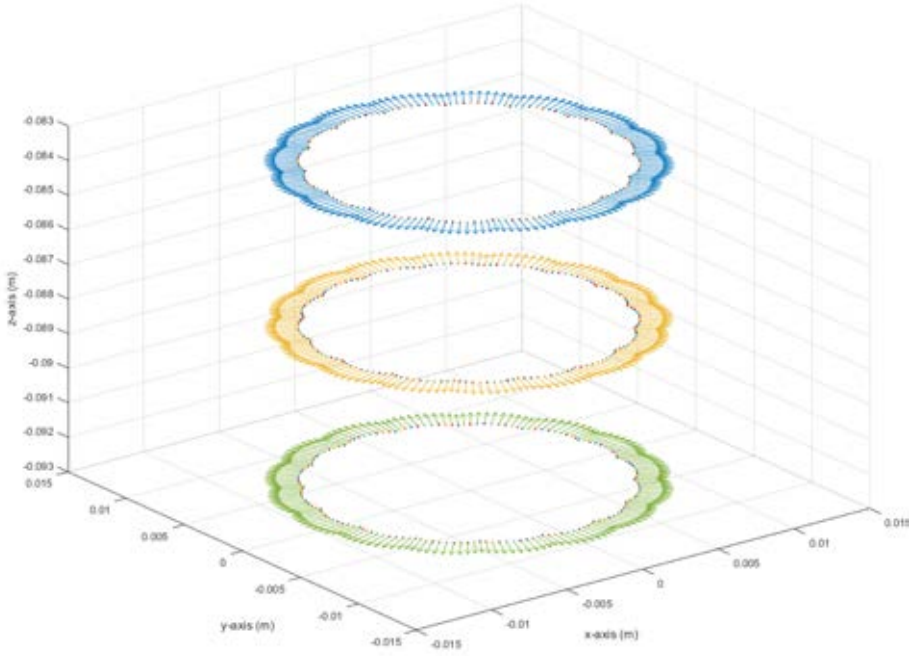

b) Cable 2

Figure 2-3: Three rotated cross sections of the two types of cables (Table 2-1) by using Equation 2-5.

Due to the fact that the modelling of EM scattering from the ACCC overhead cable type could not be found in any published literature, the surface structure of such cables is derived here .This model was based on the ACSR model described previously that was taken from [43]. The cross section of the ACCC cable was constructed by assuming that each of the *U* grooves existing along the outer surface of the cable have similar physical characteristics to an "upside-down" Gaussian shape with a variance and mean that correspond to the angular width and location respectively. Equation 2-6 shows the function that produces such a cross section and Figure 2-4 shows the resulting plot when the parameters of an example of an ACCC cable (shown in Table 2-2) are used. As with the ACSR model previously shown this cross section is then helically rotated along the length of the cable as shown by Equation 2-7; which produces Figure 2-5. The ACCC cable type is shown in Figure 2-6 which bares similar resemblance to the developed surface function which is differentiable to make the mathematics in physical optics modelling simpler.

$$\mathbf{r}_n = \left[\frac{D}{2}\left(1-\frac{L_{groove}}{D/2}\sum_{u=1}^{U}\exp\left(-\frac{(\theta-\theta_u)^2}{2\Delta\theta^2}\right)\right)\cos\theta\right]\hat{\mathbf{x}}... \\ +\left[\frac{D}{2}\left(1-\frac{L_{groove}}{D/2}\sum_{u=1}^{U}\exp\left(-\frac{(\theta-\theta_u)^2}{2\Delta\theta^2}\right)\right)\sin\theta\right]\hat{\mathbf{y}}$$

where $$\theta_u = \left[-\pi+\frac{\pi}{U},-\pi+\frac{3\pi}{U},...,\pi+\frac{\pi}{U}\right]$$

L_{groove}-Groove Depth, Δθ- Groove angular width,

U- Number of grooves, *D*-diameter of cable

Equation 2-6: Vectors that creates the cross-section of the ACCC model

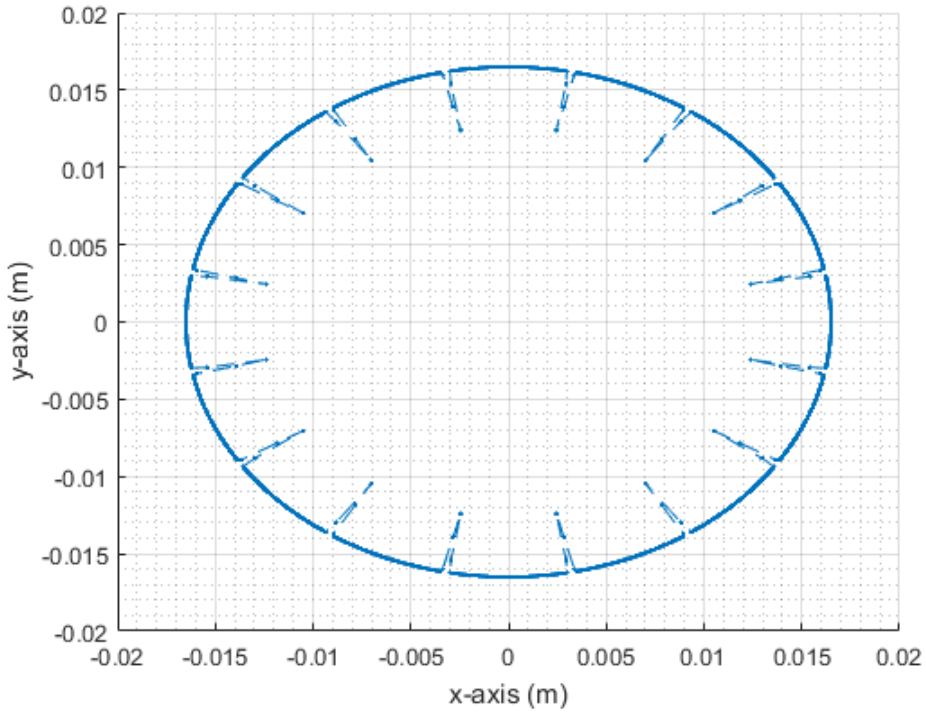

Figure 2-4: Cross section of the ACCC model when using Table 2-2

Table 2-2: Parameters of an ACCC cable

Parameter/Cable	Cable 1
Cable Radius ($D/2$)	16.5mm
Groove Depth	$D/8$=4.125mm
Helical pitch (P)	400mm;
Number of outer strands (N)	17

$$\mathbf{z} = 0, \Delta z, \ldots L_{cable} \qquad size(\mathbf{z}) = M$$

$$\mathbf{R} = \mathbf{R_x}\hat{\mathbf{x}} + \mathbf{R_y}\hat{\mathbf{y}} + \mathbf{R_z}\hat{\mathbf{z}} = \left[r_x \cos\left(\frac{2\pi \mathbf{z}}{P}\right) - r_y \sin\left(\frac{2\pi \mathbf{z}}{P}\right) \right]\hat{\mathbf{x}} + \left[r_x \sin\left(\frac{2\pi \mathbf{z}}{P}\right) - r_y \cos\left(\frac{2\pi \mathbf{z}}{P}\right) \right]\hat{\mathbf{x}} + \mathbf{z}\hat{\mathbf{z}}$$

Equation 2-7: Vector that produces the outer surface of the ACCC model

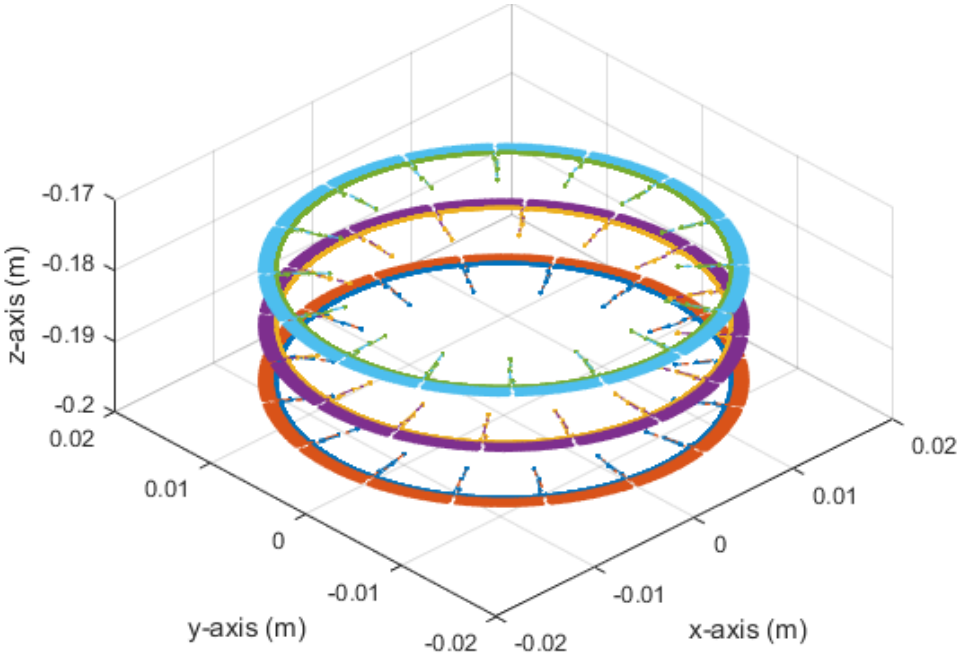

Figure 2-5: Three rotated cross sections that were computed when using Equation 2-7 and Table 2-2

Figure 2-6: ACCC parameters, sagging characteristics and surface pattern

2.2.1 Backscattered RCS

Now that the 3D locations and surface normal vectors can be computed for both the ACSR and ACCC model, a method of computing the magnitude of the surface current at each point is needed. The surface current magnitudes were calculated using the PO approximation (Equation 2-8-Equation 2-10) and these were then summed with an appropriate propagation factor (Equation 2-11) in order to produce the RCS angular profile (Equation 2-12).

Each scatterer magnitude calculated was also weighted by a Gaussian function that approximates the antenna pattern [46].

$$\hat{\mathbf{n}} = \nabla(\mathbf{R}) = \mathbf{n_x}\hat{\mathbf{x}} + \mathbf{n_y}\hat{\mathbf{y}} + \mathbf{n_z}\hat{\mathbf{z}}$$

Equation 2-8: 3D surface normal vector in terms of the grad function of the parametric equation

$$\mathbf{J}(\theta_i) = \left|2\hat{\mathbf{n}} \times \mathbf{H_i}\right|$$

Equation 2-9: Physical Optics approximation to compute the surface currents for any point of the cable surface for a given incident magnetic intensity vector

$$\mathbf{H_i}(\theta_i) = H_0\left(\cos(\theta_i)\hat{\mathbf{y}} + \sin(\theta_i)\hat{\mathbf{z}}\right)$$

Equation 2-10: Incident magnetic intensity vector where H_0 is the magnitude of the magnetic intensity in A/m

$$\mathbf{E}(\theta_i) = \frac{k}{4\pi}\sum_{i=1}^{N\times M\times O}\mathbf{F(\theta)}\mathbf{J_i}e^{-jk\boldsymbol{\rho}_\mathbf{i}}A$$

Where the distance ρ between each cable surface point ***R*** and transceiver location ***TR*** is:

$$\boldsymbol{\rho} = \sqrt{(\mathbf{R}_x - TR_x)^2 + (\mathbf{R}_y - TR_y)^2 + (\mathbf{R}_z - TR_z)^2} \text{ and } \mathbf{TR} = [TR_x\hat{\mathbf{x}} + TR_y\hat{\mathbf{y}} + TR_z\hat{\mathbf{z}}]$$

$$\mathbf{F}(\theta) = \exp\left(-0.694\left(\frac{\boldsymbol{\theta} - \theta_i}{\Delta\theta_{3dB}}\right)^2\right) \quad \text{and} \quad \boldsymbol{\theta} = \tan^{-1}\left(\frac{\mathbf{R_z} - TR_z}{\mathbf{R_y} - TR_y}\right)$$

Equation 2-11: Scattered electric field in terms of the surface current magnitudes and free-space Green's function whilst in the far-field

$$RCS = 4\pi R^2 \lim_{R\to\infty}\frac{|E_s|^2}{|E_i|^2}$$

Equation 2-12: RCS definition with respect to the scattered and incident electric fields

The following assumptions were made:

- The Free-space far-field Green's function was used instead of the complete Hankel functions [43] due to the typical distances required for overhead cable detection being much larger than the antenna extent

- Physical optics was used which assumes the radii of curvature of the surface irregularities are large compared to the wavelength
- The effect of multiple bounces is assumed to be negligible due to realistic cable detection scenarios for a monostatic transceiver

The length of each subsection simulated is equal to the Fresnel length (Equation 2-13) due the majority of energy being expected to reside in this length of cable, due to the phase variation of the incident planar wave for a flat subsection of cable as described in [18].

Table 2-3 contains the theoretical Fresnel Lengths for a straight length of cable for the frequencies of interest in this thesis.

$$L_F = 2\sqrt{\lambda R}$$

Equation 2-13: Fresnel length

The RCS assumed that each point of the illuminated scatterer has a negligible phase difference to adjacent points. Errors in this assumption are negligible when simulated at the *Fraunhofer* (or far-field) distance in (Equation 2-14) which is a criterion that allows phase errors across the target of $\pi/8$.

$$R_{far-field} = \frac{2D^2}{\lambda}$$

Equation 2-14: Far-field distance for a target with extent *D* illuminated by an incident wave with the wavelength λ

Table 2-3: Fresnel Length for the frequencies of interest at 500m using Equation 2-13

Frequency	Fresnel Length L_F
16 GHz	6.122 m
34 GHz	4.199 m
150 GHz	1.999 m
300 GHz	1.412 m

The simulated results for a straight piece of ACSR and ACCC cable, at a range of 500 metres, are shown in Figure 2-7a and Figure 2-7b respectively alongside the analytical solution for a smooth cylinder (Equation 1-12) in Figure 2-7c. All of the simulated results in Figure 2-7 have the same distance and approximately the same diameter. The length of cable simulated at each frequency corresponds to the values in Table 2-3.

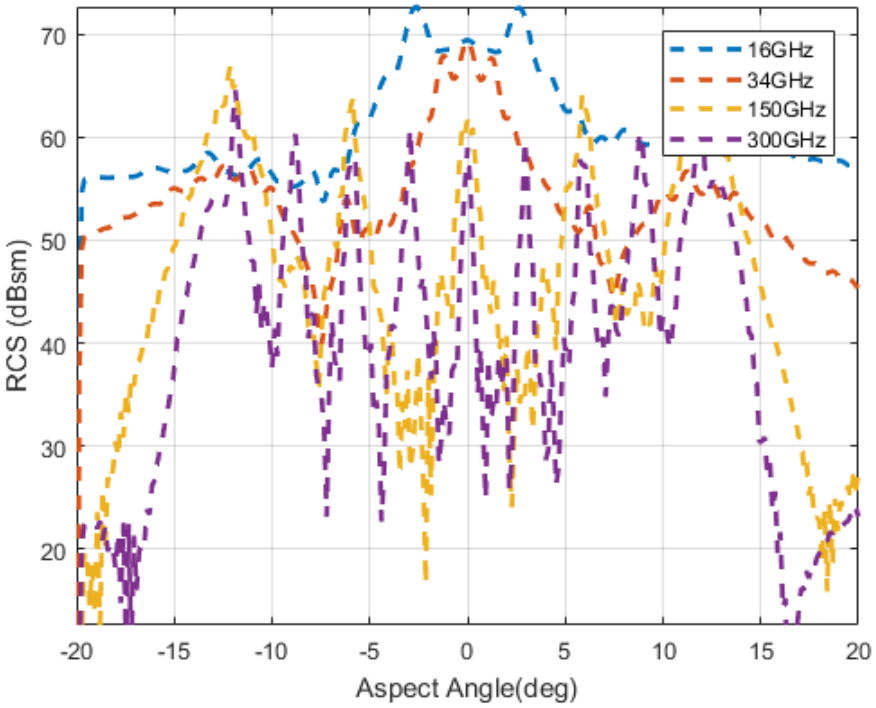

a) ACSR (Table 2-4)

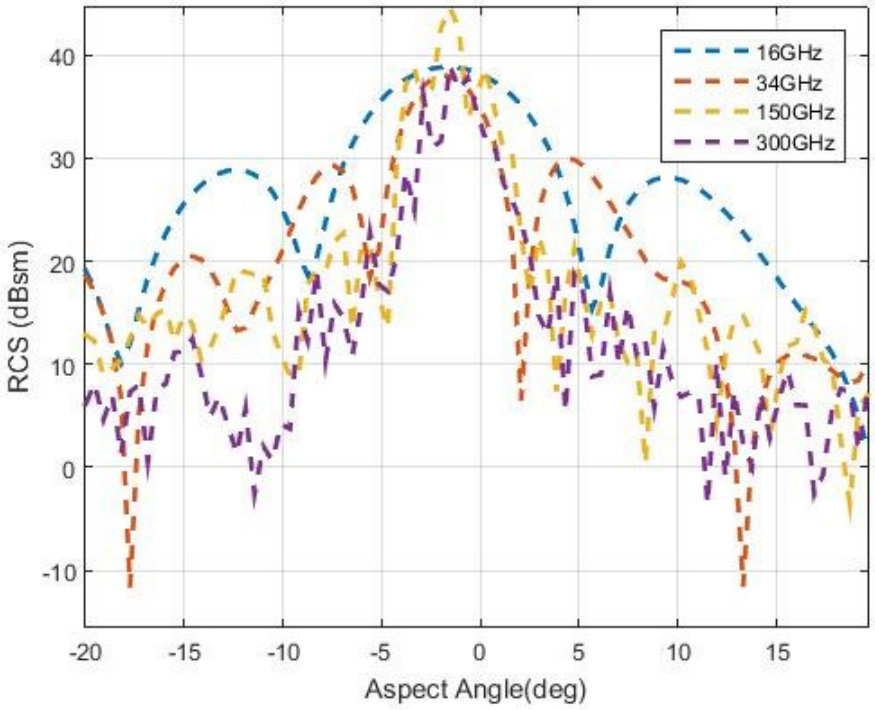

b) ACCC (Table 2-5)

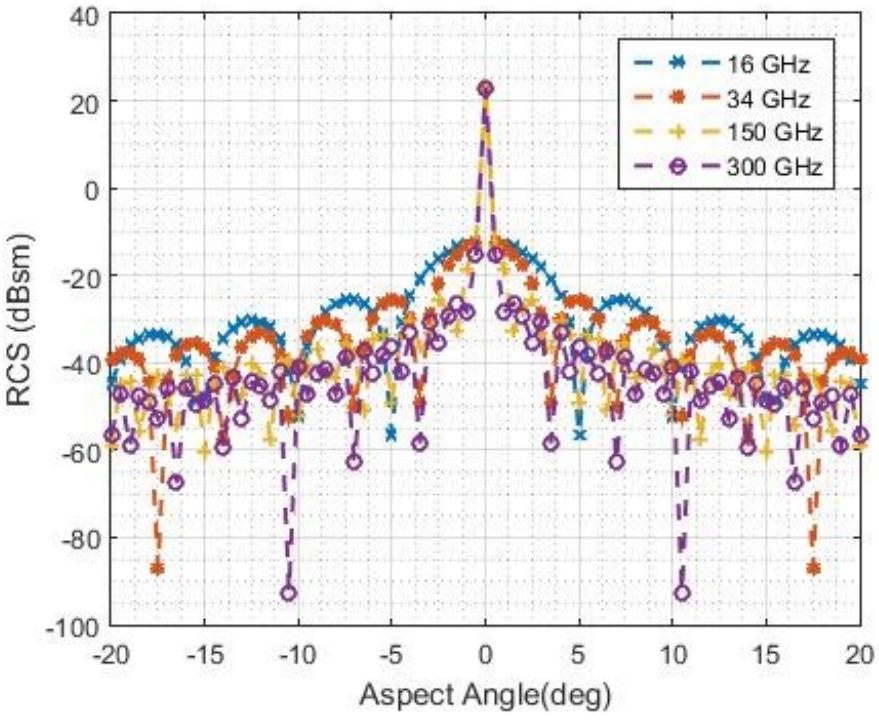

c) Smooth Cylinder (Equation 1-12) with 32mm diameter

Figure 2-7: Simulated RCS angular profiles for the ACSR, ACCC and smooth types of power cable

Table 2-4: Parameters of an ACSR cable (Figure 2-7a)

Parameter	Value
Cable diameter (*D*)	35.2 mm
Outer strand diameter (*d*)	4.46 mm
Helical pitch (*P*)	406.5 mm
Outer surface period (*L*)	24 mm
Number of outer strands (*N*)	21

Table 2-5: Parameters of an ACCC cable (Figure 2-7b)

Parameter/Cable	Cable 1
Cable diameter	33mm
Groove Depth	*D*/8=4.125mm
Helical pitch (*P*)	400mm;
Outer groove width	4°=0.07rad=1.1mm
Number of outer strands (*N*)	16

For the ACSR type, the reduced spacing of each Bragg lobe can be seen for an increase in frequency. The previous cut-off angle of around 15 degrees can also be observed. For the ACCC simulated result, Bragg lobes can be observed but at much lower magnitudes for incident angles more than around 4 degrees but these additional lobes are at a higher magnitude compared to the simulated smooth cylinder side-lobes in Figure 2-7c.

2.3 Sagging Cable Geometry

As stated in the chapter introduction, OH cables are used to distribute electrical power over large distances and such cables have suspension points (poles/pylons) separated hundreds of metres apart causing sagging to be present for a realistic cable scenario. To predict how radar signals scatter from realistic cables, this sagging will need to be included in the modelling as it is expected to change the surface normal structure along the cable for an airborne transceiver.

Equation 2-15, Equation 2-16 and Equation 2-17 can be used to describe the sagging behaviour for the simplified cable shown in Figure 2-8 which has a maximum sagging distance, *S*, and fixed suspensions points separated by D [47].

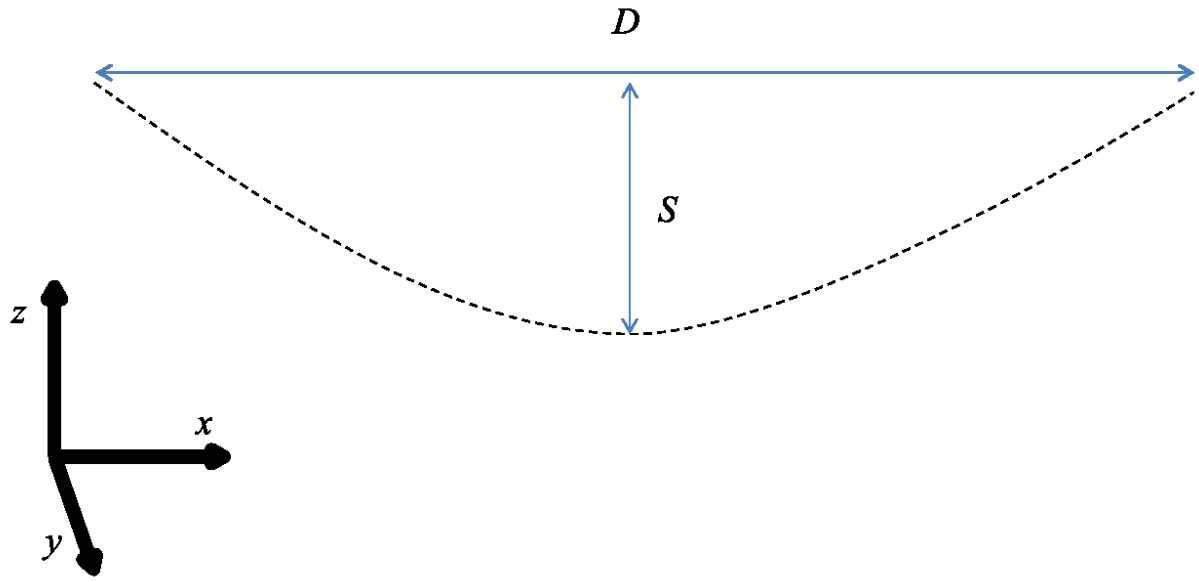

Figure 2-8: Sagging parameters and co-ordinate system

$$f(x) = \cosh(cx)/c$$

Equation 2-15: Hyperbolic cosine function with sagging parameter *c*

$$L = \frac{8S^2 + 3D^2}{3D}$$

Equation 2-16: Cable length approximation in terms of the central sagging length *S* and distance between fixed points *D*

$$c = \frac{8S}{L^2 - 4S^2}$$

Equation 2-17: Sagging parameter for the sagging distance S and length of sagging cable L

The 2D sagging geometry can be approximated by a catenary function which is equivalent to a hyperbolic cosine wave (Equation 2-18). The differential of this function, the hyperbolic sine, determines the gradient and thus is used to determine the surface normal for a given point along the cable (Equation 2-19). The sagging function can be split into infinitesimal flat subsections, as shown in Figure 2-9, each with an individual surface normal vector corresponding to (Equation 2-19) and (Equation 2-20) and its location along the cable's length. The co-ordinate system for the straight cable modelling present earlier and that described in the sagging modelling do not coincide.

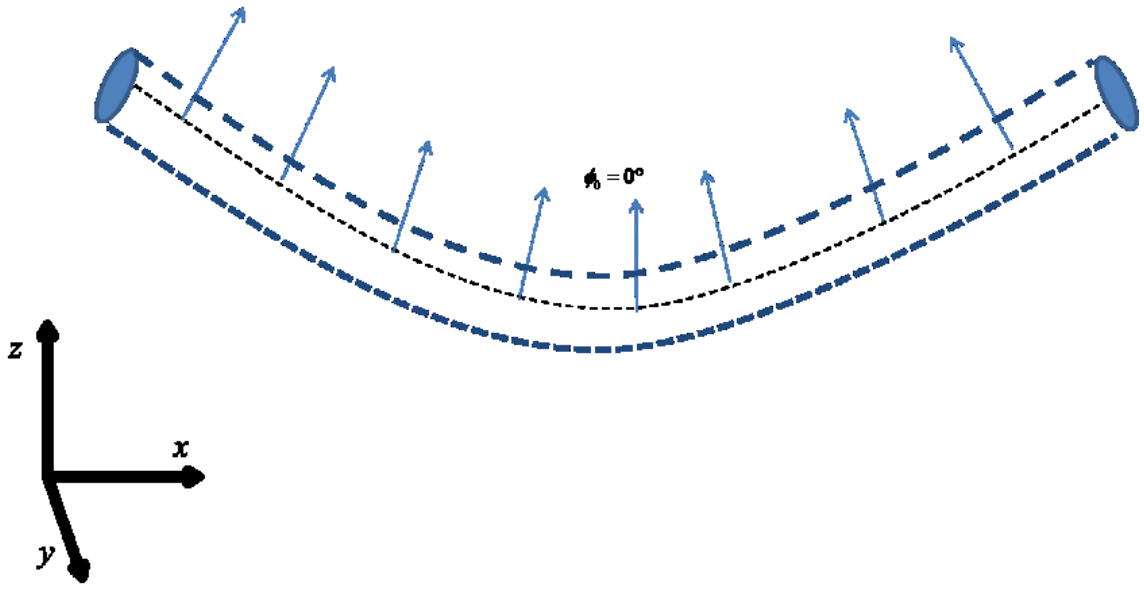

Figure 2-9: Surface normal for each cable sub-section along the sag

$$\Delta f = \sinh(cx)\Delta x \qquad \Delta x = \frac{D}{N_x}$$

Equation 2-18: Gradient (Differential) of the theoretical sagging function Equation 2-15

$$\varsigma = \tan^{-1}\left(\frac{\Delta f}{\Delta x}\right)$$

Equation 2-19: Sub-section rotation angle using Equation 2-18

Assuming that the cable is a cylinder, the cross section along the sag can be considered a circle. Circular points are generated that follow the sagging geometry for each flat subsection (Figure 2-10). The main purpose of the generation of the sagging cable geometry is to determine which subsection of the sag will dominate for a given incident planar wave and also to determine the orientation of each subsection relative to the airborne radar. The orientation of the subsections of interest is calculated by finding out which cylindrical surface norm in each individual subsection has an elevation angle closest to the depression angle of the transceiver (Equation 2-20-Equation 2-22). The surface normal of the dominating cable subsection is then inserted into a look up table of an ACSR and ACCC subsection in order to take into account the surface structure.

We assume that the transceiver has a depression angle of 45 degrees.

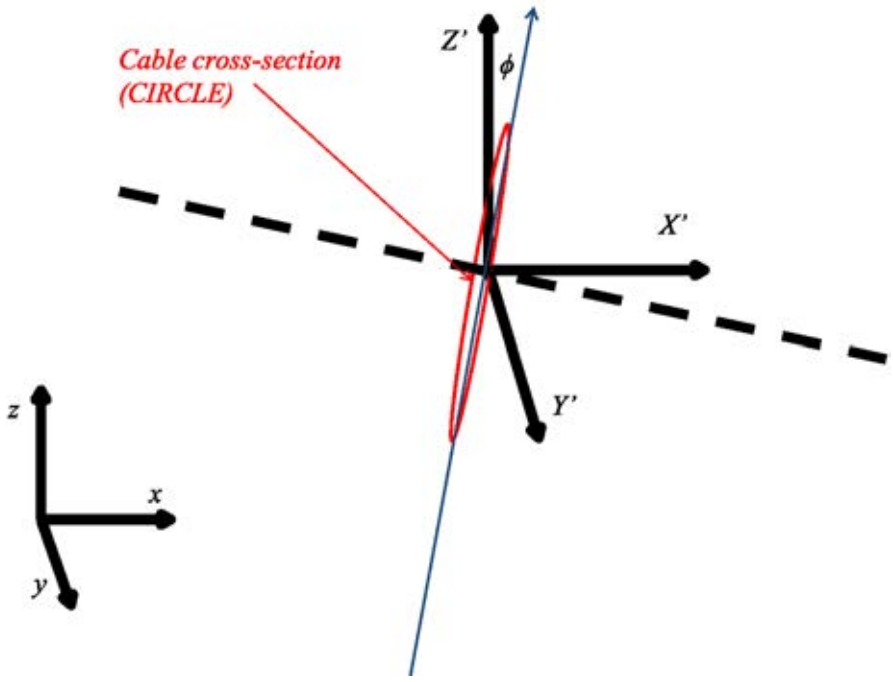

Figure 2-10: Rotation of cable cross-section so that the centre aligns with sagging

$$a(\theta') = r\cos(\theta')$$

$$b(\theta') = r\sin(\theta')$$

$$\theta' = -\pi, \delta\theta', ...\pi \qquad size(\theta') = Q$$

$$c(\theta') = a\hat{y} + b\hat{z}$$

Equation 2-20: Cylindrical subsection surface normals

$$C(\theta', \varsigma) = c(\theta')R^{y}(\varsigma)$$

where

$$R^{y}(\varsigma) = \begin{pmatrix} \cos\varsigma & 0 & \sin\varsigma \\ 0 & 1 & 0 \\ -\sin\varsigma & 0 & \cos\varsigma \end{pmatrix}$$

Equation 2-21: Surface normals for each subsection that has been rotated using Equation 2-18 for a given point along the function in Equation 2-15

To get the centre location of the strongest scatterer (normal for each subsection):

$$[\eta_x, \eta_y, \eta_z] = \min(\hat{k}_i - C(\sinh(cx)))$$

Equation 2-22: Computes the surface normal on each subsection that most closely aligns with the incident propagation vector k_i

2.4 Aircraft Model

In order to estimate the return power fluctuations from a power cable, the disturbances present on an airborne platform would need to be approximated simply, but with adequate accuracy. The research in [48] shows a simple way to produce the random variations in different types of aircraft empirically. INS measurements were taken at different attitudes whilst in autopilot and piloted operation for a small fixed winged aircraft. The INS measurements of the heading/azimuth and pitch/elevation for a small fixed-wing aircraft is shown in Figure 2-11.

Aircraft information:

- Altitude: 300 metres
- Fixed wing manned aircraft (Piper PA-28)
- Human control (experienced pilot)
- Clear slightly windy conditions
- Fixed orientation
- Positive angle of attack (AOA)
- Correlation coefficient close to zero hence negligible

Investigations in [48] show that the azimuth/heading and pitch/elevation data can be approximated by a bivariate Gaussian distribution with a zero correlation coefficient (Equation 2-23 to Equation 2-25) (Figure 2-12). The sampling rate of the INS device used to gain the measurements displayed in Figure 2-11 was 50 Hz. The extracted azimuth and elevation means and standard deviations for the data shown in Figure 2-11 are:

$$\mu_{el} \approx 4°, \sigma_{el} \approx 1.3°$$

$$\mu_{az} \approx 0°, \sigma_{az} \approx 2.45°$$

This simple model will be used to simulate the incident angle fluctuations when an airborne transceiver illuminates power cables in a realistic scenario.

$$f(az,el)=\frac{1}{2\pi\sigma_{az}\sigma_{el}\sqrt{1-\rho^2}}\exp\left(\frac{-1}{2(1-\rho^2)}\left[\frac{(az-\mu_{az})^2}{\sigma_{az}{}^2}+\frac{(el-\mu_{el})^2}{\sigma_{el}{}^2}-\frac{2\rho(az-\mu_{az})(el-\mu_{el})}{\sigma_{az}\sigma_{el}}\right]\right)$$

Equation 2-23: Bivariate Gaussian function

where the correlation coefficient ρ is defined by:

$$\rho=\frac{\mathrm{E}[az\bullet el]}{\sigma_{az}\sigma_{el}}=\frac{\mathrm{cov}[az,el]}{\sigma_{az}\sigma_{el}}$$

Equation 2-24: Correlation coefficient in terms of the expected value of the azimuth (*az*) and elevation (*el*) variables (or the covariance between the two) and the variance for both (σ_{az} and σ_{el})

$$\Sigma=\begin{bmatrix}\sigma_{az}{}^2 & \rho\sigma_{el}\sigma z\\ \rho\sigma_{el}\sigma_{az} & \sigma_{el}{}^2\end{bmatrix}$$

Equation 2-25: Covariance matrix of the Bivariate Gaussian function

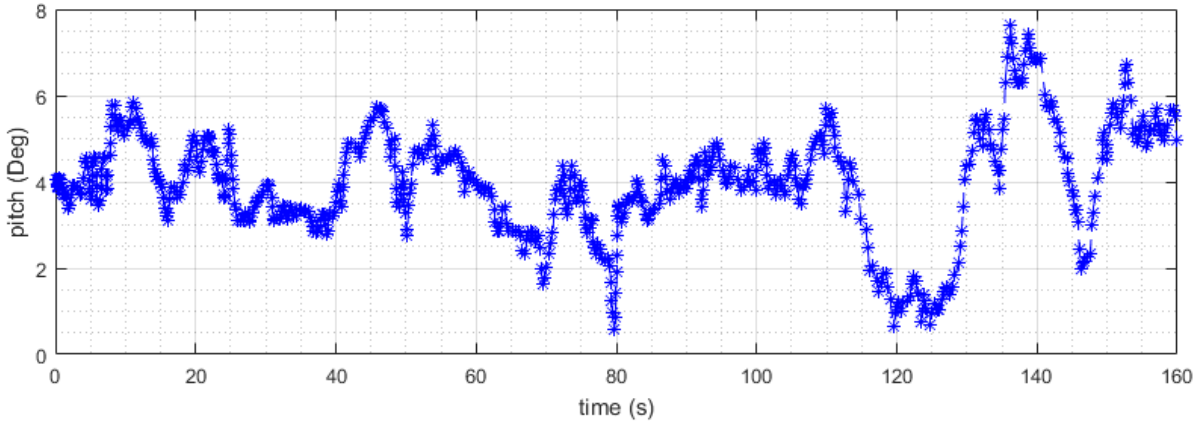

a) Pitch/Elevation

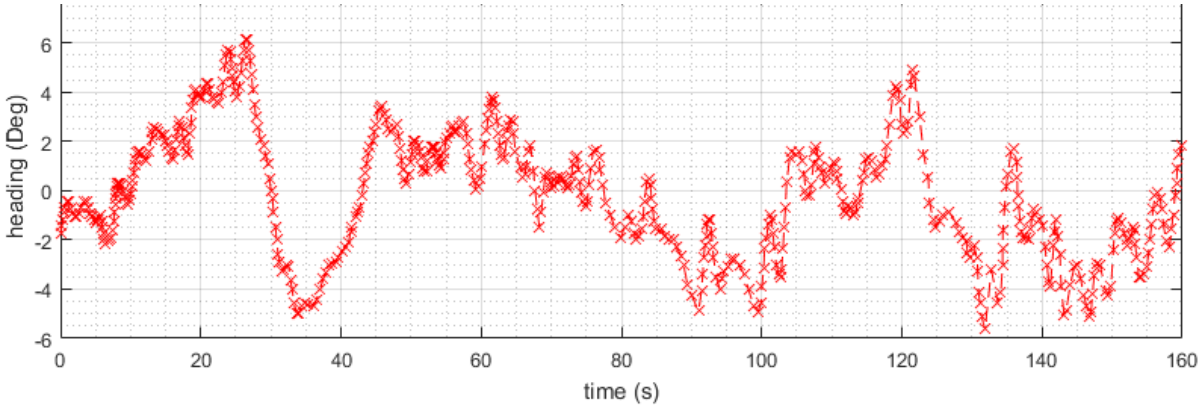

b) Heading/Azimuth

Figure 2-11: INS measurements of heading and pitch whilst on board a small fixed winged aircraft [48].

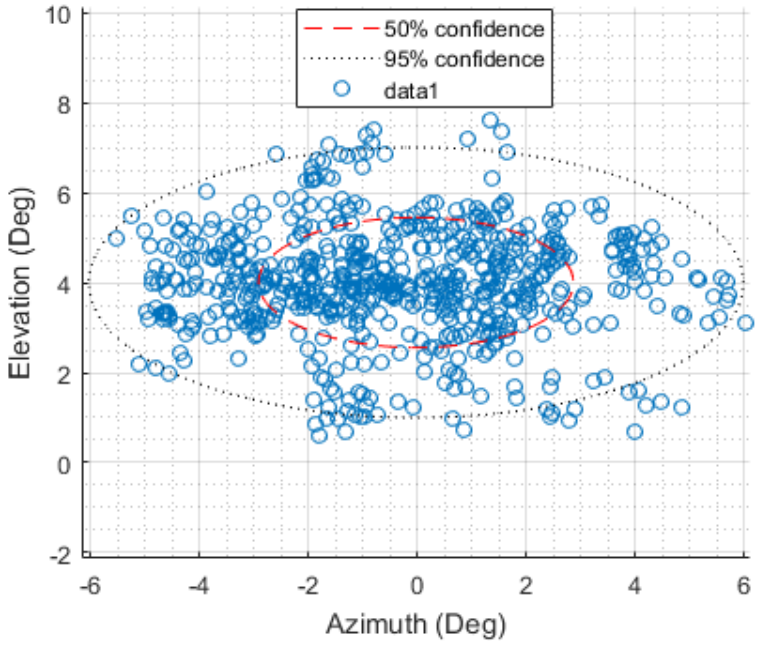

Figure 2-12: Scatter plot of azimuth and elevation measurements which show no tilt on the confidence ellipses.

2.5 Sagging Parameters

Measurements of cable sag for both the ACSR and ACCC type of overhead power cable were performed in [49] and the data presented shows that the central sagging distance for

various temperatures between 20-200 degrees Celsius (Figure 2-13). The cable were clamped 65 metres apart at a height of 2.5 metres. Both cables had an overall diameter of around 28mm.

The measurements in [49] conclude that the structure of the ACCC cable incurs less sag relative to the ACSR type for a given realistic temperature. Sagging values for a given temperature can be inserted into an approximation of this data in order to estimate the effect of sagging geometry on the backscattered signal for a realistic scenario for both types of cables.

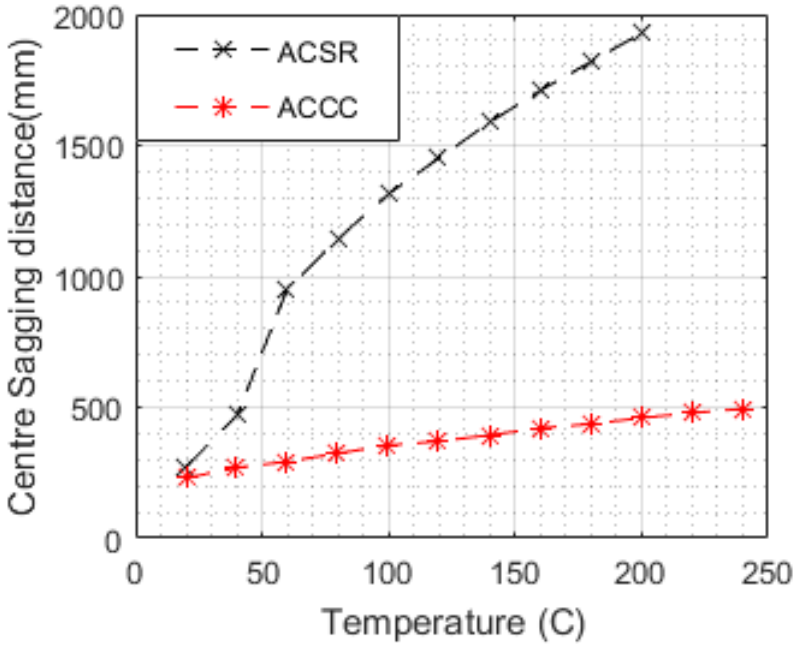

Figure 2-13: Sagging distance at cable centre with respect to temperature [49].

2.6 Atmospheric attenuation

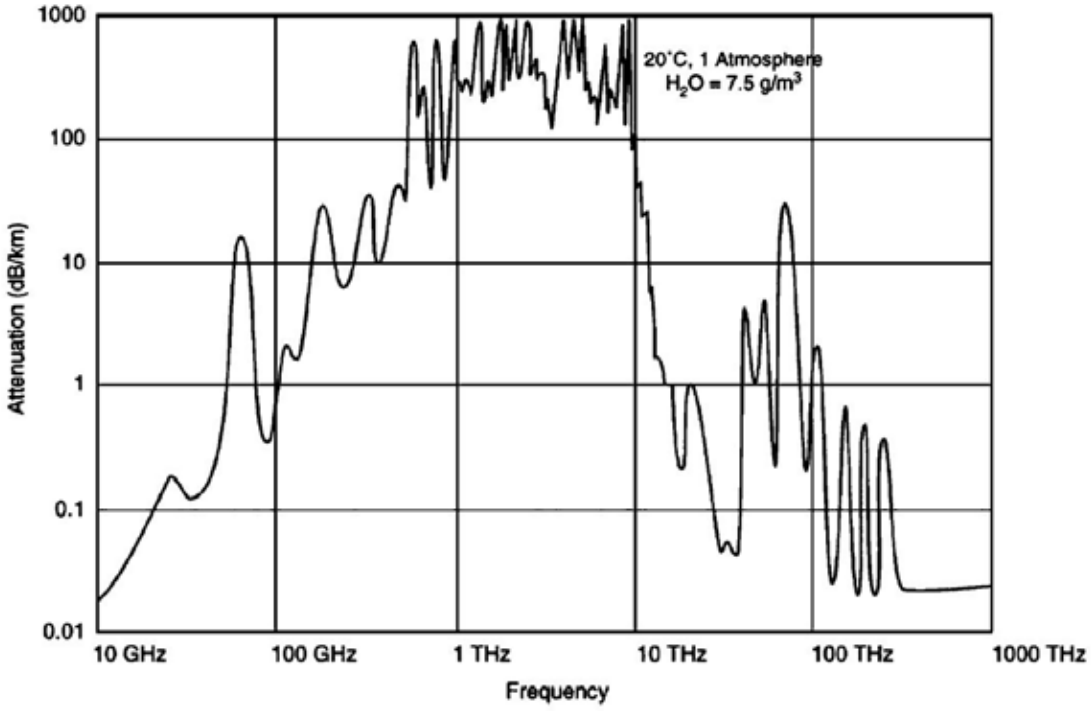

Figure 2-14: Atmospheric attenuation for clear and dry conditions from 10 GHz-1000THz [50]

In order to assess the powers required to detect power cables, the atmospheric attenuation should be taken into account especially at the upper end of the millimetre-wave band (>100 GHz). Figure 2-14, obtained from [50], shows the atmospheric attenuation over a wide range of frequencies for clear and dry conditions. This plot was used to estimate atmospheric losses at 16 GHz, 34 GHz, 150 GHz and 300 GHz. (Table 2-6). This data will be used in the modelling of power cable detection.

Table 2-6: Measured atmospheric losses at 16 GHz, 34 GHz, 150 GHz and 300 GHz [50]

Frequency	Atmospheric Attenuation (dB/km)
16 GHz	0.025
34 GHz	0.05
150 GHz	2
300 GHz	8

2.7 Power Budget

The important parameters of the power budget for overhead power cable detection will be discussed in this chapter whilst stating practical values for each.

2.7.1 Coverage and Beamwidth

The beamwidth should be 1° in both azimuth and elevation to allow the wires to be recognised and to allow the pilot to find a path around them. The cross-range resolution at 500m would then be just under 9m, which would be adequate to resolve the larger cables from the ground by detecting the gap under them. This would allow military helicopters to fly under the larger cables. Smaller cables would not be resolved from the ground until somewhat shorter ranges, but this will probably be acceptable since only more modest manoeuvres will be needed to allow a helicopter to fly over them.

2.7.2 Antenna Gain

Assuming (conservatively) that the antennas are 50% efficient, the gain can then be calculated by Equation 2-26.

$$G = \frac{4\pi}{\theta[radians]\varphi[radians]}$$

Equation 2-26: Antenna gain

θ and ϕ are the principal-plane beamwidths in radians. For a cylindrical beamwidth of 1°, this equation predicts an antenna gain of 43dB. Assuming that the antenna used will be a circular horn antenna with a uniform taper, Equation 2-27 can be used to estimate the cross section dimension for a pencil beam with a 1° 3dB beam width in both azimuth and elevation [15]. The antenna size and weight becomes extremely important for small aircraft such as UAVs and drones. Antenna diameters for the frequencies of interest are shown in Table 2-7.

$$D_H \approx \frac{\lambda}{3.413\sin(\Delta\theta[radians])} \text{ and } D_E \approx \frac{\lambda}{3.413\sin(\Delta\phi[radians])}$$

Equation 2-27: Theoretical cross-section diameter for a circular horn antenna [15]

Table 2-7: Antenna size for 3dB beamwidths, Δθ and Δφ equal to 1°.

Frequency	Antenna cross-section diameter using Equation 2-27
16 GHz	31.5 cm
34 GHz	14.8 cm
150 GHz	3.4 cm
300 GHz	1.7 cm

2.7.3 Range Resolution

The range resolution is not a significant parameter in the system design. A resolution of a few meters is very easy to achieve at these frequencies and is expected to give adequate information to allow the aircraft to manoeuvre to avoid the cables. For this baseline design we will assume that the range resolution is relatively coarse so that all the returns from the cable are within a single range cell, i.e. the effect of the range spreading is not considered here and will be discussed later.

2.7.4 Radar Equation

The signal to noise ratio is calculated by using the usual equation (Equation 2-28).

$$SNR = \frac{P_t G^2 \lambda^2 \sigma}{[(4\pi)^3 r^4 kTBLN]}$$

Equation 2-28: Theoretical Signal to Noise Ratio (SNR) assuming two-way transmission in free-space

where

P_t is the transmitted power

G is the gain of the antenna

k is Boltzmann's constant

T is the temperature of the receiver

L represents the atmospheric losses

N is the noise figure of the receiver and

B is the effective bandwidth.

The previous discussion allows the value of many of these parameters to be deduced directly, but some are not so obvious.

As is conventional, the product kT will be taken to be -174dBm/Hz.

2.7.5 Receiver Noise Figure

A receiver noise figure of 10dB will be assumed. Whilst this is somewhat better than can currently be achieved at 300GHz [51], previous experience at lower frequencies suggests that it is reasonable to assume that this will be attainable as the technology matures.

2.7.6 Aircraft Response Time

Considering that the measured aircraft speed in [48] for the aircraft that the INS measurements (Figure 2-11) were taken from is around 60 m/s, this will be taken as the 'worst case scenario' velocity and thus will be used as the aircraft velocity parameter in the cable detection simulations. Assuming that the aircraft has a human operator, which would typically require a longer response time than a UAV/drone, the response time of around 9 seconds is deemed reasonable in order for a human operator to take evasive action if a power cable is detected. Considering the previous aircraft velocity and required response time, the distance at which the cable should be detectable is:

$$R_T = v\tau = 60[m/s] \times 9[s] \approx 500m$$

2.7.7 Typical Cable RCS Values

Previously most of the RCS measurements of ACSR power cables between 18 GHz and 94 GHz were made at short ranges [43] [18] although [43] also presents 94 GHz results for a 250 metre long cable measured at ranges of 100 m and 500 m. The RCS peaks measured at 100 metres, with a radar device operating at 94 GHz, were measured to be between 43 dBsm

and 49 dBsm whereas the measured RCS peak values at the larger range have values between 50 dBsm and 58 dBsm. The modelling results that considered 150 GHz frequency at a range of 500 metres also produced peaks of the order of 60 dBsm which is not a large increase although this is expected to be because of the increased number of peaks at 150 GHz compared to 94 GHz.

Table 2-8: Main parameters of the target fluctuation simulation

Parameter	Value
Frequency array	[16 GHz, 34 GHz, 150 GHz, 300 GHz]
INS sample time	10ms
Number of Azimuth and Elevation Samples	500
Bandwidth	1 MHz
Antenna 3dB beamwidth in both azimuth and elevation	1°
Noise Figure	10 dB
Cable Span	232 m
Cable suspension height	25 m
Cable temperature	30°C
Range	500 m
Aircraft altitude	100 m
Aircraft velocity	60 m/s
Probability of false alarm	1e-6

2.8 Target Fluctuation

The aircraft model, Sagging OH power cable data/model, power link budget and straight cable RCS signatures were all integrated in order to simulate the fluctuation in returns from a realistic overhead power cable being illuminated by an airborne radar. The main parameters used in the fluctuation simulations are shown in Table 2-8.

The aircraft disturbance model was used to generate random samples for the elevation and azimuth disturbance of the simulated flying aircraft. These samples were then inserted into the sagging model alongside the position of a high altitude aircraft, so that the section of the sagging cable in which the majority of the backscatter comes from can be determined and the surface normal of this subsection can be computed relative to the airborne transceiver as discussed previously.

The modelled RCS from a straight section of cable is then used as a look-up-table, by using cubic spline interpolation, to determine the magnitude and fluctuation of the backscattered RCS. This model was used for both types of cable with the corresponding RCS look-up-table and sagging parameters for a given scenario.

The model then determines the output probability distribution function for the receiver noise with no target (Figure 2-15), and with the noise plus the fluctuating target return for a given number of samples (Figure 2-16 and Figure 2-17). Initially a very high transmit power is simulated so that a SNR can be estimated, this then is used to simulate the model for a SNR values either side of 0dB.

A compromise exists when choosing a threshold value to determine if a target has been detected or not; because if the value is set too high then targets may be missed whereas a small threshold would make the detector susceptible to clutter/noise. The statistical nature of noise

induces the possibility that the noise alone can rise above any set threshold and this is known as the false alarm probability P_{FA}. A voltage threshold is chosen to give an adequate false alarm probability, by fitting the noise (Figure 2-15) to a Rayleigh distribution and using the estimated variance value, ψ^2, .in (Equation 2-29) to estimate the required voltage threshold, V_T [14]. This threshold is then used to determine the probability of detection for different SNR values. The P_d vs SNR plot produced (Figure 2-18 and Figure 2-19) can then be used to work out the required transmit power in order to get a high enough probability of detection so that the transceiver is robust enough for its application (Table 2-9).

$$V_T = \sqrt{2\psi^2 \ln\left(\frac{1}{P_{FA}}\right)}$$

Equation 2-29: Voltage threshold for a probability of false alarm P_{FA} and Rayleigh noise variance ψ^2 [14]

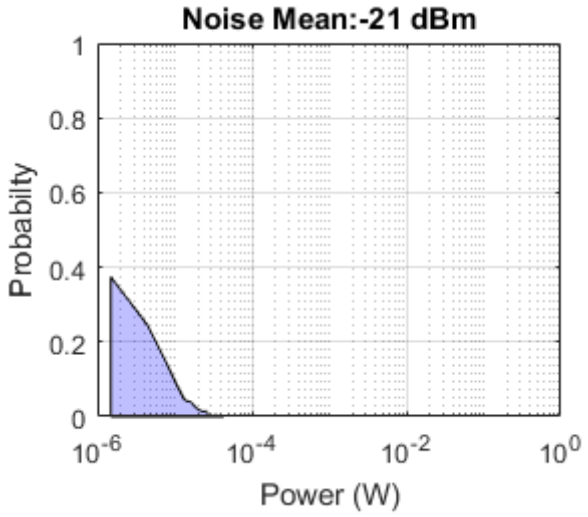

Figure 2-15: Noise (no target) probability distribution function for both cable types

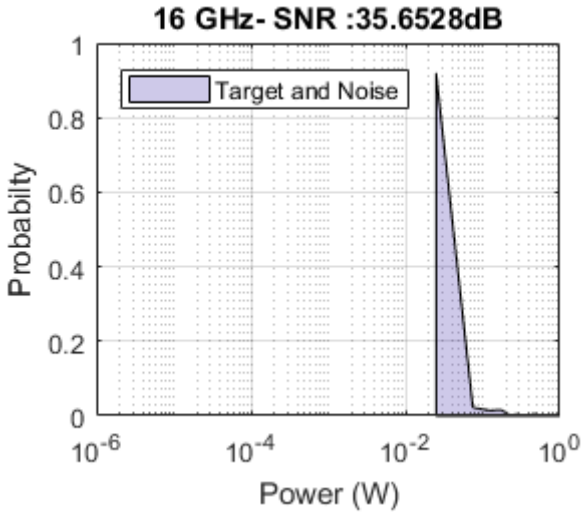
16 GHz- SNR :35.6528dB
Target and Noise
Probabilty
Power (W)

a)

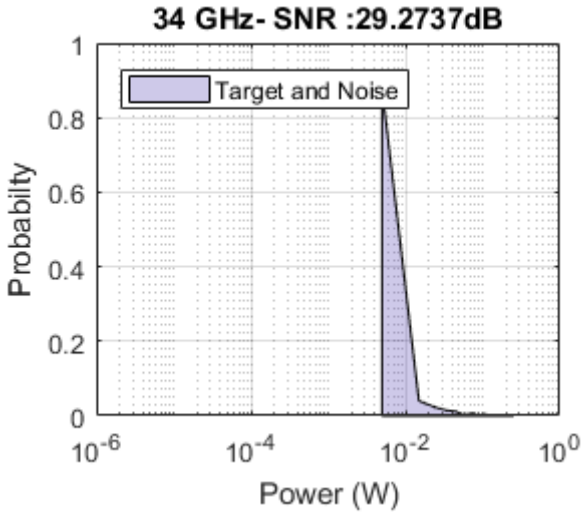
34 GHz- SNR :29.2737dB
Target and Noise
Probabilty
Power (W)

b)

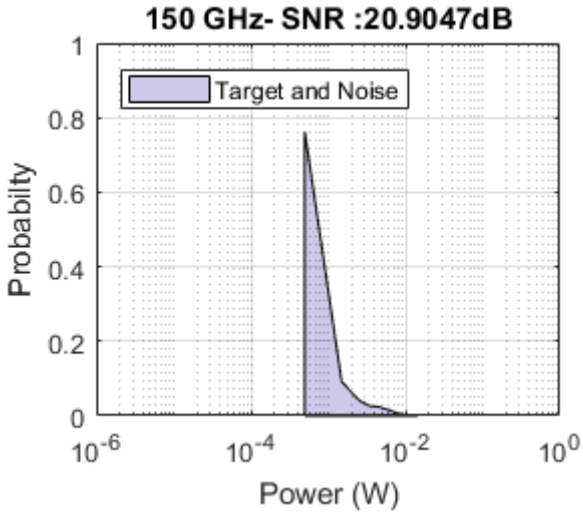
150 GHz- SNR :20.9047dB
Target and Noise
Probabilty
Power (W)

c)

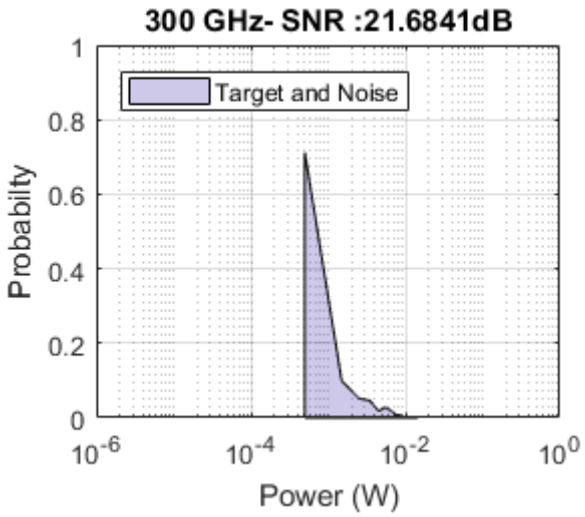

d)

Figure 2-16: Target + Noise (Figure 2-15) probability distribution function at all simulated frequencies (ACSR type)

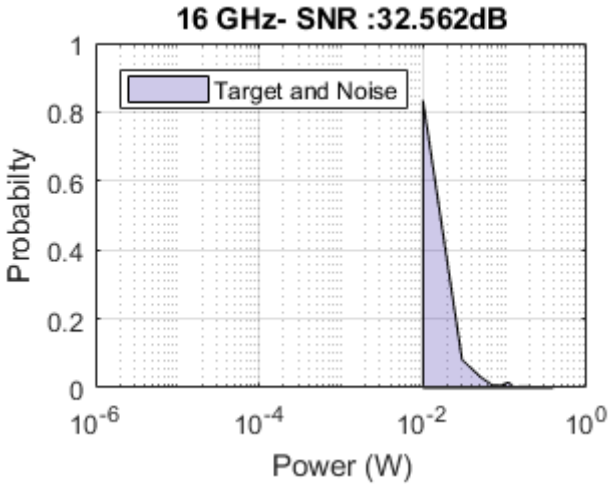
16 GHz- SNR :32.562dB
Target and Noise
Probabilty
Power (W)

a)

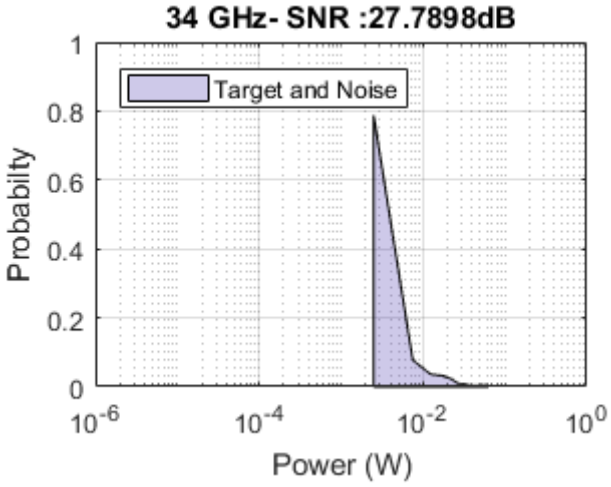
34 GHz- SNR :27.7898dB
Target and Noise
Probabilty
Power (W)

b)

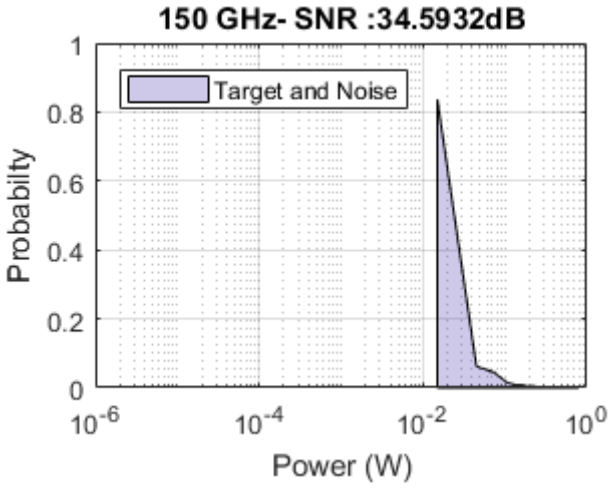
150 GHz- SNR :34.5932dB
Target and Noise
Probabilty
Power (W)

c)

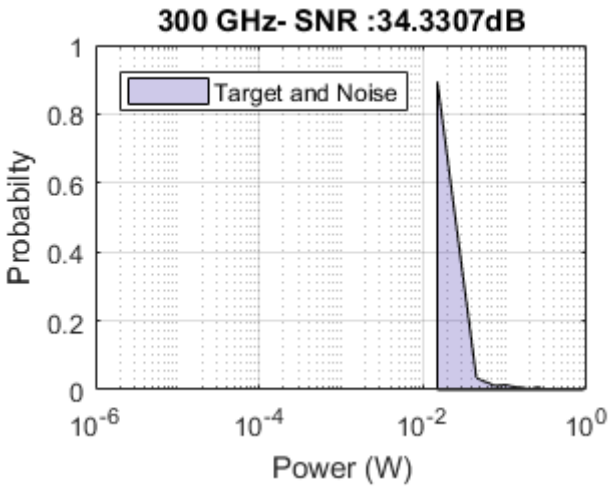

d)

Figure 2-17: Target + Noise (Figure 2-15) probability distribution function at all simulated frequencies (ACCC type)

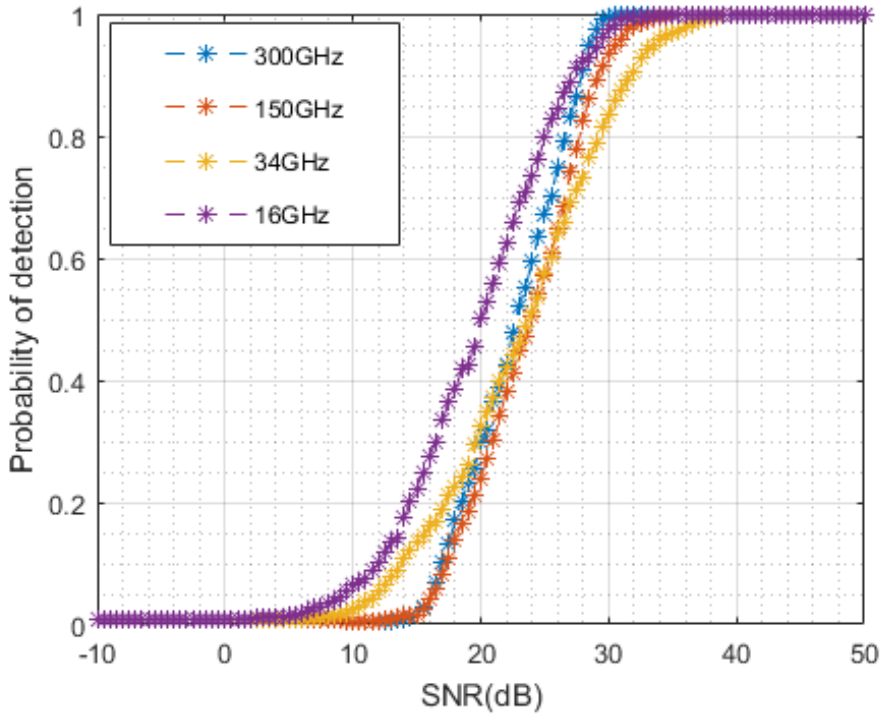

Figure 2-18: Probability of detection for sagging ACSR cable with respect to SNR either side of 0dB (σaz=2.5° & σel=1.22°)

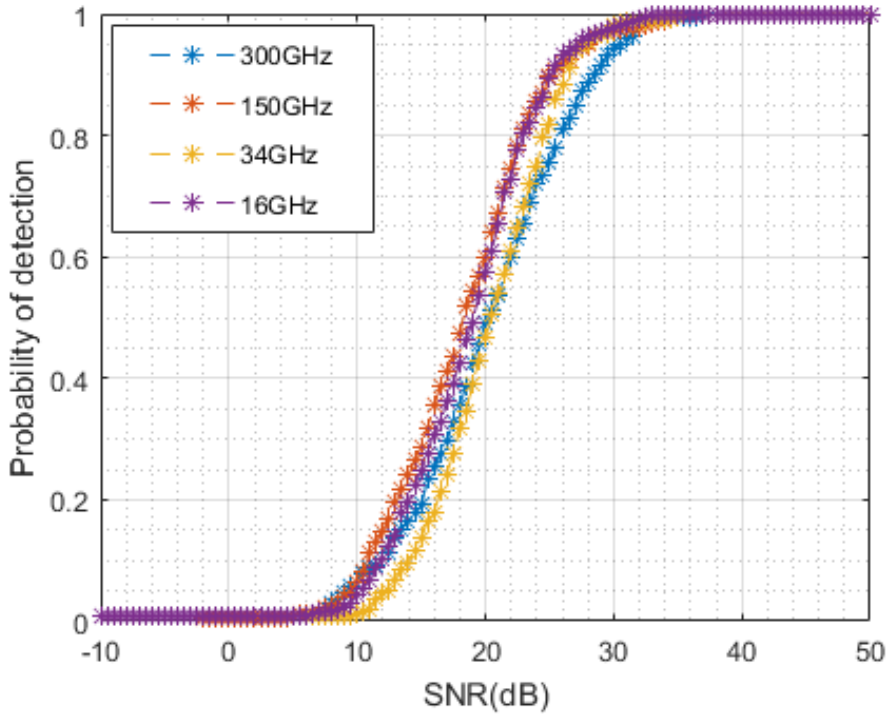

Figure 2-19 : Probability of detection for sagging ACCC cable with respect to SNR either side of 0dB (σaz=2.5° & σel= 1.22°)

Table 2-9: Simulated transmit power to achieve Pfa=10e-6 and Pd=0.99 with aircraft disturbances included (σ_{az}=2.5° & σ_{el}=1.22°)

Frequency /Transmit Power	P_t (ACSR)	P_t (ACCC)
16 GHz	9.9 dBm	10.9 dBm
34 GHz	15.9 dBm	11.4 dBm
150 GHz	11.9 dBm	12.9 dBm
300 GHz	8.4 dBm	12.9 dBm

The impact of aircraft disturbances on target fluctuations discussed here can also be reduced by rapid scanning of the antenna or by stabilising the antenna motion against variations in the platform orientation. If the random variation in the modelled platform is ignored (σ_{az}=0 & σ_{el}=0) and the previous simulations are repeated for both the ACSR and ACCC cables, the probability of detection curves in Figure 2-20 and Figure 2-21 are obtained. Further analysis

of these curves produce the transmit powers in Table 2-10 in order to get P_d=0.99. The expected improvements due to ideal platform disturbance compensation is clearly evident as reductions in the required transmit power value is seen to make a 5.6 dBm improvement on average in the simulations made (Table 2-9 and Table 2-10).

The relatively compact radar systems that can be achieved at higher frequencies will make the implementation of stabilisation or rapid scanning of a radar device more practical. The simulated results show that transmit powers can be reduced in order to get adequate detection performance.

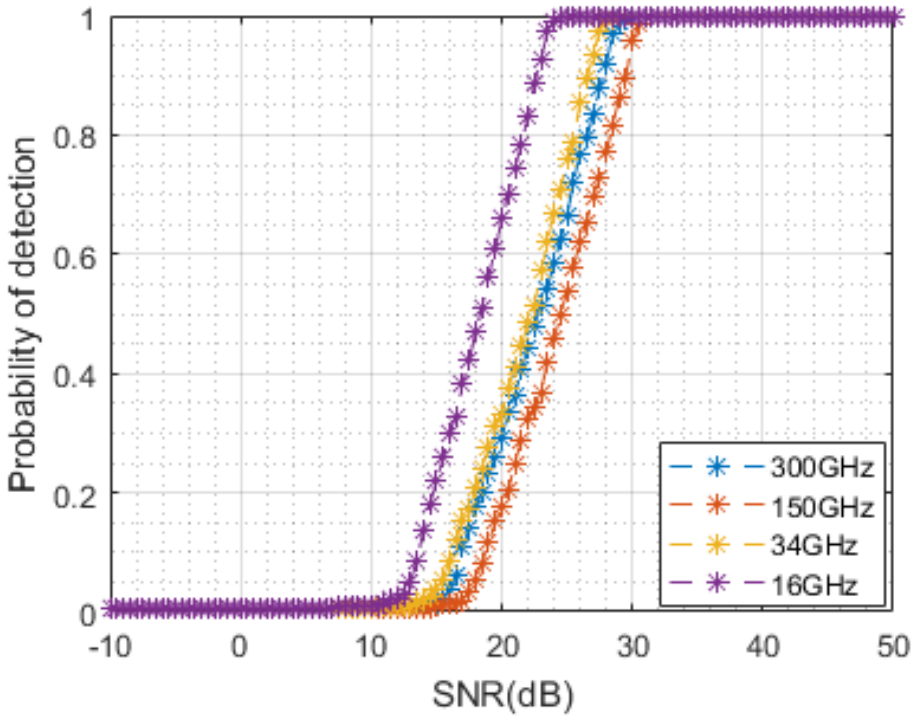

Figure 2-20: Probability of detection for sagging ACSR cable with respect to SNR either side of 0dB (σaz=0° & σel=0°)

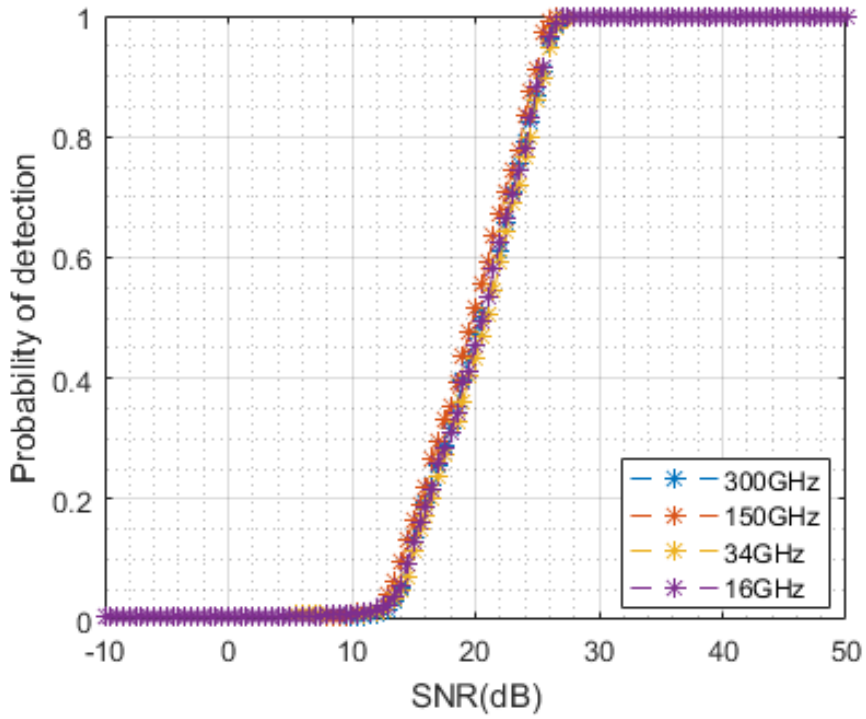

Figure 2-21: Probability of detection for sagging ACCC cable with respect to SNR either side of 0dB (σaz=0° & σel= 0°)

Table 2-10: Simulated transmit power to achieve Pfa=10e-6 and Pd=0.99 with aircraft disturbances negated (σaz=0° & σel=0°)

Frequency /Transmit Power	P_t (ACSR)	P_t (ACCC)
16 GHz	2.9 dBm	5.4 dBm
34 GHz	6.9 dBm	5.9 dBm
150 GHz	9.4 dBm	4.9 dBm
300 GHz	7.9 dBm	5.9 dBm

2.9 Conclusion

Physical optics models have been developed to simulate the high-frequency backscatter from both the ACSR and ACCC types of overhead power cables by using an analytical parametric function that describes the surface structure of each cable type. The ACSR cable signatures produced by such models have similarities to the standard Bragg model in terms of Bragg peak number and cut off angle but the presented model also includes important information such as Bragg lobe width and magnitude

A model that incorporates cable sagging was also presented and the importance of sagging geometry when illuminated by an airborne transceiver was discussed. A power budget that centred on the radar equation was described which allowed simulation parameters to be used to investigate fluctuations in power cable radar returns. The results show that due to the surface structure and less sag present for the ACCC type, it requires the transmit power to have a few more decibels relative to the ACSR type in order to achieve the same probability of detection and false alarm rate.

3. Experiment Sites, Methodology & Characterization

3.1 Introduction

This chapter of the Thesis describes the radar devices used to measure backscattering from overhead power cables. The four frequencies that power cables were measured at were within K_u-band (12-18 GHz) and K_a-band (26.5-40 GHz) and at 150 GHz and 300 GHz. The two lower frequency devices were designed and constructed by DSTL & Thales UK and were used to obtain high resolution spotlight images of outdoor scenarios containing overhead power lines. The devices operating in both the K_u-band and K_a-band have relatively large mean transmit powers of the order of a Watt, enough power to illuminate sagging power cables from several thousands of metres away whilst being compact enough to be mounted on a fixed-wing aircraft during flight. Farmland and Industrial scenarios were measured that contained different types of power transmission lines and the measurements obtained will be discussed in this chapter. The high resolution images obtained were used to measure certain parameters of the cable, such as cable span and the sag at the centre of each conductor, as well as to separate targets of interest from surrounding clutter. A spectrum analysis that was used at both K_u-band and K_a-band to convert these high-resolution spotlight images to angular profiles of the cable will also be described and illustrated.

Devices were also used at 150 GHz and 300 GHz that have lower power and poorer receiver specifications; due to the lower maturity of sources and components in this frequency range. These devices were capable of measuring straight subsections of different cable types in an indoor environment. The large range resolution and the availability of adequate absorbers at these frequencies allowed target returns to be separable from the surrounding indoor clutter. The indoor mmW measuring facility used to measure cables just over two metres in length will

also be described with the aid of photos and simplified diagrams. The basic theory of FMCW and Stepped Frequency Radar will be discussed as this was required to perform experiments with the 150 GHz and 300 GHz devices.

3.2 Experimental Equipment

3.2.1 I-Master and Bright Spark Systems

The availability of power cable measurements that were obtained by K_a-band and K_u-band radar devices whilst on-board an airborne platform warranted a data analysis to investigate the behaviour of the sagging cable backscatter in a realistic scenario. Two different but very similar devices were used to obtain the airborne measurements, the I-Master (Ku-band) [52] and the Bright Spark (Ka-band) [53] radar systems developed at Thales UK.

Both the I-Master and Bright Spark devices are intended for helicopters or small fixed-wing aircraft for ground surveillance. The I-Master system has a weight of 30 kg and the Bright Spark system is slightly heavier due to being the same system but with frequency converters. The bandwidth and carrier frequency of the I-Master system are around 1.6 GHz and 16 GHz respectively; the Bright Spark system has both double the frequency and double the bandwidth. An IMU device provides direct measurements of the antenna motion in order to compensate for high order vibration dynamics so that images can be focused effectively at K_a and K_u band by using SAR processing techniques. The down-range (DR) and cross-range (CR) resolutions after spotlight SAR processing can be from 1 metre down to around 0.3 metres.

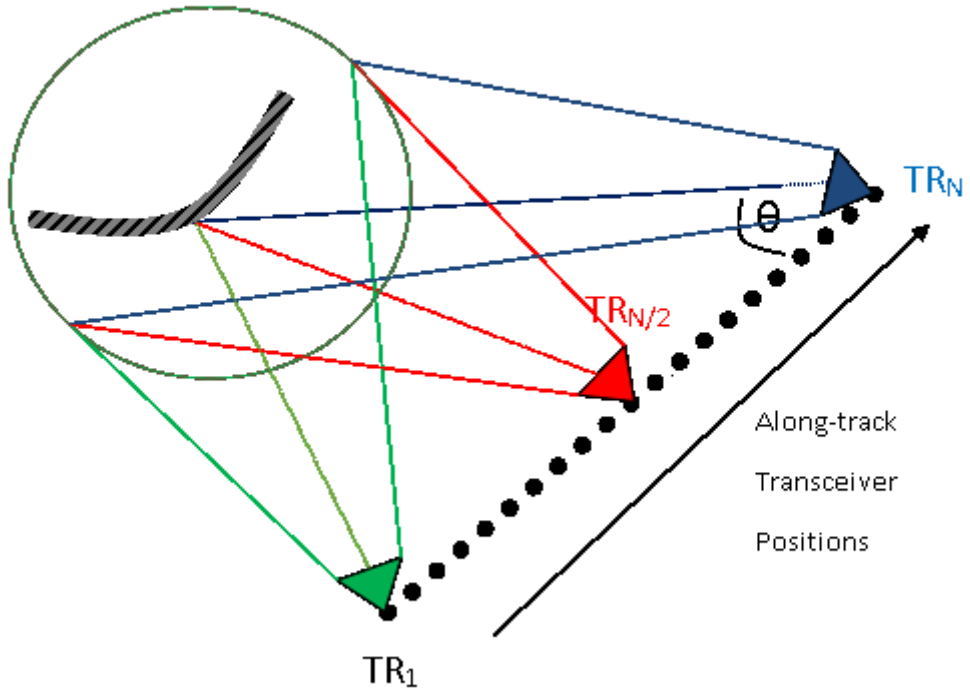

Figure 3-1: Visual representation of a radar conducting measurements in the spotlight SAR mode

The measurements of interest were collated for both of the systems whilst they were operating in the Spotlight SAR mode (Figure 3-1) which allowed the fine resolutions mentioned previously. A higher resolution allows power cables to be separated from surrounding clutter whilst also reducing speckle. Equation 3-1 and Equation 3-2 show the main parameters of Spotlight Processing which required the gaining of efficient samples over an angle extent of $\Delta\theta$ in order to be able to gain sufficient CR resolution ρ [54]. The CR resolution was chosen to be equal to the DR resolution for a given system in order to gain optical like images which also made the processing shown later on in this report simpler.

$$\Delta\theta = \frac{\lambda K_w}{2\rho}$$

Equation 3-1: Angular extent in spotlight SAR [54]

$$\frac{\rho}{K_w} = CR_{samp}$$

Equation 3-2: Cross-Range sampling in spotlight SAR [54]

Where:

$\Delta\theta$ – apparent angular extent

λ – Transmit centre wavelength

K_w – weighting factor

ρ – cross-range resolution

CR_{samp} – cross range sampling

The angle subtended at the target by the track length for the single-look spotlight SAR images shown and used in this report are shown for the two systems below:

I-Master:

$$\Delta\theta \approx 4.5°$$

Bright Spark:

$$\Delta\theta \approx 7°$$

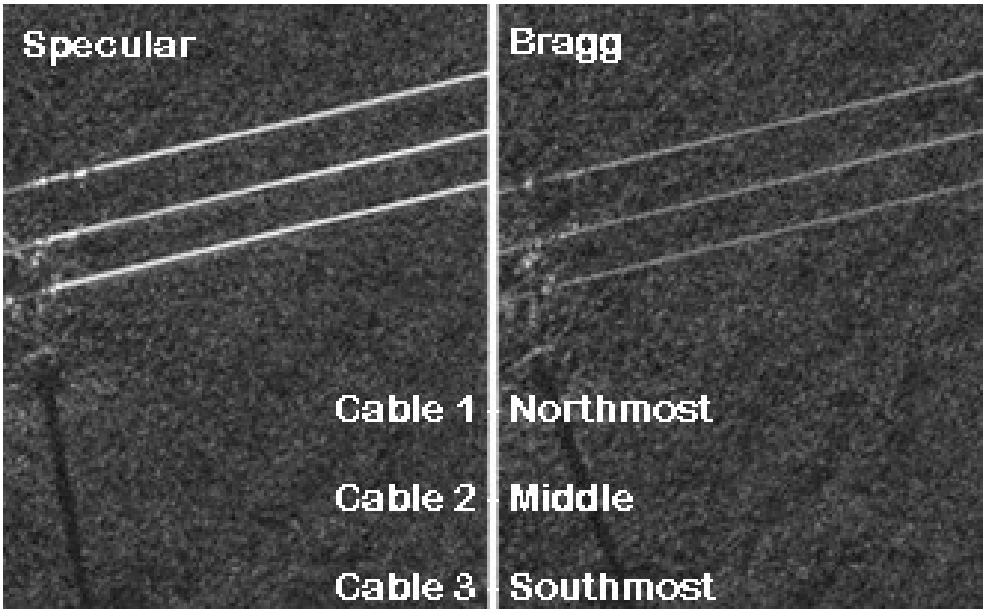

Figure 3-2: Cropped high-resolution single-look images showing a cable in the specular and Bragg scattering regions

Spotlight SAR processing by summing over the above angles to produce the high resolution images produced optical-like images of the cables measured (Figure 3-2). The cables are clearly distinguishable in this SAR image which also provides bearing angles and ranges of interest.

The main disadvantage of the processed image is that the cable as discussed before will only be detectable at discrete, relatively narrow angles, within the relatively wide range of angles used to process the image. The detectable cable returns thus will be averaged over the processed single-look image. The effect of having a windowing function to produce the weighting factor, K_w (Equation 1), produces a biasing of returns that depends on the chosen range of angles; the cable returns present at the centre-most angle within the synthetic aperture will have the largest weighting. The next section describes a spectrum analysis technique that allows angular profiles of cables to be obtained from a processed single-look image.

3.2.2 Spectrum Analysis of Multi-look Spotlight SAR Images

To estimate the Bragg peak locations that arise from the periodic surface structure of a power cable, the DR and CR axes present in a processed single-look image need to be converted into the angular domain. The processing used to both extract angular information of cable returns whilst also focusing cable returns and not diffuse returns from surrounding clutter is shown in Figure 3-3.

First of all, a single-look image containing OH power cables was manually cropped out of a processed spotlight image and rotated so that the principal axes became along-cable (AC) and cross-cable (CC). The cable can be assumed to be straight due to the negligible sag present in each cropped image. An FFT was then performed along the AC axis. To perform a 1D FFT along the cross-range axis of a single-look spotlight SAR image with M cross-cable rows and N along-cable columns, the following number of complex multiplications is required to produce the output image [55]:

$$C_N = MN \log_2 N$$

Equation 3-3: Number of complex multiplications to perform FFT method

Where N is obtained by rounding up n to the next highest power of two:

$$N = 2k$$

where k is a positive integer.

The complexity of the Fourier transform over a relatively small number of cross-cable cells is much less than that of the original image formation.

This AC FFT allows the power in the cable returns to be concentrated into a few angles where cable backscatter is strong whilst the clutter around it remains spread over all angles.

This technique allowed the cable signatures to become more prominent in both the specular and Bragg regions which allows further analysis to gain more information such as Bragg lobe positioning and lobe widths. This required the orientation of the system to be known and this information was supplied by the on-board INS device. If the cable returns are not processed at the centre sample of the single-look image then a bias due to weighting will still be present.

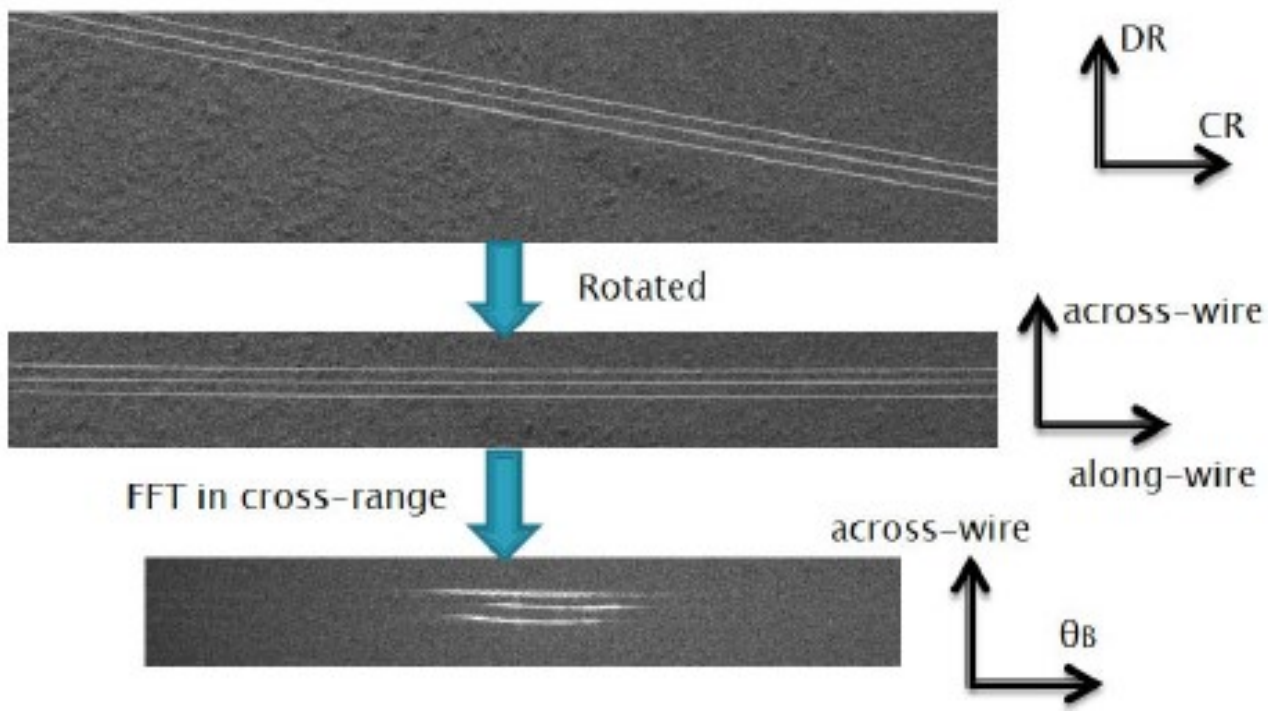

Figure 3-3: Spectral analysis overview which includes performing a Fourier transform in the CR plane to obtain condensed cable signatures

The result of performing this technique on a spotlight SAR image that contains three parallel overhead cables each suspended between two poles is shown in Figure 3-4. The resultant spectrum has three separate specular scattering regions for each sagging subsection of cable between the suspension points. The effect of not having the wire along the plane that the Fourier transform is taken, can be seen in the centre and right signatures in Figure 3-4 as a spread of power is induced which causes specular signatures from different cables to overlap. Figure 3-5 shows the centre span of the cable in Figure 3-4, after it had been cropped and the resulting spectrum signature in the specular scattering region. The Bragg scattering signature

for the same subsection of cable is shown in Figure 3-6 which is noticeably noisier than the signature in Figure 3-5 because of the lower level of power in this scattering region compared to the specular region at Ka-band.

The I-Master spectrum images were noisier and hence less clear and are not shown here.

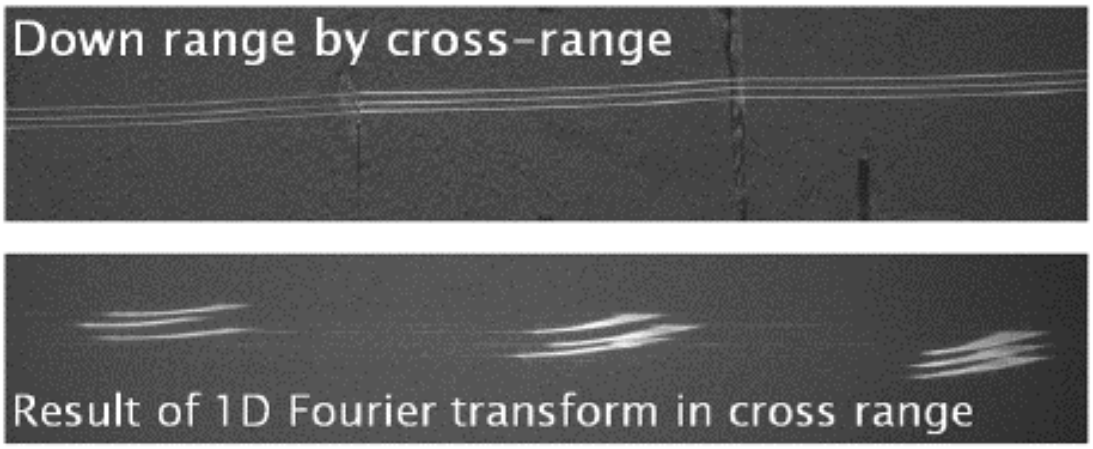

Figure 3-4: Single span of overhead power cable with three suspension points (around 100m between each) before and after the CR Fourier transform

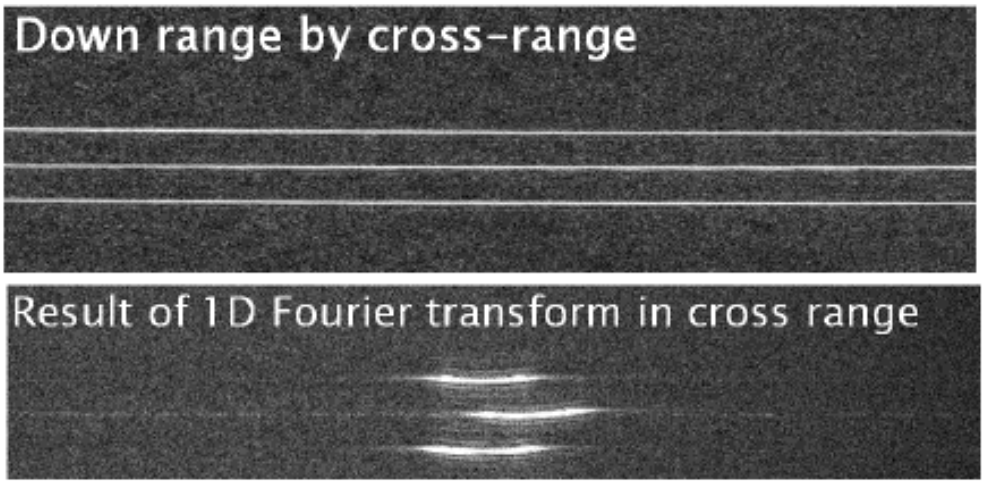

Figure 3-5: Aligned cable within the specular scattering region before and after CR Fourier transform

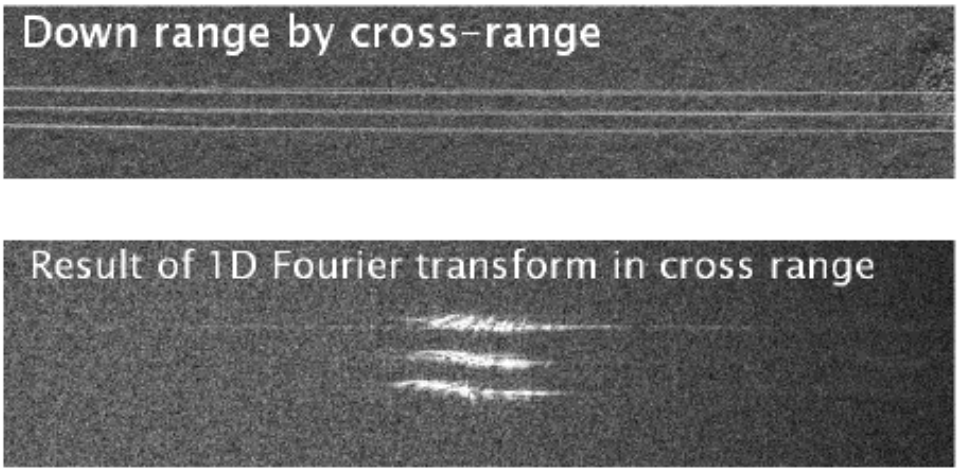

Figure 3-6: Aligned cable within the Bragg scattering region before and after CR Fourier transform. The reflection is at a bearing angle of 10.8° with respect to the specular return shown in Figure 3-5)

3.2.3 150 GHz FMCW System

3.2.3.1 Basic FMCW theory

This section will describe the 150 GHz FMCW system used to gain cable measurements at this frequency to investigate the scattering behaviour. The basic principles of FMCW radar to obtain range profiles will be put across to show how the system was adequate to perform short-range indoor measurements of a power cable subsection. This radar system was developed by the millimetre-wave division at ELVA [56] especially for the radar group at the University of Birmingham.

The typical transmitted waveform for an up-chirp linear frequency modulated wave system is shown in Equation 3-4 and the instantaneous frequency required is shown in Equation 3-5.

This up-chirp waveform, has a time period of T_{sweep}, bandwidth of Δf and a normalised transmit power.

$$\varepsilon_{tx}(t) = rect\left(\frac{t}{T_{sweep}}\right)e^{2\pi j\left(f_0 t+\frac{Kt^2}{2}\right)} = rect\left(\frac{t}{T_{sweep}}\right)e^{j\varphi}$$

$$\text{where } rect(x) = \begin{cases} =1 & if\ |z| < 1/2 \\ =0 & if\ |z| > 1/2 \end{cases}$$

Equation 3-4: Single transmitted linear FMCW

$$f_i = \frac{1}{2\pi}\frac{d\varphi}{dt} = f_0 + Kt \qquad \text{where} \qquad K = \frac{\Delta f}{T_{sweep}}$$

Equation 3-5: Instantaneous frequency of the wave in Equation 3-4

Figure 3-7 displays the frequency response of a single up-chirp signal over time and also a single received signal which is assumed to be of the same modulation shape, hence zero channel dispersion effects, but with a different amplitude and a time delay due to the time taken for signals to travel from the transmitter to the scatterer and back to the receiver

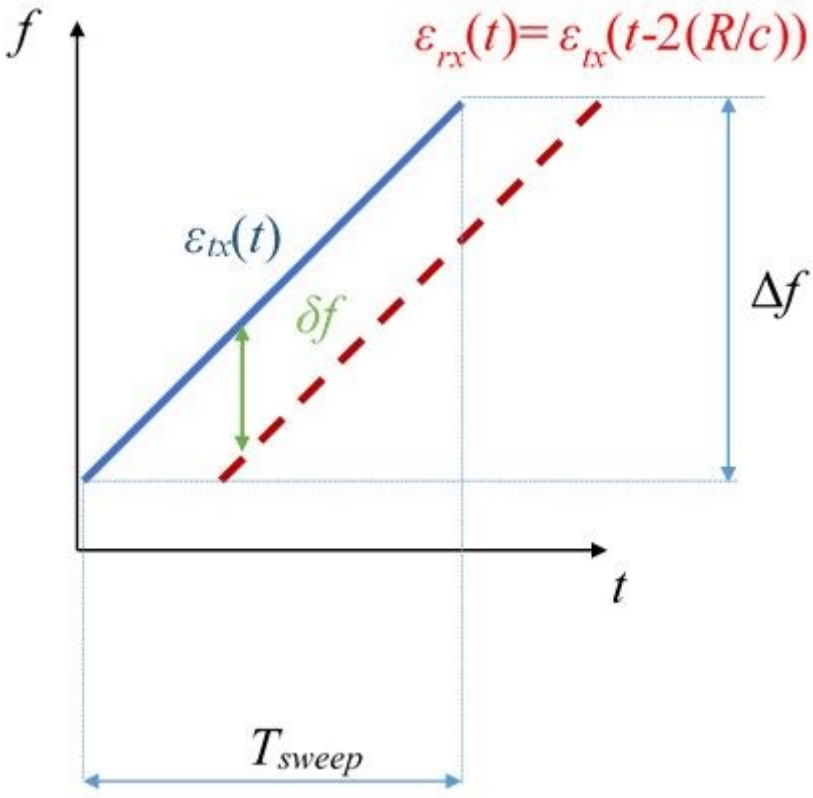

Figure 3-7: Frequency Modulation over time for a transmitted and received FMCW wave

At a given time, the difference in the transmitted and received frequencies corresponds to Equation 3-6 and this is known as the beat frequency which has a constant relationship with range and the detectability of this component depends on the mixer circuitry which is designed to filter out the unwanted signals. After subsequent post-mixer filtering and by neglecting noise sources in the receiver, the received signal will be a superposition of sine waves that have a beat frequency corresponding to the range (time delay), and an amplitude that corresponds to the reflectivity of the scatterers that reside within this range cell.

$$f_b = \frac{\Delta f}{T_{sweep}} \frac{2R}{c}$$

Equation 3-6: Beat Frequency and range relationship

$$s_R(t) = \sum_{n=1}^{N} A_n \sin(2\pi f_n^b t) \qquad \text{where} \qquad f_n^b = \frac{\Delta f}{T_{sweep}} \frac{2R_n}{c}$$

Equation 3-7: Post-mixer sinusoidal summation of *N* returns

This superposition of sinusoids (Equation 3-7) can be segregated in frequency (or range) by making use of the Discrete Fast Fourier Transform (DFFT). The post mixer filter (IF filter) spectral characteristics and DFFT parameters will also decide how $s_R(t)$ is decomposed as well as the scenario being illuminated. The number of DFFT points (N_{FFT}), swept bandwidth (Δf) and the speed of light (c) can be used to estimate the maximum range attainable using this method (Equation 3-8).

$$R_u = \frac{c.N_{FFT}}{4\Delta f}$$

Equation 3-8: Maximum range when using DFFT to distinguish beat frequencies [57]

Theoretically, the previous processing of transmitted and received FMCW waves should produce a sinc function at the beat frequency f_B .The 3 dB width of this sinc response in range is the inverse of the bandwidth of the system and hence decides the resolution in the range profile Δr as given by (Equation 3-9). Due to the fact that both the radar system and target were stationary relative to each other during experiments, the effect of Doppler shifts will be ignored. A windowing function can be applied to the mixer output in order to reduce range side lobes.

$$\Delta r = \frac{c}{2\Delta f}$$

Equation 3-9: Range resolution and bandwidth relationship

The previous FMCW theory will be used alongside other radio propagation theories in order to assess the feasibility of the 150 GHz FMCW radar system in terms of overhead power cable experiments.

3.2.3.2 150 GHz FMCW Parameters

The main parameters of the 150 GHz FMCW radar system (Figure 3-8) purchased from ELVA [56] are shown in Table 3-1.

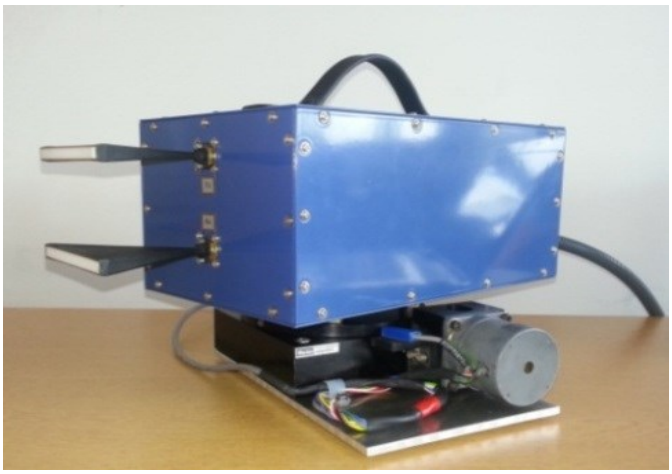

Figure 3-8: 150 GHz FMCW radar with two lens-horn antennas on a turntable to provide azimuth scanning [58]

Assuming non-linearity along the chirp are negligible, the bandwidth can be inserted into Equation 3-9 to get a range resolution of around 3 cm which is deemed more than adequate to separate the target from any surrounding clutter. The 150 GHz radar with a chirp sweep bandwidth of 5 GHz produces an IF beat frequency shift of around 800 Hz per range resolution cell. This range-resolution is actually likely to separate target returns into different cells; the effect of this will be described later in this section. This radar has both up and down chirps (Figure 3-9) for range and Doppler separating but due to the fact that is not required in stationary measurements only the up-chirp was used.

The chirp bandwidth and two-channel (I and Q) FFT points in Table 3-1 give a maximum range of 61.4 m (Equation 3-8) but the cut-off frequency of the IF filter also needs to be taken into account which corresponds to 72 m by inserting 2 MHz into Equation 3-10, this means that the maximum range measurable will be around 60 metres.

$$R_{\max}^{IF} = \frac{cT_{sweep}f_u^{IF}}{2\Delta f}$$

Equation 3-10: Maximum range for a given IF cut-off frequency

Now to assess the maximum detectable range (R_{max}) in terms of transmit power (P_t), Noise Floor (NF) and Antenna Gains (G) in a power link budget the radar equation is used. A matched-filter gain will also be present due to the compression of the waveform due to the mixing process and this parameter can be calculated using Equation 3-11 [57]. Equation 3-12 shows the re-arranged radar equation to estimate the maximum range and the parameters in Table 3-1 have been inserted into Equation 3-12 to produce the plot in Figure 3-10 which shows the maximum detectable range for RCS values between -20dBsm and 20dBsm. The marker on the plot shows that the maximum detectable range for a target with an RCS of only -20dBsm can be detectable up to a distance of around 250m. Cable simulations expect the cable to be higher than this value for the range of aspect angles of interest; although this doesn't include the effect of splitting cable returns into different range cells.

A block diagram that summarises the overall operation of the 150 GHz FMCW system is present in Figure 3-11.

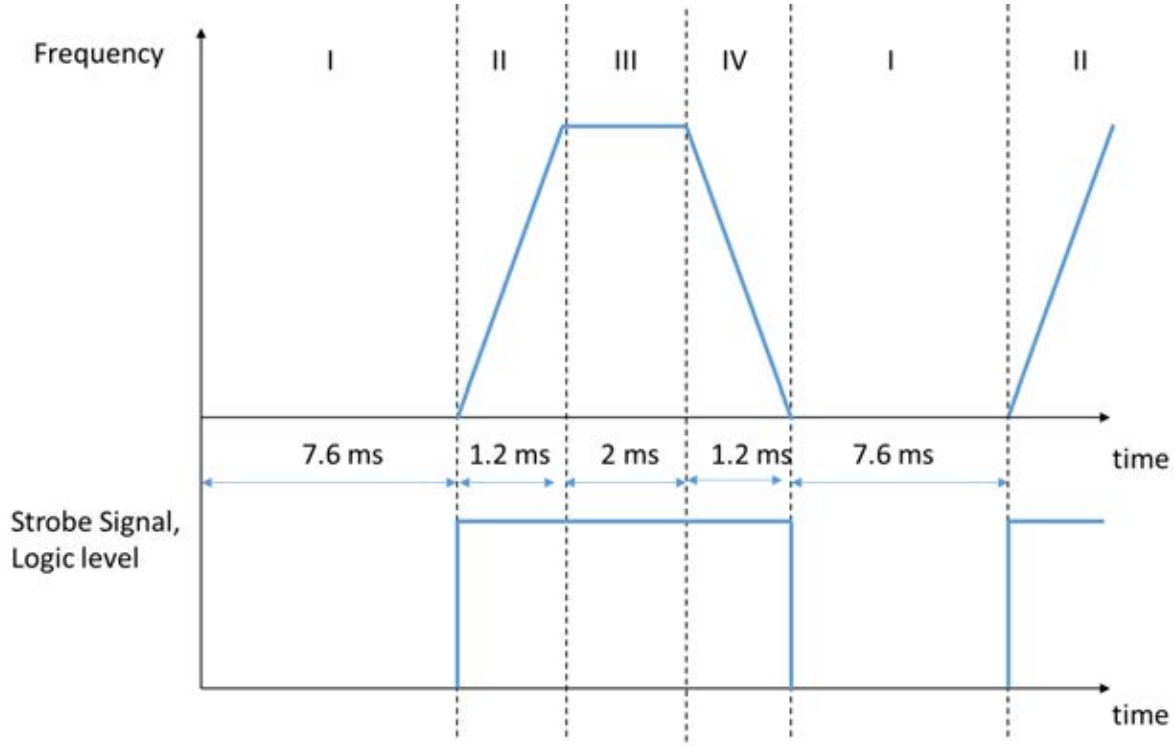

Figure 3-9: FMCW radar up-chirp and down-chirp with the strobe pulse [58].

$$G_{MF}^{FMCW} = \Delta F \cdot T_{sweep}$$

Equation 3-11: Matched filter gain

$$R_{\max} = \sqrt[4]{\frac{P_t G^2 \lambda^2 G_{MF} \sigma}{(4\pi)^3 P_{\min}}} \qquad \text{where}$$

$$P_{\min} = k_B T B_{IF} NF$$

Equation 3-12: Maximum range when considering typical radar equation parameters

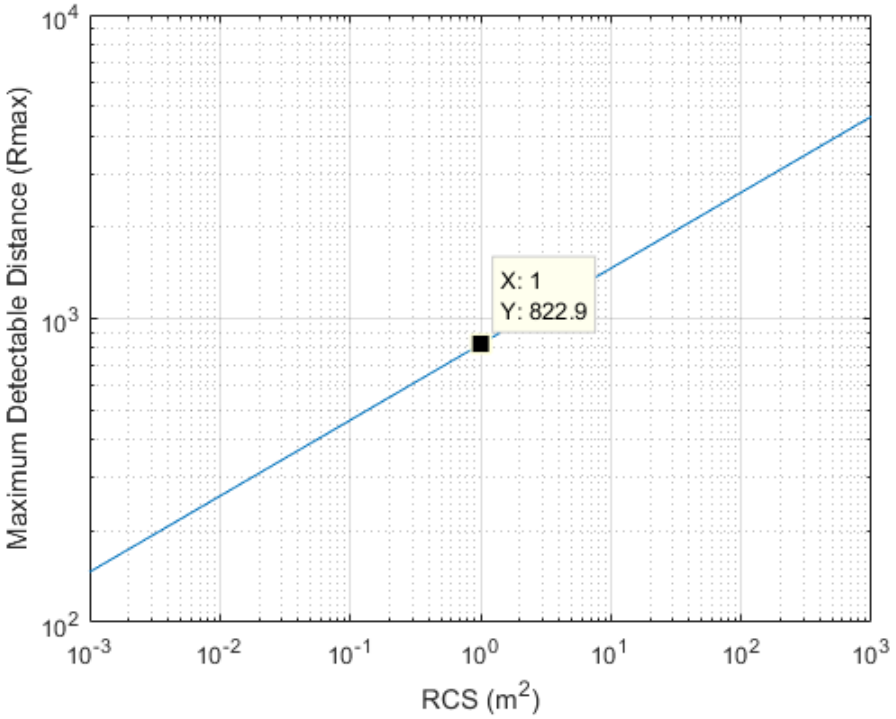

Figure 3-10: Maximum detectable distance using Equation 3-12 for a range of RCS values

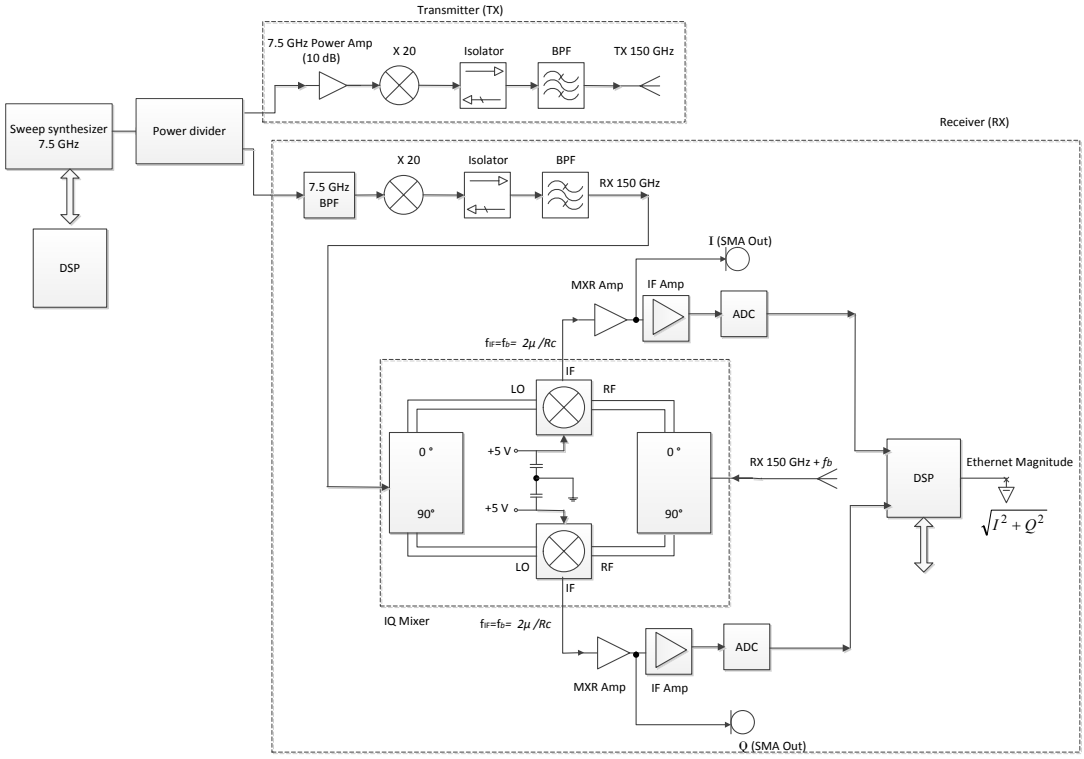

Figure 3-11: Summarised Block diagram of the 150 GHz FMCW radar [58]

Table 3-1: ELVA 150 GHz FMCW radar device parameters [58]

Parameter	**Values**
Transmitter	
Power output into antenna	15 mW
Frequency sweep	145 - 150 GHz
Sweep bandwidth	5 GHz
Chirp Sweep Time	1.2 ms
Total sweep time (duty cycle)	30 ms
Lens horn Antenna	
Antenna type	
Gain	29 dBi
Tx/Rx isolation	60 dB
Antenna beamwidth (2 way) azimuth	+/- 1.1°
Antenna beamwidth (2 way) elevation	+/- 5°
Polarization	Vertical
Farfield distance ($2d^2/\lambda$)	6 m
Receiver	
Noise figure	11 dB
IF bandwidth	10 kHz -2 MHz
Processor Unit and Digital Data	
Number of range cells per sweep	2048 (2^{11} FFT points)
Digital data output	Via Ethernet after FFT
Data range	16 bits
Interface protocol	UDP
Other parameters	
Data outputs	Strobe, I channel, Q channel
Power supply	12 V at 2.5 A
Size (Length, Width, Height)	L 320 mm, W 150 mm, H 200 mm

3.2.4 300 GHz Stepped Frequency System

3.2.4.1 Stepped Frequency Theory

Stepped frequency radars transmit pulses at different centre frequencies in order to perform discrete modulation over time. Measuring the ratio between the outgoing (V^+) and incoming voltage (V^-) waves for a scene at multiple frequencies (Figure 3-12) allows a response (S_{21}) to be measured of the illuminated scene (Equation 3-13 and Equation 3-14). Performing the inverse Fourier transform (Equation 3-15) on these measured responses in frequency produces the time-domain response by including the propagation velocity of the EM wave. Accurate knowledge of the transmit waveform allows the returns to be calibrated (Equation 3-16). A modulation in the wave is required to separate target returns from clutter.

A VNA device measures the amplitude and phase between transmit and receive ports over a wide frequency range and thus is capable to be used as a Stepped Frequency Radar. The Agilent Fieldfox [59] was used due to its availability and frequency range between 2 GHz and 18 GHz. The reason being due to the fact that the frequency converters produced by VIVAtech [60] can covert signals between 2-18 GHz up to 282-298GHz.

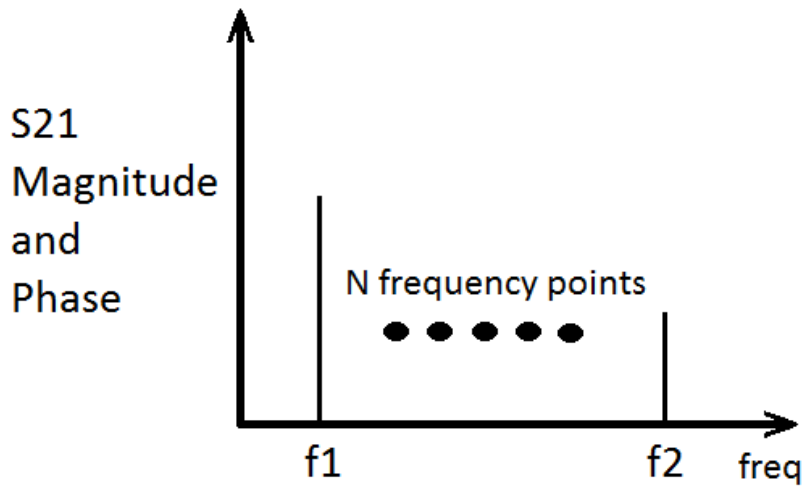

Figure 3-12: S21 scattering parameter measured over a span of equally spaced frequency values

$$\overset{\mathrm{v}}{S}_{21} = \frac{\overset{\mathrm{v}}{V}^{-}_{down\_converter}}{\overset{\mathrm{v}}{V}^{+}_{up\_converter}} = |A|e^{j\varphi}$$

Equation 3-13: Scattering parameter measured by the VNA device at the frequency converter ports

$$10\log\left(\frac{P_{rx}}{P_{tx}}\right) = 20\log\left(\frac{V^{-}_{down\_converter}}{V^{+}_{up\_converter}}\right) = 20\log(S_{21})$$

Equation 3-14: Scattering parameter in terms of the transmit power (P_{tx}) and received power (P_{rx})

$$x(n) = \frac{1}{N}\sum_{k=0}^{N-1} X(k)e^{j\frac{2\pi nk}{N}} \qquad n = 0...N-1$$

Equation 3-15: Discrete Inverse Fourier Transform (Frequency domain to Time domain conversion)

$$P_{rx} = S_{21} + P_{tx}$$

Equation 3-16: Scattering parameter to received power conversion (dB to dBW conversion)

The 300GHz system, comprising of a VNA and frequency converters, was used to measure the complex *S21* scattering parameter at discrete frequency points in between the upper and lower extents of the available bandwidth (282GHz-298GHz). The signal in the time domain was then obtained by superimposing the response from each frequency point and converting the complex spectrum to the time domain by using the Inverse Discrete Fourier Transform (IDFT). The time-delay was then converted into range by noting the speed of the two-way EM propagating wave.

The swept bandwidth is the important parameter in regards to range resolution and the equation used to determine the size of each range bin is the same as the FMCW (Equation 3-17).

The maximum range for stepped frequency systems still has to take into account the power-link budget as well as the filter characteristics of components in the system but the dominating factor for the stepped frequency setup in these experiments is the frequency step

between pulses as the inverse determines the maximum delay that can be present within the processed signal (Equation 3-18).

$$\Delta r = \frac{c}{2\Delta f}$$

Equation 3-17: Range resolution in terms of swept bandwidth

$$R_{\max} = \frac{c}{2\delta f} \qquad \text{where} \qquad \delta f = \frac{\Delta f}{N-1}$$

Equation 3-18: Maximum range that can be processed for a given frequency step

3.2.4.2 300 GHz SFR VNA System Parameters

Figure 3-13 shows the 300GHz system which consists of a Vector Network Analyser (VNA) device (Agilent Fieldfox N9918A [59]) connected to frequency converters that were developed at the company VIVAtech [60] to convert signals from 2-18 GHz up to 282-298 GHz. A block diagram describing the connections and signals is shown in Figure 3-14 although this diagram assumes that the 10 MHz reference signal is obtained from the internal oscillator in the VNA, although for all of the 300 GHz experiments present here, the reference this reference signal was acquired from a Rubidium oscillator (circled in Figure 3-15).

The rubidium generator was used as the reference oscillator to synchronise the transmitter and receiver as it has a lower phase drift over time which allows for a higher integration gain when summing the complex reflected signal over a number of samples. The main parameters of the stepped frequency 300 GHz system are visible in Table 3-2.

Figure 3-13: Agilent VNA and VIVAtech frequency converters

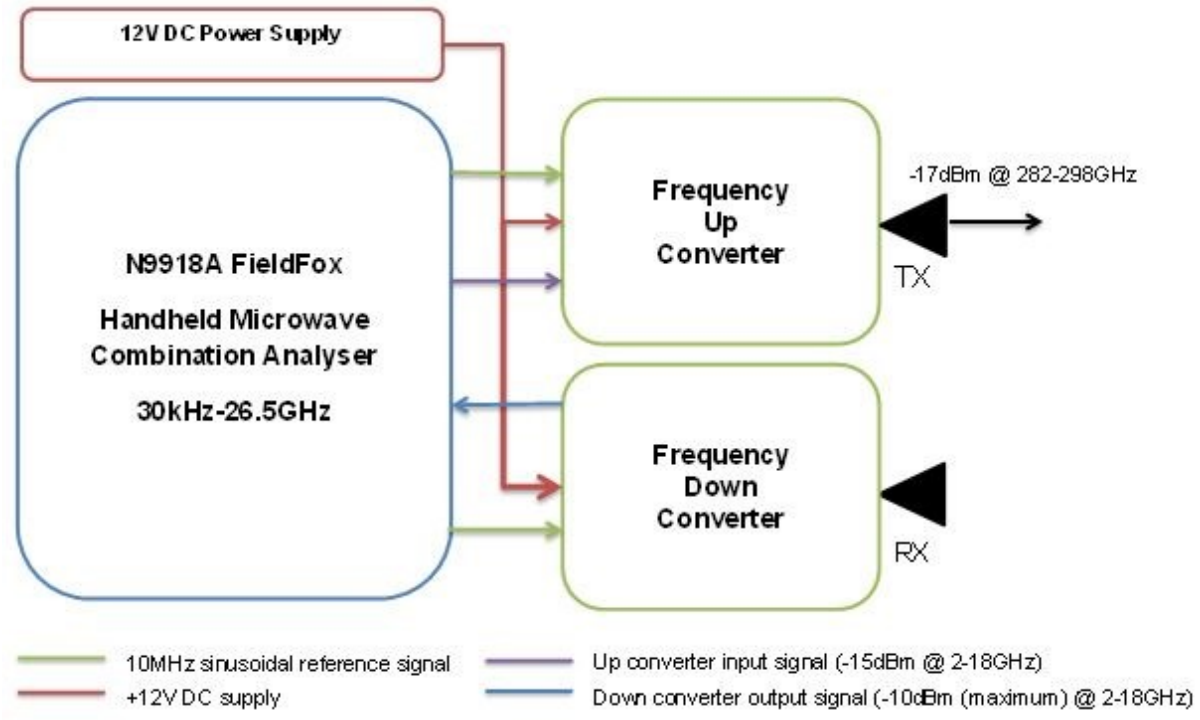

Figure 3-14: Simplified Block diagram of VNA and frequency converter connections and signals

The system that consists of the VNA device and frequency converters when connected by low-loss (at 2-18 GHz) SMA cables is shown in Figure 3-16.

The 300 GHz system can vary the modulation scheme transmitted and the variability in the IF bandwidth also allows different receiver noise values to be achieved. The main disadvantage of the system is the low transmit power and also the very large measurement time required for each sweep to be performed. To achieve the parameters present for the 150 GHz FMCW ($T_{sweep} = 1.2$ms) system, the VNA-based SFR system requires measurement times in the order of a second per sweep. This measurement time is acceptable for a stationary indoor scenario.

Table 3-2: 300 GHz Frequency converter specifications [60]

Frequency band	**281.6-297.6 GHz**
Maximum bandwidth of linear chirp	**16 GHz**
Output power	**-17 dBm**
Noise Figure (Specification)	**<17 dB**

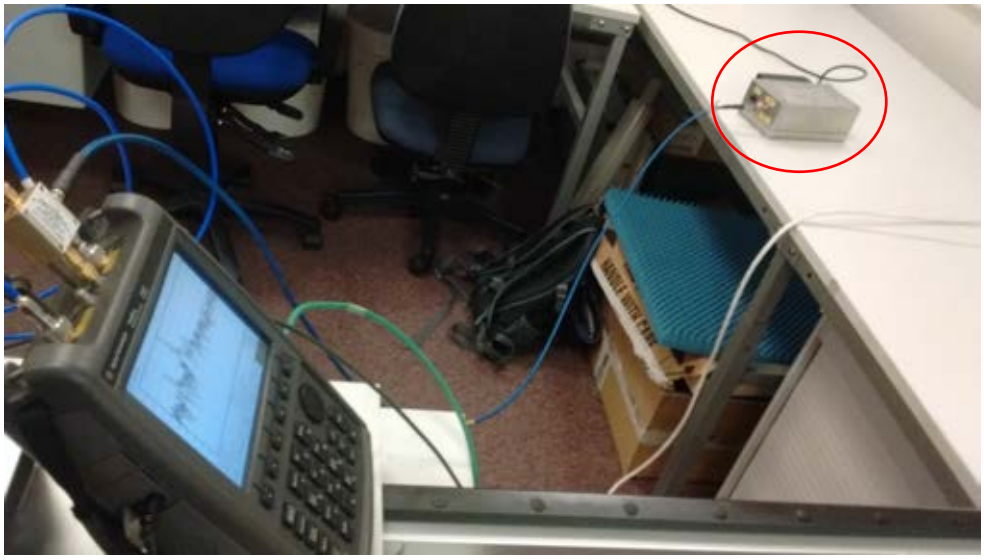

Figure 3-15: Circled Rubidium Oscilator that was used as the reference to synchronise subcomponents

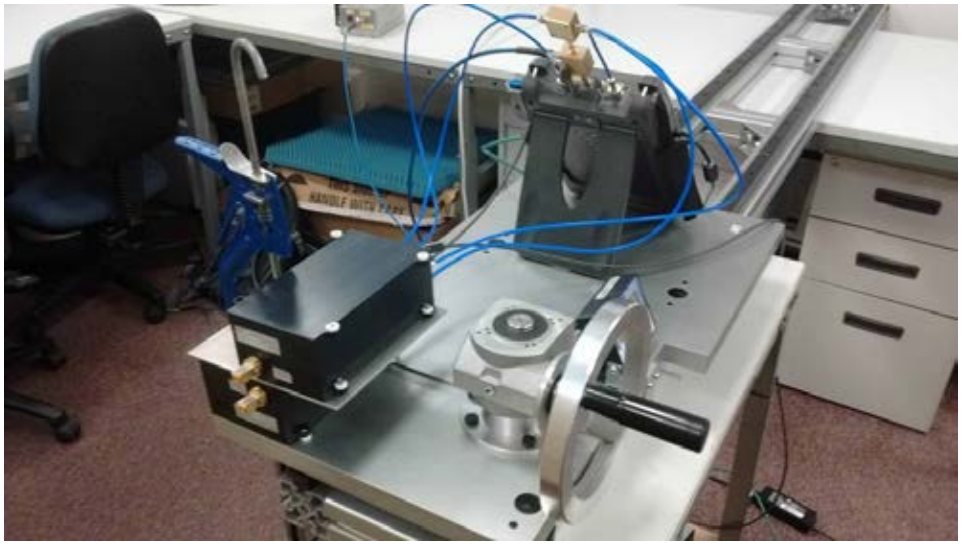

Figure 3-16: VNA and Frequency converters connected using SMA cables onboard a linear positioner device

As a power cable should be detectable considering the modelled RCS values and the previous power budget assessment, the modulation parameters of the stepped frequency waveform can be designed. The required frequency increment within the modulation of the transmit waveform is needed and the number of points required N_{req} for a desired maximum range R_{max} and swept bandwidth Δf can be calculated using Equation 3-19. For a target distance of 8 m, measured with a chirp bandwidth of 16 GHz, Equation 3-19 suggests that around 850 points evenly spaced in frequency would be adequate.

$$N_{req} = \frac{2\Delta f R_{\max}}{c}$$

Equation 3-19: Number of frequency points required for a given maximum range and frequency span

Similar to the FMCW analysis at 150 GHz, the stepped frequency device parameters can be inserted into the radar equation (Equation 3-20) although instead of using the constant bandwidth of the physical stand-alone filter, the IF bandwidth can be set for each pulse.

The antenna gain was equivalent to the measured gain of the pyramidal horns shown in Figure 3-16 (24 dBi) and a temperature of 17 °C. A IF bandwidth of 100 Hz was used in experiments due to this value producing acceptable refresh times in practice. The maximum distance for a range of RCS values is shown in Figure 3-17 which clearly show higher attainable distances even though the transmit power is much lower than the 150 GHz FMCW system which is largely due to the much lower receiver bandwidth . Although a very low receiver bandwidth is achievable for such a large swept bandwidth, this device would be impractical due to the measurement times scales being of the order of seconds (Equation 3-21). So for the required 850 points with a bandwidth of 16 GHz, the measurement time were of the order of 10 seconds.

$$R_{\max} = \sqrt[4]{\frac{P_t G^2 \lambda^2 \sigma}{(4\pi)^3 P_{\min}}} \qquad \text{where} \qquad P_{\min} = k_B T B_{IF} NF$$

Equation 3-20: Re-arranged version of the typical radar equation which determines maximum range for a given receiver and scenario

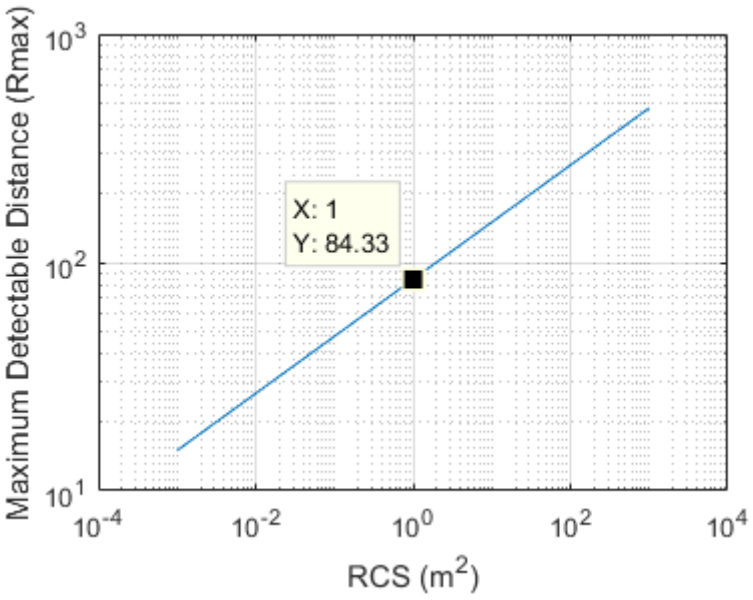

Figure 3-17: Estimated maximum detectable range of the 300 GHz (

Table 3-2 and Equation 3-20) device for a range of RCS values

$$t_s \geq \frac{N-1}{B^{IF}}$$

Equation 3-21: measurement time estimation for a given IF bandwidth (user defined) although this doesn't take into account any VNA latency

Finally, all experiments performed with the 300 GHz device contained a target which had zero velocity with respect to the transceiver, so the effect of Doppler shifts on the Stepped Frequency Performance will not be considered here.

3.3 Experimental Sites

This section will describe all of the sites that were used to measure power cables with the devices discussed previously. Both indoor and outdoor sites were used that were suitable for a given radar measurement device. Outdoor sites are described that contain realistic sagging cables that span hundreds of metres. These sites were measured by the relatively high power devices in the K_a band and K_u band whilst each were independently on-board a small fixed-wing aircraft. Two rural areas that contained different power cable setups will be discussed. The indoor measuring laboratory, constructed for radar devices between 150 GHz and 300 GHz will also be described. This indoor site only had a measuring distance of 8 metres which was deemed adequate for the low-power devices that are currently available at these frequencies.

3.3.1 Farmland Site

Spotlight SAR images were formed by illuminating a farm-land area (Scenario 1) located in Waddesdon, Aylesbury in the UK. This scenario contained three separate spans of power cables which were suspended using wooden telegraph-style poles. Cable Spans 'A' and 'C' consist of three subsections between suspension poles whilst span 'B' has four of these subsections. All subsections consist of three individual parallel power cables. An optical image of this site is visible in Figure 3-18 and a high resolution multi-look spotlight SAR image is shown in Figure 3-19. The power distribution map (Figure 3-20) from [61] states that the lines located south from the farm, are 33 kV cables owned and maintained by UK Power Networks. Spotlight SAR imagery was measured for Scenario 1 using both the I-Master (K_u-Band) and Bright Spark (K_a-band) radar devices on separate occasions (11 months apart). Using full-resolution Single-look images on the SAR viewer software developed at Thales UK, the wooden poles (example shown in Figure 3-21) were estimated to have a height of around 8.5m and a distance of approximately 100m was measured between each adjacent pair of wooden poles.

The sagging distance at the centre of cables could also be estimated in the high-resolution images and the average of these measurements was around 0.8m.

Figure 3-18: Optical image of the farm scenario taken from Google Maps. [62]

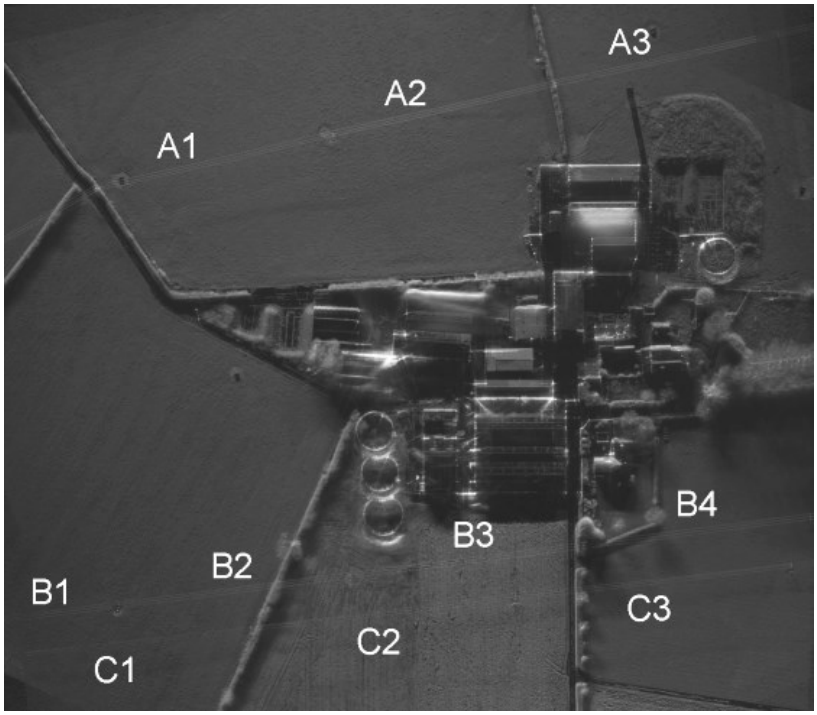

Figure 3-19: Labelled multi-look spotlight SAR image of the farm scenario that consists of three spans of OH power cables.

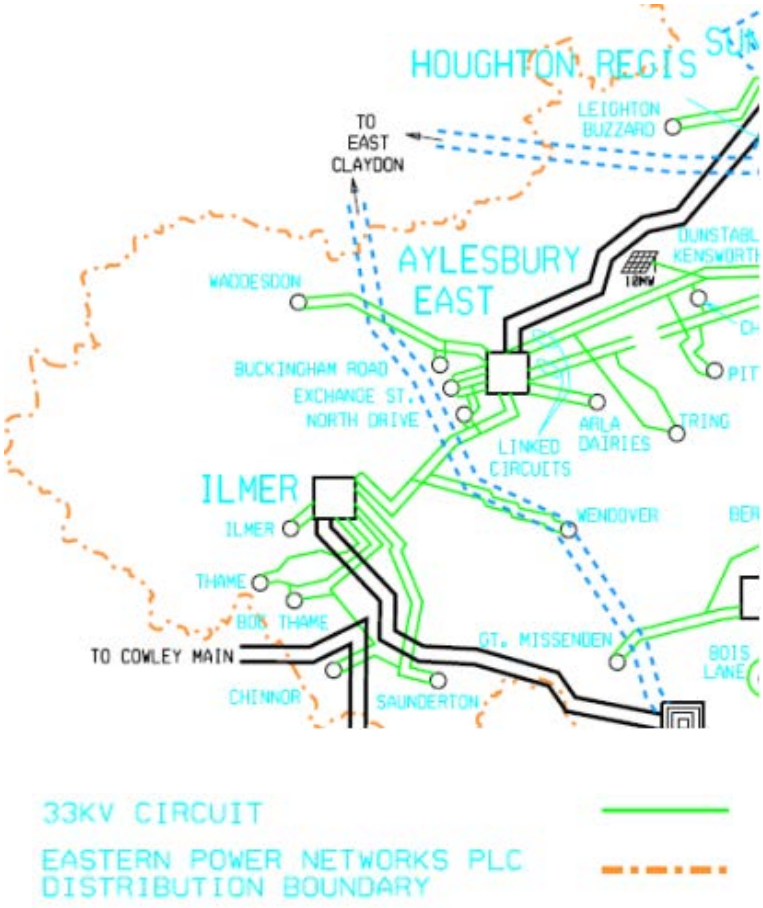

Figure 3-20: Distribution map that includes the Waddesdon farmland (scenario 1) [61]

Figure 3-21: Example of a wooden suspension pole used to suspend three lines of overhead power cables [63]

3.3.2 Pylons Site

The second outdoor scenario measured (Scenario 2) was a single span of higher voltage overhead power cables, and one earth cable, which are located to the North-West of Spalding in the UK (Figure 3-22). Sufficient data for this site was only available from the Bright Spark (K_a-band) system. The power distribution map (Figure 3-23) from [64] and the overlaid image in Figure 3-24 jointly suggest that the span of cables in Scenario 2 consists of 275 kV cables which are owned and maintained by National Grid [65]. The information contained in the full resolution single-look spotlight images processed at Thales UK (Figure 3-25) allowed the cable span and pylon height for this scenario to be estimated to be around 230 m (Figure 3-26) and 60 m (Figure 3-27) respectively. The sagging distance at the centre of the span was estimated to be around 5m. The clutter surrounding the cables consisted of vegetation which was seen to have significant diffuse scattering at K_a band whereas the cable scattering observed did not due to difference in surface roughness (Figure 3-25).

Figure 3-22: 275 kV cable scenario which consisted of two pylons (Source: Google) [66]

Figure 3-23: National grid overhead voltage map North-East of Spalding with Scenario 2 location circled [64]

Figure 3-24: Lines created by using Pylons visible from Google earth within the vicinity of Scenario 2 which has a high-resolution multi-look Spotlight SAR image overlaid (circled)

Figure 3-25: Cable extent between the pair of Pylons in Scenario 2 which was measured to be around 232 m by using a Bright Spark multi-look image

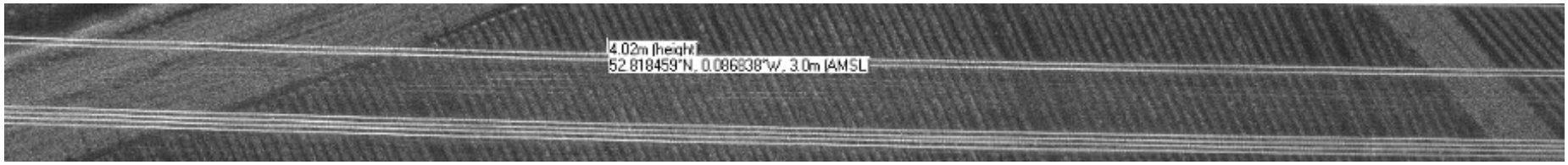

Figure 3-26: Scenario 2 cable sagging measurement (4 m) taken using Bright Spark multi-look image

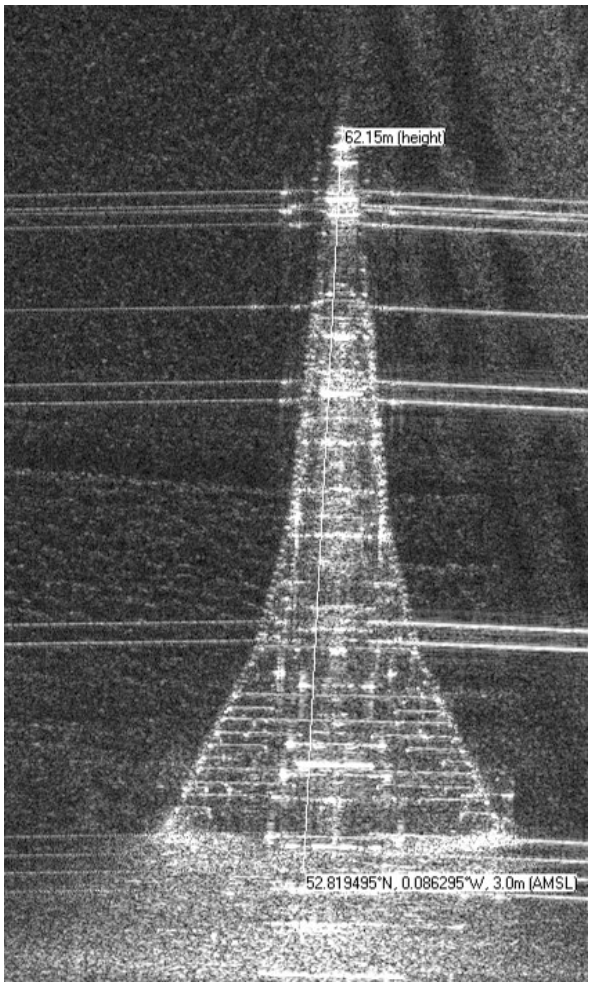

Figure 3-27: Pylon height measurement (62 m) from a Bright Spark multi-look Spotlight SAR image

3.3.3 Indoor mmW Measurement Facility

3.3.3.1 OH Power Cable Subsections

After making contact with the National Grid research centre at the University of Manchester [67] they were kind enough to donate two OH power cable subsections to this research project. One cable subsection was the more common ACSR type and the other was the modern ACCC type, both of which were described earlier. The geometrical parameters, physical dimensions and visual appearance of the ACSR cable is shown in Figure 3-28 and Figure 3-29 shows the equivalent information for the ACCC type of cable. As expected the ACCC type has much less sagging compared to the more common type. A tabular version of the cable physical parameters can be seen in Table 3-3.

Figure 3-28: ACSR parameters, sagging characteristics and surface pattern

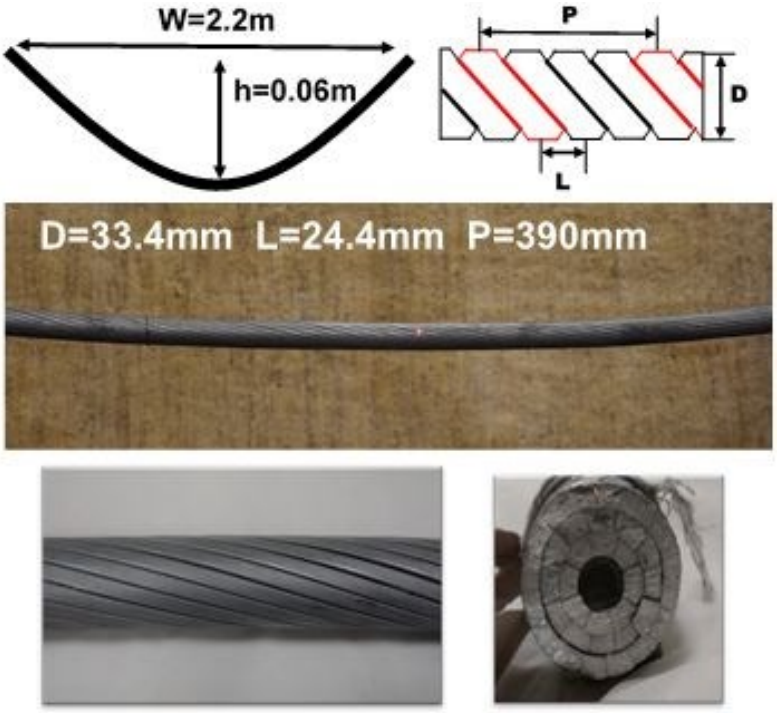

Figure 3-29: ACCC parameters, sagging characteristics and surface pattern

Table 3-3: Main ACSR and ACCC geometrical parameters

Cable Parameter	Quantity (ACSR)	Quantity (ACCC)
Cable diameter (D)	31.59 mm	33.4 mm
Number of outer strands (N)	24	16
Outer surface period (L)	20 mm	24.37 mm
Length between turns (P)	355.6 mm	390 mm
Cable length	2.05 m	2.23 m
Outer strand diameter/height (d)	3.51 mm	4 mm

3.3.3.2 Indoor Measurement Facility

Measurements have been made using the 300 GHz stepped-frequency radar and the 150 GHz FMCW radar, both described earlier in this section (Figure 3-30).

In order to get acceptable illumination of the cable, Signal to Noise Ratio, and clutter level an indoor facility containing a mmW absorber was used to perform experiments to obtain angular profiles of the cable subsections (Figure 3-31). Persian carpet which has high absorption at 150 GHz and 300 GHz [68] was placed on the floor between the radar and cable in order to reduce the effect of multipath reflections (Figure 3-31).

A fibre glass stand was constructed using non-metallic (nylon) screws to suspend a straight subsection of cable in order to reduce unwanted backscatter. The stand was a square shaped structure (2m by 2m) and was attached to the floor via a stepper motor turntable and driver (Parker PD-E series [69]) using a large bolt. The cable was attached to the stand by using nylon cable ties. An increment angle of 0.1 degrees was achievable by the stepper motor used due to the design of the gearing ratio within the device.

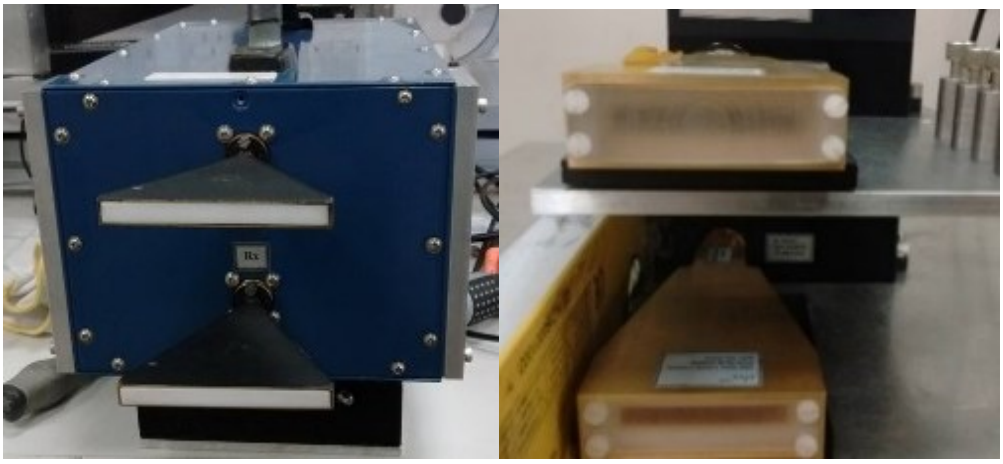

Figure 3-30: Low-THz radar systems used in experiments, 150 GHz, FMCW system with lensed horn antennas (left), 300 GHz, stepped frequency system with lensed horn antennas (right)

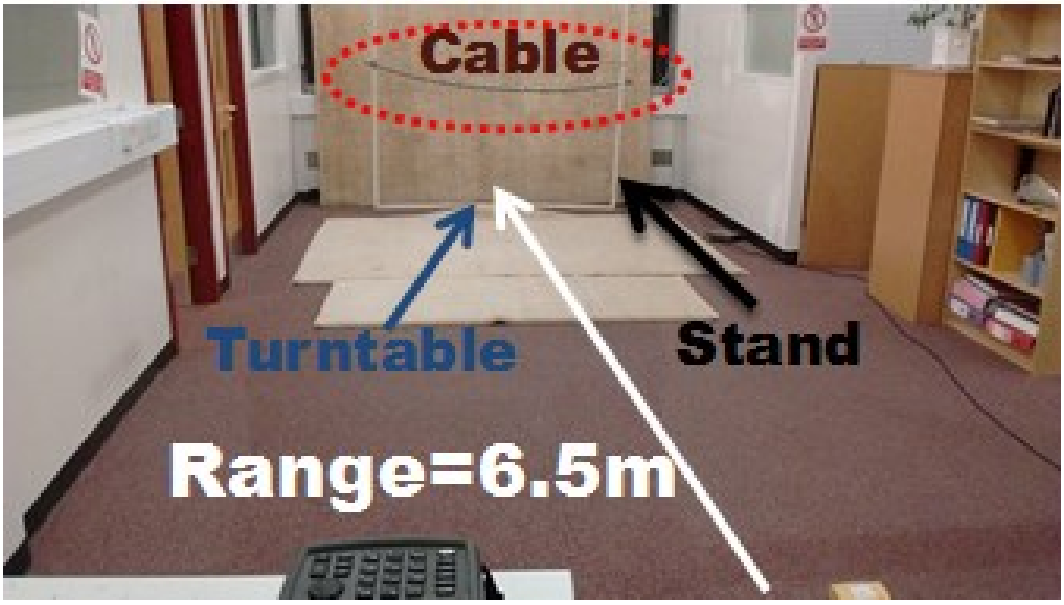

Figure 3-31: Indoor Experimental setup realised for the 150 GHz and 300 GHz devices

A measurement of the empty background was also performed to check that the available dynamic range was adequate. The absolute RCS values were calibrated using small stainless steel spheres as calibration targets which could be placed within the field of view of the radars.

This setup will allow a subsection of cable to rotate in a circular motion and hence enable an angular profile of cable backscatter to be measureable. The maximum bandwidth was used in order to spread the clutter away from target returns. The measurement area allows the target to be illuminated by a radar device at a distance of around 6.5 metres. A simple depiction of the measurement setup is shown in Figure 3-32.

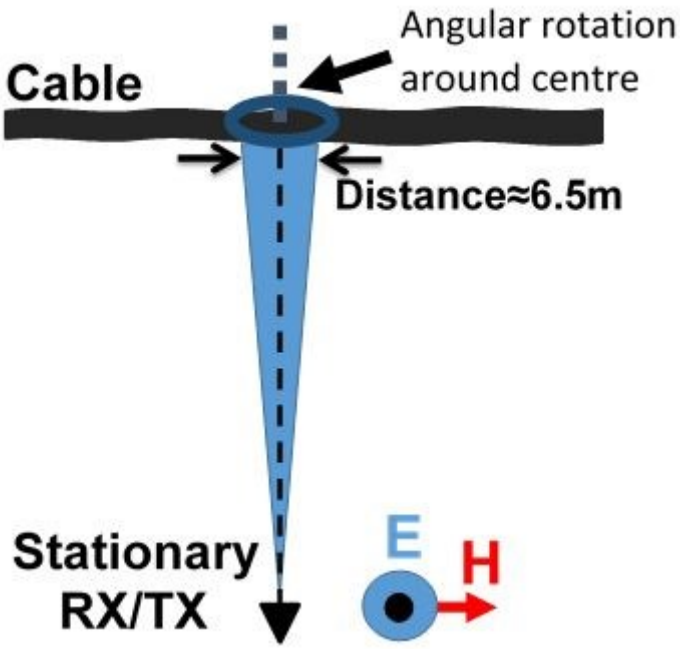

Figure 3-32: Indoor cable experimental setup visual overview

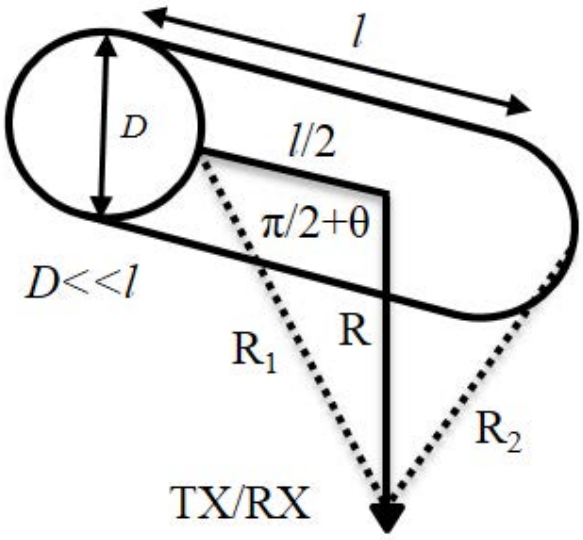

Figure 3-33: Ranges for a cylinder rotated by angle θ about its central diameter

In terms of target resolution cells, the thin cable would extend 2m perpendicular to the line that connects the cable centre to the transceiver at a distance of 6.5m. As the cable was rotated from θ=±20° in increments of 1°, the minimum in the spread of targets returns will be at 0 degrees and the maximum will be at ±20°.

The difference in the range of the nearest and furthest returns (Figure 3-33) can be calculated by Equation 3-22 for θ=20° and Equation 3-23 for θ=0° (Figure 3-34):

$$R^{1}_{spread} = R_1 - R_2$$

Equation 3-22: Spread of ranges present along a thin rotating cylinder ($R_{spread}^{1} > R_{spread}^{2}$)

$$R^{2}_{spread} = R_1 - R$$

Equation 3-23: Spread of ranges present along a thin rotating cylinder ($R_{spread}^{2} > R_{spread}^{1}$)

where

$$R_1 = \sqrt{\left[l^2 / 4 + R^2 - lRcos\left(\pi / 2 + \theta\right)\right]}$$

Equation 3-24: Range to the left (Figure 3-33) extent of the rotating cylinder

$$R_2 = \sqrt{\left[l^2 / 4 + R^2 - lRcos\left(\pi / 2 - \theta\right)\right]}$$

Equation 3-25: Range to the right (Figure 3-33) extent of the rotating cylinder

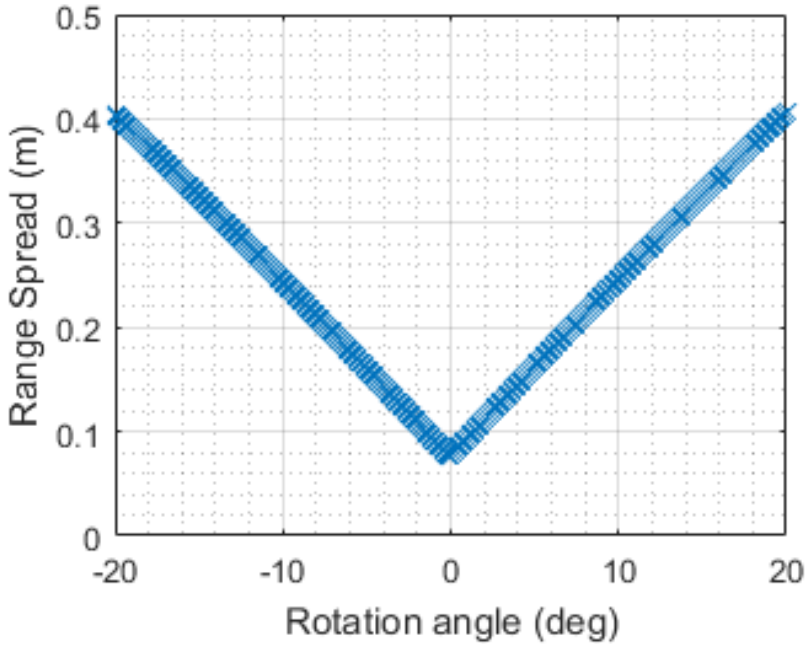

Figure 3-34: Range spread of the 2m non-sagging cable subsection at 6.5m

The processed signal will be this spread across a number of range cells (Equation 3-26).

$$\Delta N^{cells} = \left\lceil \frac{\Delta R_{spread}}{\Delta r} \right\rceil$$

Equation 3-26: Number of DR cells that returns reside in

where Δr is the range resolution and the symbol, $\lceil \cdot \rceil$, denotes the ceiling function.

$$L_{\text{SPREAD}} = -20\log(\Delta N^{cells})$$

Equation 3-27: Range cell spread loss assuming returns spread equally in each cell

If we assume that the voltages are spread evenly into each range cell then we can add an extra "range spreading" loss to estimate the power in each cell with Equation 3-27.

Putting in the numbers, D=6.5m, L=2m:

Δf=6 GHz (150 GHz FMCW device):

ΔN^{CELLS}=4 at θ=0° and ΔN^{CELLS}=17 at θ=20°

Δf=16 GHz (300 GHz Steeped Frequency device):

ΔN^{CELLS}=9 at θ =0° and ΔN^{CELLS}=44 at θ=20°

These expected number of range cells that contain the extended target produce the following using Equation 3-27:

Δf=6 GHz (150 GHz FMCW device):

L_{SPREAD}=-12 dBsm at θ=0° and L_{SPREAD}=-15 dBsm at θ=20°

Δf=16 GHz (300 GHz Steeped Frequency device):

L_{SPREAD}=-20 dBsm at θ =0° and L_{SPREAD}=-33 dbsm at θ=20°

This range spread factor will be considered when analysing the magnitude of the RCS values measured from cables that are extended in range.

3.3.3.3 Propagation and Noise Floor

In order to assess the performance of the developed indoor facility for both the 150 GHz and 300 GHz systems, experiments were performed to investigate both the propagation and Noise Floor of the devices with the antennas and other sub-components connected via appropriate SMA cables. The wave propagation was of interest due to the fact that the presence of the physical floor, which is rough at these frequencies, thus free-space propagation (R^4) cannot be assumed.

Noise Floor experiments were also performed to make sure that the manufacturer values stated were accurate and that no attached cable or antenna was having a significant effect on the performance. Smooth metal spheres with circumferences (90-1000 mm) much larger than the wavelength were used as the calibration target in order to ease the alignment requirement and also due to the simplicity of the analytical RCS value.

Figure 3-35: Realised relatively non-reflective stand with metal sphere attached using a suction cup

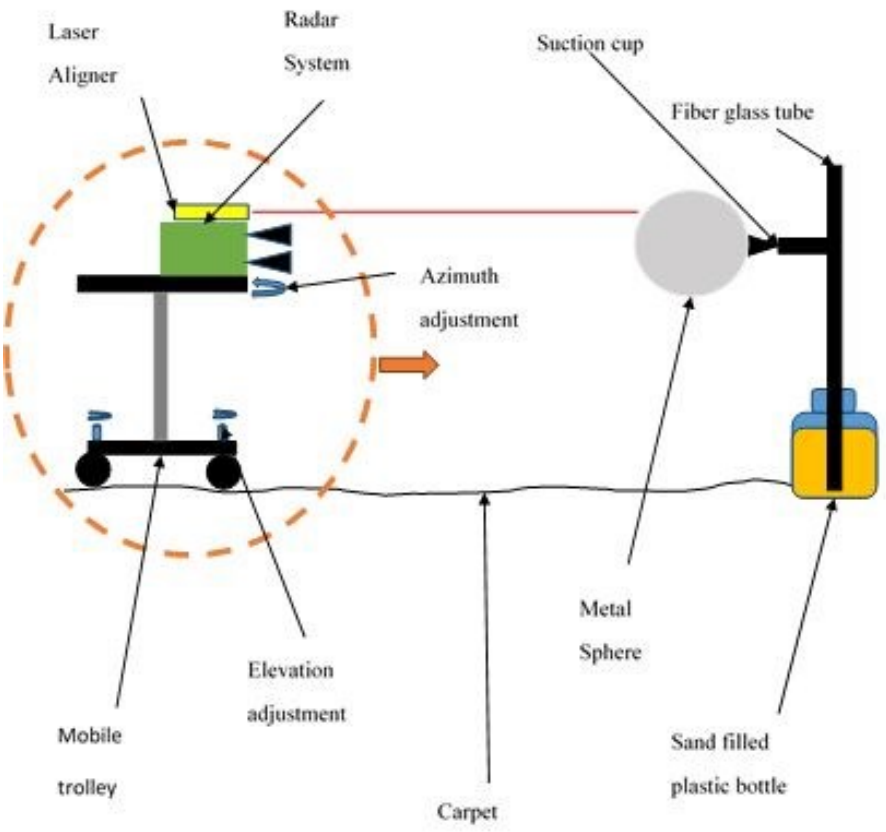

Figure 3-36: Diagram of the propagation and noise floor experimental setup

A setup that allowed large spheres to be suspended whilst removing significant clutter in the same range cells is shown in visual form in Figure 3-35 and as a sketch in Figure 3-36. The sphere was attached to a relatively non-reflective fibre glass pole via a plastic clamp and a suction cup which are in the shadow region of the sphere relative to the illuminating radar. As shown in Figure 3-36, the transceiver and target lie above a rough ground plane and thus the wave propagation will not behave as it would do in free space.

By using a laser pointer and as well as azimuth and elevation alignment knobs on a wheeled trolley in which the sphere was suspended, measurements were taken at multiple distances between 4 metres and 7.5 metres. This was performed using standard gain pyramidal horns for both the 150 GHz FMCW device and 300 GHz stepped frequency system.

The resulting plots are shown in Figure 3-37 and Figure 3-38 alongside a linear-fit and the free space R^4 expectation on a log-log scale with respect to distance. This plot is normalised relative to the nearest measurement made so that the reduction with respect to distance can be estimated. Similar propagation was measured for both devices for the same indoor environment and target. A difference in propagation would also be expected due to the difference in the 'floor roughness to wavelength' ratio for the two devices. Also measurement error in alignment were minimised but are expected to be measurable due to the accuracy of the alignment method. The obtained path loss information can be used to aid in estimating the noise floor of each of the devices. The measured range profiles for each distance are shown in Appendix A and Appendix B for the 150 GHz and 300 GHz devices respectively.

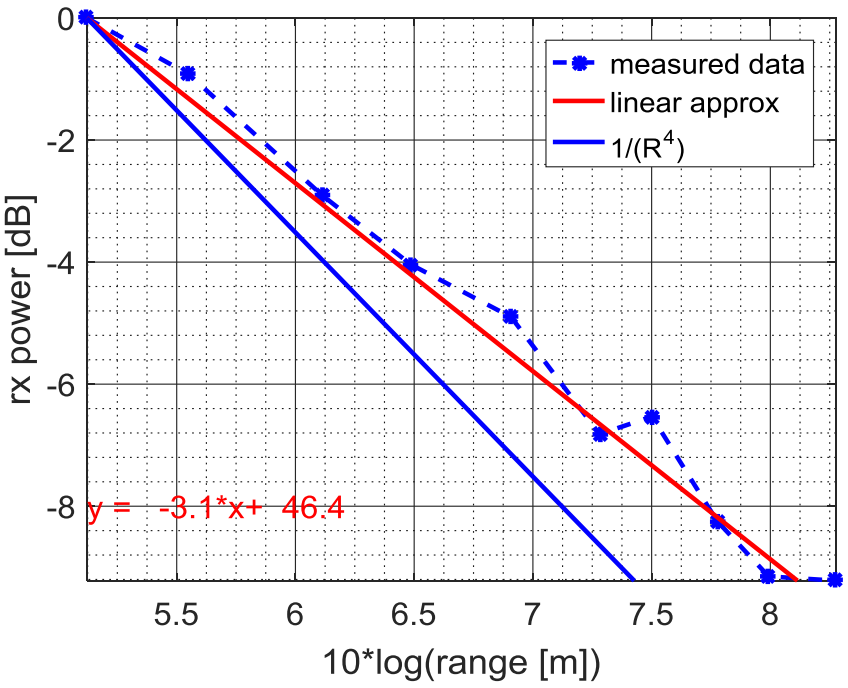

Figure 3-37: Normalised received power from a sphere at different distances to the transceiver; using the measured data in comparison to the theoretically calculated values

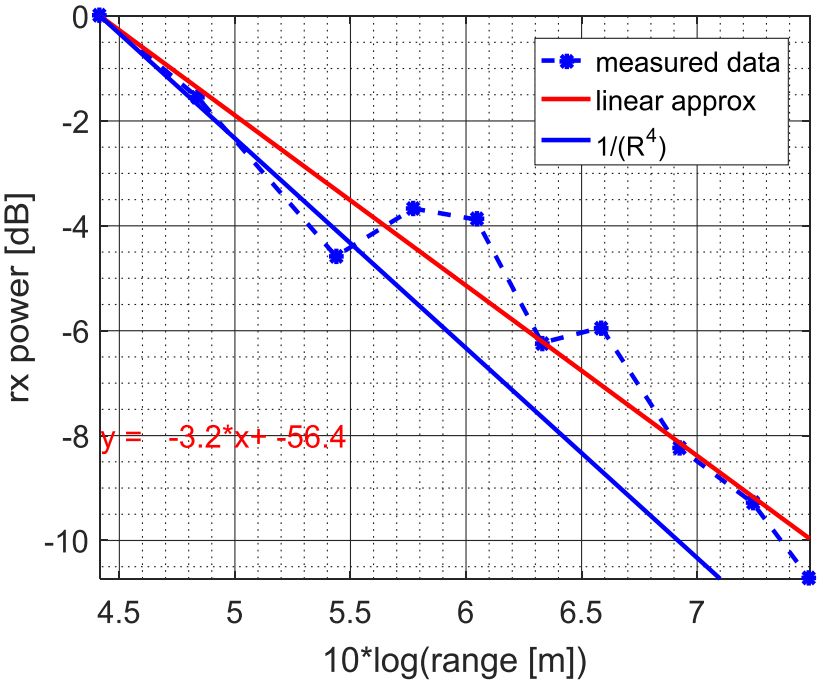

Figure 3-38: Normalised received power from a sphere at different distances to the transceiver; using the measured data in comparison to the theoretically calculated values

A plot that contains the theoretical SNR with respect to distance and the measured SNR, gained by using noise statistics, is shown in Figure 3-39 and Figure 3-40. The range power used was estimated from these propagation plots. The difference between the estimated and measured SNR are visible in Figure 3-41 and Figure 3-42. The Noise figure is supposed to be not related to distance and the small variations, which are a fraction of a decibel, are expected to be due to errors in the alignment of the transceiver and target for each measurement. The specification of the ELVA 150 GHz FMCW is 12 dB [58] and the mean measured value agrees well with this. The 300 GHz system is vague [60] and states that the Noise Figure is less than 17 dB and the measurements are around 11 dB for this setup.

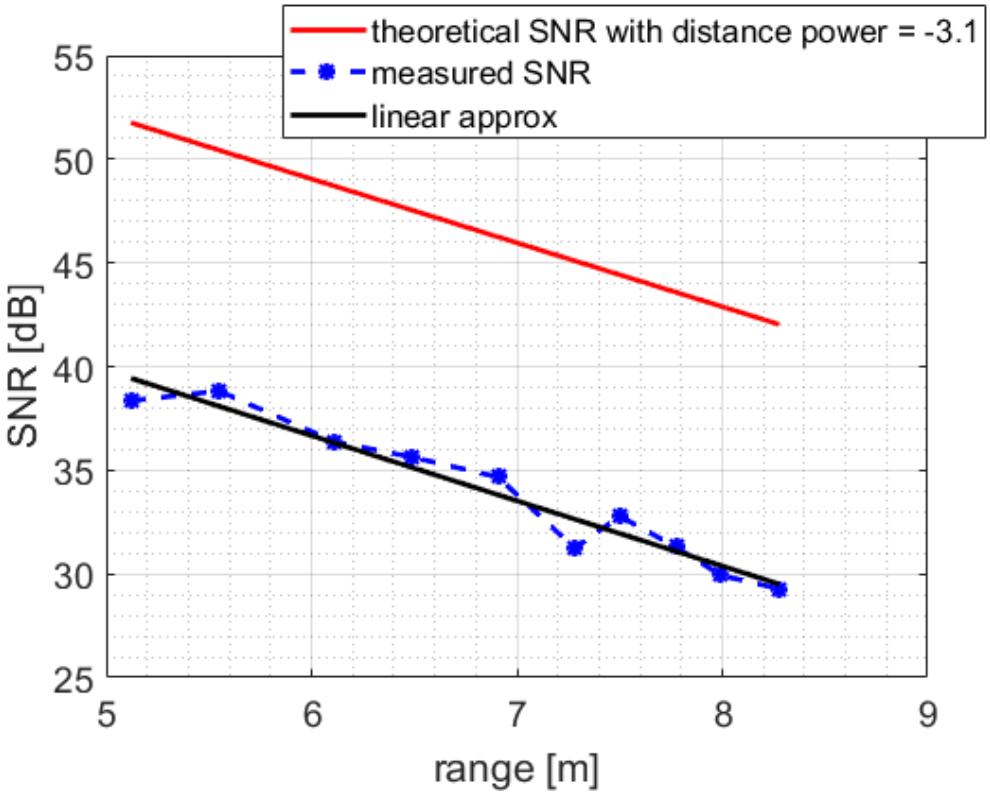

Figure 3-39: Theoretical SNR (with 0dB Noise Figure) plotted against measured SNR [150 GHz]

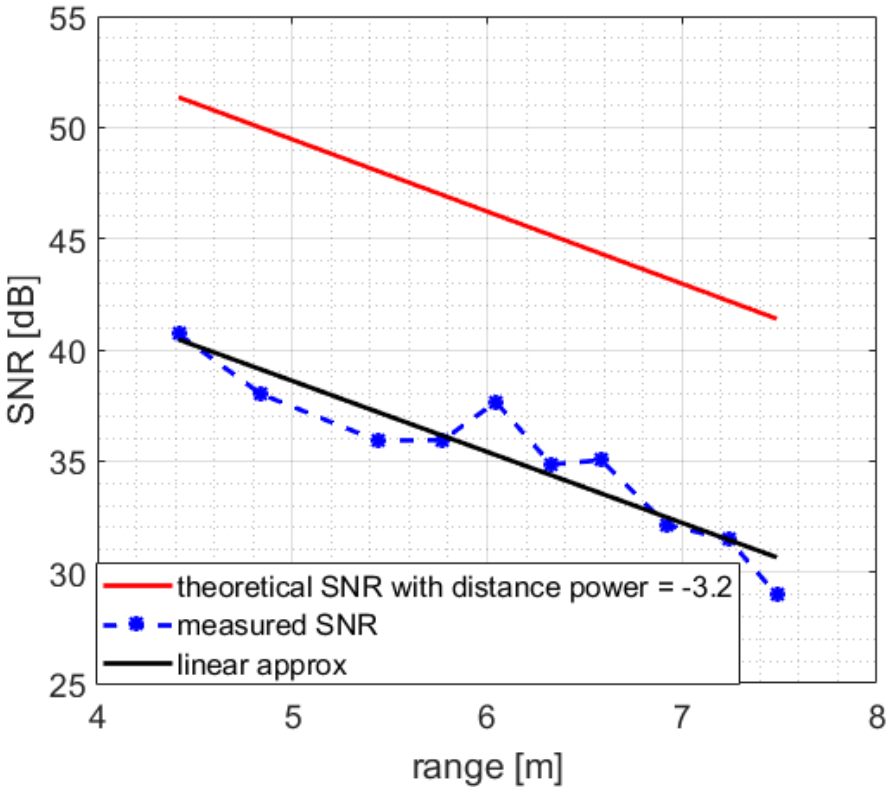

Figure 3-40: Theoretical SNR (with 0dB Noise Figure) plotted against measured SNR [300 GHz]

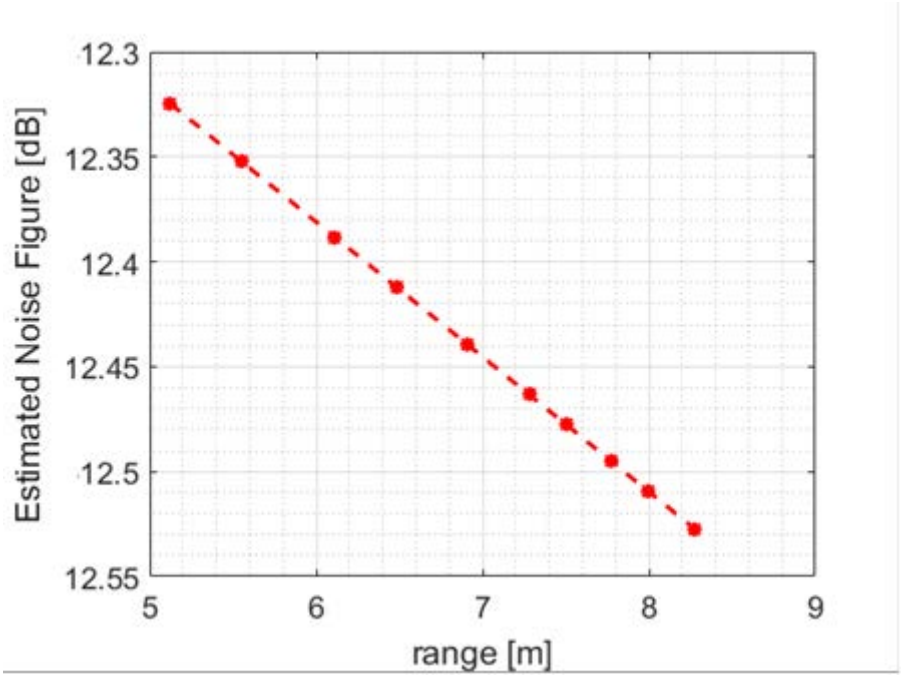

Figure 3-41: Estimated Noise Figure of the 150 GHz system at a range of distances

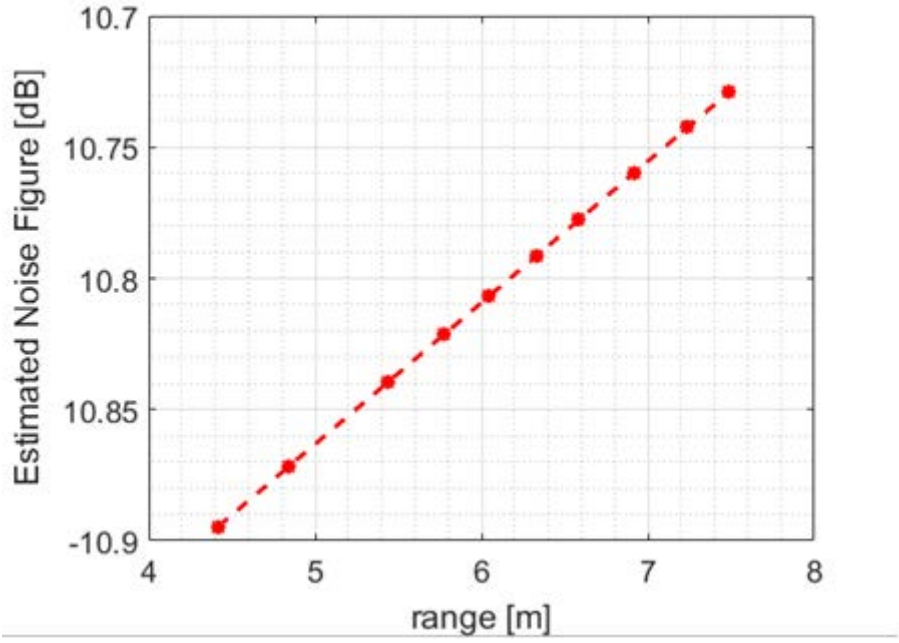

Figure 3-42: Estimated Noise Figure of the 300 GHz system at a range of distances

The gained knowledge on both the propagation of the waves at 150 GHz and 300 GHz within the experimental site and also of the noise figure performance of both the FMCW and

Stepped Frequency device were jointly used to analyse measurements made. The estimated loss due to target returns splitting into multiple range cells was also considered when planning the cable experiments and analysing the results obtained.

3.4 Conclusion

Two high resolution SAR systems developed by Thales UK and DSTL, the I-Master and Bright Spark systems, have been briefly described in terms of the main spotlight SAR processing parameters and the intended application. The information gained from Spotlight SAR imagery whilst under the supervision of *Malcolm Stevens* (Chief Engineer at Thales UK) was presented. A novel spectrum analysis suggested by Mr. Stevens that enabled further enhancement of power cable signatures has also been described.

Two millimetre-wave radars, currently at the University of Birmingham have also been described, a 150 GHz FMCW system purchased from ELVA and a 300 GHz VNA system which makes use of frequency converters designed by VIVA tech. The basic principles of FMCW radar and Stepped Frequency Radar have been stated in order to understand the main parameters and also the compromises that are required when planning OH power cable measurements.

All of the experimental sites used to gather overhead power cable measurements have been discussed. Two outdoor sites, both in rural areas of the UK, but each with completely different power cable setups were analysed and the main parameters of each stated. The indoor experimental mmW laboratory developed to perform measurements at 150 GHz and 300 GHz has been described. The effect of ground clutter on wave propagation was stated and experimental results that show a difference for both devices compared to the simplified free-space model. Noise floor experimental results were shown that agree with the specifications of both the 150 GHz and 300 GHz systems. The effect of target returns being spread into multiple

range cells was stated and estimations of target returns in each cell were defined. All of the investigations performed in the indoor measurement site at 150 GHz and 300 GHz allowed a more accurate assessment to be made of the results acquired.

4. Ku-band & Ka-band Cable Measurements

4.1 Introduction

This section will display the results gained from using the spectrum analysis technique on the spotlight SAR images obtained by the I-Master and Bright Spark systems whilst each were on-board aircraft mid-air.

The angular profiles measured from the farmland and pylon scenarios will be presented, analysed and compared with theoretical expectations. The positions and widths of all the measured peaks in the cable backscatter will be estimated using a simple quadratic fitting process and the outline of the process and results produced will be described. The similarities and differences in both peak position and width were compared across all measurements.

The PO modelling of a straight OH power cable will be combined with the sagging model, presented in Section 2.3, in order to model the effect of varying sagging characteristics on the power backscattered to an airborne radar. The results gained from these simulations, which include parameters extracted from both high-resolution SAR and optical images, will be compared with measurements made. This comparison will include observations made from range-Doppler images which are shown in Appendix C and Appendix D.

4.2 Measured Angular Profiles

4.2.1 Farm Scenario

Subsequent to using the along-cable Fourier Transform based technique on all of the cable subsections in Figure-4-1, for both the Ka-band and Ku-band sets of measurements, the

processed data obtained was plotted with respect to the centre of the specular lobe; the resulting figures are shown in Figure 4-2 and Figure 4-3. The levels in these plots are normalised to the maximum value measured for a given cable subsection.

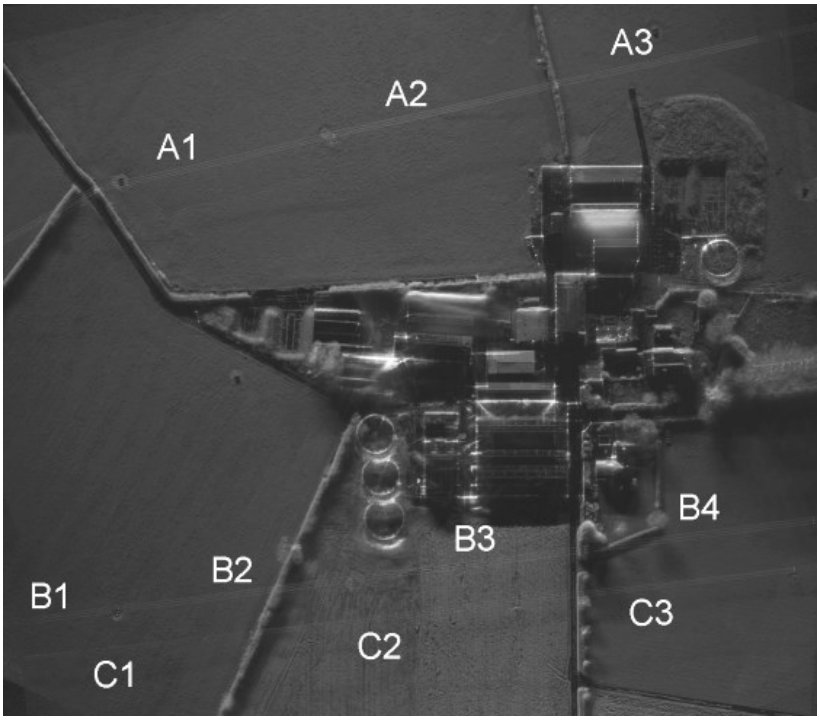

Figure-4-1: Multilook spotlight SAR image of farmland scenrio

The main observations in Figure 4-2 and Figure 4-3 are as follows:

- Figure 4-2 *(Ku band angular profiles)*: The only angular profile measured, at Ku band, with both positive and negative Bragg lobes shows good symmetry with respect to the centre of the specular lobe with magnitude of the angular difference being 22.4° for the positive Bragg lobe and 22.2° for the negative lobe. A further consistency in Figure 4-2a to Figure 4-2c is that all of the Bragg lobes are in the range of 22-23 degrees away from the specular lobe for a given cable and these four figures were constructed using strands of cable along the 'A' power line in Figure-4-1. The Bragg peaks in Figure 4-2d can been seen to be observed at slightly lower angular separation of 19 degrees which may be due to a different cable type

being present along line ‘B’ . All Bragg peaks were observed to be -30 to -20 decibels down relative to the specular peak.

- Figure 4-3 *(Ka band angular profiles)*: All of the peaks measured off normal incidence were at much smaller angular positions (relative to specular) compared to those measured at the lower frequency in Figure 4-2 which was expected from theory. All of the off-normal peaks measured within the scenario in Figure-4-1 were in the angular range 9-12 degrees. Due to the Bragg peaks at Ka-band for these cables being at an angular position closer to specular, all of the plots in Figure 4-3 contain both the Positive and Negative Bragg lobes that are all reasonably symmetrical around the specular lobe centre. The increase in frequency has caused the Bragg lobes to become less noisy and to have a lobe structure similar to its specular counterpart at around normal incidence; although the Bragg lobes to become nosier for patterns with large specular lobe widths as evident in Figure 4-3d. As with the Ka band results the Bragg peaks were consistent for a given line which suggests that each line has the same type of cable throughout which would be a more than reasonable assumption to make as cable type relates to current capacity and no voltage/current transformers were observed. It also shows that each line has slightly different surface periods on the surface of the cable used for each line.

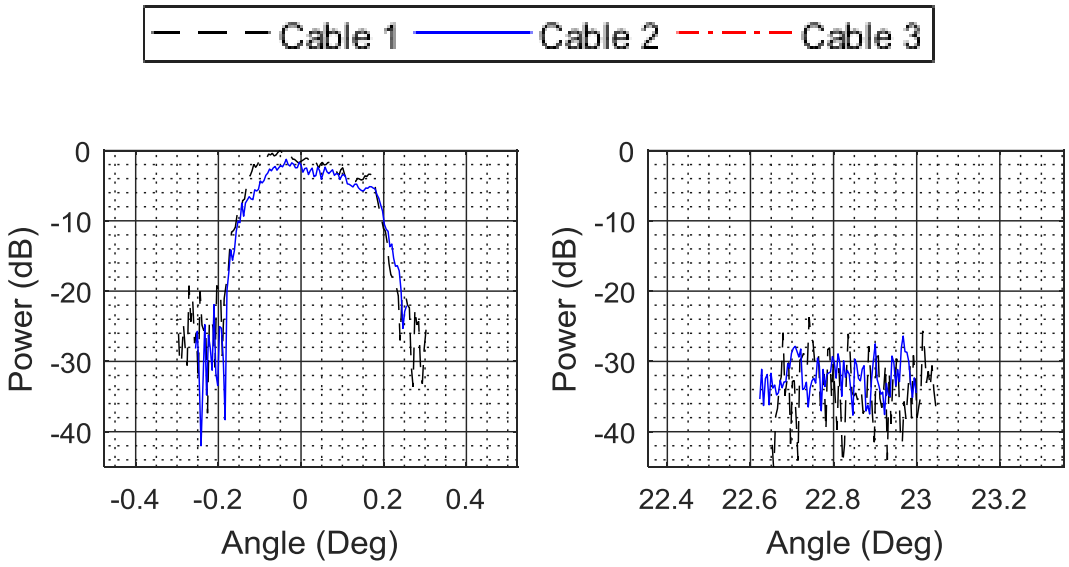
Cable 1
Cable 2
Cable 3
Power (dB)
Angle (Deg)
0
-10
-20
-30
-40
-0.4
-0.2
0
0.2
0.4
22.4
22.6
22.8
23
23.2

a)

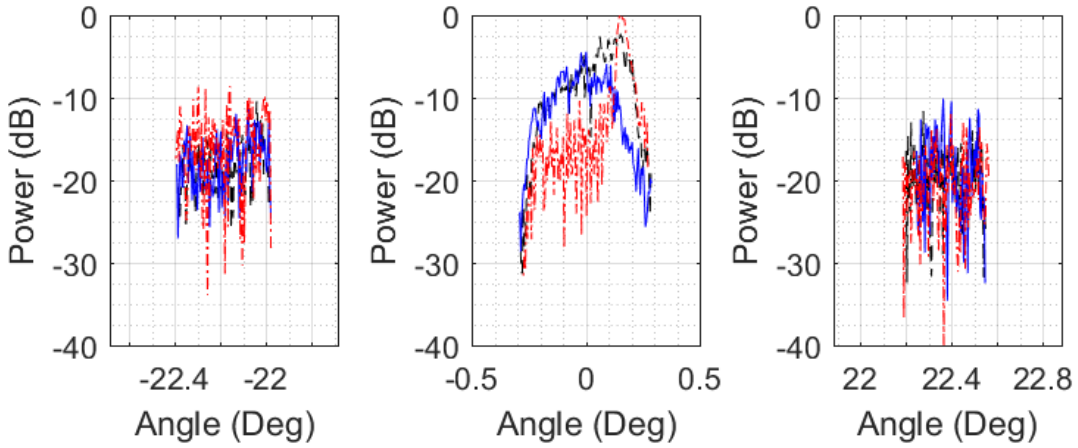
Power (dB)
Angle (Deg)
0
-10
-20
-30
-40
-22.4
-22
-0.5
0
0.5
22
22.4
22.8

b)

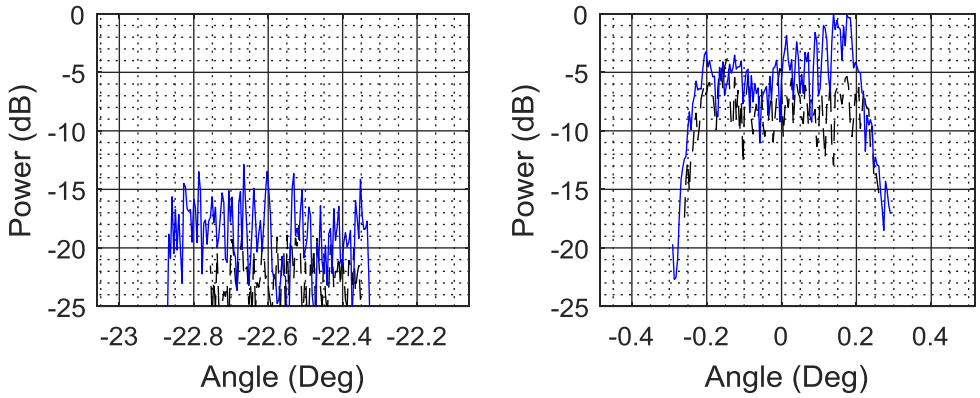
Power (dB)
Angle (Deg)
0
-5
-10
-15
-20
-25
-23
-22.8
-22.6
-22.4
-22.2
-0.4
-0.2
0
0.2
0.4

c)

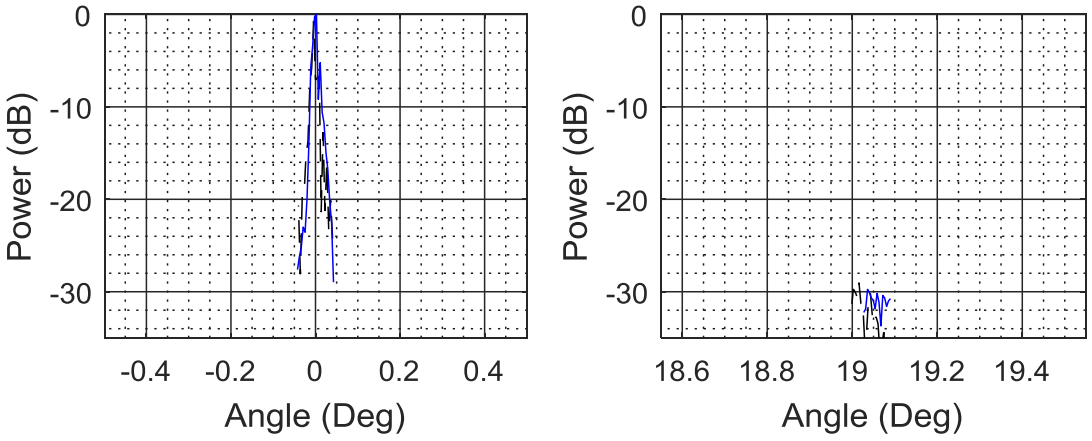

d)

Figure 4-2: : Cable backscattered power with respect to angle measured by the I-Master radar (Ku band) for various cable subsections in Figure-4-1: *(a) A1, (b) A2, (c) A3, (d) B3, Note: Cable 1: Northmost, Cable 2: middle and Cable 3: Southmost.*

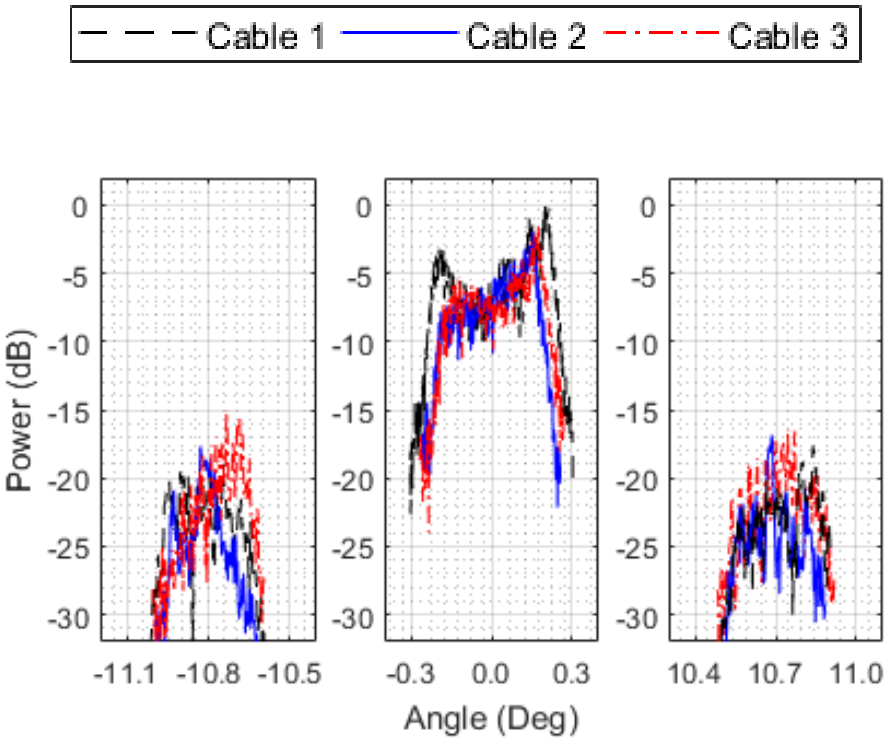
Cable 1
Cable 2
Cable 3
Power (dB)
0
-5
-10
-15
-20
-25
-30
-11.1
-10.8
-10.5
-0.3
0.0
0.3
10.4
10.7
11.0
Angle (Deg)

a)

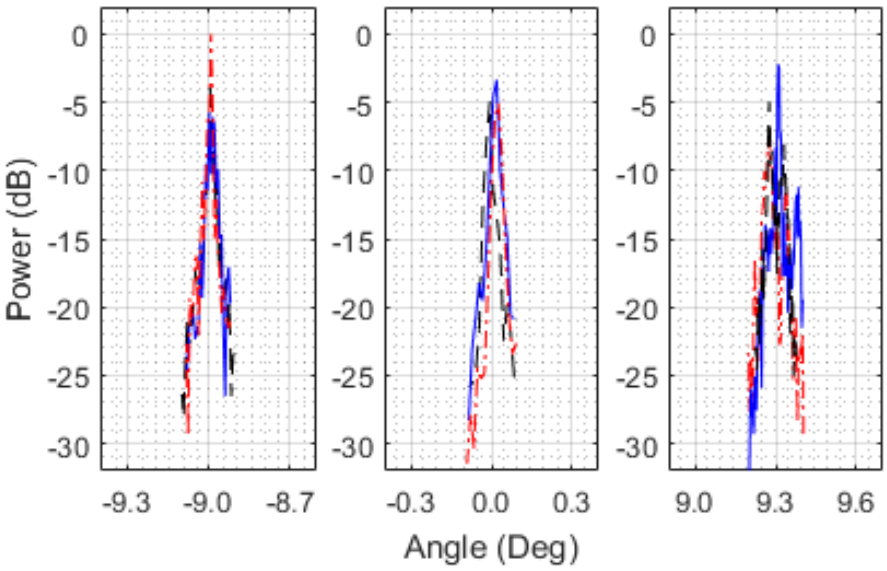
Power (dB)
0
-5
-10
-15
-20
-25
-30
-9.3
-9.0
-8.7
-0.3
0.0
0.3
9.0
9.3
9.6
Angle (Deg)

b)

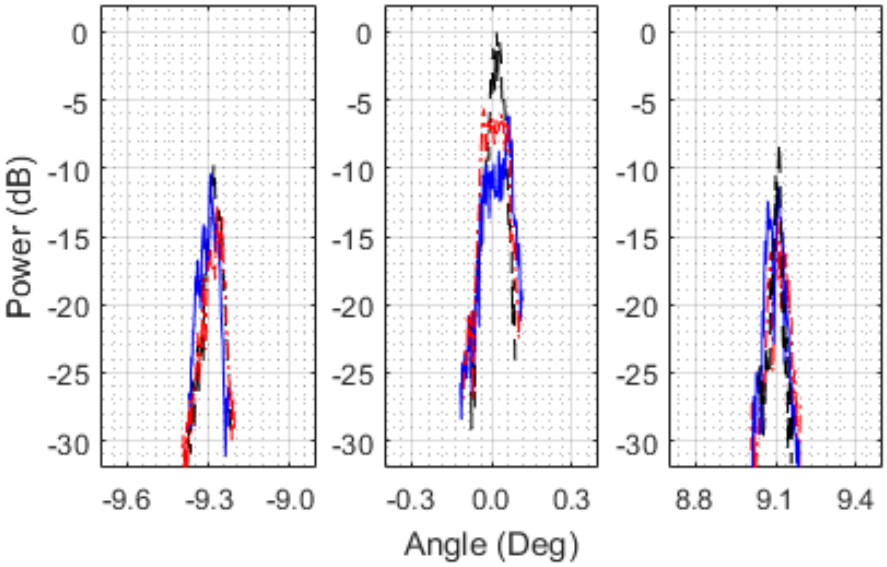

c)

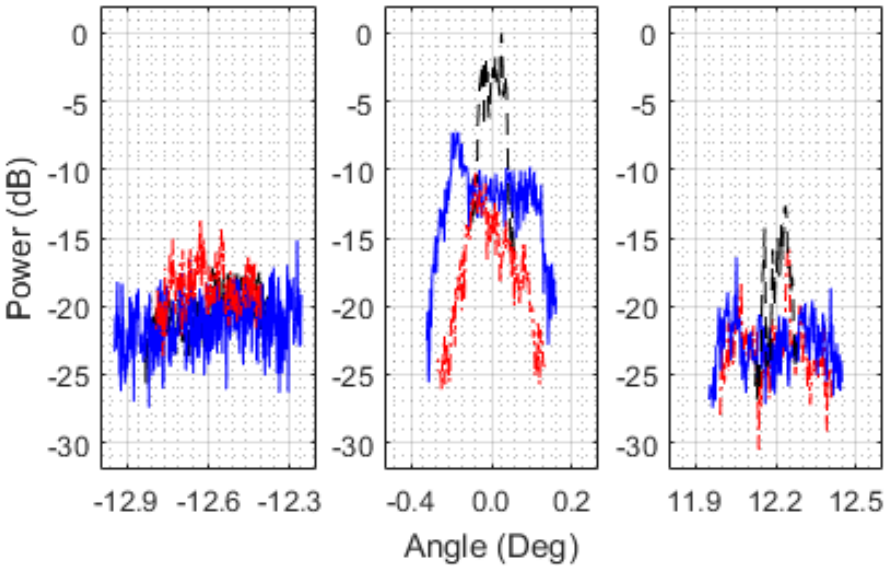

d)

Figure 4-3: Cable backscattered power with respect to angle measured by the Bright Spark radar (Ka band) for various cable subsections in Figure-4-1: *(a) A3, (b) B1, (c) B2, (d) C2, (e) C3. Note: Cable 1: Northmost, Cable 2: middle and Cable 3: Southmost.*

4.2.2 Pylons Scenario

Figure 4-4 shows the scenario that contains a single span of OH power cables that were suspended by Pylons. This cable scenario was measured by the Bright Spark system at Ka band and following the formation of the spotlight SAR image, the spectrum analysis technique was also used on the data collected. The resulting plots that contain the backscattered power measured by the radar system with respect to the aspect angle relative to the centre of the specular lobe are shown in Figure 4-5.

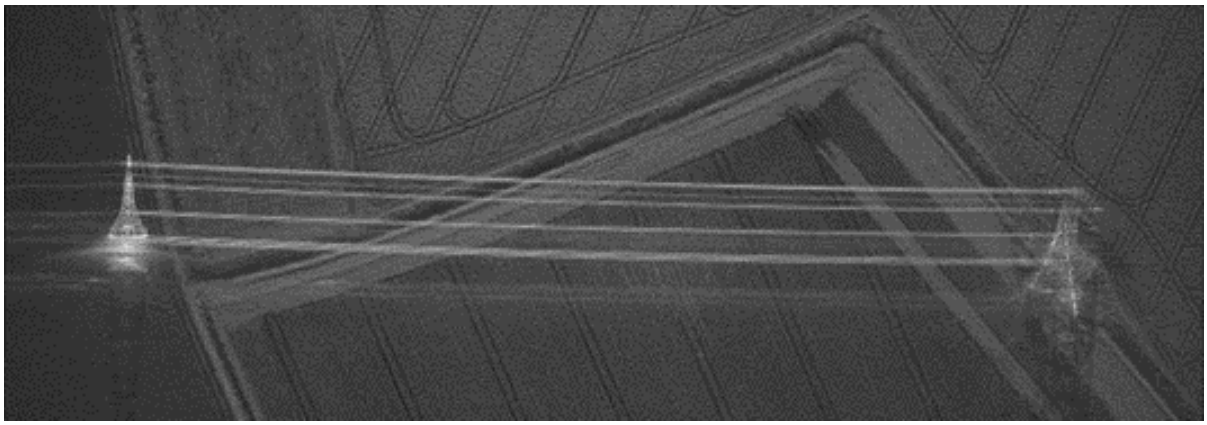

Figure 4-4: Multilook spotlight SAR image of rural Pylon scenario

Figure 4-5: As with the farm scenario, the negative and Bragg peaks were measured to be approximately symmetrical round the centre of the specular peak. This suggests that all of the 275 kV cables will have around the same surface period on the outer strands of the cable. The asymmetry of the Bragg lobe magnitudes with respect to normal incidence, of around -25dB, is expected to be due to the weighting process used to form the original spotlight SAR image prior to the spectrum analysis technique. The lobe widths and lobe positions and not the magnitude will be analysed here. The lobe widths measured for the Pylon scenario were on average the largest out of all the measurements processed. Figure 4-6 was constructed by using

the peak location data, Aircraft INS data and Google maps database in order to gain further confidence in the results.

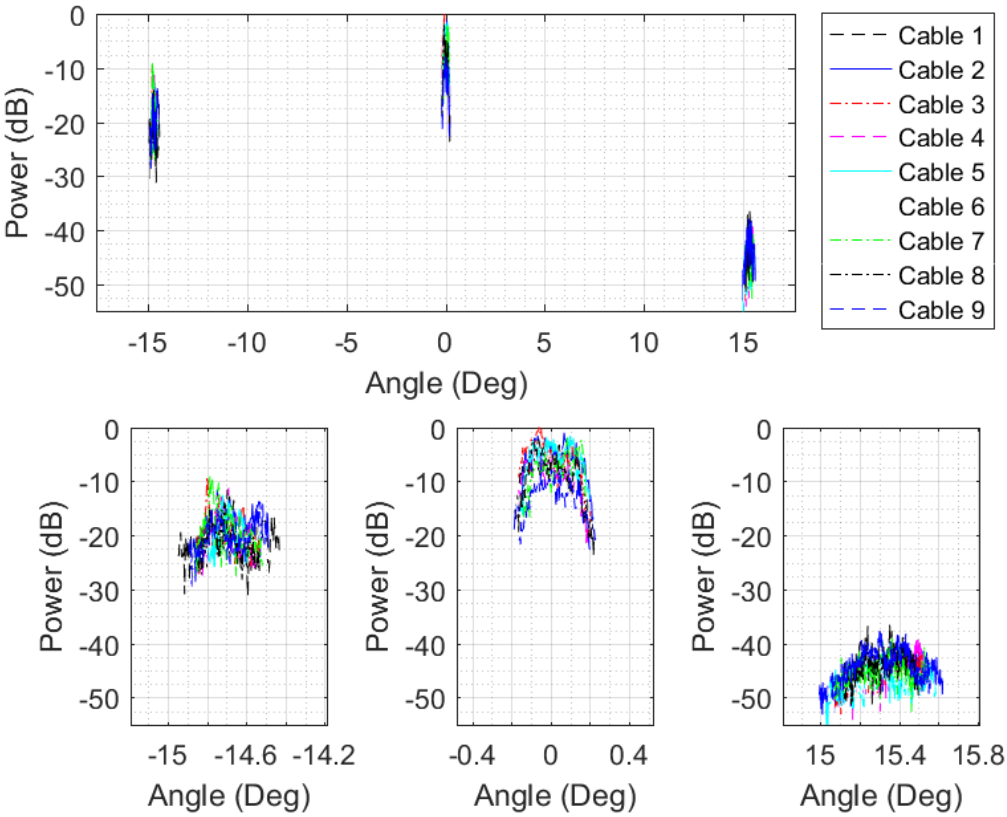

Figure 4-5: : Cable backscattered power with respect to angle measured by the Bright Spark radar (Ka band) for all of the detected cables present in Figure 4-4.

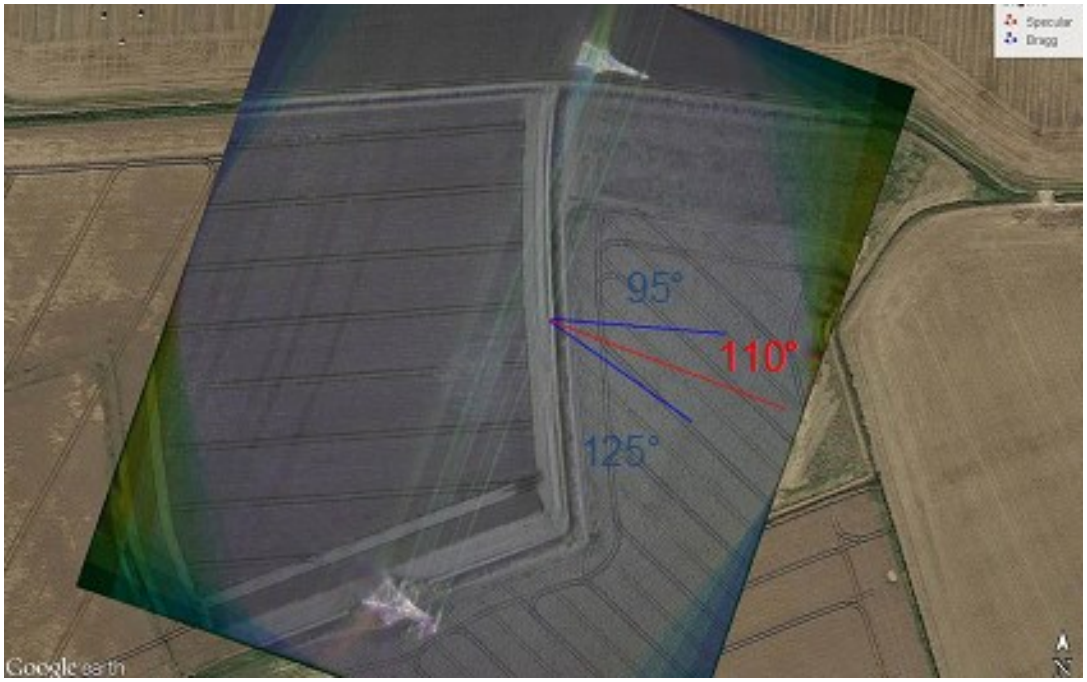

Figure 4-6: Constructed Image that overlays the specular and Bragg locations with respect to to the aricraft (with radar and INS onboard) with the Google maps image

4.3 Quadratic Lobe Fitting

A curve fitting procedure was used to analyse the data in Figure 4-2, Figure 4-3 and Figure 4-5 with higher accuracy and this section will discuss the fitting technique used and the results gained.

In order to obtain a continuous, easily modifiable function that comprises the main features of each specular and Bragg lobe measured, the quadratic function in Equation 4-1 was fitted to each set of normalised data by using the non-linear least square fitting method [70]. Once the fitting procedure has gained values of a, b and c to approximate a set of data, the estimated peak position can be simply calculated by using Equation 4-2. The estimated width of each lobe, Δw^{ref}, has to be relative to a certain value, K^{ref} (Equation 4-3), down from the peak value. The value of Δw^{ref} (Equation 4-5) can be simply calculated by finding the solution x_{sol} (Equation 4-4). K^{ref} was arbitrarily chosen to be 6 decibels for all the results presented here.

The specular and positive Bragg lobes from cable 1 in Figure 4-5 alongside the quadratic function fitted for each are all visible in Figure 4-7.

$$y^{fit} = ax_{data}{}^2 + bx_{data} + c$$

Equation 4-1: Quadratic equation for fitting

$$x_{pk} = \frac{-b}{2a}$$

Equation 4-2: Peak location for a fitted quadratic curve

$$y_{pk} - K^{ref} = ax_{sol}{}^2 + bx_{sol} + c$$

Equation 4-3: Location of amplitude that is below the peak value

$$x_{sol} = -\left(\frac{b \pm 2\sqrt{-aK^{ref}}}{2a} \right)$$

Equation 4-4: Analytical solution for x position (x_{sol}) at K^{ref} down from the peak position

All the results presented here were gained with K^{ref}=6 dB

$$\Delta w^{ref} = \left| x_{pk} - x_{sol} \right|$$

Equation 4-5: Width of the fitted quadratic peak for a given reference value (-6 decibels in this case)

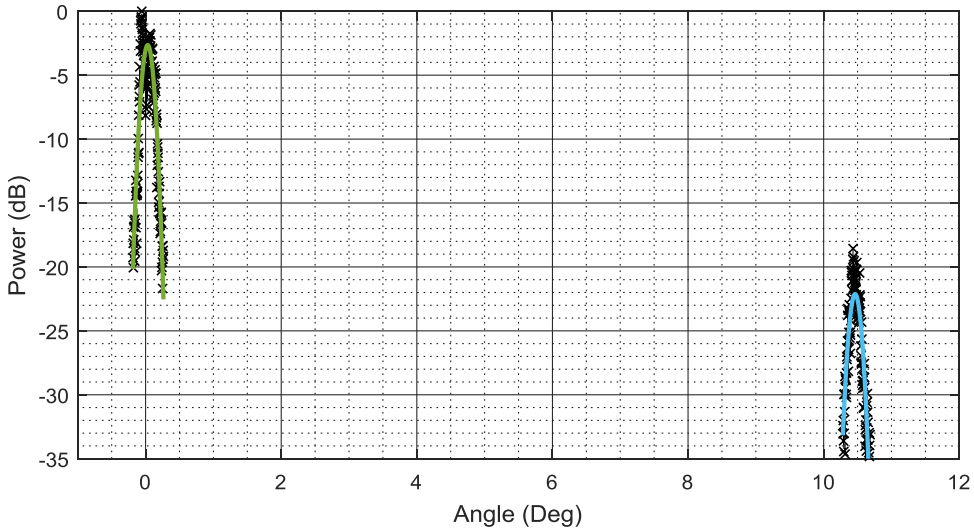

Figure 4-7: Specular and Bragg peak of cable 1 in Figure 4-5 (black with crosses) alongside the fitted quadtrtic curved for each (solid green and solid sky blue respectively)

4.4 Tabular Results

The peaks and widths estimated by using the non-linear least square fitting method and the quadratic function on the Farmland cable data are presented in tabular form as follows:

- Table 4-1-Estimated Bragg lobe angular positions
- Table 4-2- Estimated period of the periodic cable surface structure
- Table 4-3- Estimated Specular and Bragg lobe widths

The following observations were made from the tabular data:

Table 4-1: A clear consistency in the estimated Bragg peak location can be seen for a given power line at both frequencies. The relative error of the Bragg peak location lies between around 10 – 1% amongst different strands. Approximately double the centre carrier frequency can be also seen to roughly half the Bragg lobe positions in all cases which agrees with expectations.

Table 4-2: Inserting the mean of the Bragg positions for each line and also the centre wavelength of the Bright Spark and I-Master devices produces consistent estimates in the

estimated surface period for a given power line. The difference in the mean estimations is submillimetre.

Table 4-3: The Specular and Bragg lobe widths estimated have a consistency again for a given line but this consistency is much lower than that of the Bragg positions present in Table 4-2. The consistency was enough to notice abnormally narrow peak widths for line 'B' at both Ku band and Ka band. This observed peculiarity warranted the processing of a small area of Figure-4-1 which produced Figure 4-8. Figure 4-8 shows that a large tree is pressing against this line causing it to become taut. Figure 4-9 was obtained from Google maps which shows that this line is terminated at a substation around 300 metres south-west from the farm and this explains the tautness present because of a line termination at both ends (at the substation and farm). This vulnerability in the line was found by analysing any relatively narrow peaks in the cable backscatter and by analysing asymmetries in the high-resolution signatures.

Table 4-1: Estimated magnitude of Bragg peak locations with the mean and standard devivation values for the three cable measurments for both positive and negative lobes [μ (mean) ± σ (Standard deviation)]

Line/ Span	**1**		**2**	**3**	**4**
A	K_a	$\|\phi_D\|$: 10.5 ± 0.011°	$\|\phi_D\|$: 10.75 ±0.017°	$\|\phi_D\|$: 10.6 ± 0.024°	
	K_u	$\|\phi_D\|$: 22.9 ± 0.012°	$\|\phi_D\|$: 22.2±0.144°	$\|\phi_D\|$: 22.9 ± 0.174°	
B	K_a	$\|\phi_D\|$: 9.15 ± 0.007°	$\|\phi_D\|$: 9.15 ± 0.006°	$\|\phi_D\|$: 9.1 ± 0.005°	$\|\phi_D\|$: 9.45 ± 0.005°
	K_u			$\|\phi_D\|$: 19 ± 0.013°	
C	K_a	$\|\phi_D\|$: 12.35 ± 0.053°	$\|\phi_D\|$: 12.2±0.01°	$\|\phi_D\|$: 12.7 ± 0.076°	

Table 4-2: Estimated cable surface period that uses the values in Table 1 and Equation 1-26

[μ (mean) ± σ (Standard deviation)]

Span	Mean Surface Period (*L*) [K_u band]	Mean Surface Period (*L*) [K_a band]
A	24 ± 0.118 mm	24 ± 0.038 mm
B	28 ±0.017 mm	27± 0.138 mm
C		20 ±0.055 mm

Figure 4-8: Small processed section of Figure-4-1 where measured specular and Bragg lobe widths were measured to be minimal.

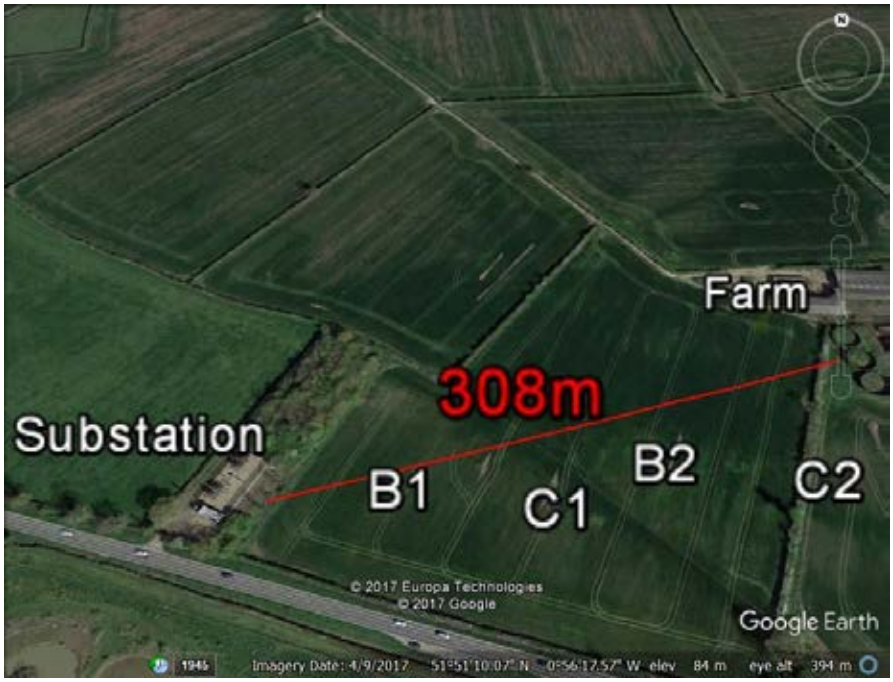

Figure 4-9: Annotated Google Earth image of the power cable substation location, around 308 m southwest from the farm, that cables spans B and C are physically coupled (Figure-4-1).

Table 4-3: Estimated Specular and Bragg lobe widths with the mean and standard deviation values for all strands [μ (mean) ± σ (Standard deviation)]

Line/ Span		**1**	**2**	**3**	**4**
A	K_a	Specular: 0.113 ± 0.012° Bragg: 0.172 ± 0.022°	Specular: 0.121 ± 0.011° Bragg: 0.24 ± 0.015°	Specular: 0.2166 ± 0.028° Bragg: 0.1847 ± 0.022°	
	K_u	Specular: 0.125 ± 0.005° Bragg: 0.627 ± 0.026°	Specular: 0.187± 0.025° Bragg: 0.332± 0.026°	Specular: 0.279 ± 0.063° Bragg: 0.842 ± 0.383°	

B	K_a	Specular: 0.053 ± 0.002° Bragg: 0.059 ± 0.007°	Specular: 0.062 ± 0.013° Bragg: 0.0511 ± 0.008°	Specular: 0.084 ± 0.01° Bragg: 0.0679 ± 0.01°	Specular: 0.0575 ± 0.003° Bragg: 0.051 ± 0.007°
	K_u			Specular: 0.0221 ± 0.001° Bragg: 0.156 ± 0.075°	
C	K_a	Specular: 0.132 ± 0.06° Bragg: 0.525 ± 0.29°		Specular: 0.184 ± 0.094° Bragg: 0.4177 ± 0.226°	

The quadratic lobe fitting method was also performed on the data gathered by measuring the cables suspended by pylons in Figure 4-5. The mean and standard deviations of the estimated Bragg positions, specular lobe widths and Bragg lobes widths estimated for all nine cables present in Figure 4-4 are as follows:

- $|\phi_D|$: 15.012 ± 0.101°
- Δw^{ref} (Specular): 0.157 ± 0.025°
- Δw^{ref} (Bragg): 0.169 ± 0.088°

The Bragg lobe location with respect to the specular peak were observed to have a relative error of less than 1% which allows us to confirm that the same type of wire was used on each

section of the line. The mean Bragg lobe location was slightly higher than those measured in the farmland scenario which is expected due to the high current capacity of these cables relative to those suspended by wooden telegraph poles at a lower height. The mean value of the specular and Bragg lobe widths was measured to be almost equal for the single span of cables.

4.5 Cable Sag Simulations

In order to validate and also reproduce the observed behaviour in measured data, the PO model for a straight ACSR cable was combined with the sagging model described earlier in the thesis. Parameters gained from analysing the high-resolution SAR images and certain measured results will be inserted into these models to see the effect of sagging and changing between Ka band and Ku band radar devices.

First of all, by jointly taking into the estimated surface period in Figure 1-18 and the cable structure information available in literature [38], a straight ACSR cable with the following parameters was simulated with the length of $(\lambda R)^{1/2}$ at a distance of 4 km at both Ka band and Ku band:

- D=35.2 mm (Total Cable Diameter)
- d=4.446 mm (Outer Strand Diameter)
- P=146 mm (Helical Pitch)
- L=24 mm (Surface Period)
- N=45 (Number of strands)

This simulation produced the angular profiles visible in Figure 4-10.

Ku band: The Ku band profile is very similar to all of the measured profiles; in terms of the number of peaks and the location of each of these peaks. A single Bragg peak either side of specular position was simulated at an angular position of around 21 degrees.

Ka band: The Ka band profile is similar to the measured profiles at Ku band in terms of the location of the first peak off normal-incidence which was around -14 degrees in simulations. The absence of additional peaks beyond this first peak were not measured due to the lack of measurements at these angles.

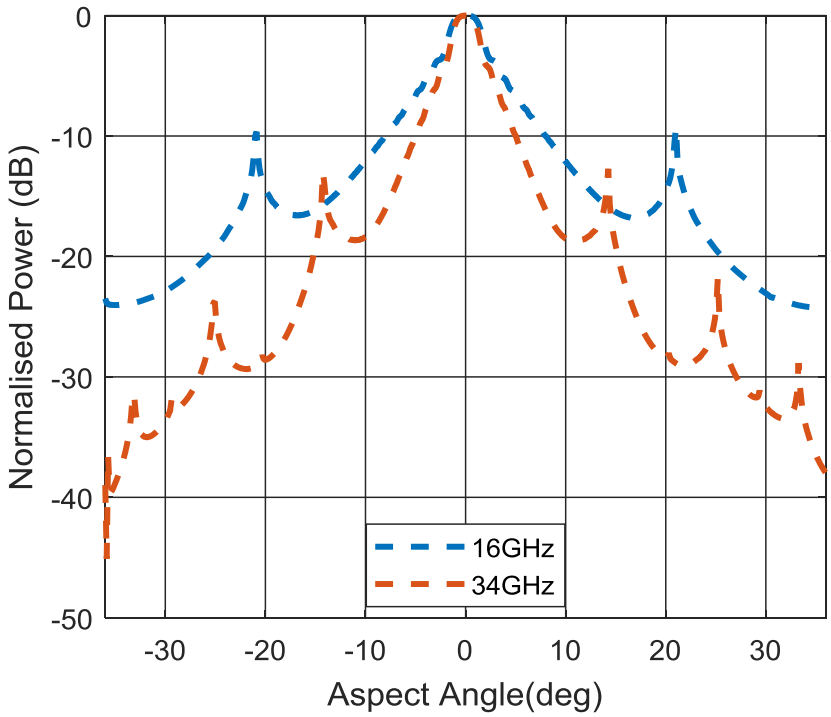

Figure 4-10: Simulated Angular profile for a small section (Fresnel length at 4 km) at both Ka band and Ku band using the theory presented in Section 2.2

The angular profile for the straight ACSR cable in Figure 4-10 was then incorporated into the sagging model in Section 2.3.

The sagging characteristics, cable spans and transceiver parameters simulated were chosen to equal the measurements gained from both the on-board sensors and processed spotlight SAR data which were outlined in sections 3.3.1 and 3.3.2:

Farmland scenario parameters:

Cable span: 100m

Cable suspension height: 8m

Transceiver altitude: 1.5 km

Range to cable centre: 4 km

Pylon scenario parameters:

Cable span: 232m

Cable suspension height: 60m

Transceiver altitude: 1.5 km

Range to cable centre: 4 km

The Farmland parameters produced the angular profiles in Figure 4-11 and Figure 4-12 for Ku band and Ka band respectively. The plots in these figures were normalised to the maximum value for each cable tautness simulated so that the effects were clearly visible. Figure 4-15 has the simulation results for the Pylon scenario at Ka band.

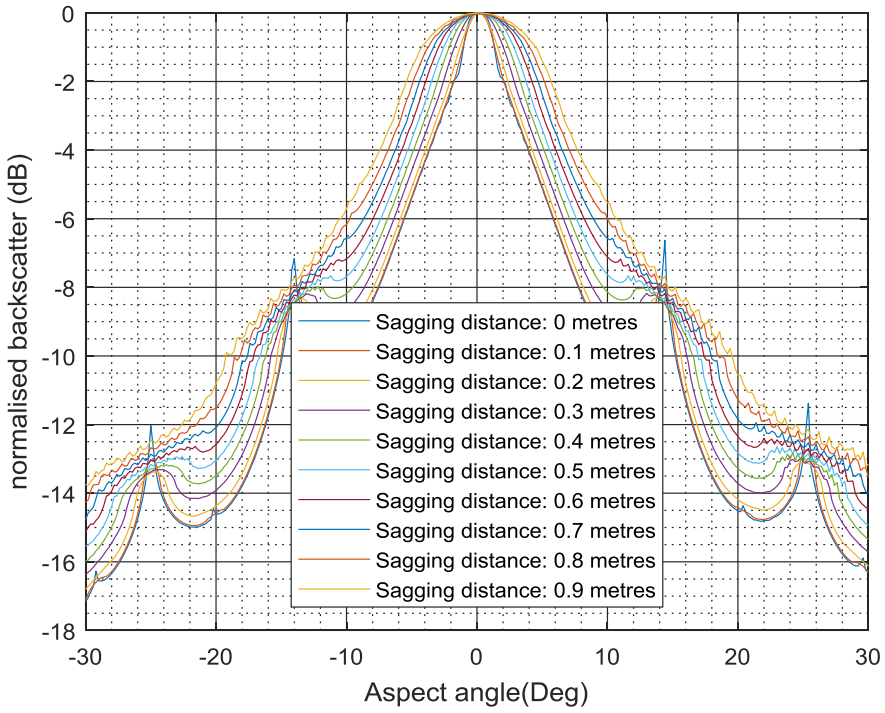

Figure 4-11: Simulated angular profiles (using Figure 4-10) for a span of ACSR cable with different sagging distances at the centre (Ka-band for Farmland scenario)

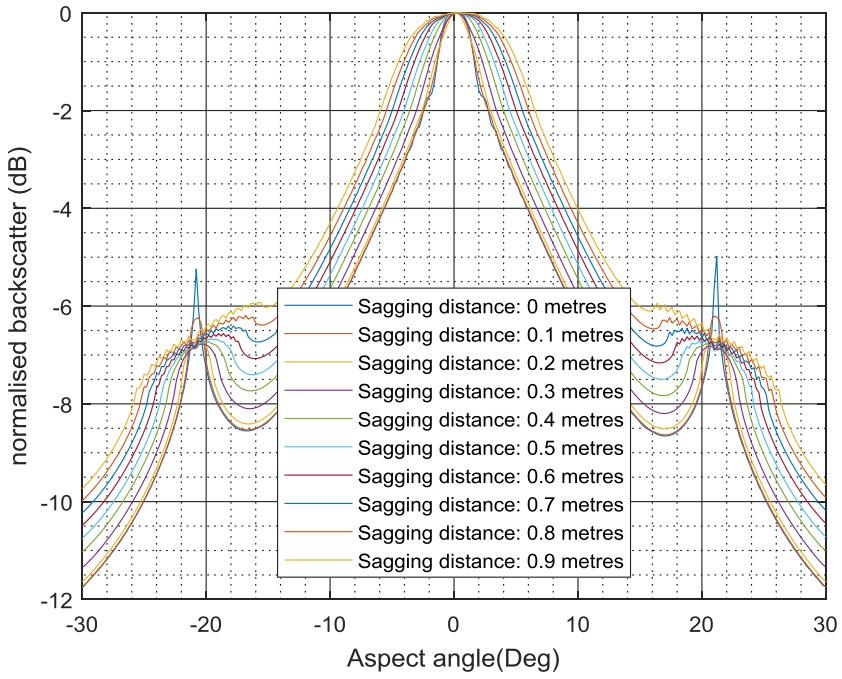

Figure 4-12: Simulated angular profiles (using Figure 4-10) for a span of ACSR cable with different sagging distances at the centre (Ku-band for Farmland scenario)

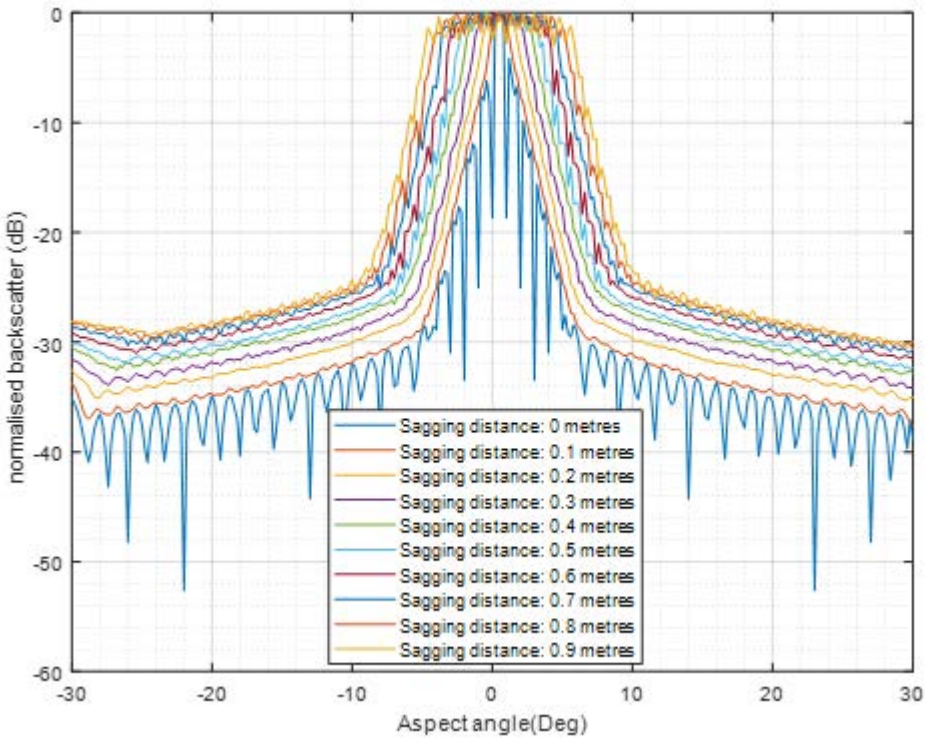

Figure 4-13: Simulated angular profiles (using Equation 1-12) for a span of Smooth cable with different sagging distances at the centre (Ka-band for Farmland scenario)

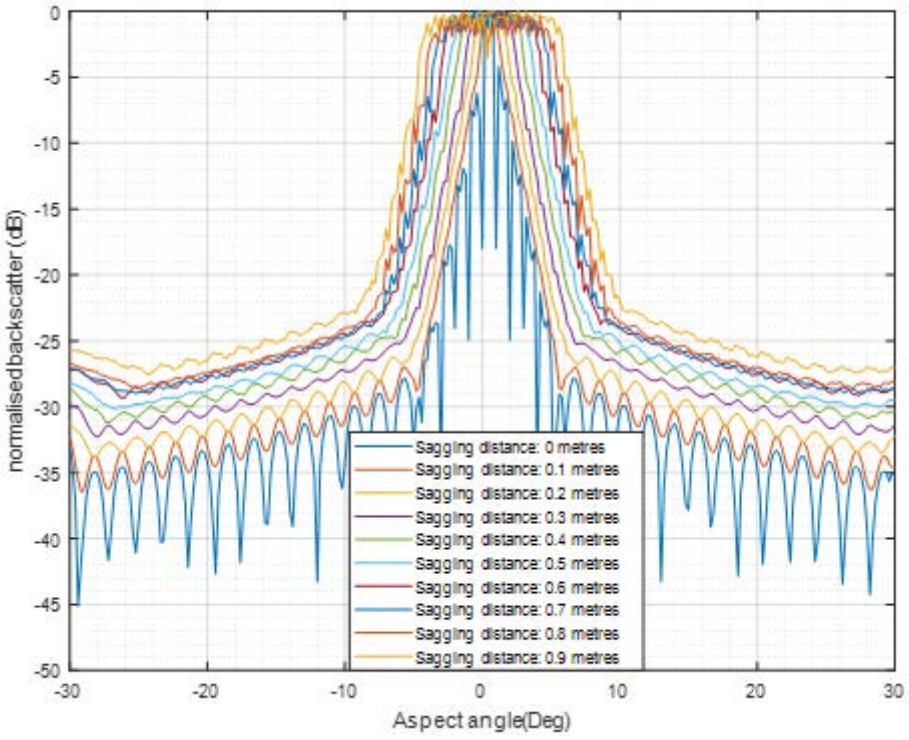

Figure 4-14: Simulated angular profiles (using Equation 1-12) for a span of smooth cable with different sagging distances at the centre (Ku-band for Farmland scenario)

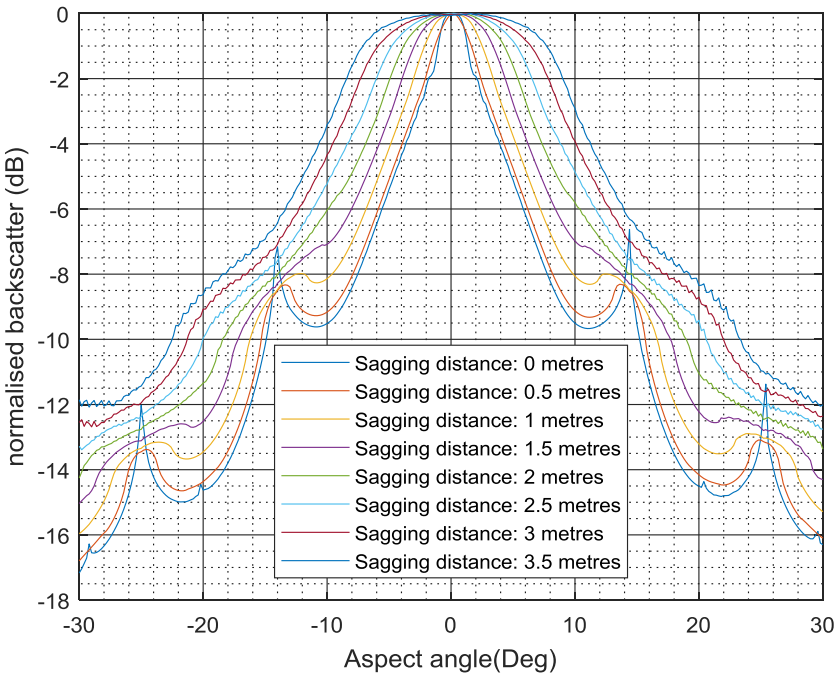

Figure 4-15: Simulated angular profiles (using Figure 4-10) for a span of ACSR cable with different sagging distances at the centre (Ka-band for Pylons scenario)

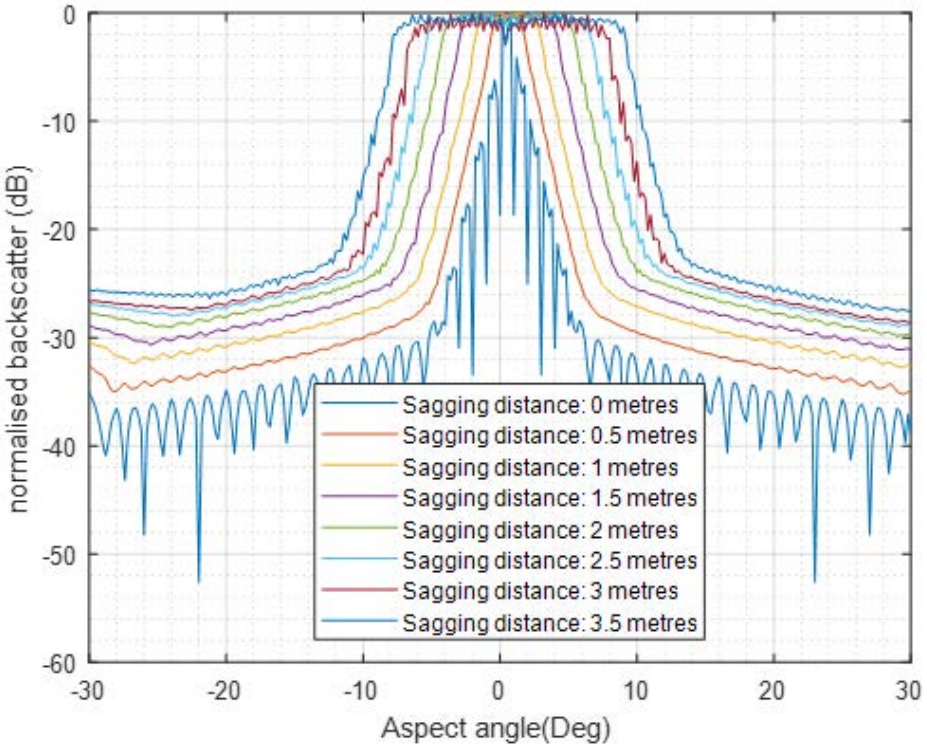

Figure 4-16: Simulated angular profiles (using Equation 1-12) for a span of smooth cable with different sagging distances at the centre (Ka-band for Pylons scenario)

All of the simulated results conclude that an increase in tautness (central sagging distance /cable span) produces a lobe widening and peak magnitude reduction in both the specular and Bragg lobes until the Bragg lobes merge into the specular lobe to form ripples.

This effect is evident throughout the farmland results (Figure 4-2 and Figure 4-3). Figure 4-3d in particular shows the effect between strands as the widest specular lobe has the nosiest Bragg lobe measurement. The tautness and lobe width effect was validated previously by gaining "high resolution" truth in Figure 4-8.

The most extreme effect of the Bragg lobes disappearing to form a rippling effect along the relatively wide specular lobe was observed in Range-Doppler imagery of the pylon scenario which is visible in Appendix C and Appendix D. Although a Bragg peak was detectable in the Range-Doppler images in Appendix D an extreme widening of this relatively low magnitude peak was observed which swept the entire span of the cable span (around 232 metres) and this did have a clear rippling structure in the images.

Figure 4-11, Figure 4-12 and Figure 4-15 display the same effect at different extremes where the simulation results in Figure 4-15 appears to have the most extreme effect which is no surprise due to the ratio between the maximum sagging distance at centre and cable span.

The results for a sagging smooth cable in Figure 4-13, Figure 4-14 and Figure 4-16 also show a widening of the main lobe and a merging of the side lobes is pressing for an increased central sagging distance, although due to the absence of periodic grooves, a reduction in magnitude is seen off normal incidence as expected.

4.6 Conclusion

This chapter has displayed the results of performing the spectrum technique on high- resolution spotlight SAR images at both Ka band and Ku band. These results showed consistencies in the Bragg peak locations for a given power line and these Bragg peak locations allowed cable surface period estimations to be made that has the potential to classify cables by type and hence estimate the current capacity. This cable surface period estimate also validated the Bragg relationship with wavelength as the results shown have an error range of 2-10% in both the Ka band and Ku band results which is equivalent to a fraction of a millimetre accuracy. The specular and Bragg lobe widths were fairly consistent for a given strand and subsection although these widths were seen to vary significantly for different lines. Abnormally small specular and Bragg lobe widths which allowed the finding of a tree pressing on the line to be found on the high-resolution SAR images which was causing the cable to become taught. The Physical Optics model for a straight cable was incorporated into the sagging model presented in this thesis to validate the Bragg peak locations and the effect of sagging on both specular and Bragg lobe widths. A rippling effect that was observed along sagging power lines in Range-Doppler images was also seen in the simulated results for sufficient sagging distance to cable-span ratios.

5. mmW/Low-THz Power Cable Results

5.1 Introduction

This section will display the results gained from measuring OH power cables at 150 GHz and 300 GHz. Quantitative values of the RCS will be shown. These are available because the measuring instruments have been calibrated against standard reflectors. The ACSR and ACCC type of cables were rotated individually at several aspect angles (Figure 5-1) between -20° and 20° and a high resolution range profile was measured for each of these which produces a three dimensional image; the axes being range, rotation angle and magnitude. The magnitudes in this image for the two types of cables at the two frequencies of interest was then summed in range to form angular profiles in order to observe any Bragg scattering behaviour. The measured image with the axes: aspect angle (z-plane), range(y-plane) and RCS (z-plane) was then used to produce a threshold value by taking the mean of the noise/clutter in a section of the image. This was then used to measure the nearest and furthest ranges the cable was detectable at each aspect angle which enabled range spread plots to be created.

All the previous measurements will be supported with the Bragg, Range Spread and Physical Optics theories described earlier in the thesis (Sections 1.3.3, 1.3.4 and 2.2 respectively).

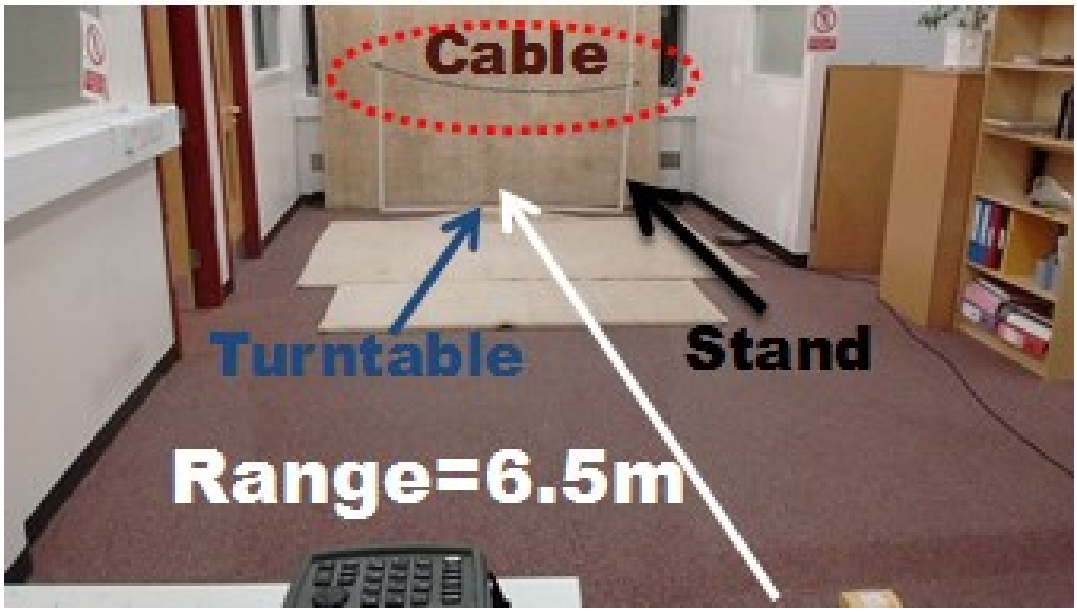

Figure 5-1: Indoor Experimental setup realised for the 150 GHz and 300 GHz devices

5.1.1 Experimental Parameters

Table 5-1 shows the main parameters of the experiments performed at the upper part of the millimetre-wave band. The devices had approximately the same 3dB beamwidths in azimuth and elevation in which the former plane had a narrower resolution. The range resolution of the 300 GHz devices was finer although the distance of all the measurements were all approximately 6.5 m causing the illumination length by the antenna to be consistent for all measurements.

Table 5-1: Bragg scattering experimental parameters

Parameter	Experiment 1	Experiment 2
Frequency (f_0)	150 GHz	300 GHz
Range Resolution (Δr)	25 mm	10 mm
3dB Azimuth Beamwidth (H-plane)	≈1.5°	≈1.5°
3dB Elevation Beamwidth	10º	10º

Distance (R)	≈6.5m	≈6.5m
3dB illumination length	≈170mm	≈170mm
Fresnel length, $2\sqrt{(\lambda r)}$	≈125mm	≈72.5mm

5.2 Experimental Results

5.2.1 High-Resolution Images

5.2.1.1 Results

As briefly described, the measurements of each of the two types of power cables involved processing a range profile with the bandwidths stated in Table 5-1. To make sure that no physical movement was present along the target, so that the range-Doppler coupling in the linear modulation can be neglected, a sufficient period of time (around 5 seconds) occurred between each measurement.

After subsequent FMCW (150 GHz) and Stepped Frequency (300 GHz) processing the backscattered RCS images produced for the ACSR and ACCC cable types are shown in Figure 5-2 to Figure 5-5. The plots of summing the RCS amplitudes in range are shown in Figure 5-6 to Figure 5-9:

- Figure 5-2 *and* Figure 5-6 *(ACSR-150 GHz)*: contains the expected distinct peak structure predicted from Bragg theory with 7 peaks clearly detectable with a max summed RCS of -5.5 dBsm. The cut-off angle of around ±15° is also clearly visible as the furthest detectable peaks away from normal incidence are around ±13°.
- Figure 5-3 *and* Figure 5-7 *(ACSR-300 GHz)*: Peaks are again visible in the expected range of ±15° at 300 GHz although they are not easily separable. An increase of frequency has not only caused the Bragg peaks to be relatively condensed

compared to the rotation increment of 0.1° but it has also produced a random displacement in the specular constructive/destructive interference which is expected to be caused by surface roughness becoming significant at this wavelength. The maximum peak value in the summed RCS plot is around -1.5dBsm and the average RCS within the detectable cable backscatter is around -10dBsm.

- Figure 5-4 *and* Figure 5-8 *(ACCC-150 GHz)*: The measured image shows a dominant main lobe around normal incidence and not much backscatter detectable away from a few degrees off-normal. This is typical of a smooth metallic cylinder although some constructive/destructive interference is visible within the main lobe which may be due to the surface structure of the ACCC cable. The main lobe peak amplitude was measured to 4dBsm which is the highest amplitude measure for all cases which makes sense as the vast majority of the ACCC RCS profile at 150 GHz is contained in the main lobe. A couple of peaks with an amplitude of around - 5 dBsm were seen near the extreme angle at which Bragg returns would be expected, although, for some reason, these are only apparent on one side of the profile.
- Figure 5-5 *and* Figure 5-9 *(ACCC -300 GHz)*: Within this image the main lobe still dominates, as with Figure 5-4, although a reduction in the incident wavelength and hence an increase in surface sampling has caused some of the lower order Bragg lobes, up to around 6°, to become more significant in the cable signature but these lobes are around 10 dB lower than the dominant lobe around normal incidence. The amplitude of the main lobe amplitude has a decreased value of 1.5 dBsm. Figure 5-9 also shows, between about 2 degrees and about ten degrees either side of broadside, a significant broad backscatter which decreases steadily with angle

off broadside. The fact that this phenomenon is not visible at 150GHz (Figure 5-8) provides strong evidence that it is caused by diffuse scattering. The power which is scattered into this mode has, of course, been taken from that which would otherwise have been scattered coherently and this is why the level of the coherent 'flashes' is slightly lower than it was at 150GHz.

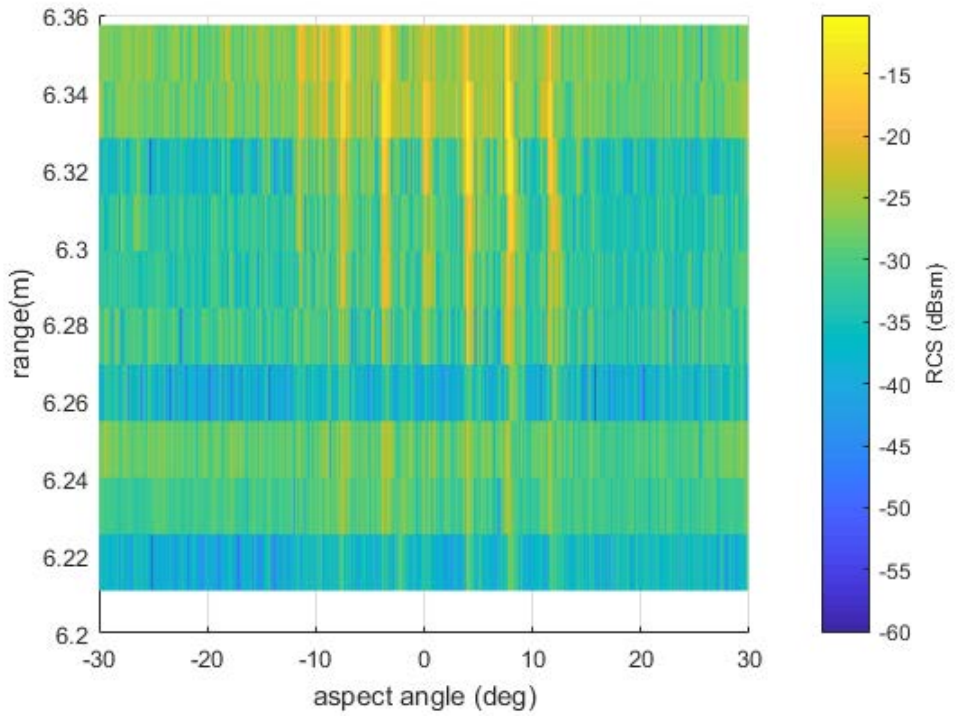

Figure 5-2: Measured image using the calibrated 150 GHz FMCW radar with $\Delta f \approx 5$ GHz to measure high-resolution range profiles of the ACSR cable at multiple aspect angles

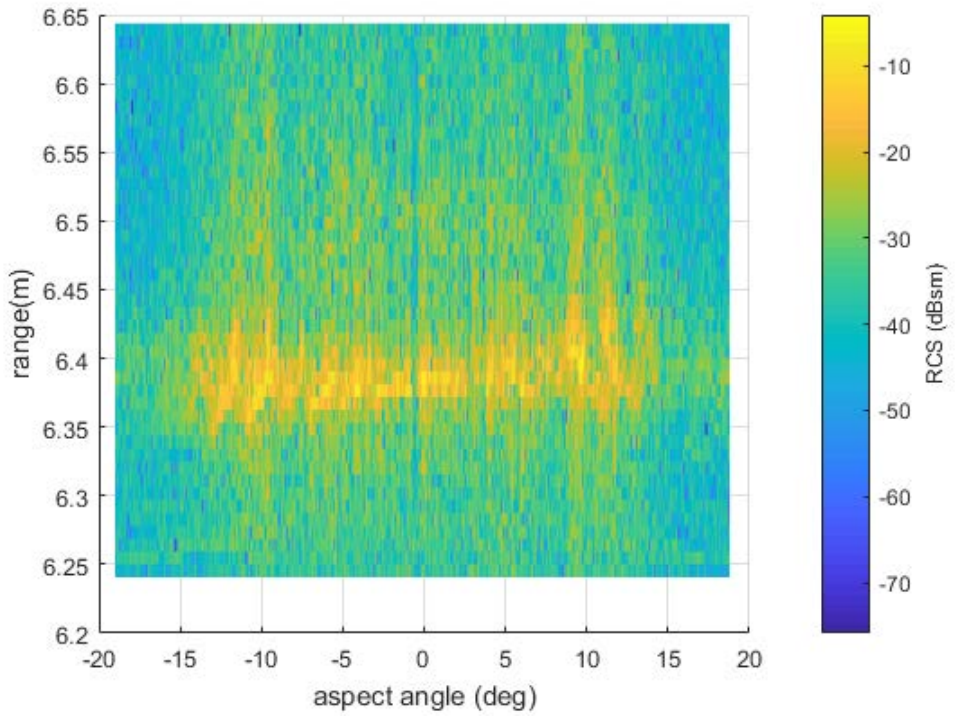

Figure 5-3: Measured image using the calibrated 300 GHz Stepped Frequency radar $\Delta f \approx 16$ GHz to measure high-resolution range profiles of the ACSR cable at multiple aspect angles

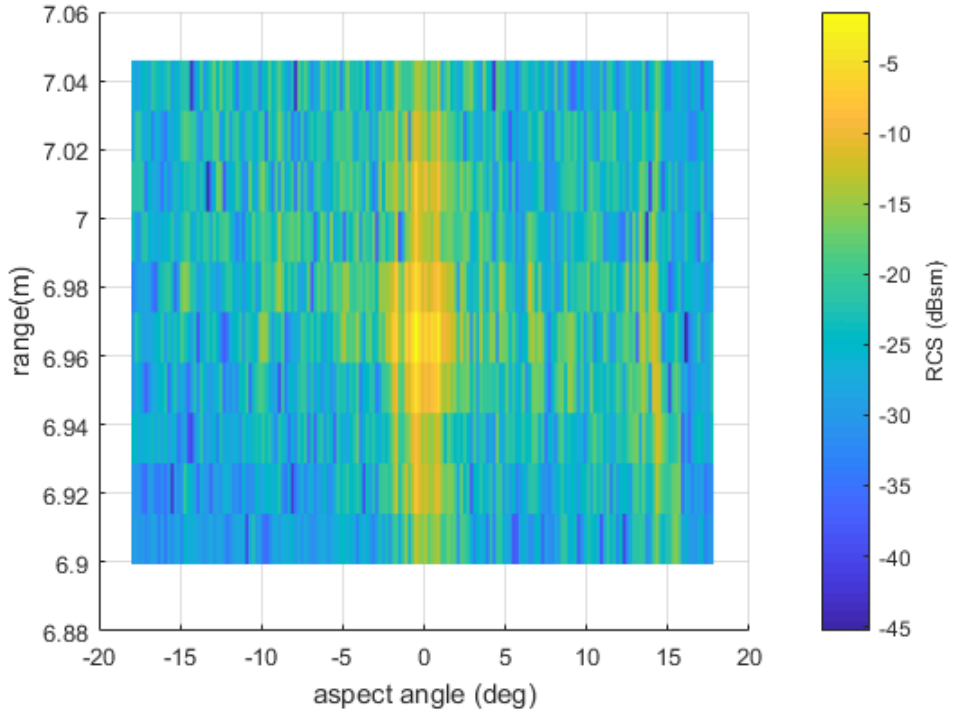

Figure 5-4: Measured image using the calibrated 150 GHz FMCW $\Delta f \approx 5$ GHz radar to measure high-resolution range profiles of the ACCC cable at multiple aspect angles

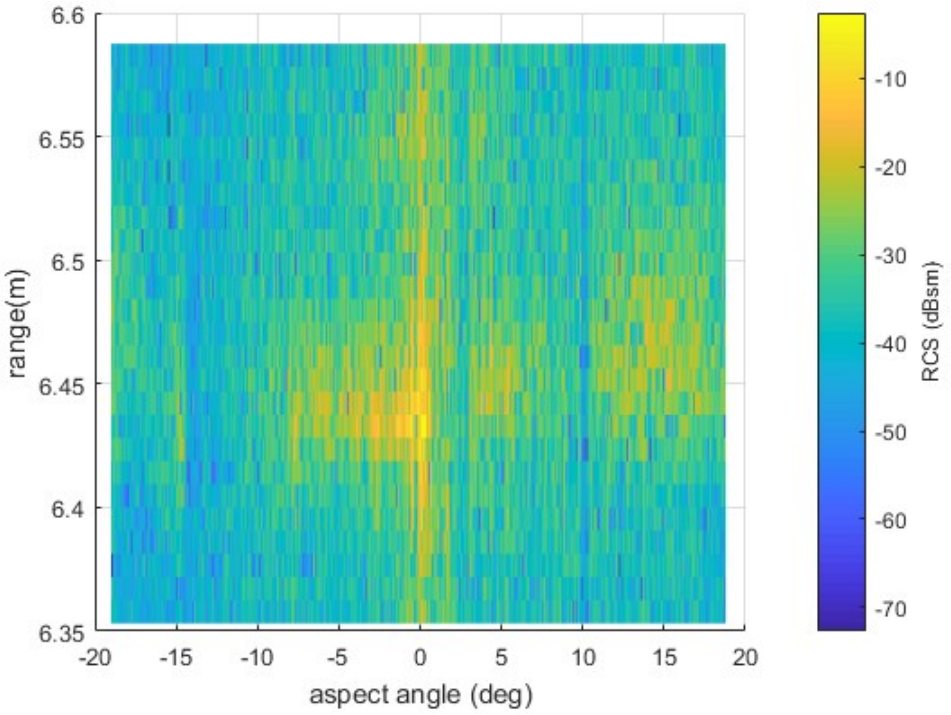

Figure 5-5: Measured image using the calibrated 300 GHz Stepped Frequency radar $\Delta f \approx 16$ GHz to measure high-resolution range profiles of the ACCC cable at multiple aspect angles

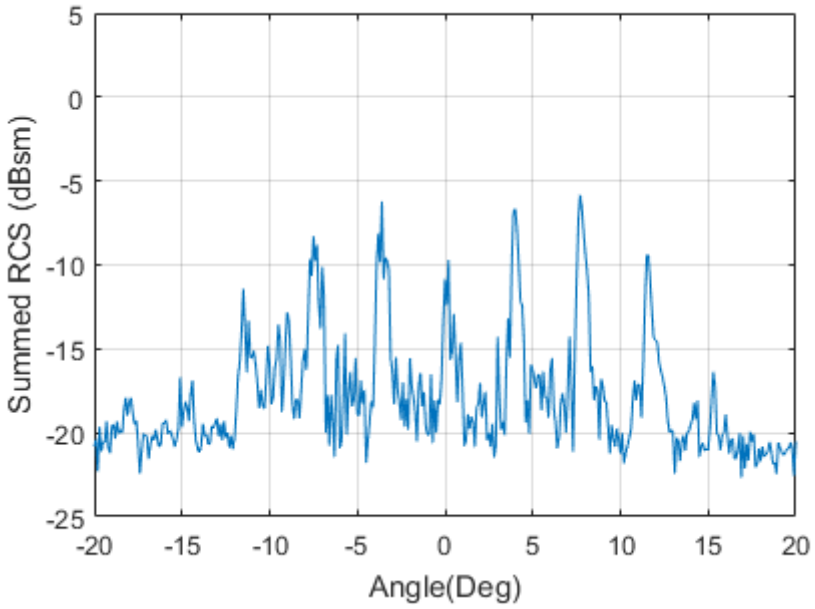

Figure 5-6: Measured image in Figure 5-2 summated in range (ACSR 150 GHz)

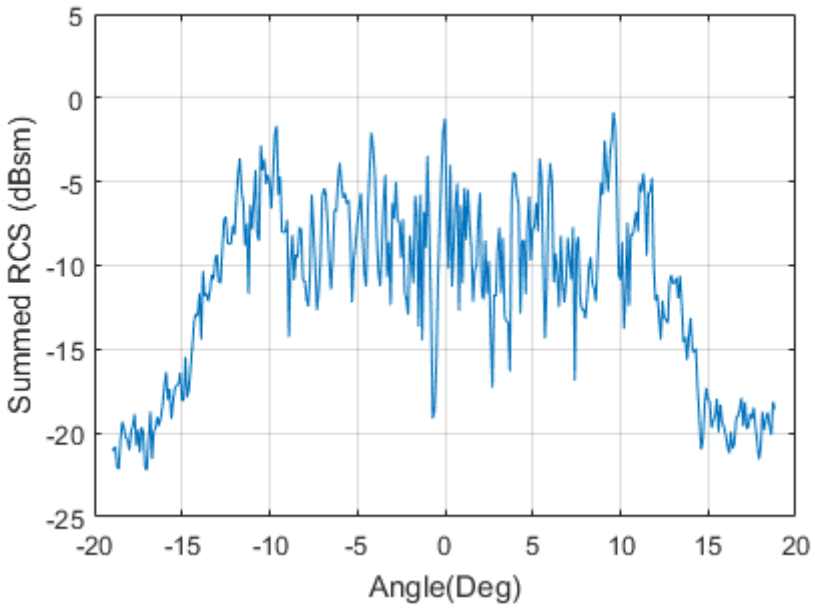

Figure 5-7: Measured image in Figure 5-3 summated in range (ACSR 300 GHz)

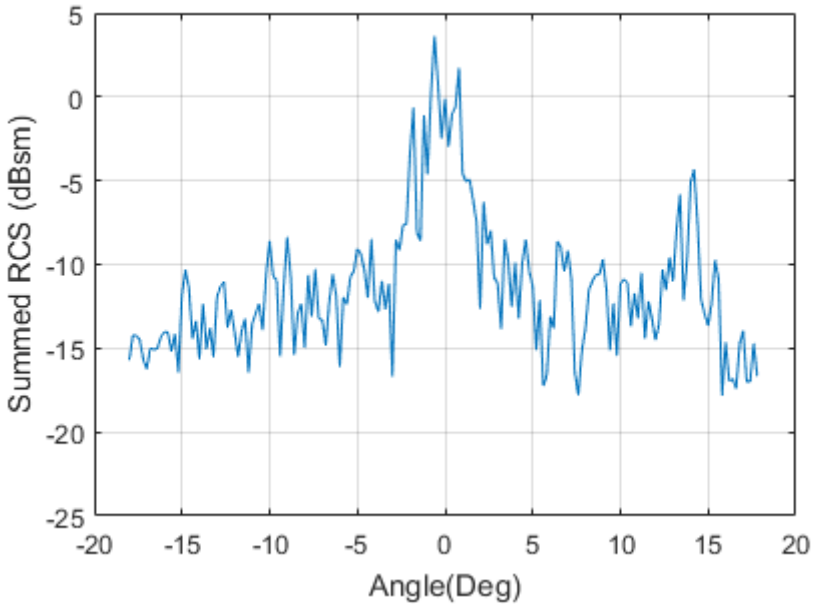

Figure 5-8: Measured image in Figure 5-4 summated in range (ACCC 150 GHz)

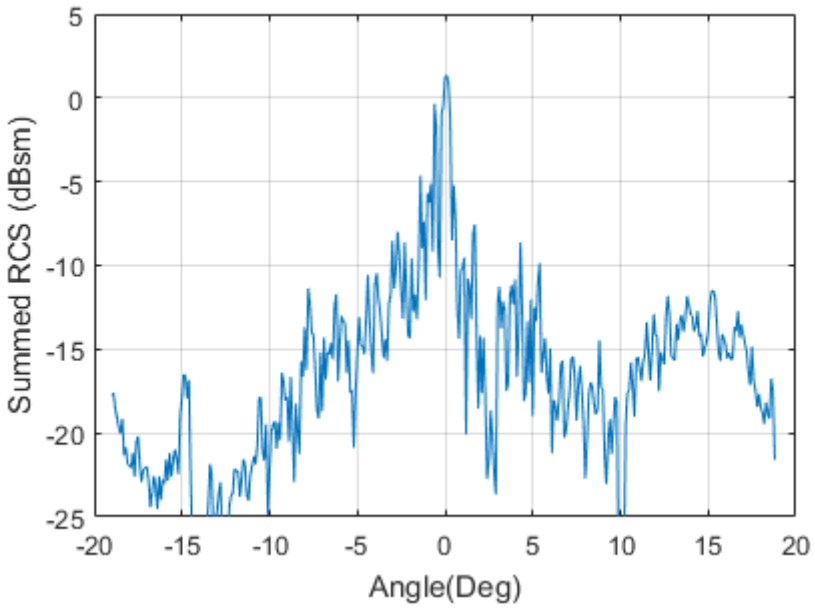

Figure 5-9: Measured image in Figure 5-5 summated in range (ACCC 300 GHz)

5.2.1.2 Analysis

To confirm that the models described in this thesis incorporate the main features of the measured high-resolution backscatter from both the ACSR and ACCC power cables, the experimental parameters were inserted into the Physical Optics model described in the modelling chapter. The far-field azimuth patterns simulated were normalised to gain estimates into the RCS magnitudes in the indoor experimental setup at the short range present (Figure 5-1 and Table 5-1). The normalisation makes use of the analytical far-field RCS equation for a smooth cylinder (Equation 5-1) and the assumptions that all the Bragg lobes will be the same amplitude (Equation 5-2) with the backscatter also spread evenly in Range (Equation 5-3 and Equation 5-4). The effects of Bragg lobes and Range spread are incorporated to produce the normalisation equation for the far-field cable patterns. Equation 5-5 will be used to compare expected RCS magnitudes with measured calibrated values.

$$\sigma^{norm}{}_{cyl} = \frac{2\pi r l^2}{\lambda}$$

Equation 5-1: Far-Field RCS of a smooth PEC cylinder

where l - cylinder length, r - cylinder radius, λ - incident wavelength

$$\sigma^{bragg}{}_{peak} = \sigma^{norm}{}_{cyl} - 10\log(N_{pk})$$

Equation 5-2: RCS of Equation 5-1 divided into the number of peaks

where N_{pk} –Number of peaks

$$\Delta N^{cells} = \left\lceil \frac{\Delta R_{spread}(\theta)}{\Delta r} \right\rceil$$

Equation 5-3: Number of cells that the target is spread in range

where ΔR_{spread} – Spread in Range, Δr – Range resolution

$$L_{\text{SPREAD}} = -10\log(\Delta N^{cells})$$

Equation 5-4: Loss due to returns being split evenly into different cells

$$\sigma^{extented} = \sigma^{norm}{}_{cyl} - 10\log(N_{pk}) - 10\log(\Delta N^{cells})$$

Equation 5-5: Theoretical extended straight perioic cable RCS

Using Equation 5-2 to normalise the magnitudes of the angular profiles in the modelling chapters produces Figure 5-10 to Figure 5-13. Using the peak locations, which are not expected to be related to range for an incident planar-wave, with the Range Spread theory presented earlier in the thesis the images in Figure 5-14 to Figure 5-17 are created.

The following comparisons can be made between the measured and simulated results:

- ACSR 150 GHz
    - *RCS profile (*Figure 5-6 *and* Figure 5-10*)*

      The measured angular profile had 7 clearly distinguishable peaks with magnitudes that range between -6 dBsm to -12 dBsm with an average of around -9dBsm. The simulated response had 5 peaks with a space of -5 dBsm to

- 12.5 dBsm with an average of -10 dBsm. The magnitudes of each peak were consistent for both measurement and simulations although the measured cable signature had two extra peaks. The possible reason for these extra peaks being measured is the frequencies in which the FMCW chirps to get a bandwidth of 5 GHz although this bandwidth is less than 5% of the central carrier frequency. The simulated response only considered a single narrow-band centre frequency so it is unsurprising that additional constructed interference happens for the chirp response.

    - *Image (*Figure 5-2 *and* Figure 5-14*)*

      The modelled and simulated images both have the same discrete peak structured distributed over a number of range cells. The main difference between the images is that spread in range when the cable is indeed detectable increases slightly with range but this increase is not clear in the measured image.

- ACSR 300 GHz

    - *RCS profile (*Figure 5-7 *and* Figure 5-11*)*

      The simulated response had 9 easily distinct peaks between ±15° with peaks that span between -7 dBsm and -15dBsm with an average of around -10dBsm. As mentioned previously the peaks measured were not easily separable although they are indeed more condensed as the modelling predicts. The peaks measured range in between -1 dBsm and -10 dBsm with an average of -7.5 dBsm. This deviation is attributed to the diffuse scattering becoming significant due to the ratio of surface roughness to wavelength increasing. An increase in the number of peaks is also expected due to the frequency being stepped through a bandwidth of 16 GHz around the carrier frequency. The range at which an

increase in backscatter was observed is consistent for both the model and measurements.

- *Image (*Figure 5-3 *and* Figure 5-15*)*

  At 300 GHz, the discrete peaks become less distinguishable compared to the simulated results although due to the higher range resolution, the spread in range in cable backscatter can be clearly seen to increase as the aspect angle increases as in the measured results.

- ACCC 150 GHz
  - *RCS profile (*Figure 5-8 *and* Figure 5-12*)*

    The simulated angular profile had a maximum at normal incidence with a magnitude of 4.5 dBsm with two peaks either side at ±2° a few decibels lower in magnitude. The pattern also displays minor but observable asymmetries. The measured main lobe had also a magnitude of around 4dBsm with two peaks either side at ±2° although one was a few decibels lower than simulated. A distinct peak at around -4dBsm was detected in measurements although this was absent in simulations. The simulations assumed that the grooves of the ACCC cable are Gaussian shaped to keep the modelling simple although the groove edges of the actual cable were discontinuous which may be causing this extra detail at 15° to be not present in modelling. Physical Optics would not have included edge diffraction even if the actual discontinuous surface structure would have been present, this would have required a much more advanced and computationally intensive model such as UTD (Unified Theory of Diffraction) [71].

  - *Image (*Figure 5-4 *and* Figure 5-16*)*

The simulated and measured images for the ACCC at 150 GHz are very similar as a dominant main lobe spread in range can be observed for both. Some relatively weak backscatter can be seen in the measured results at angles over 5 degrees but this is expected to be due to both wear in the cable and the absence of the discontinuous groove edges in modelling the ACCC type.

- ACCC 300 GHz
    - *RCS profile (*Figure 5-9 *and* Figure 5-13*)*

      The simulated profile had a main lobe at normal incidence at around 0 dBsm although this has small rapid fluctuations of few decibels between ±3°. The measured results also show low order lobes up to 7.5° with peak magnitudes at approximately -16dBsm. The simulated results show a narrower main lobe at around 2 dBsm and lobe structure up to around 8° although these were slightly higher in magnitude (-12 dBsm on average) than the simulated lobes off normal incidence.

    - *Image (*Figure 5-5 *and* Figure 5-17*)*

      The measured and simulated image for the ACCC type at 300 GHz are similar in the fact that both have a dominant main lobe although the spread in range of this lobe is observed to be much larger than any returns at higher aspect angles in the measured results. The dominant scattering at normal incidence may be providing a wider response after processing and this coupling between backscattered lobe amplitude and width was not taken into account in modelling.

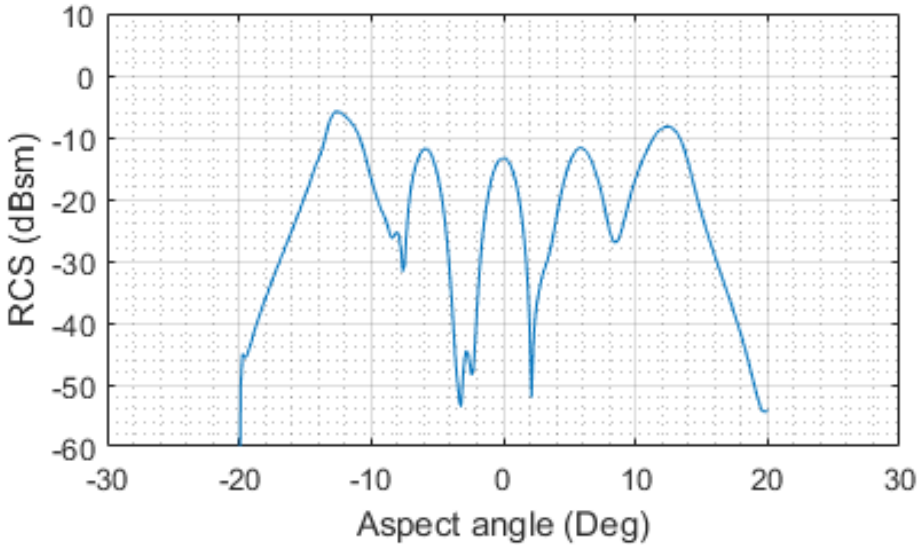

Figure 5-10: Normalised simulated PO angular profile for a ACSR at 150 GHz

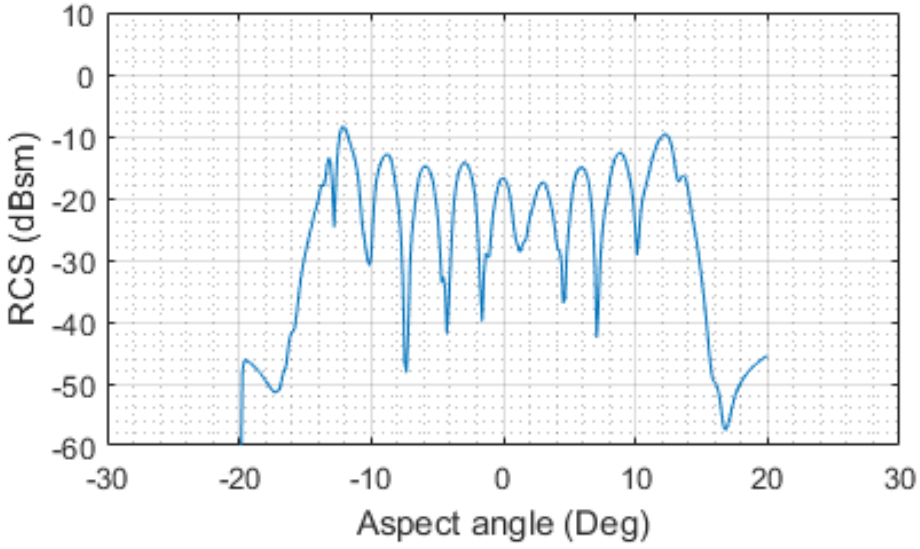

Figure 5-11: Normalised simulated PO angular profile for a ACSR at 300 GHz

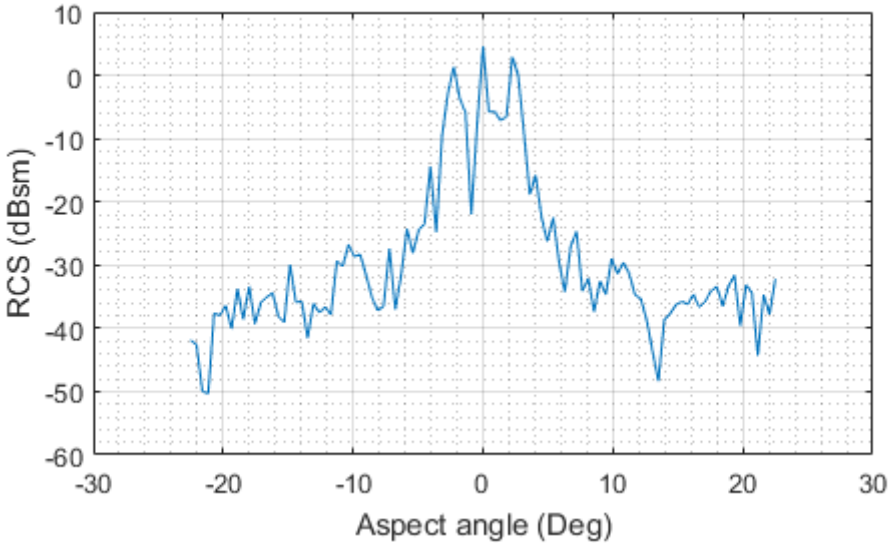

Figure 5-12: Normalised simulated PO angular profile for a ACCC at 150 GHz

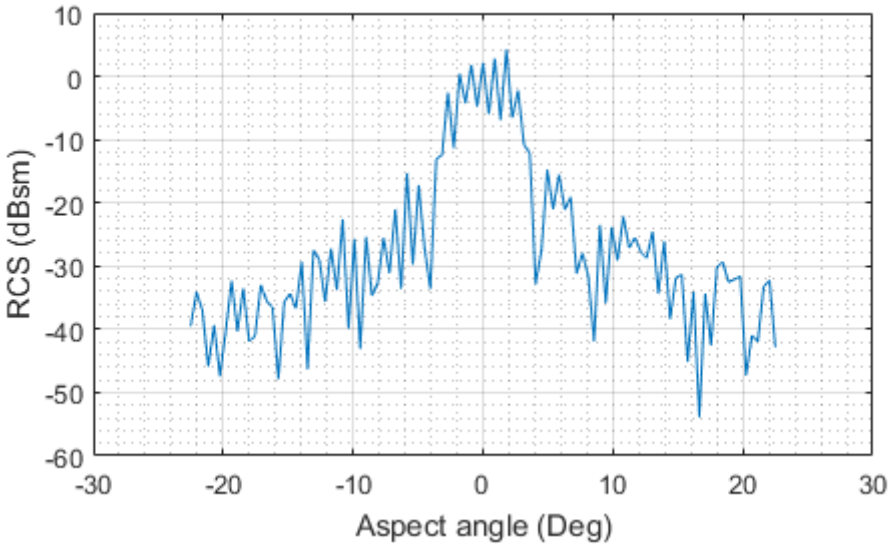

Figure 5-13: Normalised simulated PO angular profile for a ACCC at 300 GHz

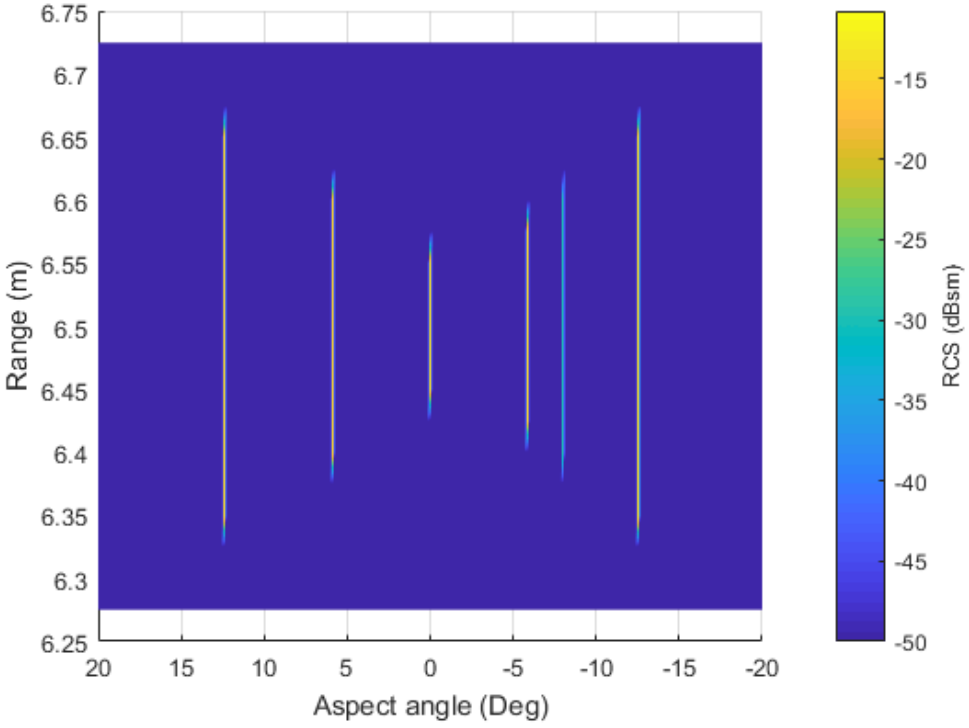

Figure 5-14: Image constructed by appling peak detection to the simulated Angular Profile (Figure 5-10) and combining this with the theoretical Range Spread model for a rotated cylinder [ACSR 150 GHz and $\Delta f \approx 5$ GHz]

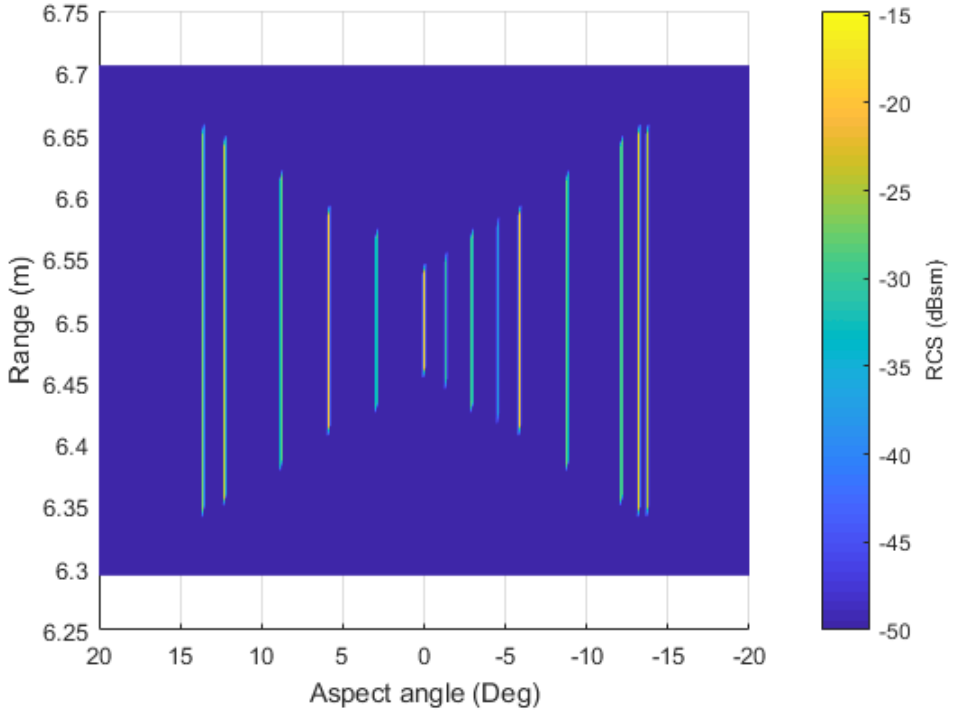

Figure 5-15: Image constructed by appling peak detection to the simulated Angular Profile (Figure 5-11) and combining this with the theoretical Range Spread model for a rotated cylinder [ACSR 300 GHz and $\Delta f \approx 16$ GHz]

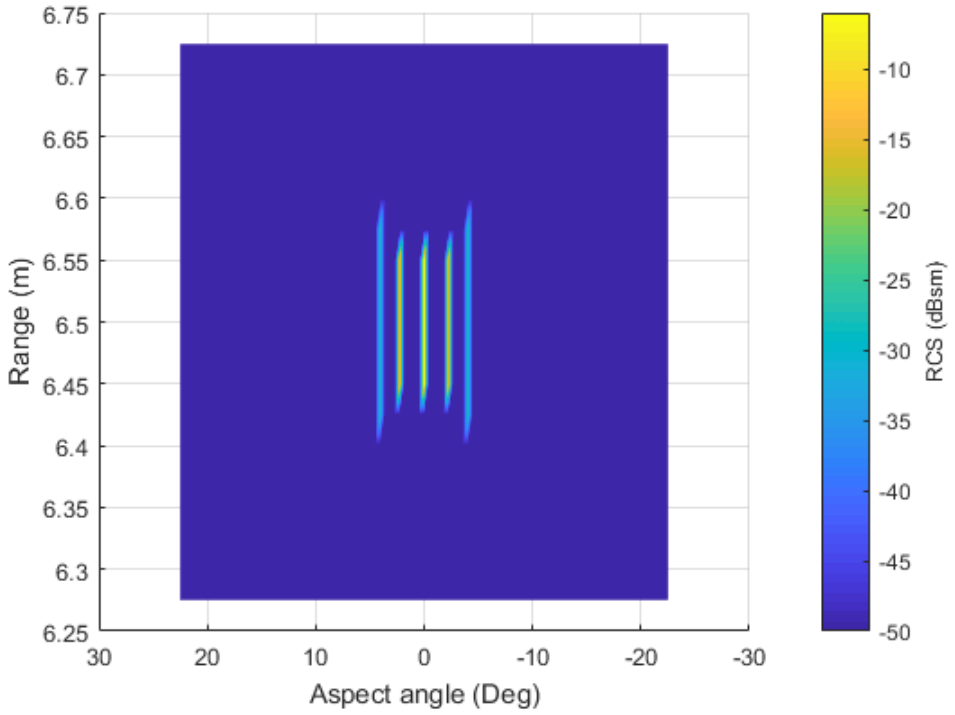

Figure 5-16: Image constructed by appling peak detection to the simulated Angular Profile (Figure 5-12) and combining this with the theoretical Range Spread model for a rotated cylinder [ACCC 150 GHz and $\Delta f \approx 5$ GHz]

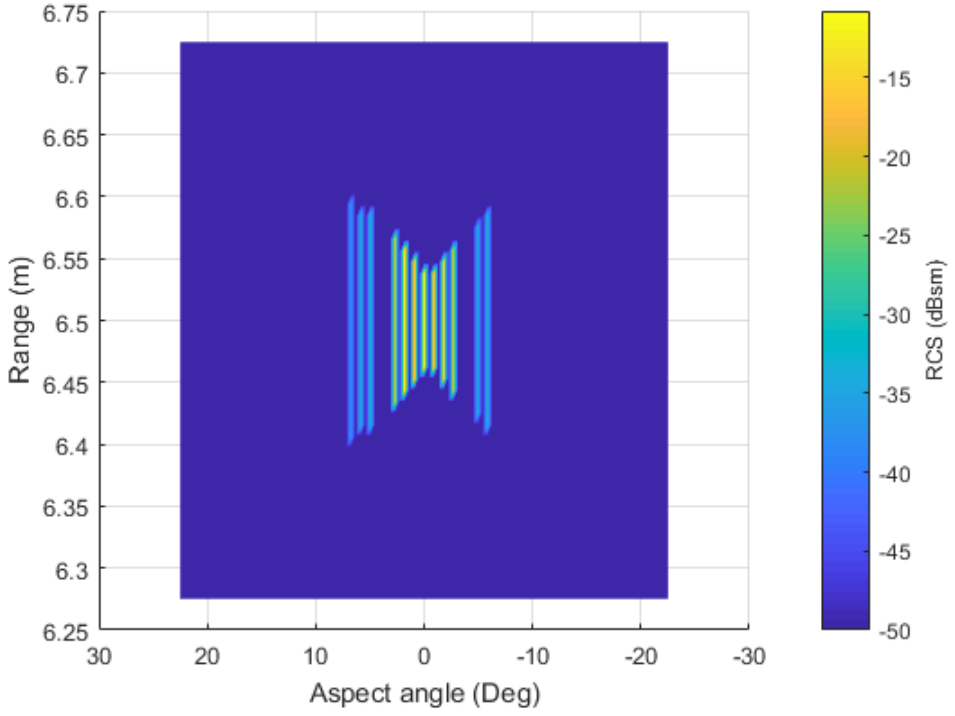

Figure 5-17: Image constructed by appling peak detection to the simulated Angular Profile (Figure 5-13) and combining this with the theoretical Range Spread model for a rotated cylinder [ACCC 300 GHz and $\Delta f \approx 16$ GHz]

5.2.2 Range Spread and Bragg Coupling

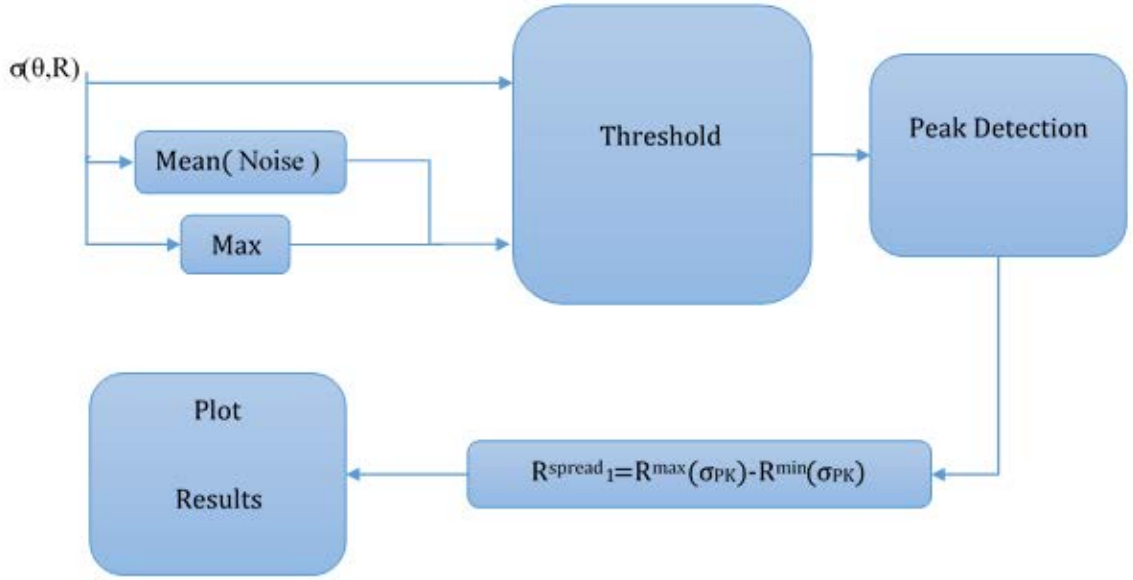

Figure 5-18: Range spread processing of measured image which consists of thresholding, peak detection and max and min range finding in the range profile gained at each aspect angle.

To measure the spread of cable backscatter in range, so that unique signatures for such targets can be obtained by processing high-resolution radar images, a technique was required that was robust to noise, clutter and other processing effects. Figure 5-18 shows a block diagram that is an overview of the processing performed to measure the range spread signatures presented. After measuring range profiles for a number of aspect angles a threshold method was required to separate cable returns from the noise and surrounding clutter. To do this without a large computation requirement and sophisticated theoretical basis, N_{min} samples of the lowest returns in the measured image was averaged and the maximum return from the cable was also stored. Through varying N_{min} and analysing the probability distribution function shape and mean value, a value of 50 samples was selected to calculate the threshold value. This

threshold value was halfway between the maximum stored value and the mean noise value on a decibel scale and only returns that were above or equal to this threshold were considered.

Subsequent to applying the previously defined threshold, a digital peak detection method that uses the derivative and second derivative of the 2D data to decide where maxima/peaks are present in the image was used. This peak finding method was performed to remove the effect of lobe widths on the range spread signature.

The final step in range spread processing was computing the nearest and furthest peak within the span of ranges and aspect angles that the cable was detectable.

5.2.2.1 Results & Analysis

This section will show the power cable range spread signatures obtained by using the processing previously described. These results will be compared with simulated results that were produced by using both the PO theory of cable scattering and the range spread theory described earlier in the thesis.

Figure 5-19 to Figure 5-22 are the resulting range spread signatures that were produced by inserting the measured images (Figure 5-2 to Figure 5-5) into the processing method described in Figure 5-18. Figure 5-23 to Figure 5-26 are a result of processing the theoretical images in Figure 5-14 to Figure 5-17 with the same technique.

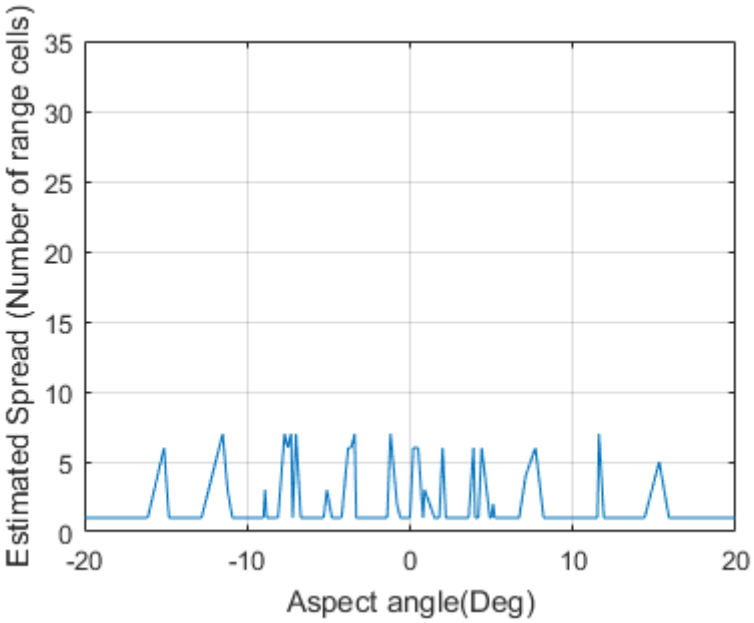

Figure 5-19: Measured range spread [ACSR, 150 GHz and $\Delta f \approx 5$ GHz]

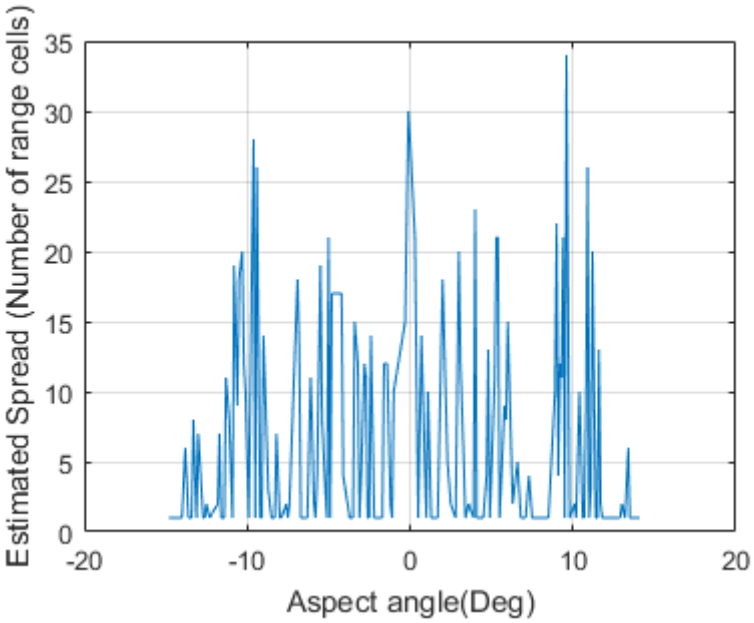

Figure 5-20: Measured range spread [ACSR, 300 GHz and $\Delta f \approx 16$ GHz]

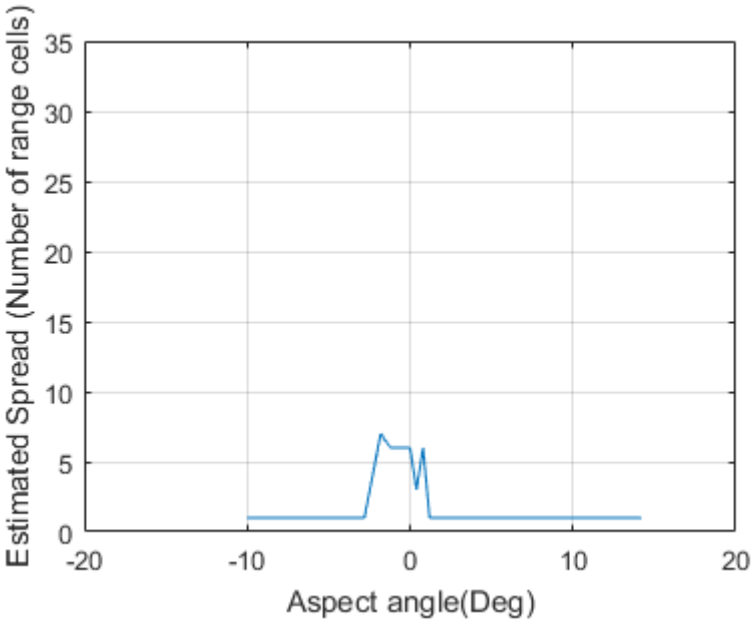

Figure 5-21: Measured range spread [ACCC, 150 GHz and $\Delta f \approx 5$ GHz]

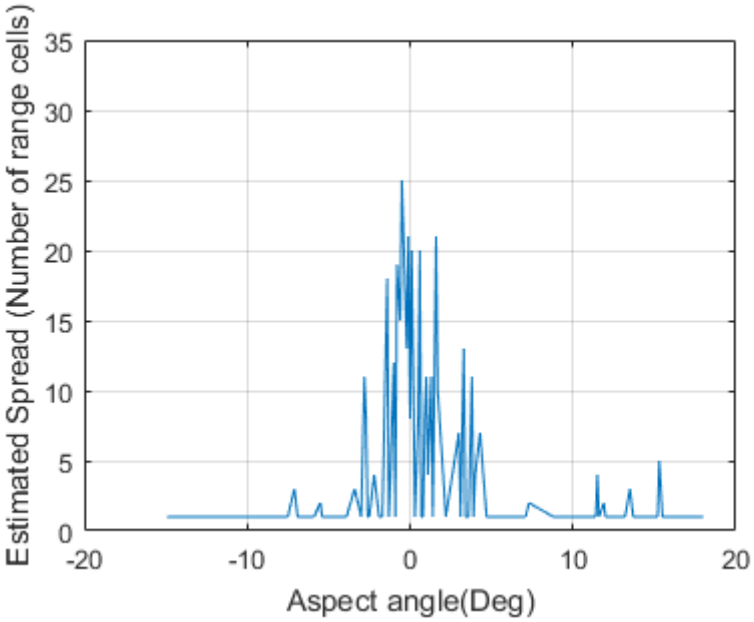

Figure 5-22 : Measured range spread [ACCC, 300 GHz and $\Delta f \approx 16$ GHz]

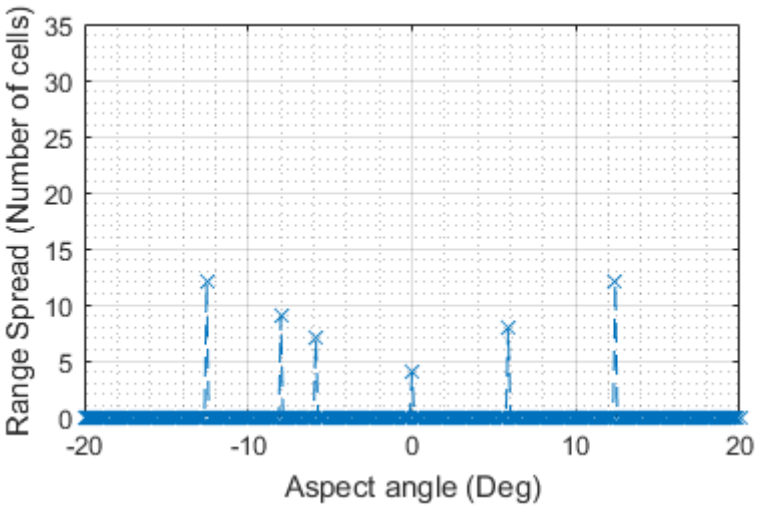

Figure 5-23: Simulated range spread [ACSR, 150 GHz and $\Delta f \approx 5$ GHz]

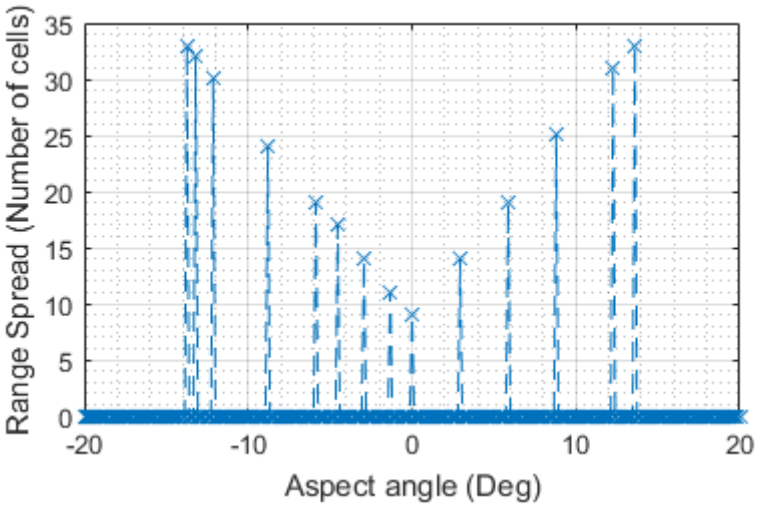

Figure 5-24: Simulated range spread [ACSR, 300 GHz and $\Delta f \approx 16$ GHz]

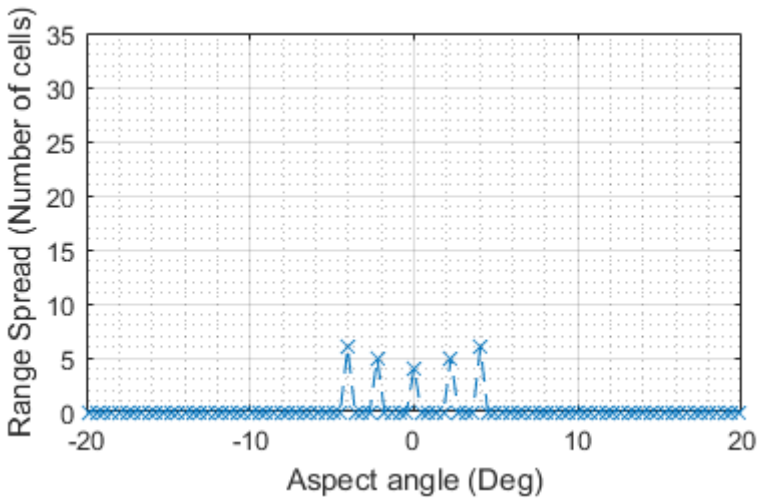

Figure 5-25: Simulated range spread [ACCC, 150 GHz and $\Delta f \approx 5$ GHz]

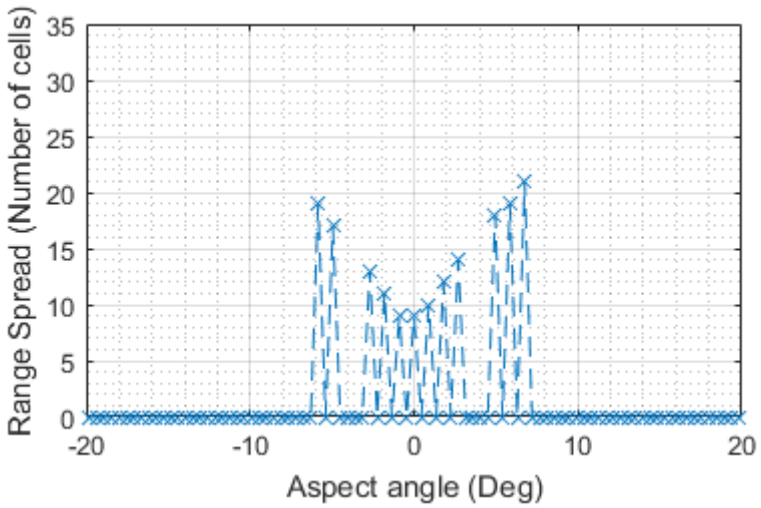

Figure 5-26: Simulated range spread [ACCC, 300 GHz and $\Delta f \approx 16$ GHz]

The measured and simulated mean, minimum and maximum range spread due to the cable being at a squint angle with respect to the radar (Figure 3-33) for each measurement are as follows:

- *ACSR, 150 GHz (*Figure 5-19 *and* Figure 5-23*)*

  Theory-Min: 4, Max: 12, Mean: 8.66

  Measured-Min: 3, Max: 7, Mean: 5.8

- *ACSR, 300 GHz (*Figure 5-20 *and* Figure 5-24*)*

Theory-Min: 9, Max: 33, Mean: 22.21

Measured-Min: 2, Max: 30, Mean: 9.45

- *ACCC, 150 GHz (*Figure 5-21 *and* Figure 5-25*)*

  Theory-Min: 4, Max: 6, Mean: 5.2

  Measured-Min: 3, Max: 7, Mean: 5.67

- *ACCC, 300 GHz (*Figure 5-22 *and* Figure 5-26*)*

  Theory-Min: 9, Max: 21, Mean: 14.3

  Measured-Min: 2, Max: 21, Mean: 9.6

Comments: The increased range resolution at 300 GHz (10mm) relative to the 25mm range resolution present with the 150 GHz system did ensure a larger spread for a given physical extent. One noticeable difference between theory and measurement was the minimum range spread measured remained at 2/3 cells regardless of the range resolution and this was not measured at around normal incidence as expected from theory. The scenario in which the measurement signature resembled most closely to the signature expected from a rotating cylinder was the ACSR measurement at 300 GHz (Figure 5-20). The increase in range resolution for this measurement as well as an expected increase in diffuse scattering are both the causes of the enhancement of the signature. Although diffuse scattering is expected to allow the radar to detect more of the cables' extent it will also reduce the distinct Bragg signature because of both the random variations of lobes angular positions and amplitudes which is clearly evident in Figure 5-7.

5.3 Summary

This chapter has displayed the results gathered from measuring both the ACSR and ACCC types of overhead power cables by using the 150 GHz FMCW and 300 GHz Stepped Frequency radar devices within the indoor Terahertz laboratory.

Images constructed by concatenating the range profiles measured at several aspect angles were analysed and compared with images constructed by combining the Physical Optics models and range spread theory. Each image was then summed in range to gain a RCS range profile that was compared with the simulated narrowband RCS profiles at the centre carrier frequencies used. The processing technique used to gain Range spread signatures from each of the images was described and the obtained plots were again compared with theoretical plots that combined range spread theory with the Physical Optics angular signatures that were normalised using the number of peaks in the profile and an analytical RCS formulae for a smooth PEC cylinder.

6. Conclusions and Future Work

6.1 Conclusions

Electromagnetic simulations of the most common type of overhead power cable (ACSR) are presented in Section 2.2 which use the Physical Optics approximation alongside the cable surface model in [43] at 16 GHz, 34 GHz, 150 GHz and 300 GHz. These simulations confirm the expectation of a higher number of Bragg modes at higher frequency values (Figure 2-7a) which was also expected in previous power cable theory [18] [38] [39]. A novel theoretical model of a more modern type of overhead power cable, ACCC, is also presented and show a reduction in Bragg Mode scattering due to the less prominent surface structure (Figure 2-7b).

Modelling that takes into account measured aircraft disturbances, atmospheric attenuation and overhead cable sagging parameters at 16 GHz, 34 GHz, 150 GHz and 300 GHz is presented in Section 2.8 that simulates the required transmit power for a given set of detection parameters. These transmit powers (Table 2-9) were compared with those obtained with idealised motion compensation (Table 2-10) to confirm the importance of motion compensation techniques in airborne radar and thus overhead cable detection. The transmit powers estimated for cable detection at 150 GHz and 300 GHz were deemed achievable in the near future by comparing them with current trends at these frequencies [7][8]. Validation for using devices at higher frequencies on airborne platforms is also discussed in terms of the practical antenna sizes in Section 2.7.2.

Airborne measurements of multiple overhead power cable lines presented here (Section 4) alongside simulations that combine a Physical Optics model of a straight power cable and Geometrical Sagging (Section 2.2, Section 2.3 and Section 4.5) jointly show a significant effect of cable sag on both the specular and Bragg lobe widths at Ku-band and Ka-

band. The previous effect allowed a cable hazard to be found in SAR imagery as a line had abnormally narrow lobes in the angular pattern measured which was caused by a tree pressing on the line (Figure 4-8) (Table 4-3). The Bragg lobe positions relative to specular were measured to be consistent for a given power line (Table 4-1) and these Bragg peaks produced reasonable estimated surface periods (Table 4-2) which were attainable using simple Bragg theory (Equation 1-26) and knowledge of the transmitted wavelength.

A developed model that combines both overhead cable signatures gained from the Physical Optics simulations (Section 2.2) with the cable extent at multiple incident angles (Section 1.3.4) was described in Section 5. This model becomes realistic for radar devices with sufficient range resolution and also resembles the cable signatures measured by devices at 150 GHz and 300 GHz that have range resolutions of the order of a centimetre (Section 3.2.3 and Section 3.2.4). This coupling between Bragg signatures (Section 5.2.2) and spread in range is a novel technique which has the potential to supress clutter in a practical scenario.

Some of the main parameters that are important when considering the feasibility of an airborne radar device operating above 100 GHz have been mentioned in the thesis. The main advantage of using devices in between 100 GHz and IR is the compactness of a potential radar device especially when rapid scanning is required for collision avoidance. Another important factor for the outdoor airborne application is the low scattering loss requirement in order to gain suitable detection distances even with the presence of dust/smoke. A device robust to adverse outdoor condition may not be possible using IR or optical devices and a practical microwave device may not have sufficient resolution to separate targets from clutter.

Transit powers estimations were shown in Section 2.8 for an airborne OH power cable detector with an acceptable probability detection whilst also having a satisfactory probability of false alarm due to noise. The estimated transmit power values at both 150 GHz and 300 GHz are

slightly larger than that present with current devices, such as the 150 GHz FMCW used to gather measurements, although technological advancements in the near future are expected to allow these transmit powers to be achievable at these frequencies. Another important factor is the target fluctuation as this will decide the alignment accuracy and scanning mechanism required. Moving up in frequency will cause fluctuations to increase for specular targets, however as shown here, Bragg and Diffuse scattering can reduce the target fluctuations with respect to aspect angle and this has the potential to reduce the need for expensive motion compensation devices for an airborne platform. So in all, advancements in power generation devices and other component manufacturing are considered the main requirements in regards to submillimetre-wave and Terahertz radar devices to become an affordable and hence a viable option for airborne radar in the future.

6.2 Future Research and Development

6.2.1 Airborne Overhead Cable Vulnerability Detector

The Ka-band and Ku-band results presented in Section 4 show the capability of measuring power line faults and vulnerabilities with currently available devices. The resolutions achievable with the I-Master and Bright Spark systems (Section 3.2.1) also allowed individual cables of a multi-cable distribution line to be observed in different range cells which allows any severe asymmetries in the overhead lines to be observed. It is proposed that a comparison is made between the costs of having one of these airborne systems to measure regions of interest with the cost of having ground inspectors inspecting distribution lines on a visually clear day. The radar devices would not necessarily need a reference cable signature for comparison to detect power line vulnerabilities as detecting changes in cable profiles over time may in fact give more information regarding the change in the condition of the cables. Climate information

may also be gained due to the effect of temperature and certain adverse weather conditions on cables.

6.2.2 Airborne Bragg Signature Detector

The theoretical results presented in Section 5.2.2, which were supported by measurements in Section 5.2.1, show the potential of measuring target extent within the Bragg peaks within a cable signature. This coupling between range spread and Bragg scattering will cause cable backscatter to be distinct from other types of illuminated objects such as vegetation or urban structures. This frequency also allows resolution of the order of a centimetre to be practical as well as having compact devices that can be mechanically scanned at high speeds to obtain images at an adequate refresh rate. Section 2.8 estimated the required transmit powers to get a high enough probability of detection of cables and low enough false alarm rate for Rayleigh noise for a potential transceiver. These presented cable detection simulation results (Figure 2-18 to Figure 2-21) did not include clutter suppression and a proposed millimetre-wave system that can measure adequately in range and scanning angle by measuring the spread in range (alongside appropriate range gating) should vastly reduce the presence of surrounding clutter due to the expected distinct high-resolution cable signatures. When devices that operate at around 150 GHz become available with transmit powers of the order of 10 dBm, it is proposed that such a system takes into account the ideas present in this work in order to produce a compact cable detection system which is robust to the presence of clutter.

Appendix A. 150 GHz Sphere Range Profiles

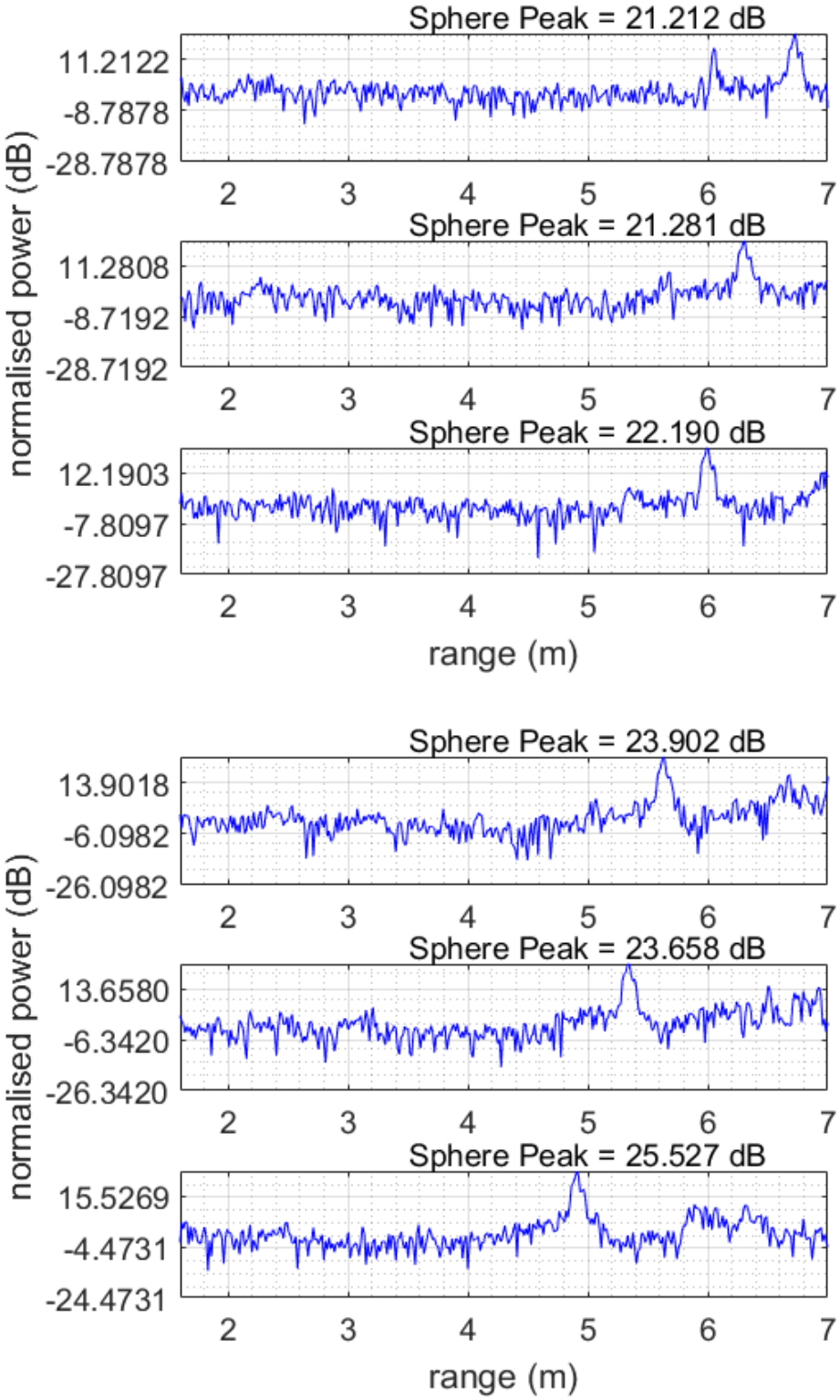

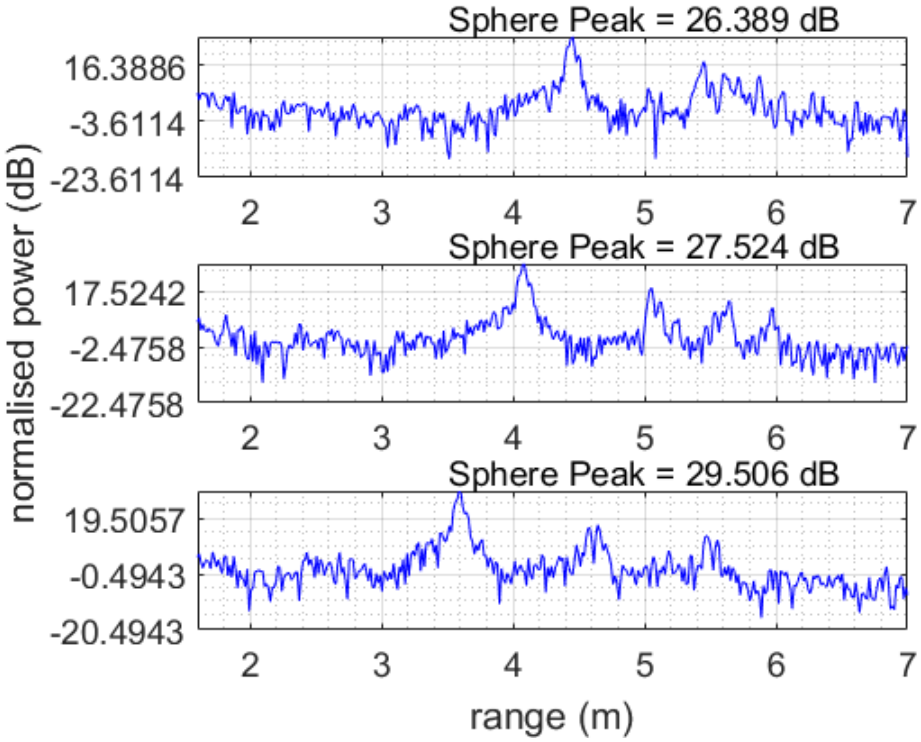
Sphere Peak = 26.389 dB
16.3886
-3.6114
-23.6114
Sphere Peak = 27.524 dB
17.5242
-2.4758
-22.4758
Sphere Peak = 29.506 dB
19.5057
-0.4943
-20.4943
2
3
4
5
6
7
normalised power (dB)
range (m)

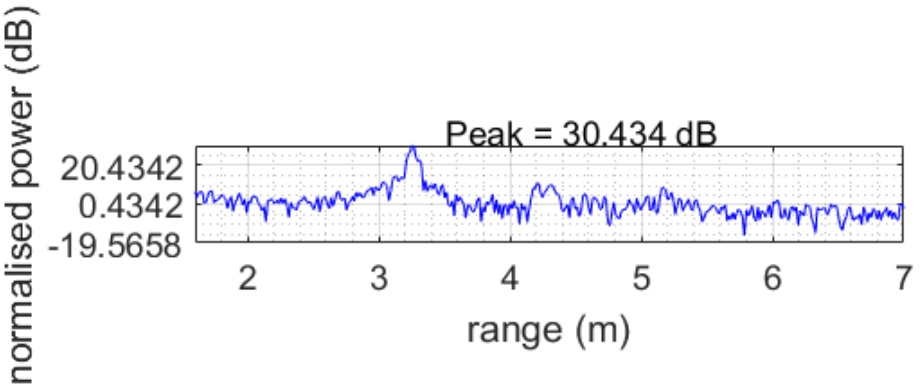
Peak = 30.434 dB
20.4342
0.4342
-19.5658
2
3
4
5
6
7
normalised power (dB)
range (m)

Appendix B. 300 GHz Sphere Range Profiles

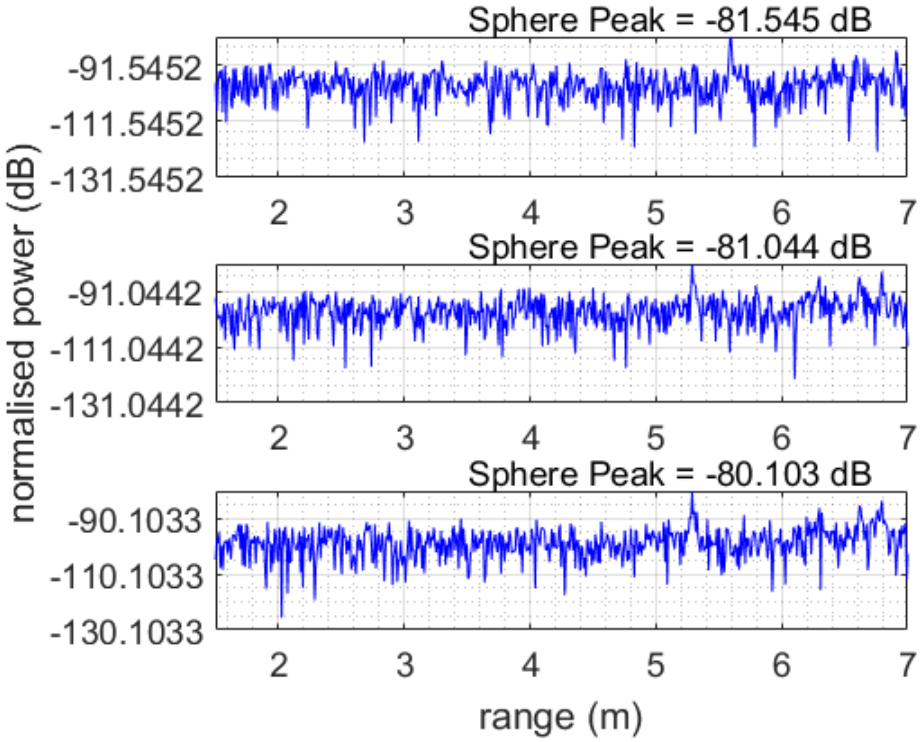

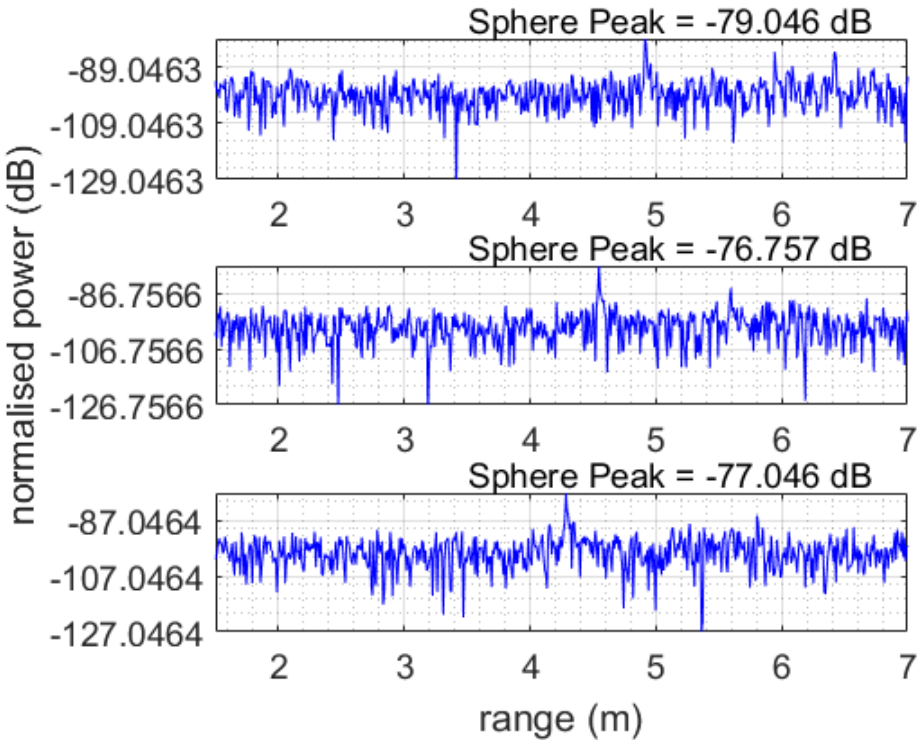

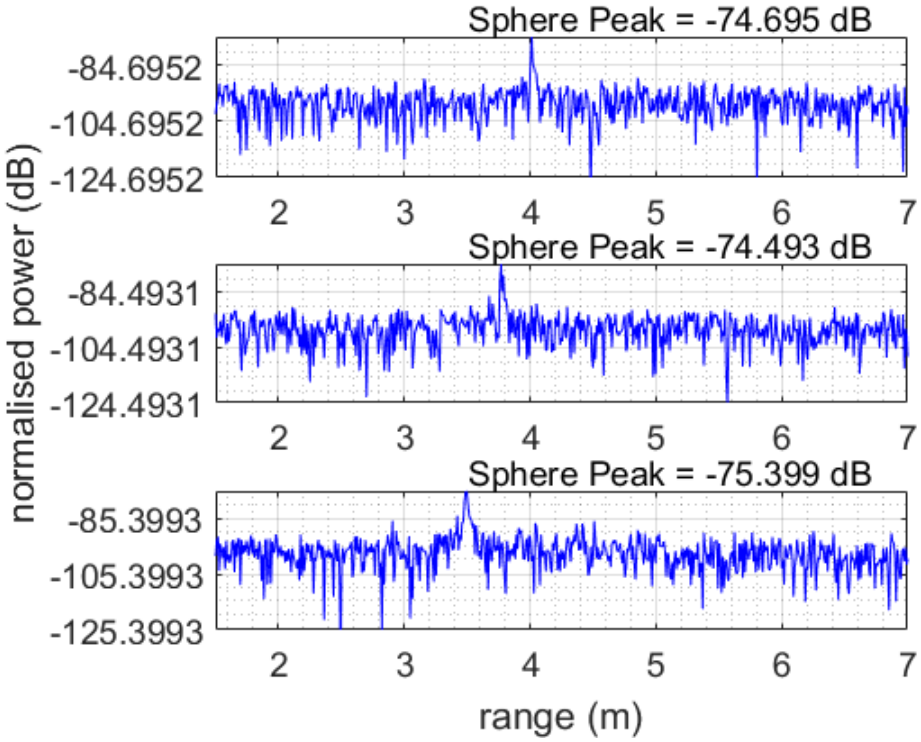
Sphere Peak = -74.695 dB
-84.6952
-104.6952
-124.6952
Sphere Peak = -74.493 dB
-84.4931
-104.4931
-124.4931
Sphere Peak = -75.399 dB
-85.3993
-105.3993
-125.3993
normalised power (dB)
2
3
4
5
6
7
range (m)

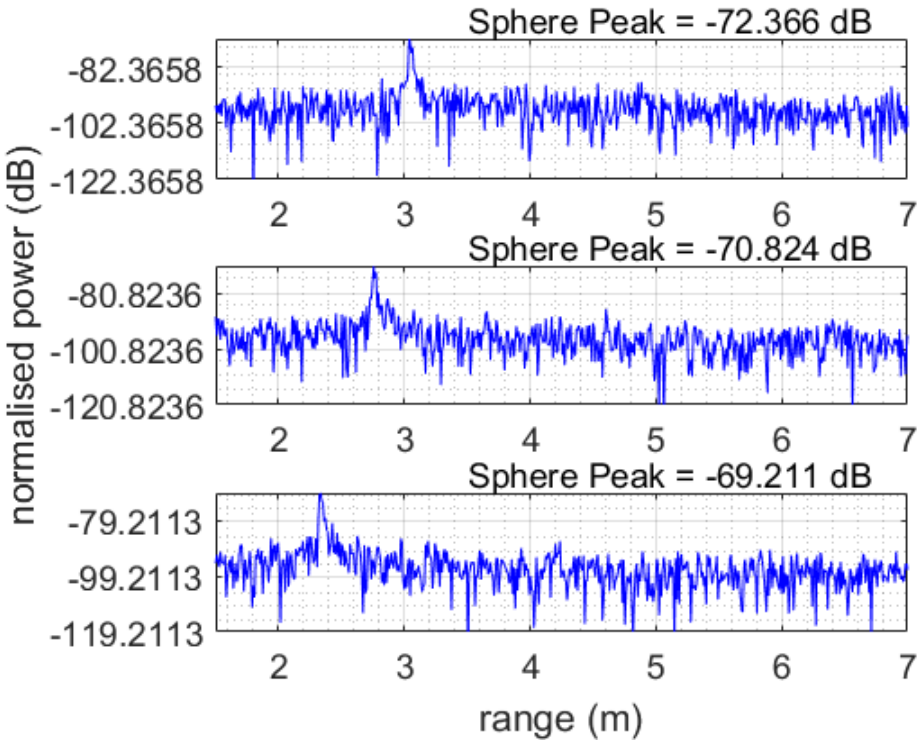
Sphere Peak = -72.366 dB
-82.3658
-102.3658
-122.3658
Sphere Peak = -70.824 dB
-80.8236
-100.8236
-120.8236
Sphere Peak = -69.211 dB
-79.2113
-99.2113
-119.2113
normalised power (dB)
2
3
4
5
6
7
range (m)

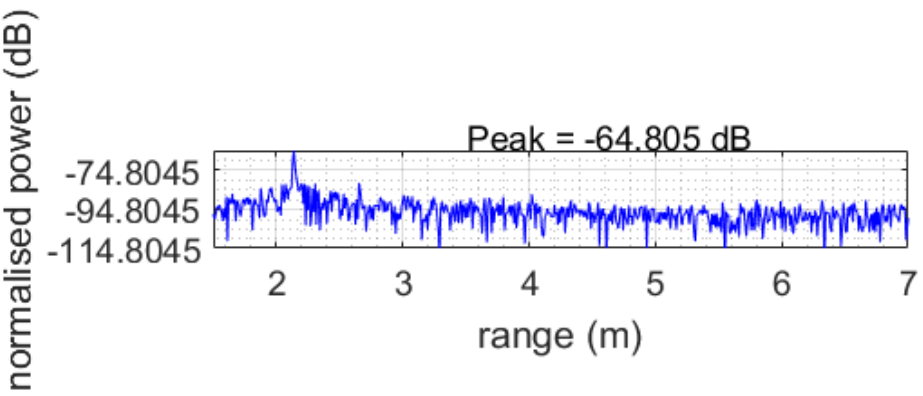
normalised power (dB)
Peak = -64.805 dB
-74.8045
-94.8045
-114.8045
2
3
4
5
6
7
range (m)

Appendix C. Ka-band Range-Doppler images of the Pylon Scenario (Specular region)

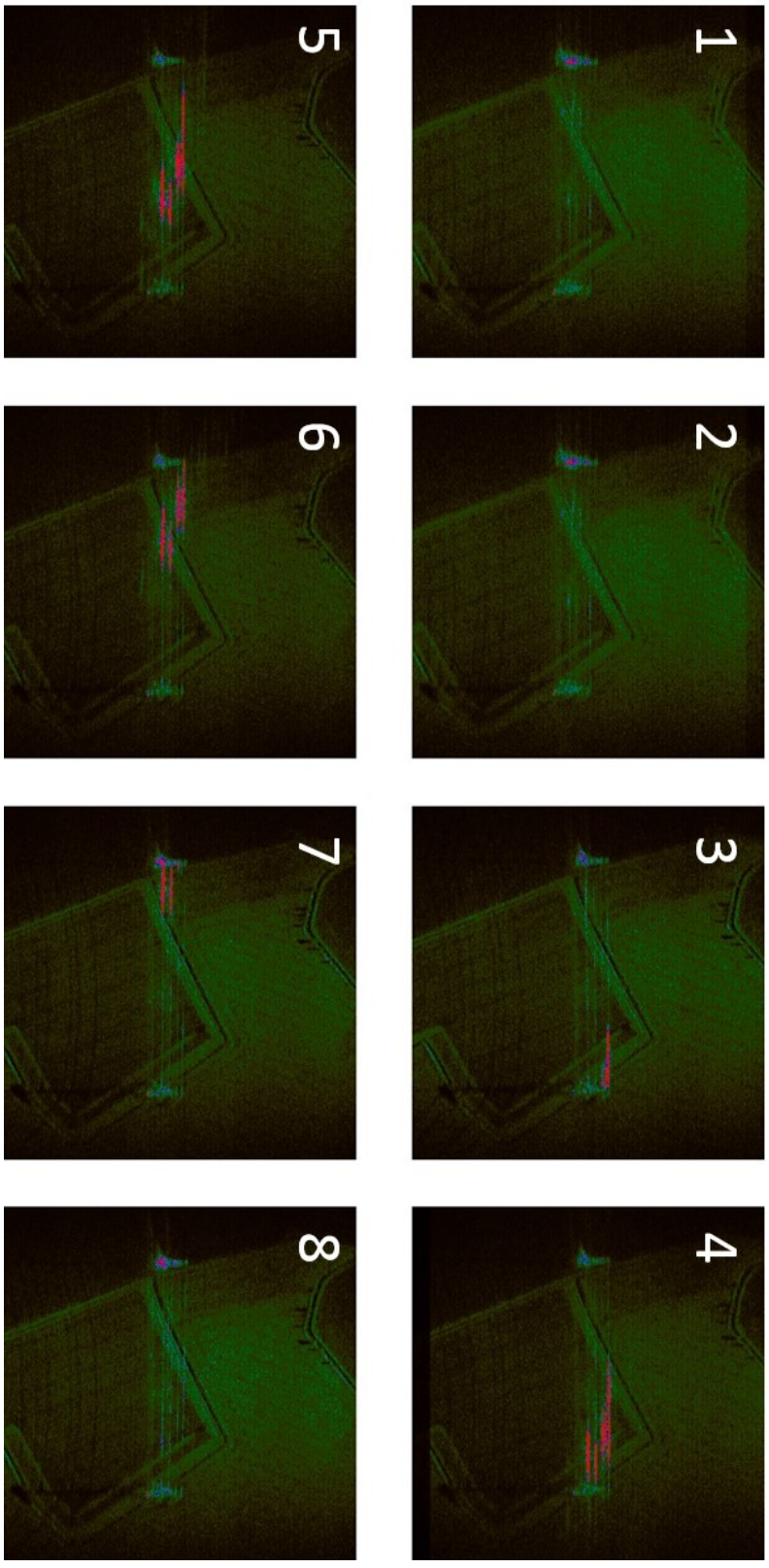

Appendix D. Ka-band Range-Doppler images of the Pylon Scenario (Bragg region)

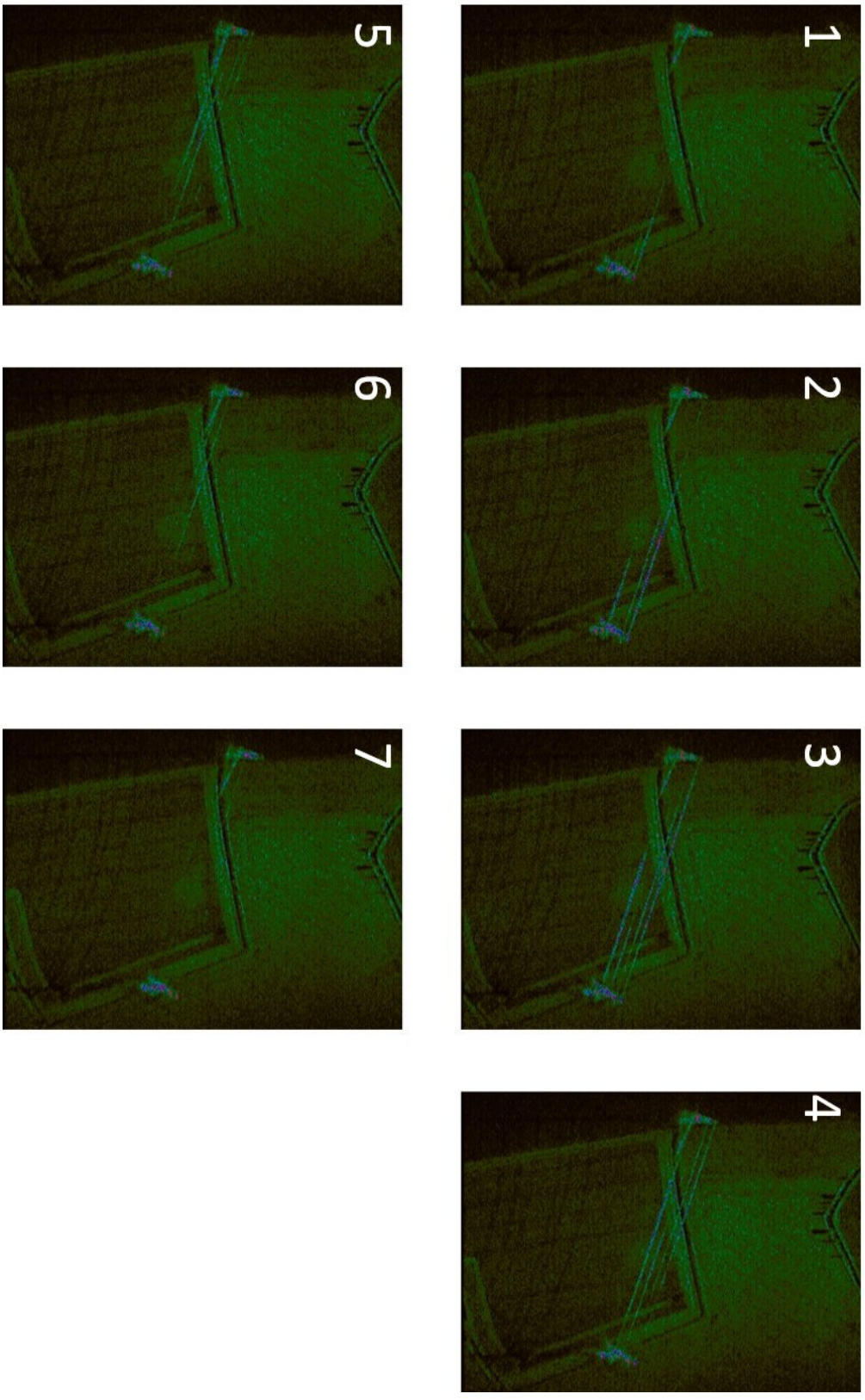

References

[1] Air Accidents Investigation Branch, “AAIB Bulletin 12/2011”, December 2011.
[2] Air Accidents Investigation Branch, “AAIB Bulletin 9/2012”, September 2012.
[3] Air Accidents Investigation Branch, “AAIB Bulletin 5/2014”, May 2014.
[4] C.L. Hayes, “Reflection Coefficients for Wires and Cables at 10.6μm," Appl. Opt., Vol. 12, No. 7, pp. 1564-1569, 1973.
[5] M. Savan, D. N. Barr, Retroreflectance of wires and cables at 10.6 micrometers, Fort Belvoir, Virginia, Report, January 1988.
[6] CCIR Report 233-3 Question 2-2/5.Specialists, "Flying in the Wire Environment," 2013. [Online]. Available: http://www.helicoptersafety.com/training/fitwe.php [Accessed 27 August 2014].
[7] Stove, "Potential applications for low- Tera-Hertz radar", Radar Symposium (IRS) 2015 16th International, pp. 191-196, 24–26 June 2015.
[8] D. R. Vizard, E. G. Hoare, M. Gashinova and M. Cherniakov, "A novel 670 GHz hybrid frequency extender for portable automotive radar applications," 2017 18th International Radar Symposium (IRS), Prague, 2017, pp. 1-5.
[9] J. R. Klauder, A. C. Price, S. Darlington and W. J. Albersheim, "The theory and design of chirp radars," in The Bell System Technical Journal, vol. 39, no. 4, pp. 745-808, July 1960.
[10] H. Griffiths, Some Reflections on the History of Radar from its Invention up to the Second World War, James Clerk Maxwell Foundation, Issue No. 8, Spring 2017.
[11] Lovell, *Echoes of war*. Hilger, 1991.
[12] C. Jenn, Radar and Laser Cross Section Engineering; Second Edition. 2005.
[13] J. Arthur and D. Forfar, The Changing Notation of Maxwell’s Equations, James Clerk Maxwell Foundation, Issue No. 2, Autumn 2012.
[14] M. Skolnik, Introduction to radar systems. Boston , Boston: McGraw-Hill 2007.
[15] C. Balanis, “Advanced engineering electromagnetics”. Hoboken: J. Wiley & Sons, 2012.
[16] G. Brooker, Sensors for ranging and imaging. Raleigh: SciTech, 2009.
[17] Knott, J. Shaeffer and M. Tuley, Radar cross section. Broadstairs: Scitech, 2013.
[18] H. Al- Khatib, "Laser and millimeter-wave backscatter of transmission cables,” Proc. SPIE 0300, p.212, 1981.
[19] J. A. Richards, Remote Sensing with Imaging Radar, 1st ed., Heidelberg: Springer, 2009.
[20] J. W. Strutt, "Resolving or separating power of optical instruments", Phil. Mag., vol. VIII, pp. 261-274, 1879.
[21] M. M. Horst and B. Perry, "MMW Modeling Techniques," in Principles and applications of millimeter-wave radar, N. C. Currie and C. E. Brown, Eds., Norwood, ARTECH HOUSE INC, 1987, pp. 313-394.
[22] R. Hua et al., " Experimental Investigation on LGJ-400/50 ACSR Surface Erosion Characteristics in Wind Sand Environment", Advanced Materials Research, Vol. 1035, pp. 36-40, 2014.
[23] M. B. Stevens and D. L. Perks, "I-Master RADAR: Recent trials results," IET International Conference on Radar Systems (Radar 2012), Glasgow, UK, 2012, pp. 1-5.
[24] M. Jahangir, D. Coe, A. P. Blake, P. G. Kealey and C. P. Moate, "PodSAR: A versatile real-time SAR GMTI surveillance and targeting system," 2008 IEEE Radar Conference, Rome, 2008, pp. 1-6.

[25] W. C. Carrara, Spotlight Synthetic Aperture Radar: Signal Processing Algorithms, 1995.
[26] D. T. Emerson, "The work of Jagadis Chandra Bose: 100 years of millimeter-wave research," in IEEE Transactions on Microwave Theory and Techniques, vol. 45, no. 12, pp. 2267-2273, Dec 1997.
[27] M. Tonouchi, "Cutting-edge terahertz technology," Nature Photonics , vol. 1, pp. 97 - 105 , 2007.
[28] R. W. McMillan, "TERAHERTZ IMAGING, MILLIMETER-WAVE RADAR," in Advances in Sensing with Security Applications , vol. 2, J. Byrnes and G. Ostheimer, Eds., Springer Netherlands, 2006, pp. 243-268.
[29] U. Shian, K. B. deSilva and C. T. Jih, "Terahertz (THz) Wireless Systems for Space Applications," 2013. [Online]. Available: http://ntrs.nasa.gov/archive/nasa/casi.ntrs.nasa.gov/20130009186.pdf. [Accessed 12 September 2014].
[30] D. Jasteh, "THz sensing in front of Vehicle (Ground Profiling)," 2014. [Online]. Available: http://www.birmingham.ac.uk/Documents/college-eps/eece/research/MISL/220-THz-Sensing-In-Front-of-the-Vehicle-NEW.pdf. [Accessed 22 November 2014].
[31] N. Oda, "Development of Terahertz Focal Plane Arrays and Handy Camera," 2011.
[32] B. Wallace, "Analysis of RF imaging applications at frequencies over 100 GHz," APPLIED OPTICS, vol. 49, no. 19, pp. E38-E47, 2010.
[33] W. D. Palmer, I. Abdomerovic, P. M. Asbeck, T. LaRocca and S. Raman, "Advancing silicon mm-wave transmitter ICs for satellite communications," 2014 IEEE International Microwave and RF Conference (IMaRC), Bangalore, 2014, pp. 49-52.
[34] M. Gashinova, E. Hoare and A. Stove, "Predicted sensitivity of a 300GHz FMCW radar to pedestrians," 2016 European Radar Conference (EuRAD), London, 2016, pp. 350-353.
[35] E. Marchetti et al., "Comparison of pedestrian reflectivities at 24 and 300 GHz," 2017 18th International Radar Symposium (IRS), Prague, 2017, pp. 1-7.
[36] D. Jasteh, E. G. Hoare, M. Cherniakov and M. Gashinova, "Experimental Low-Terahertz Radar Image Analysis for Automotive Terrain Sensing," in IEEE Geoscience and Remote Sensing Letters, vol. 13, no. 4, pp. 490-494, April 2016.
[37] B. Wallace, DARPA MMW Systems programs and how they drive technology needs, DMRC Millimeter-Wave Technology Workshop, October 2014.
[38] K. Sarabandi, "Power line: radar measurement and detection algorithm for polarimetric SAR images," IEEE Trans. Aerosp. Electron. Syst., Vol. 30, No.2, pp.632-643, 1994.
[39] K. Sarabandi, "Millimeter-Wave Radar Phenomenology of Power Lines and a Polarimetric Detection Algorithm," IEEE Trans. Antennas Propag., Vol. 47, No. 12, pp.1807-1813, 1999.
[40] B. Kapilevich, "Detecting power lines using 330GHz FMCW sensor," 2011.
[41] Southwire Company, "ACSR," 2015. [Online]. Available: http://www.southwire.com/products/ACSR.htm. [Accessed 18 March 2015].
[42] zmscable.com , "ACSR Conductor, Aluminum Conductors Steel Reinforced," 2010. [Online]. Available: http://www.zmscable.com/ACSR-conductor.html. [Accessed 18 March 2015].
[43] K. Sarabandi and Moonsoo Park, "A radar cross-section model for power lines at millimeter-wave frequencies," in IEEE Transactions on Antennas and Propagation, vol. 51, no. 9, pp. 2353-2360, Sep 2003.
[44] CTC Global Corporation, “Engineering Transmission Lines with High Capacity Low Sag ACCC Conductors”, 2011.

[45] B. Willetts, M. Gashinova, A. Stove, C. C. Constantinou, E. G. Hoare and E. Marchetti, "Low-THz overhead power cable signatures: The effect of surface features on Low-THz reflectivities," 2016 17th International Radar Symposium (IRS), Krakow, 2016, pp. 1-6.
[46] D.P. Meyer, H.A. Mayer, "Radar Target Detection: Handbook of Theory and Practice", Academic Press, pp. 77, 1973.
[47] A.S. Hall, F.E. Archer, R.I. Gilbert, "Engineering Statics", 2nd Edition, New South Publishing, 1999.
[48] B. Persson and P. Bull. "Empirical Study of Flight-Dynamic Influences on Radar Cross-Section Models", Journal of Aircraft, Vol. 53, No. 2, pp. 463-474, 2016
[49] C. Pon, "High Temperature – Sag characterization test on 1020 kcmil ACCC/TW conductor for composite technology corporation", Kenectrics North America Inc. Report No.: K-422024-RC-0003-R00, February 2004.
[50] R. Appleby and R. N. Anderton, "Millimeter-Wave and Submillimeter-Wave Imaging for Security and Surveillance," in Proceedings of the IEEE, vol. 95, no. 8, pp. 1683-1690, Aug. 2007.
[51] M. Gashinova, E. Hoare, and A. Stove, "Predicted Sensitivity of a 300GHz FMCW Radar to Pedestrians," Proc. 13th.European Radar Conf., Eurad-2016, London, pp 350-3, 2016.
[52] M. B. Stevens and D. L. Perks, "I-Master RADAR: Recent trials results," IET International Conference on Radar Systems, Glasgow, UK, 2012, pp. 1-5.
[53] M. B. Stevens, O Jones, P Moyse, S Tu, A Wilshire, "Bright spark: Ka-band SAR technology demonstrator", IET RADAR 2017.
[54] W. C. Carrara, 'Spotlight SAR and Polar Format Algorithm' in *Spotlight Synthetic Aperture Radar: Signal Processing Algorithms*, Artech House, 1995.
[55] J. G. Proakis and D. G. Manolakis, Digital signal processing. Upper Saddle River, New Jersey: Prentice-Hall International, 1996.
[56] Elva-1(Millimeter Wave Division). [Online]. Available: http://www.elva-1.com.
[57] M. Jankiraman, Design of multi-frequency CW radars: SciTech Publishing, 2007.
[58] D. Jasteh, "Experimental Low-THz Imaging Radar for Automotive Applications ", Doctoral Thesis, UOB, 2016.
[59] N9918A FieldFox Handheld Microwave Analyzer, 26.5 GHz | Keysight (formerly Agilent's Electronic Measurement)", Keysight.com, 2017. [Online]. Available: http://www.keysight.com/en/pdx-x201927-pn-N9918A/fieldfox-handheld-microwave-analyzer-265-ghz?cc=GB&lc=eng. [Accessed: 29- Sep- 2017].
[60] VivaTech", Vivatech.biz, 2017. [Online]. Available: http://www.vivatech.biz/. [Accessed: 29- Sep- 2017].
[61] "Eastern Power Networks PLC Distribution Area, 400kV, 275kV, 132kV and 33kV systems" in UK Power Networks, 2013. [Online]. Available: http://www.ukpowernetworks.co.uk/internet/asset/756bb4e3-719f-43f2-a0de-0b40dafd267P/EPN-132-EHV-NG-Map-Nov2013.pdf/. Accessed: Nov. 2017.
[62] "Waddesdon", Waddesdon, 2017. [Online]. Available: https://www.google.co.uk/maps/place/Waddesdon,+Aylesbury/@51.8525338,-0.9359405,646m/data=!3m1!1e3!4m5!3m4!1s0x4876f00b429f05ed:0xdbb8c6f6bf5fbe8a!8m2!3d51.845396!4d-0.917426. [Accessed: 29- Sep- 2017].
[63] Health and Safety Executive, "Avoiding danger from overhead power lines", GS6, HSE Books, 2013.
[64] " TF - National Grid high-voltage cable location, Electricity Network Overhead Lines National Grid", Www2.nationalgrid.com, 2017. [Online]. Available:

http://www2.nationalgrid.com/uk/services/land-and-development/planning-authority/electricity-network-overhead-lines/. [Accessed: 29- Sep- 2017].

[65] "UK | National Grid", Www2.nationalgrid.com, 2017. [Online]. Available: http://www2.nationalgrid.com/uk/. [Accessed: 29- Sep- 2017].

[66] Spalding Marsh", Spalding Marsh, 2017. [Online]. Available: https://www.google.co.uk/maps/place/Spalding+Marsh,+Spalding/@52.8182396,-0.0881565,628m/data=!3m1!1e3!4m5!3m4!1s0x4878066af82dbcff:0x850a3960461c9500!8m2!3d52.85015!4d-0.076256. [Accessed: 29- Sep- 2017].

[67] "The National Grid Power Systems Research Centre, The University of Manchester: School of Electrical and Electronic Engineering", Eee.manchester.ac.uk, 2017. [Online]. Available: http://www.eee.manchester.ac.uk/our-research/research-groups/eeps/the-national-grid-psrc/. [Accessed: 29- Sep- 2017].

[68] F. Norouzian et al., "Monostatic and bistatic reflectivity measurements of radar absorbers at low-THz frequency," 2016 European Radar Conference (EuRAD), London, 2016, pp. 117-120.

[69] Parkermotion.com. Stepper Drive/Controllers - PDS & PDX Packaged Mini-stepping Systems, Parker Hannifin, 2009, [online] Available at: http://www.parkermotion.com/products/Stepper_Drives_and_Motors__1901__30_3_80_567_29.html [Accessed 3 Aug. 2015].

[70] Gill P.E., Murray W. (1976) Nonlinear least squares and nonlinearly constrained optimization. In: Watson G.A. (eds) Numerical Analysis. Lecture Notes in Mathematics, vol 506. Springer, Berlin, Heidelberg.

[71] R. G. Kouyoumjian and P. H. Pathak, "A uniform geometrical theory of diffraction for an edge in a perfectly conducting surface," in Proceedings of the IEEE, vol. 62, no. 11, pp. 1448-1461, Nov. 1974.